UNIVERSITÀ DEGLI STUDI DI VERONA

SCIENZE CHIRURGICHE ODONSTOMOLOGICHE E MATERNO-INFANTILI
SCUOLA DI DOTTORATO DI SCIENZE DELLA VITA E DELLA SALUTE
DOTTORATO DI RICERCA IN SCIENZE CARDIOVASCOLARI

DEVELOPMENT AND IMPLEMENTATION OF NOVEL STRATEGIES TO EXPLOIT 3D ULTRASOUND IMAGING IN CARDIOVASCULAR COMPUTATIONAL BIOMECHANICS

S.S.D. ING-IND/34

Tutor:
Prof. Giovanni Battista LUCIANI

Advisors:
Prof. Emiliano VOTTA
Dott. Francesco ONORATI
Prof. Alberto REDAELLI

Supervisor of the Ph.D. Program:
Prof. Giovanni Battista LUCIANI

Ph.D. Candidate:
MATTEO SELMI

XXXI Cycle

“Essentially

all models are wrong,

but some are useful”

(George Edward Pelham Box, 1919-2013)

... to everyone who (wilfully or not) took part in this umpteenth (life) project.

Table of Contents

Abstract

Introduction

In the past two decades, major advances have been made in cardiovascular diseases assessment and treatment owing to the advent of sophisticated and more accurate imaging techniques, allowing for better understanding the complexity of 3D anatomical cardiovascular structures[1]. Volumetric acquisition enables the visualization of cardiac districts from virtually any perspective, better appreciating patient-specific anatomical complexity, as well as an accurate quantitative functional evaluation of chamber volumes and mass avoiding geometric assumptions[2]. Additionally, this scenario also allowed the evolution from generic to *patient-specific* 3D cardiac models that, based on *in vivo* imaging, faithfully represent the anatomy and different cardiac features of a given alive subject, being pivotal either in diagnosis and in planning guidance[3]. Precise morphological and functional knowledge about either the heart valves' apparatus and the surrounding structures is crucial when dealing with diagnosis as well as preprocedural planning[4]. To date, computed tomography (CT) and real-time 3D echocardiography (rt3DE) are typically exploited in this scenario since they allow for encoding comprehensive structural and dynamic information even in the fourth dimension (i.e., time)[5,6]. However, owing to its cost-effectiveness and very low invasiveness, 3D echocardiography has become the method of choice in most situations for performing the evaluation of cardiac function, developing geometrical models which can provide quantitative anatomical assessment[7].

Complementing this scenario, computational models have been introduced as numerical engineering tools aiming at adding qualitative and quantitative information on the biomechanical behavior in terms of stress-strain response and other multifactorial parameters[8]. In particular, over the two last decades, their applications have been ranging from elucidating the heart biomechanics underlying different patho-physiological conditions[9] to predicting the effects of either surgical or percutaneous procedures, even comparing several implantation techniques and devices[10]. At the early stage, most of the studies focused on FE modeling in cardiac environment were based on paradigmatic models[11–15], being mainly exploited to explore and investigate biomechanical alterations following

a specific pathological scenario or again to better understand whether a surgical treatment is better or worse than another one. Differently, nowadays the current generation of computational models heavily exploits the detailed anatomical information yielded by medical imaging to provide patient-specific analyses, paving the way toward the development of virtual surgical-planning tools[16–19].
In this direction, cardiac magnetic resonance (CMR) and CT/micro-CT are the mostly accomplished imaging modality, since they can provide well-defined images thanks to their spatial and temporal resolutions[20–25]. Nonetheless, they cannot be applied routinely in clinical practice, as it can be differently done with rt3DE, progressively became the modality of choice[26] since it has no harmful effects on the patient and no radiopaque contrast agent is needed.
Despite these advantages, 3D volumetric ultrasound imaging shows intrinsic limitations beyond its limited resolution: i) the deficiency of morphological detail owing to either not so easy achievable detection (e.g., tricuspid valve) or not proper acoustic window, ii) the challenge of tailoring computational models to the patient-specific scenario mimicking the morphology as well as the functionality of the investigated cardiac district (e.g., tethering effect exerted by chordal apparatus in mitral valve insufficiency associated to left ventricular dilation), and iii) the needing to systematically analyse devices performances when dealing with real-life cases where ultrasound imaging is the only performable technique but lacking of standardized acquisition protocol.

Main findings

In the just described scenario, the main aim of this work was focused on the implementation, development and testing of numerical strategies in order to overcome issues when dealing with 3D ultrasound imaging exploitation towards predictive patient-specific modelling approaches focused on both morphological and biomechanical analyses.

Specifically, the first specific objective was the development of a novel approach integrating in vitro imaging and finite element (FE) modeling to evaluate tricuspid valve (TV) biomechanics, facing with the lack of information on

anatomical features owing to the clinically evident demanding detection of this anatomical district through *in vivo* imaging.

- An innovative and semi-automated framework was implemented to generate 3D model of TV, to quantitively describe its 3D morphology and to assess its biomechanical behaviour. At this aim, an image-based in vitro experimental approach was integrated with numerical models based on FE strategy. Experimental measurements directly performed on the benchmark (mock circulation loop) were compared with geometrical features computed on the 3D reconstructed model, pinpointing a global good consistency. Furthermore, obtained realistic reconstructions were used as the input of the FE models, even accounting for proper description of TV leaflets' anisotropic mechanical response. As done experimentally, simulations reproduced both "incompetent" (FTR) and "competent-induced" (PMA), proving the efficiency of such a treatment and suggesting translational potential to the clinic.

The second specific aim was the implementation of a computational framework able to reproduce a functionally equivalent model of the mitral valve (MV) sub-valvular apparatus through chordae tendineae topology optimization, aiming at chordae rest length arrangement to be able to include their pre-stress state associated to specific ventricular conformation.

- We sought to establish a framework to build geometrically tractable, functionally equivalent models of the MV chordae tendineae, addressing one of the main topics of the computational scientific literature towards the development of faithful patient-specific models from *in vivo* imaging. Exploiting the mass spring model (MSM) approach, an iterative tool was proposed aiming to the topology optimization of a paradigmatic chordal apparatus of MVs affected by functional regurgitation, in order to be able to equivalently account for tethering effect exerted by the chordae themselves. The results have shown that the algorithm actually lowered the error between the simulated valve and *ground truth* data, although the intensity of this improvement is strongly valve-dependent.

Finally, the last specific aim was the creation of a numerical strategy able to allow for patient-specific geometrical reconstruction both pre- and post- LVAD implantation, in a specific high-risk clinical scenario being rt3DE the only available imaging technique to be used but without any acquisition protocol.

- We proposed a numerical approach which allowed for a systematic and selective analysis of the mechanism associated to intraventricular thrombus formation and thrombogenic complications in a LVAD-treated dilated left ventricle (LV). Ad-hoc geometry reconstruction workflow was implemented to overcome limitations associated to imaging acquisition in this specific scenario, thus being able to generate computational model of the LV assisted with LVAD. In details, results suggested that blood stasis is influenced either by LVAD flow rate and, to a greater extent, by LV residual contractility, being the positioning of the inflow cannula insertion mandatory to be considered when dealing with LVAD thrombogenic potential assessment.

Bibliography

1. Zoghbi, W. A. Cardiovascular Imaging: A Glimpse Into The Future. *Methodist Debakey Cardiovasc. J.* **10,** 139–145 (2014).
2. Hung, J. *et al.* 3D Echocardiography: A Review of the Current Status and Future Directions. *J. Am. Soc. Echocardiogr.* **20,** 213–233 (2007).
3. Chandra, S. *et al.* A three-dimensional insight into the complexity of flow convergence in mitral regurgitation: adjunctive benefit of anatomic regurgitant orifice area. *Am. J. Physiol. Heart Circ. Physiol.* **301,** H1015-24 (2011).
4. Ionasec, R. I. *et al.* Patient-specific modeling and quantification of the aortic and mitral valves from 4-D cardiac CT and TEE. *IEEE Trans. Med. Imaging* **29,** 1636–51 (2010).
5. Caiani, E. G. *et al.* Quantification of mitral annulus dynamic morphology in patients with mitral valve prolapse undergoing repair and annuloplasty during a 6-month follow-up. *Eur. J. Echocardiogr.* **12,** 375–83 (2011).
6. Elattar, M. A. *et al.* Dynamics of the aortic annulus in 4D CT angiography for transcatheter aortic valve implantation patients. *PLoS One* **12,** e0184133 (2017).
7. Noack, T. *et al.* Four-dimensional modelling of the mitral valve by real-time 3D transoesophageal echocardiography: proof of concept. *Interact. Cardiovasc. Thorac. Surg.* **20,** 200–8 (2015).
8. Zuin, M., Rigatelli, G., Faggian, G. & Roncon, L. Mathematics and Cardiovascular Interventions: Role of the Finite Element Modeling in Clinical Decision Making. *JACC. Cardiovasc. Interv.* **9,** 507–8 (2016).
9. Votta, E. *et al.* A novel approach to the quantification of aortic root in vivo structural mechanics. *Int. j. numer. method. biomed. eng.* **33,** e2849 (2017).
10. Tasca, G. *et al.* Aortic Root Biomechanics After Sleeve and David Sparing Techniques: A Finite Element Analysis. *Ann. Thorac. Surg.* **103,** 1451–1459 (2017).
11. Kunzelman, K., Reimink, M. S., Verrier, E. D. & Cochran, R. P. Replacement of mitral valve posterior chordae tendineae with expanded polytetrafluoroethylene suture: a finite element study. *J. Card. Surg.* **11,** 136–45; discussion 146
12. Labrosse, M. R., Boodhwani, M., Sohmer, B. & Beller, C. J. Modeling leaflet correction techniques in aortic valve repair: A finite element study. *J. Biomech.* **44,** 2292–2298 (2011).
13. Ovcharenko, E. A. *et al.* Modeling of transcatheter aortic valve replacement:

Patient specific vs general approaches based on finite element analysis. *Comput. Biol. Med.* **69,** 29–36 (2016).

14. Prot, V., Skallerud, B. & Holzapfel, G. A. Transversely isotropic membrane shells with application to mitral valve mechanics. Constitutive modelling and finite element implementation. *Int. J. Numer. Methods Eng.* **71,** 987–1008 (2007).
15. Stevanella, M., Votta, E., Lemma, M., Antona, C. & Redaelli, A. Finite element modelling of the tricuspid valve: A preliminary study. *Med. Eng. Phys.* **32,** 1213–23 (2010).
16. Wong, V. M. *et al.* The effect of mitral annuloplasty shape in ischemic mitral regurgitation: A finite element simulation. *Ann. Thorac. Surg.* (2012). doi:10.1016/j.athoracsur.2011.08.080
17. Votta, E. *et al.* Toward patient-specific simulations of cardiac valves: State-of-the-art and future directions. *J. Biomech.* (2013). doi:10.1016/j.jbiomech.2012.10.026
18. Ge, L. *et al.* Measurement of mitral leaflet and annular geometry and stress after repair of posterior leaflet prolapse: Virtual repair using a patient-specific finite element simulation. *Ann. Thorac. Surg.* (2014). doi:10.1016/j.athoracsur.2013.12.036
19. Baillargeon, B. *et al.* Human Cardiac Function Simulator for the Optimal Design of a Novel Annuloplasty Ring with a Sub-valvular Element for Correction of Ischemic Mitral Regurgitation. *Cardiovasc. Eng. Technol.* (2015). doi:10.1007/s13239-015-0216-z
20. Khalighi, A. H. *et al.* Development of a Functionally Equivalent Model of the Mitral Valve Chordae Tendineae Through Topology Optimization. *Ann. Biomed. Eng.* (2018). doi:10.1007/s10439-018-02122-y
21. Kong, F. *et al.* Finite Element Analysis of Tricuspid Valve Deformation from Multi-slice Computed Tomography Images. *Ann. Biomed. Eng.* **46,** 1112–1127 (2018).
22. Kodama, Y. *et al.* Morphological Assessment of Single-Ventricle Atrioventricular Valve Regurgitation on Dual-Source 128-Slice Multidetector Computed Tomography and 4-Dimensional Imaging. *Circ. J.* **80,** 2555–2556 (2016).
23. Rim, Y., Choi, A., McPherson, D. D. & Kim, H. Personalized computational modeling of mitral valve prolapse: Virtual leaflet resection. *PLoS One* (2015).

doi:10.1371/journal.pone.0130906

24. Villard, P.-F., Hammer, P. E., Perrin, D. P., Del Nido, P. J. & Howe, R. D. Fast image-based mitral valve simulation from individualized geometry. *Int. J. Med. Robot.* **14,** e1880 (2018).

25. Sturla, F. *et al.* Functional and Biomechanical Effects of the Edge-to-Edge Repair in the Setting of Mitral Regurgitation: Consolidated Knowledge and Novel Tools to Gain Insight into Its Percutaneous Implementation. *Cardiovasc. Eng. Technol.* (2015). doi:10.1007/s13239-014-0208-4

26. Chambers, J. B., Myerson, S. G., Rajani, R., Morgan-Hughes, G. J. & Dweck, M. R. Multimodality imaging in heart valve disease. *Open Hear.* **3,** e000330 (2016).

Introduction

1.1 Anatomical and clinical background

The present section is aimed at providing some basic knowledge about the anatomy and physiology of the anatomical districts considered in this work, specifically focusing on the atrioventricular valves' anatomy and physiology and their functionality associated to the surrounding structures.

First, some basic notions will be provided with respect to the function and the physiology of the mitral valve apparatus focusing on its peculiar substructures: annulus, mitral leaflets, chordae tendineae and papillary muscles. A deeper description of each component will be then provided concerning geometry, tissue microstructure and mechanical properties. The same approach will be followed for the tricuspid valve, although not all of its sub-structures have been as deeply characterized as the mitral ones in the scientific literature.

Along their functional description mainly elucidating geometrical and functional relationships with surrounding anatomical structures, the reader will be introduced to the dysfunctions and pathologies which may affect atrioventricular valves apparatus focusing, in particular, on functional regurgitation disorder owing to alterations in ventricular morphology and its mechanical impairment. Concerning this latter aspect, dilated cardiomyopathy affecting the left ventricle leading to heart failure is presented: the physiological morphology and syndrome-induced alterations are discussed in detail, as well as the influence of the pathology on intraventricular hemodynamics, describing its main surgical treatment (i.e., ventricular assist device implantation).

1.1.1 Mitral Valve

The mitral valve (MV) is located between the left atrium (LA) and the left ventricle (LV), allowing for diastolic ventricular filling and preventing backflow towards the atrium during systole. Its whole apparatus consists of different substructures: the mitral annulus (MA), the two valvular leaflets, the chordae tendineae and the papillary muscles (PMs) (Figure 1-1). Physiological conditions of each of them, as well as proper geometrical relationships and interactions between them, are essential to the correct function of the valve

during the cardiac cycle. MV pathologies can hence be associated to a malfunction of any of these substructures or to their altered interaction; as a consequence, the same pathology can be secondary to different etiologies.

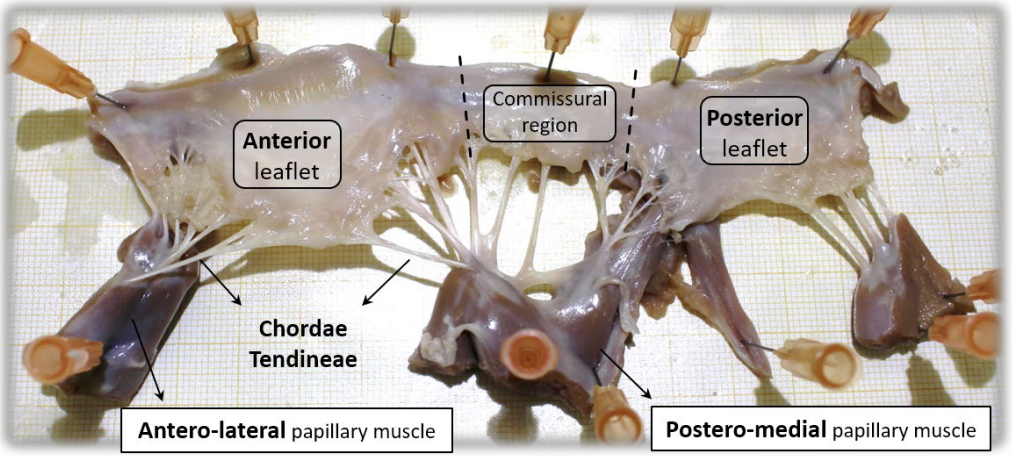

Figure 1-1 Mitral valve as it appears once it is extracted from the heart and excised along the ventricular axis. Figure shows MV principal substructures.

The mitral complex as a whole has two important features. First, the connection between its boundaries to the ventricular wall strongly couples the valve and the surrounding myocardium, so that they influence each other. This is the reason why the MV can be affected by pathologies that are secondary to dysfunctions of the myocardium, although its sub-structures are healthy. Second, the mitral apparatus is an active structure; even though its opening and closure are guided by the trans-valvular pressure gradient, the valve itself can contract. In particular, during ventricular systole the annulus shortens and bends, thus contributing to the action of the surrounding myocardium, and the leaflets stiffen to withstand the increased pressure.

Mitral annulus appears approximately like an ellipse, whose eccentricity is closer to 1 in diastole and becomes lower in systole. The ellipse minor axis corresponds to its *antero-posterior* or *septo-lateral* (SL) dimension, and its major axis consists in its *intercommissural* (IC) dimension, namely the distance between the two commissures, which are the limits delimiting MA anterior and posterior portions.

It is well known that, when observed in the three-dimensional view, the MA appears non-planar and characterized by a saddle-shaped profile (Figure 1-2)

with its peaks located at the ends of the septo-lateral (SL) dimension and the "valleys" nearby the commissures.

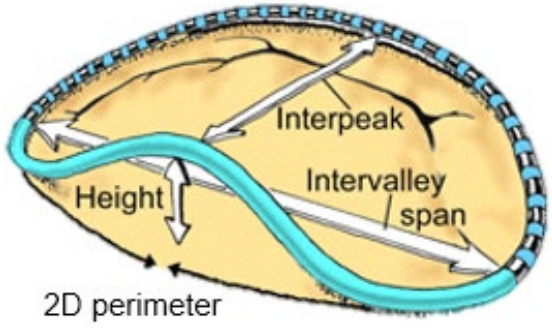

Figure 1-2 Scheme of the saddle shape profile of the annulus. The anterior tract is colored in the cyan, the remaining part corresponds to the posterior tract.

Concerning the MA dynamics, the annular profile modifies during the cardiac cycle, due to the contraction of the surrounding myocardium and of the posterior (muscular) portion of the annulus itself. A qualitative example of annular movement and contraction is provided in Figure 1-3 where its profile is depicted for four different timeframes during the cardiac cycle[1].

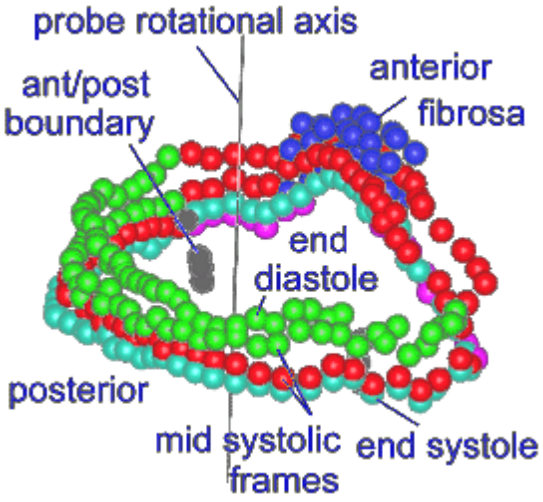

Figure 1-3 Three-dimensional annular profile reconstructed by means of 3D echocardiography during the cardiac cycle[1].

When the systolic configuration of the mitral valve is compared to the diastolic one, two aspects emerge: i) the IC distance increases slightly and the SL one decreases, so that the annulus becomes more eccentric and the orifice area is reduced; ii) the saddle-shaped annular profile becomes more evident[2]. As

regards the first aspect, data reported by Fyrenius et al.[3] show quantitatively that during ventricular systole the valve orifice becomes more eccentric; with respect to the open valve configuration, it becomes slightly wider in the IC direction, while its SL dimension become smaller.

From a strictly anatomical point of view, the mitral leaflets are in continuity and form a single membranous structure inserted on the annulus, but they can be easily discriminated being separated at the commissures. The proportions of the two leaflets and the shape of their profile have been quantitatively estimated by Kunzelman et al.[4] examining 18 human and 10 porcine mitral valves and observing that they did not differ significantly. Notably, the extent and the shape of the anterior leaflet, as well as the geometry of its insertion on the annulus, are such that it can completely obstruct the valve orifice during ventricular systole, when the orifice area reduces by about 25%.

Furthermore, from annulus to free margin, both leaflets show two different zones, respectively the *clear zone* and the *rough zone* (Figure 1-4), being the former slightly thicker and with an opaque surface, while the latter is slightly thinner, and its surface is translucent. The rough zone of each leaflet is the one actually involved in leaflet coaptation and adheres to its counterpart during the valve closure process.

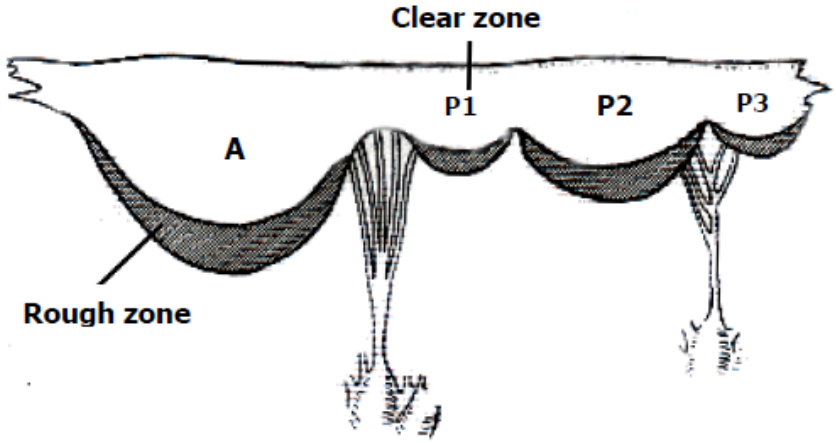

Figure 1-4 Mitral valve excised along the longitudinal direction, i.e. perpendicular to the annulus. In every cusp, the rough zone and the clear one are indicated. Notably the rough zone is wider in the mid part of each cusp and smaller close to the commissures and the scallops between the posterior cusps.

The complex microstructure of mitral leaflet tissue can be described as a multi-layer, fibre-reinforced material. Water, collagen, elastin and glycosamminoglycans (GAGs) are the four main constituents of the mitral leaflets extracellular matrix (ECM). Among them, collagen and elastin play a pivotal role and determine the biomechanical behaviour of the leaflets tissue. On the one hand, the elastin fibers in mitral leaflets form a matrix, characterized by a low stiffness ($E \approx 0.6$ MPa) and capable of undergoing large deformations and high strain rates. On the other hand, collagen fibers, which are characterized by a much higher stiffness ($E \approx 1000$ MPa), provide mechanical reinforcement and are progressively recruited as strain increases.

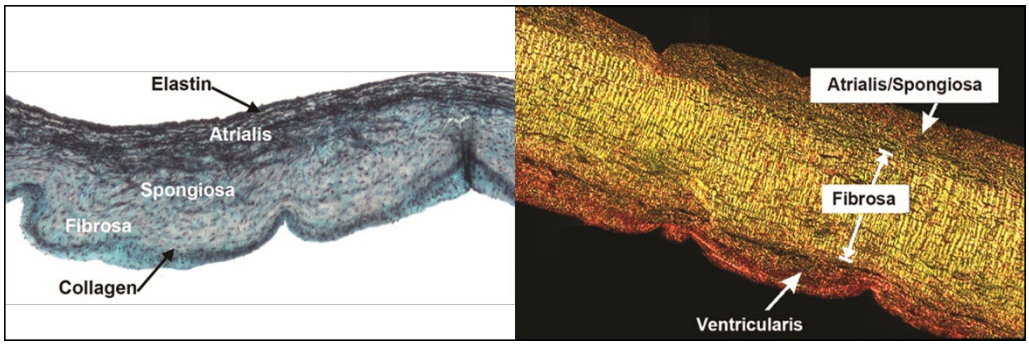

Figure 1-5 Layered mitral valve microstructure (left panel) shown in a radially oriented cross-section stained with Movat pentachrome, which colors elastic fibers black, hydrated proteoglycans and glycosaminoglycan blue, and collagen yellow. Polarized light micrographs of mitral valve leaflet cross-section (in the clear zone, right panel) showing the crimped nature of collagen in the fibrosa. The ventricularis is a thin layer of elastic fibers and loose collagen on the outflow surface of the mitral valve leaflet. A atrialis; F fibrosa; GAGs glycosaminoglycans; PGs proteoglycans; S spongiosa. Adapted from Grande-Allen et al.[5].

The multi-layered structure of the leaflets tissue (Figure 1-5) was studied quantitatively in 1993 by Kunzelman et al.[6], who assessed the thickness and the composition of the layers in the different areas of the two mitral leaflets, as well as their contribution to leaflets mechanical properties. Rectangular specimens were excised from the leaflets of 8 porcine MVs and histologically analysed. The lamina *atrialis* has comparable thickness in both mitral leaflets and elastin and collagen fibers are randomly within it, arranged with no preferential direction. Along with them, bigger bundles of collagen fibers are present. The lamina *fibrosa* is the thickest layer, located in the central portion, and it is in continuity with the annulus; large bundles of collagen fibers originate from the latter and diffuse into the lamina, being directed towards the leaflets free edge. The lamina

ventricularis is the thinnest layer and is characterized by a high concentration of elastin fibers, which form a thin layer that end beyond the leaflets free edge and merges with the proximal part of the chordae tendineae.

Such a microstructural organization leads to a really complex mechanical response. Mitral leaflet tissue is known to contain a highly organized collagen network, spanning circumferentially across the entire mitral leaflet[7]. They can be described as a fiber-reinforced material which consists of an elastin matrix reinforced with collagen fibers. As a consequence, the main characteristics of leaflets extracellular matrix mechanical response are likely to be the following:

- ***Elasticity*** **-** when examined by means of mechanical loading-unloading cycles, elastin and collagen show minor energy dissipation.
- ***Transverse isotropy*** - mechanical response in the direction of the fibers is different from the one in any other direction and is characterized by a higher stiffness, while in any direction perpendicular to the fibers the mechanical response will be the same.
- ***Non-linearity*** - when examined by means of tensile mechanical tests, soft tissue characterized by the presence of oriented collagen fibers normally show a non-linear stress-strain response with a progressively increasing slope as the fibers recruitment mechanism happens.

Numerous studies have characterized the non-linear mechanical behavior of the MV leaflets using *ex vivo* experimental mechanical tests[8–10]. May-Newman and colleagues[9] performed biaxial mechanical tests on porcine mitral leaflets at different strain rate values. The comparison between results obtained for different strain rates allowed the authors to conclude that the viscous aspects of leaflets mechanical response are negligible, proving what has been already reported by Kunzelman and Cochran[8]. Moreover, they highlighted the nonlinear, transverse isotropic response of both leaflets, which were much stiffer in the circumferential direction than in the posterior one. However, recent studies[11,12] suggested that the leaflets are not just passive collagen structures; their composition includes large quantities of excited, neutrally controlled contractile

tissue which, although inactive in studies of isolated tissues, may be active to stiffen the leaflets in the intact beating heart.

Chordae tendineae are fibrous chords that connect the mitral leaflets to the two papillary muscles and, hence, to the ventricular wall. They constrain leaflets movement during the cardiac cycle, in particular during ventricular systole, when the valve is closing, preventing from the billowing of the leaflets into the atrium (Figure 1-6).

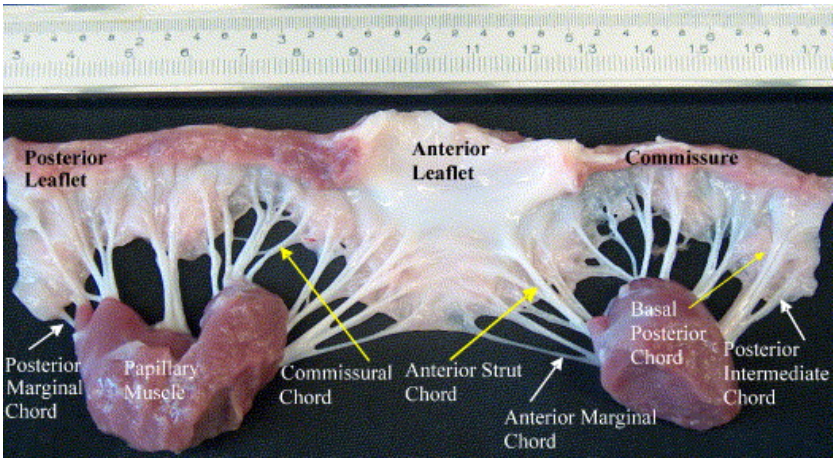

Figure 1-6 Scheme and classification of chordae tendinae according to their different insertion area on mitral valve leaflets[13].

According to the classification proposed by Lam et al.[14], a first distinction is made between chordae that insert respectively into the commissures (commissural chordae), into the cusps of the posterior leaflet (posterior chordae) and into the anterior leaflet (anterior chordae). For each of these three categories, a further classification can be done, as reported in Table 1.

Table 1 Characteristic dimensions of human chordae tendineae (mean ± SD); adapted from Lam et al.[14].

Insertion area	Chordae type	Length [mm]	Thickness [mm]
Anterior leaflet	Marginal	1.75 ± 0.25	0.84 ± 0.28
	Structural	1.86 ± 0.43	1.24 ± 0.51
Posterior leaflet	Marginal	1.40 ± 0.08	0.65 ± 0.24
	Basal	0.84 ± 0.21	0.40 ± 0.29
	Cleft	1.30 ± 0.18	0.78 ± 0.15

Commissures	Antero-medial	1.20 ± 0.31	0.70 ± 0.20
	Postero-medial	1.40 ± 0.40	1.00 ± 0.30

As regards their mechanical response, within chordae tendineae, the load-bearing function is accomplished by collagen bundles, which are oriented along the chorda long axis and are crimped when the chorda is unloaded. Chordae tendineae stress-strain behaviour is hence approximately elastic, non-linear, and non-symmetric. Non-linearity is due to the progressive recruitment of collagen fibers; additionally, to note, chordae elastic modulus in their post-transition configuration is about 10 times greater than the one measured in pre-transition conditions (Figure 1-7).

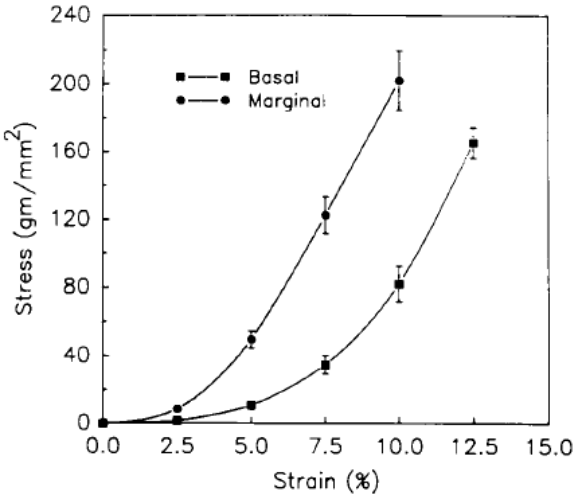

Figure 1-7 Stress-strain curves obtained through uniaxial testing of hydrated marginal chordae (31 specimens) and basal chordae (29 specimens)[15].

The two papillary muscles (PMs), respectively named antero-lateral (APM) and postero-medial (PPM), originate from the free portion of the ventricular wall and host the distal ends of chordae tendineae. From a morphological point of view, the two papillary muscles share some characteristics. Both have the shape of a cone with an ellipsoidal transverse section, whose axis is oriented perpendicularly to the valve leaflets surface in systole. Moreover, each papillary muscle hosts the distal end of approximately a half of the total amount of chordae tendineae. Moreover, Both papillary muscles are located at the lowest third of the inner wall of the left ventricle, but are located on opposite sides; the base of

the APM is on the anterolateral side of the ventricular wall, next to the left boundary of the posterior wall of the ventricle, while the PPM originates by the junction of the posterior ventricular wall with the interventricular septum. A precise definition of the position of papillary muscles with respect to the other substructures of the mitral apparatus has been provided by different authors[16,17]. In an *ex-vivo* study, Sakai et al.[16] examined 57 human hearts, in order to measure the characteristic dimensions of mitral substructures. PM position was estimated also by Dagum et al.[17] through an *in vivo* study on 16 adult sheep. This study is particularly important, since it provides precise *in vivo* data for the whole cardiac cycle through twelve miniature radiopaque tantalum markers placed on the valvular apparatus. From a functional point of view, during systole, when the myocardium contracts and the intraventricular volume decreases, PMs contract and shorten. In this way they stretch the chordae tendineae and prevent the leaflets from invading the atrial volume, thus guaranteeing their correct coaptation. On the other hand, during ventricular diastole, when the intraventricular volume increases, PMs relax and return to their initial length.

Functional Mitral Regurgitation (FMR)

As clearly elucidated, the function of the sub-valvular apparatus, i.e. chordae tendineae and PMs, strictly depends on ventricular geometry and kinetics since they guarantee the continuity between the valvular plane and the ventricular wall.

When chordae-PMs interplay is lost owing to alteration in their spatial relationships, mitral valve regurgitation occurs. MV regurgitation is the most common valvular disease[18], and in its functional origin, namely FMR, is secondary to dilated or ischemic cardiomyopathy and is associated with mitral annulus dilation mainly in antero-posterior direction and apical and postero-lateral PMs displacement due to left ventricle (LV) wall dilation[19–22]. These two events are associated with the lost coaptation between the MV leaflets. Indeed, the LV dilation results in a leaflets' tethering by the chordae leading to valve hypomobility as well as to an overstressing of the tissues. In this scenario, chordal stiffness, and thus their rest length, plays a crucial role[23]. Surgical repair

is recommended in case of severe chronic FMR[22]. The gold standard, mitral annuloplasty, decreases the regurgitation severity, but it is often insufficiently done and has tremendous one-year recurrence (>30%)[24]. Complementing this context, transcatheter-delivered devices have been recently emerging, as a promising interventional solution for high-risk patients[25].

Echocardiography is the imaging technique of choice for evaluating MR-affected patients[26], exploiting 3D transthoracic echocardiography which allow for assessing the valvular and sub-valvular geometry of the MV. Nonetheless, evaluation of tenting height, principal annular diameters and interpapillary muscles distance may be required and easily accomplished by means of cardiac magnetic resonance (CMR) or computed tomography (CT). When these latter diagnostic investigations are contraindicated, 3D transesophageal echocardiography can be performed[27]. Additionally, recently echocardiographic technologies such as Colour Doppler and Strain Echocardiography might be accomplished to better quantify the regurgitation jet, and thus the severity of the pathology, and to possibly detect regions of akinesis and imbalance between closing and tethering forces on the MV leaflet[28].

1.1.2 Tricuspid Valve

The tricuspid valve separates the right atrium from the right ventricle. As for MV, during diastole the valve is opened in order to allow blood to flow unidirectionally from the atrium to the ventricle; during systole the valve is closed in order to avoid regurgitation of blood towards the atrium.
The tricuspid valve complex, similarly to the mitral one, is composed of different structures[29]: fibrous annulus, three leaflets, chordae tendineae and papillary muscles (Figure 1-8).

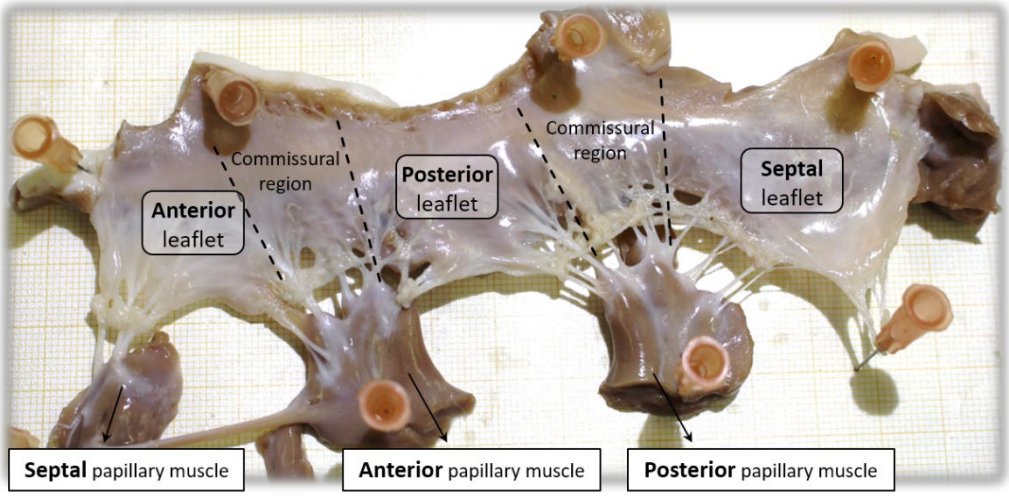

Figure 1-8 Tricuspid valve as it appears once it is extracted from the heart and excised along the ventricular axis. Figure shows TV principal substructures.

The tricuspid annulus (TA), differently from the mitral one, is larger[30] and is not a well-defined structure. It has a non-planar saddle-shape profile, whose highest points are located towards the atrium anteriorly, near the aortic valve, and posteriorly, on the opposite side of the orifice. From an atrial view, its shape is almost ellipsoidal. Specifically, as more recently elucidated by Ton-Nu and Fawzy in their 3D-echo based investigations[31,32], in its non-planar oval shape, TA presents the highest and the lowest points nearby the antero-septal and postero-septal commissures, respectively.

From a dynamic standpoint, the first study of the tricuspid annulus *in vivo* was performed by Tsakiris et al.[33] using lead markers on five dogs. Their results showed that the tricuspid annular dimensions vary dynamically during the cardiac cycle, and that the annulus has the maximal area at end-diastole, while the minimal area is reached at mid-systole. Also, they identified an early systolic decrease in the area, associated with the right atrial systole.

An almost similar study was proposed by Hiro and colleagues[34] who analysed the TA dynamic changes on seven adult sheep using sonomicrometric crystals, implanted both at the annular and PMs level. The TV area and perimeter were calculated in their approximating least-squares plane to represent only cross-sectional area and length changes. Overall, TA experienced an expansion of 28.6 ± 3.6%, however being not uniform for each leaflet (septal 10.5 ± 1.2%, anterior 13.0 ± 1.5% and posterior 14.0 ± 1.6%). Furthermore, the eccentricity of the

annulus changed from 0.45 ± 0.05 to 0.55 ± 0.05 meaning that th TA had an elliptical shape and became slightly more circular when it achieves maximum area and perimeter.

Finally, Fukuda et al.[35] studied 15 healthy subjects and 16 patients with tricuspid regurgitation (TR) using real-time 3D echocardiography. Both the maximum (7.5±2.1 vs. 5.6±1.0 cm2/m2) and minimum (5.7±1.3 vs. 3.9±0.8 cm2/m2) annular areas in patients with TR were larger than those in healthy subjects. Healthy subjects had a non-planar shaped annulus with homogeneous contraction, with a normal reduction of 19% in average in annular circumference with atrial systole[36], whereas in TR patients the annulus was dilated in the septal to lateral direction, resulting in a more circular and flatter shape[37,38].

The tricuspid valve is composed of three leaflets[29,39]: anterior leaflet, posterior leaflet and septal leaflet, appearing more translucent with respect to the mitral one given the low-pressure pulmonary environment[40]. The anterior leaflet is the largest and most mobile of the three leaflets with a semi-circular shape, the septal leaflet is the least mobile with a semi-oval shape and the posterior leaflet is the smallest one featuring variable shape[41].

They are separated by three commissures of different depth: antero-septal, antero-posterior and postero-septal. Differently from MV, the TV commissures never reach the annular level, thus the three leaflets are not completely separated one from each other.

From a histological standpoint, the tricuspid leaflets exhibit a layered microstructure very similar to the mitral ones. The thickest layer is the central one, called *fibrosa*, composed of a dense collagen network, in continuity with the fibrous annulus and the mitral fibrous trigones. Chordal extremities insert in this layer, merging with it. This layer is covered by a fibroelastic layer, mainly composed of PGs. The third layer is a thin endothelial plate, in continuity with the endothelium that covers le heart chambers[40].

TV chordae tendineae are histologically very similar to the MV ones, but concerning the topology they are really different: the majority of the true chordae

branch soon after their origin; some branch just before insertion; a few do not branch at all. On the average, 25 chordae insert into the tricuspid valve: seven of them insert into the anterior leaflet, six into the posterior leaflet, nine into the septal leaflet, and three into the commissural areas. Silver et al.[29] classified the tricuspid chordae on the basis of their insertion on the leaflets.

Fan-shaped Chordae. The morphology of the fan-shaped chordae in both the tricuspid and mitral valves is similar. Such chordae insert into the commissures between the leaflets and into the clefts in the posterior leaflet (Figure 1-9).

Rough Zone Chordae. These chordae insert into the "rough zone" on the ventricular aspect of each leaflet. Each chorda splits into three cords soon after its origin. One chorda inserts into the free margin of the leaflet, one into the upper limit of the rough zone at the line of closure, and the third between the other two.

Free Edge Chordae. These single, threadlike, often long chordae usually originate from the apex of the papillary muscle, but may come from its base. They insert into a leaflet's free edge, frequently near its apex.

Deep Chordae. Deep chordae are long. They pass deep to a leaflet's free margin to insert on its ventricular surface either in the upper part of the rough zone or in the clear zone. They may be single or they may branch into two or three cords just before insertion.

Basal Chordae. To be defined as such, a basal chorda has to be completely separated from the wall of the ventricle. Thus, the triangular folds of membranous tissue that were attached to the ventricular wall and joined the apices of trabeculae carnae to the base of the TV leaflet are not included in this class. Basal chordae are usually single.

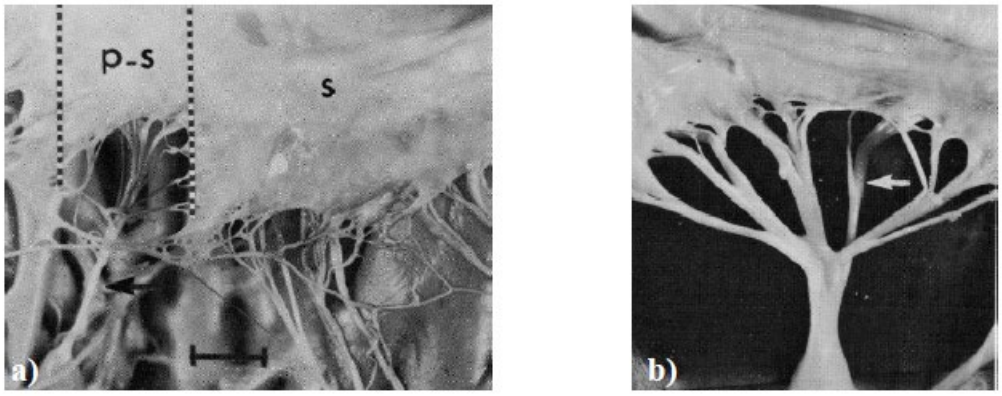

Figure 1-9 (a) Thread-like communications between chordae passing to the apex of a septal leaflet (s). A fan-shaped chorda (arrow) defines the postero-septal commissure (p-s). (b) Fanshaped chordae attached to the tricuspid valve. The branches in both spread radially and attach to the free margin, but in some the main stem of the chorda (arrow) runs deep to the leaflet free margin to insert into the adjacent rough zone on one or the other side of the midline.

The papillary muscles (PMs) anchor the three tricuspid leaflets to the right ventricular wall through the chordae tendineae. Nigri and colleagues[42] define three tricuspid PMs: the anterior, the septal and the posterior. Nonetheless, with respect to the MV, TV sub-valvular apparatus has a greater variability: i) anterior (the most prominent) which provides chordae to anterior and posterior leaflet; ii) posterior (missing in 20% of healthy population[43]) that gives chordae to posterior and septal cusps; iii) septal, which mostly does not feature any specific tip, being the chordae directly arising from ventricular wall toward anterior and septal leaflets.

Concerning their mechanics, again according to the study proposed by Hiro et al.[34], the PMs contract synchronously with the right ventricle, in order to constantly keep in tension the chordae tendineae during systole. In details, considering the relative distanced among the three PMs, authors were able to investigate and quantify the contraction/expansion motion of the sub-valvular apparatus. As moving toward systolic closure, an expansion (about 37.3 ± 8.5%) of the area encompass by the PMs was found, being coherent and almost synchronized with what happening at the annular level. Moreover, the change in apical distance between the annulus and each papillary muscle changed from minimum to maximum was smaller for the anterior PM (12.6 ± 6.9%) compared with the septal PM (20.6 ± 9.2%) and the posterior PM (19.5 ± 8.2%).

Functional Tricuspid Regurgitation (FTR)

As pointed out for the MV, tricuspid valve functioning is strictly related to the interaction between papillary muscles and chordae as well. Indeed, pressure overload or left-sided diseases can induce TA enlargement and right ventricle (RV) dilation. Enlargement of TA advances the leaflets displacement in antero-posterior direction. The RV dilation leads to displacement of PMs attached to the ventricular wall causing tethering of TV leaflets. As the final result the leaflets lose their proper coaptation leading to functional tricuspid regurgitation (FTR)[44,45]. Currently, FTR affects 1.6 million people in the USA[46] and represents a serious public health problem[47].

Until recently, FTR was neglected or was repaired via conservative, surgical approach only if severe and only during concurrent mitral valve surgery[48]. Nowadays, available options for FTR treatment are applied to TA, TV commissures or TV leaflets which counteract the first of FTR mechanisms, TA enlargement. Nonetheless, they were associated with residual and recurrent FTR (11% and 17% of severe FTR occurrence in three-months and five-years follow-up, respectively)[49,50]. In this context, nobody has yet proposed interventional strategies to address the second mechanism which involved sub-valvular apparatus, however being clinically evident that current treatment approaches are not sufficient in eliminating FTR. Additionally, it is noteworthy that recent advancements in transcatheter technology can provide a solution for TV FTR repair[51], but it can be predicted a similar rate of recurrence since they share the same concepts as surgical techniques.

1.1.3 Left Ventricle

The left ventricle (LV) is one of four chambers of the heart. It is located in the bottom left portion of the heart below the left atrium, separated by the mitral valve. It exerted the maximum pressure regimes, achieving a maximum value of about 120 mmHg every cardiac cycle, in physiological condition. The LV shape approximates to an inverted tapered cone, with the right ventricle hugging it, with a consequent curved septal wall dividing them[52].

Observing its longitudinal section, the ventricular chamber consists in three virtual compartments: the inlet portion comprising the MV apparatus, an outlet portion leading to the aortic valve (AV), and an apical portion containing fine trabeculations (Figure 1-10).

Outlet region appears as the smoother one, mainly consisting of muscular and fibrous tissue[52]. Even the thickness is not uniform: the interventricular septum is about 7-10 mm thick, nearby the LV base, similarly to the free wall (7-9 mm), whereas the apical zone is significantly thinner (3 mm)[53]. Its thickness is overall highly greater with respect to the right counterpart (namely, the right ventricle), since LV musculature has to counteract higher intracavitary pressure loading.

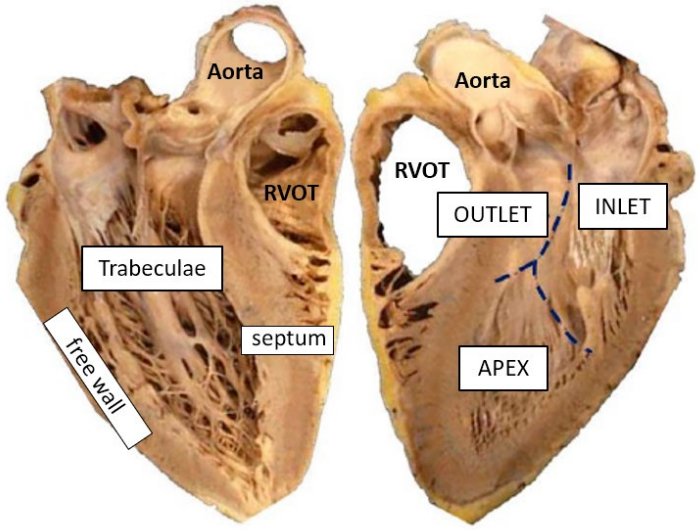

Figure 1-10 LV longitudinal section. The three portions of the ventricular chamber are depicted (namely inlet, outlet and apex), as well as the main surrounding anatomical districts (Aorta, RVOT=right ventricular outflow tract).

Along the whole cardiac cycle, LV experienced several conformations and pressure regimes, exerting a functional work depicted in Figure 1-11.

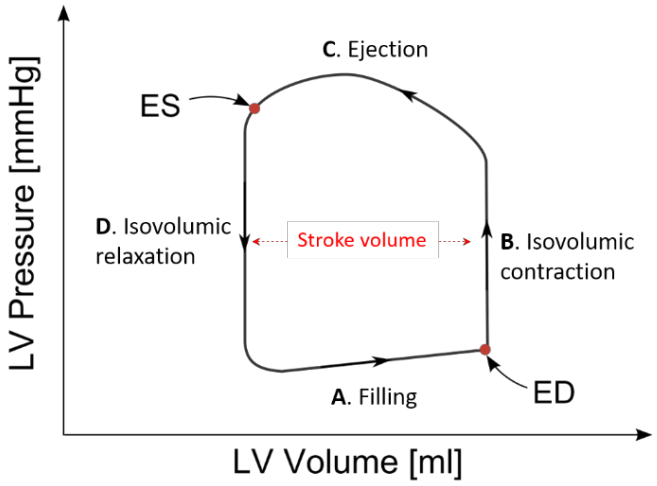

Figure 1-11 LV Pressure-Volume curve. ED and ES indicate End-Diastolic and End-Systolic instants, respectively.

A. Atrial systole and ventricular filling occur, lasting about 100 ms. Indeed, the increase in the atrial pressure lead to MV opening when it overcomes the LV pressure, blood flows into the ventricle up to a maximum filling of about 120 ml in volume, namely the end-diastolic volume (EDV).

B. The ventricle contracts, leading to an intracavitary pressure increasing and, consequently, to the MV closure. However, pressure is not enough to allow for AV opening.

C. LV inner pressure exceeds aortic blood pressure (80 mmHg), AV opens, and blood is ejected towards the systemic circulation. This phase lasts about 270 ms. The blood amount ejected, defined as the stroke volume (SV) and corresponds to the difference between the end-diastolic and end-systolic LV volume, respectively. To better quantify the efficiency of LV in ejecting the blood, the ejection fraction (EF) is usually the variable computed, defined as follows:

$$EF = \frac{SV}{EDV} \cdot 100 \tag{1}$$

D. At the end of the ejection phase, the LV relaxes, the inner pressure decreases leading to AV closure. To note, at end-diastole (ED) the ventricular chamber is not completely empty, otherwise half of the

maximum filling volume (about 50 ml) still remains within it, namely the end-systolic volume (ESV).

Left ventricle mechanics

During the whole cardiac cycle, LV experiences a specific motion that is a combination between a contraction/dilation and twist/untwist around its long axis, and it is induced by the myofibers contraction within the LV wall[54]. They are hierarchically organized in oblique oriented sheets, moving from the endocardium toward the epicardium. Subendocardial fibers are right-hand-oriented; subepicardial fibers are left-handed[55]. As shown in the model (Figure 1-12), on one hand the contraction of the epicardial fibers will rotate the apex in counter-clockwise and the base in clockwise direction, whereas on the other hand, contraction of subendocardial region will rotate the LV apex and base in exactly the opposite direction. Specifically, during IVC (phase B) the apex and the base both rotate in a counter-clockwise direction[56] when viewed from apex to base. Subsequently, during systole (phase C) the base changes direction and starts to rotate in a clockwise direction, while the apex continues to rotate in counter-clockwise direction. LV torsion is followed by rapid isovolumic untwisting of the ventricle (phase D): indeed, potential elastic energy stored in the collagen matrix during contraction subsequently leads to a recoil untwisting phenomenon[57] contributing to active suction of blood from the atria (phase A).

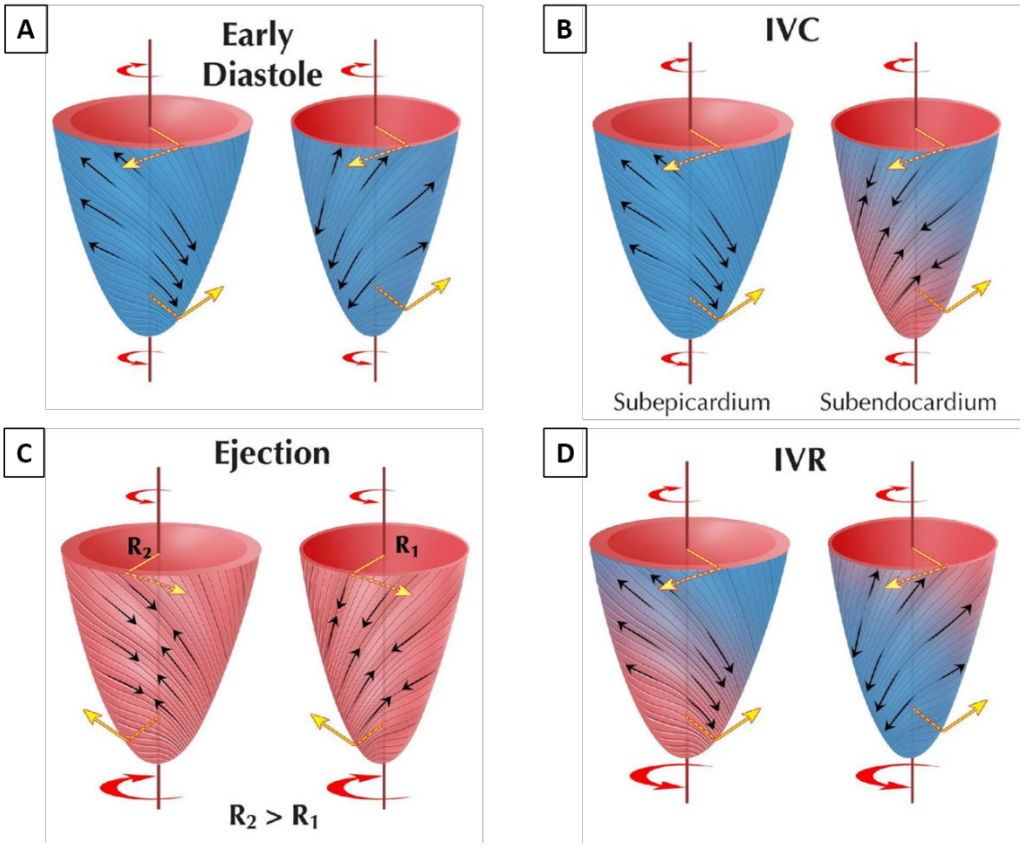

Figure 1-12 Scheme of the LV myofibers orientation and the twist mechanics of the LV systolic/diastolic torsional motion. A, B, C and D coherently indicate the same phases depicted in Figure 1-11. This figure has been adapted from Sengupta et al.[58].

Dilated Cardiomyopathy (DCM)

Approximately half of the patients with HF is affected by dilated cardiomyopathy (DCM), a syndrome characterized by enlargement, wall hypokinesis, and reduction of the overall contractility of left or both ventricles[59–61] which acquire a pathological-dilated nearly spherical shape[62] (Figure 1-13).

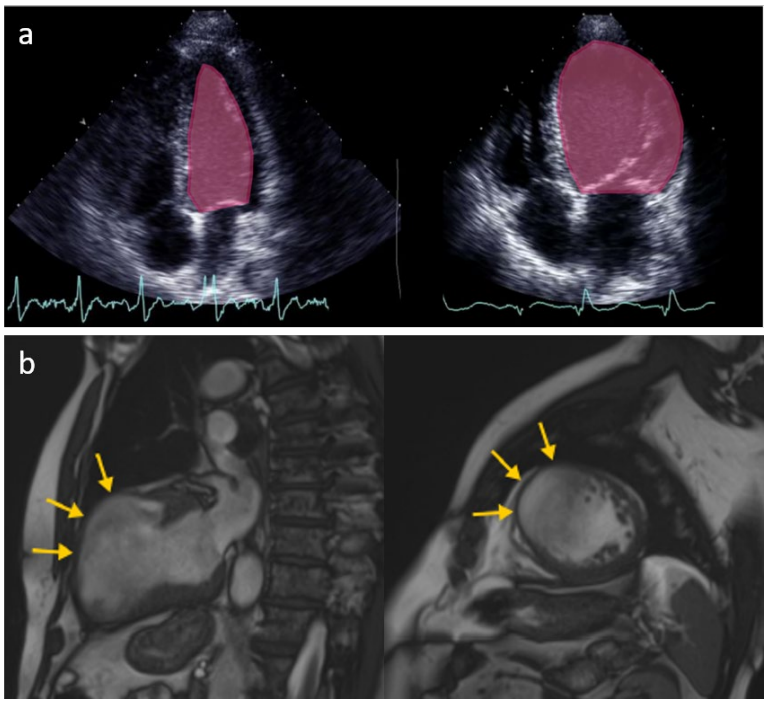

Figure 1-13 a) Apical four chamber 3D TTE view of a subject with a structurally normal LV (left) and DCM-affected LV (right); b) DCM-affected LV with prevalent anterior wall dilation (yellow arrows), acquired by means of CINE CMR in long axis (left) and short axis (right) plane, respectively.

When overloaded, the myocardium attempts to dampen wall shear stress through structural adaptation phenomena, the most relevant one being hypertrophy. At first, it provides hemodynamic compensation; thereafter, biochemical and structural modifications in the myocardium lead to ventricular remodelling, characterized by gradual dilation, reduction in the wall thickness, and increase in wall shear stress[63].

DCM is characterised by both systolic and diastolic dysfunctions, in which the LV capability to contract and pump blood during systole, and achieve a complete relaxation in diastole, is reduced or completely compromised. In systolic dysfunction, changes to the LV (enlargement of the chamber and impaired contractility) mean that a much smaller volume of blood (typically < 40% vs. 50% in physiological conditions) is ejected. Impaired filling of the LV (diastolic dysfunction) is the main factor underlying the development of diastolic heart failure, including thickening of the ventricular wall and LA enlargement.

In patients with DCM, there is risk of systemic or pulmonary embolization, because blood stasis and reduced shear rate in the hypocontractile ventricle lead

to the activation of coagulation processes, so that long-term anticoagulation therapies are needed[64]. Furthermore, in advanced DCM cases, limited treatment options are available, with a really low possibilities for qualifying for cardiac transplantation. Consequently, ventricular assist devices (VADs) implantation has been introduced as an alternative, long-term, viable treatment to heart transplantation. A VAD is a surgically implanted mechanical pump that is implanted into the heart in order to provide full or partial mechanical circulatory support to one (Left-VAD – Right-VAD) or both ventricles (Bi-VAD). VADs are used clinically as destination therapy, as bridge to transplant or, as bridge to recovery to allow myocardial remodelling.

Left Ventricular Assist Device (LVAD)

Left Ventricular Assist Device (LVAD) implantation is either a therapeutic option that provides circulatory support while waiting for heart transplantation or a definitive therapy alternative to transplant.

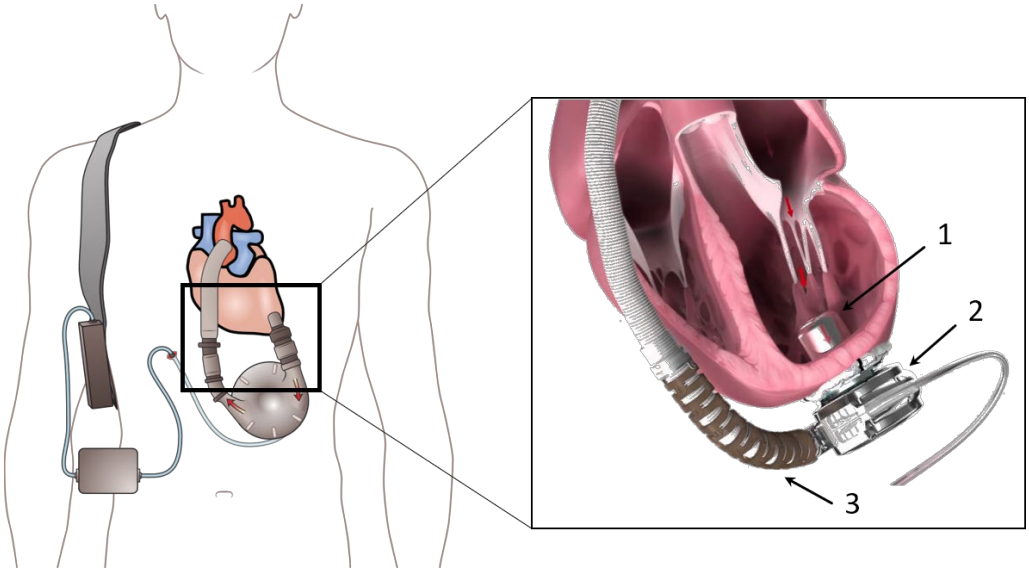

Figure 1-14 LVAD components. Only the subcutaneous components are here depicted: inflow cannula (1), pump (2) and outflow cannula (3).

The components of a LVAD are (Figure 1-14):

- an inflow cannula, inserted into the apex of the left ventricle;
- a pump (pulsatile or continuous) placed within the abdominal wall or peritoneal cavity, or "on board" of the heart itself;
- an outflow cannula, anastomosed to the ascending aorta;

- a percutaneous drive line which carries the electrical cable and air vent to the external battery packs;
- an electronic controller, that monitors LVAD performances and provides input for the pump operation.

Oxygenated blood is drained from the LV, through the inflow cannula, into the pump body, then actively pumped through an outflow cannula to the downstream ascending aorta.

Improvements in technology and patients' outcomes, including development of smaller LVADs suitable for use in a larger number of patients, have led to progressive growth in the number of LVAD implants. As shown by the seventh annual report of the Interagency Registry for Mechanically Assisted Circulatory Support (INTERMACS), the number of VAD implants is approaching 2500 per year, with the INTERMACS database including more than 15000 patients. Equally encouraging, the survival curve for devices implanted since 2008 shows an overall 80% of 1- year survival and 70% of 2-year survival[65,66].

Despite these advancements, there are a number of clinical complications associated with LVAD therapy.

The most common postoperative complication following LVAD implantation is bleeding, that is associated to high mortality when the central nervous system is involved and can lead to ischemic stroke.

LVAD recipients are also exposed to an elevated risk of developing Von Willebrand's disease, in which large multimers of Von Willebrand factor (a blood glycoprotein) are destroyed by mechanical stress, increasing bleeding risk[67].

A major concern about LVADs is also device-related thrombogenicity, which is attributable to several mechanisms such as non-physiologic blood flow patterns leading to red blood cell damage or haemolysis, endothelial dysfunction and chronic platelet activation. As a matter of example, The ENDURANCE[68] and MOMENTUM 3[69] clinical trials compared the performances of the *HeartWare* VAD (HVAD HeartWare Inc., Miami, FL, USA), which is a small intrapericardial centrifugal-flow device, the *HeartMate II* (Thoratec Corp., Pleasanton, CA, USA), an axial-flow mechanical-bearing pump, and the

HeartMate3TM (Abbott, Chicago, Illinois, USA), a bearing-less magnetically levitated centrifugal continuous-flow pump. The *HVAD* was found to be noninferior to the axial flow device with respect to survival free from disabling stroke or need for device replacement. The rate of device replacement, explant, or need for urgent transplantation due to device malfunction was higher for the *HeartMate II* if compared to the *HVAD* (16.2% vs. 8.8% respectively), as it was for the risk for LVAD thrombosis. The *HeartMate3TM* was reported to significantly reduce the incidence of pump thrombosis, but it was not free from thromboembolic complications and strokes. Thrombus formation was demonstrated[70,71] to often develop at the interface between the ventricular endocardial surface and the LVAD inflow cannula, with subsequent thrombotic apposition on the cannula and, eventually, their migration.

Several mechanisms have been suggested to trigger and promote intraventricular thrombus formation:

- blood contact with an artificial surface at the LV apex - LVAD inflow cannula interface;
- platelets that, activated/sensitized by the supra-physiologic hypershear environment within the pump, once returned to the LV, tend to aggregate, generating thrombi, because of the prothrombotic hemodynamic conditions within the LV;
- the altered ventricular hemodynamics (stagnation regions and recirculation patterns) due to:
    i. enlargement of the LV chamber and reduced myocardial contractility;
    ii. LVAD implantation, in particular the LVAD inflow cannula/outflow graft surgical implantation configuration.

1.2 From clinics to research, and *vice versa*

As reported by the World Health Organization (WHO), nowadays cardiovascular heart diseases (CVDs) take the lives of almost 18 million people per year, 31% of all global deaths. In specific, most of them are valve-pathology related: in western countries, approximately 2% of the population is affected by valvular heart diseases[72].

In the past two decades, major advances have been made in CVDs assessment and treatment owing to the advent of sophisticated and more accurate imaging techniques, allowing for better understanding the complexity of anatomical structures as well as improving the preoperative planning of critical surgical interventions, even creating 3D-printed models thanks to high resolution features[73,74]. In the next section, a brief description of such these imaging technologies.

1.2.1 Imaging Modalities

Medical in-vivo imaging technologies are crucial in every day clinical practice, being extensively exploited for diagnostics and risk evaluation[75], as well as in the research fields. *Volumetric* acquisition enables the visualization of cardiac districts from virtually any perspective, better appreciating patient-specific anatomical complexity, as well as an accurate quantitative functional evaluation of chamber volumes and mass avoiding geometric assumptions[76].

Cardiac **computed tomography** (cardiac **CT**) is a procedure that uses a special X-ray machine to generate detailed images of the heart. During the cardiac CT scan the X-ray tube rotates around the body to acquire multiple images from different angles and combines them to reconstruct three-dimensional volumes of the heart.

A Computed Tomography Angiography (CTA) procedure uses Iodine-based contrast dye injected into veins while scanning to highlight blood vessels and soft tissue areas. Each portion of the heart can be scanned at several phases of the cardiac cycle. Retrospective Electrocardiography (ECG) gating is used to

correlate the CT data with the corresponding phase and reconstruct a series of volumes which cover a complete cardiac cycle (Multiphase CT or CTA). New scanners, as the SOMATOM Definition Flash CT, Siemens Healthcare, Forchheim, Germany, achieve a temporal resolution of 75 milliseconds and require 0.6 seconds for a complete thorax scan at a radiation dose of 1 millisievert (mSv).

The main limitation of cardiac CT is the radiation caused by the X-rays. Nevertheless, due to its relatively high spatial resolution, this imaging modality provides accurate morphologic rendering of the heart, which is useful in various clinical scenarios such as calcium assessment and scoring, or the visualization of the coronary arteries. Cardiac CT is reliable in depicting the aortic and mitral valve in contrast enhanced CTA procedures. It has been reported that CT imaging can quantify the mitral regurgitant orifice as well as the mitral valve morphology[77,78]. Recent studies demonstrated the usage of CTA to measure the orifice area in normal and stenotic aortic valves in close correlation with transesophageal echocardiography[79]. As regards the right heart investigation, CT has been found to provide high-resolution anatomical evaluation as well as accurate functional assessment without any geometric assumptions[80]. Furthermore, currently, when dealing with the investigation of the ventricular chamber in heart-failure patients referred to ventricular assist device implantation, CT is rarely performed, due to its invasiveness, typically to assess post-implant alteration of the surrounding structures or thrombosis within device compartment, not in the cardiac environment[81,82].

Finally, multi-slice computed tomography (MSCT) may contribute to evaluation of the severity of valve heart disease (VHD), such as in aortic stenosis[83,84], and of the thoracic aorta. MSCT plays a key role in the workup of patients with VHD considered for transcatheter intervention, in particular transcatheter aortic valve implantation (TAVI), and provides valuable information for pre-procedural planning.

Cardiac magnetic resonance (**CMR**) imaging uses a high-strength magnetic field, mainly 1.5 Tesla, to excite hydrogen nuclei within a body region by a pulse of radio waves, at a resonance frequency of 63MHz. Images are built from wave

echoes emitted during excitation decay, while contrast arises from different particle concentration of individual tissues. Discrimination between blood and myocardium tissue is possible in arbitrary planes without contrast medium.

After growing considerably over the past years, CMR is now firmly established in large centers and considered the most versatile non-invasive diagnostic modality. It enables high-resolution static and moving images of cardiac structures when combined with ECG synchronization. Furthermore, phase-contrast protocols produce velocity-encoded images of the blood flow. The nonionizing technology offers CMR a fundamental advantage compared to X-ray and gamma ray modalities. Nevertheless, relative long examination times of 45-90min, compared to 15min for CT studies, obstruct CMR application for full 4D imaging.

CMR offers invaluable information about the valvular anatomy and function. It is the modality of choice for the analysis of dilated aorta with aortic regurgitation and most accurate to evaluate ventricular function[85], even if completely contraindicated when a device is present. It is ideally suited in pediatric cardiology to assess complex congenital heart disease of the valves and great vessels. Since it is flow-based imaging sequence, CMR even allows for assessment of valvular and hemodynamic abnormalities[80], such as tricuspid regurgitation.

Echocardiography is the principal imaging modality to evaluate all cardiovascular disease related to morphological, functional or hemodynamic dysfunctions[86]. Echocardiography is based on ultrasound technology, which uses a transducer loaded with an array or matrix of piezo-electric elements to generate ultrasound pulses, with a frequency between 1-15MHz. These traverse the human body and produce echoes captured by the device to assemble images. The result is a virtually risk-free, non-invasive imaging modality, which in comparison with other techniques, such as CT or MRI, is cost-effective and widely available in most clinical units.

The downsides of ultrasound are low signal-to-noise ratio due to tissue frequency attenuation, artifacts caused by echo dropouts and speckle noise as well as suboptimal acoustic windows and insufficient depth penetration, which

overall lead to limited image quality. Nevertheless, a wide range of techniques were developed to overcome these limitations and enable ultrasound technology not only for diagnosis, but also to guide interventional procedures, such as valve replacement or repair, or apply therapy for example in fragmentation of kidney and gall bladder stones.

- **Transthoracic Echocardiography (TTE)** - the ultrasound transducer is coupled to the skin surface using a special gel and angulated to obtain images from four standard positions: parasternal, apical, subcostal and suprasternal. TTE is the standard diagnostic method for patients with valvular heart disease, as it provides quantitative and qualitative information about the anatomy and function of the valves, as well as the etiology and severity of valvular stenosis and regurgitation[87]. Evaluation usually includes aortic and mitral valve area, LV volume, mass and ejection fraction, aortic root anatomy and right heart structure and function.
- **Transesophageal Echocardiography (TEE) -** To obtain images from the proximity of the major cardiovascular structures, a special probe is introduced in the esophagus during the exam. TEE provides high-resolution images and is considered essential in many cases including studies in presence of prosthetic valves or evaluation of mitral valve and aortic lesions and regurgitant severity. Recently introduced real-time 3D scanners enable unique perspective and time resolved imaging of the valves, which advance visualization and quantification capabilities and improve severity assessment and treatment planning[86].
- **Doppler and Color Flow Imaging -** Doppler echocardiography quantifies blood flow velocity based on the shift in frequency of the reflected ultrasound waves, a phenomenon known as the Doppler Effect. In color flow imaging, the measured blood velocities are color coded and displayed superimposed to the anatomical echo images. Doppler provides essential measurement in VHD assessment, including regurgitant volumes, valve areas and pressure gradients.

The advance of medical imaging technology over the last decades has allowed the evolution from generic to *patient-specific* 3D cardiac models that faithfully represent the anatomy and different cardiac features of a given alive subject. In detail, **image-based morphological analysis** and **computational simulation approach** are the two complementary and well-established applications of such cardiac models. Exploiting the just mentioned advantages of imaging investigation, they can be crucial for anatomical qualitative and quantitative analysis either in diagnosis or in planning and therapy guidance[88].

1.2.2 Morphological analysis

Precise morphological and functional knowledge about either the heart valves' apparatus and the surrounding structures which they interface with is a prerequisite during diagnosis, preprocedural planning as well as patient monitoring and follow-up[89]. This scenario increasingly relies on imaging modalities such as cardiac CT and real-time 3D transesophageal echocardiography (TEE), which enable for dynamic 4-D scans of the beating heart over the whole cardiac cycle, encoding comprehensive structural and dynamic information (e.g., LV outflow tract-mitral annulus district or the AV complex itself[84,90]). Indeed, considering the dynamically changing configuration of the cardiac structures within the cardiac cycle, one should be aware of the relevance of introducing fourth-dimension information, namely the time[90,91].

Although this extensive amount of information is barely exploited in the clinical practice due to its complexity, there has been growing interest in developing geometrical models, which can provide quantitative anatomical assessment by means of semi- or fully-automated images analysis[92,93].

The widespread bedside availability, cost, and non-invasive nature of echocardiography has meant that this technique has become the method of choice in most situations for performing the evaluation of cardiac function. In detail, when dealing with atrioventricular valves, 3D TEE is accomplished since provides more complete and higher resolution comparing to 2D TEE and 3D TTE, respectively[94].

Mitral Valve: several previous studies[85,88,91] have stressed the importance of the quantification of global annular dimensions and leaflet area for the accurate classification of the causes of MV disease and for the determination of the course of treatment in such cases. In particular, Maffessanti and colleagues[85], as well as Chandra et al.[88], demonstrated that a volumetric analysis can be crucial when assessing the effects induced by a prolapse on MV anatomy (e.g., in FED or BD scenarios) to accurately improve the specific surgical planning. Clinically, in such cases, the most common used parameters are planarity and eccentricity of MV annulus as well as tenting height and volume; however, it was shown that when a single plane-based evaluation is performed the measurements were inaccurate[95,96].

CMR has been exploited as a valid alternative in MV disorder investigation, especially when evaluating valve motion as well as valvular flow characteristics in regurgitant or stenotic diseases in patients with poor acoustic window[97,98]. Although echocardiography remains gold-standard, a fair number of studies have already proved cine-CMR as a valid imaging modality for assessment of significant regurgitation in patients with MV prolapse, pinpointing CMR-derived hallmarks associated to MV disease[99,100]. Maffesanti et al.[87] demonstrated the feasibility of 3D dynamic CMR-based comprehensive morpho-functional assessment of cardiac chambers and MV apparatus in specific pathologies.

Finally, the growing interest in minimally invasive procedures is leading to increasing demand on accurate and reliable MV morphological assessment in the research field, in which CT might be more appropriate for geometric measurement in transcatheter intervention planning[75]. Pre-operative CT can provide structural details, such as calcification, as well as valvular thickening, being important in the geometrical complexity evaluation thanks to its superior spatial resolution[78].

Tricuspid Valve: it has been under-investigated for many years (referring to as "forgotten valve") since it was originally believed "to be designed to be incompetent"[101] and even because right heart abnormalities are usually asymptomatic[102]. However, recently the interest in the TV has been increasing,

in part due to evidence that dysfunction of this valve may be more influential in patients' outcomes, to establish, for instance, if dilatation of the annulus is progressing to regurgitation and to appreciate that the annulus dimensions change during the cardiac cycle[38,103]. In this regard, even more than MV and AV, there is still much to learn about the TV complex as well as the natural changes occurring during ageing in order to better investigate and explain the alterations that may arise to its dynamic and highly mobile structure during disease, also exploiting the advent of multimodality imaging.

The primary imaging of choice for the TV morphological assessment is echocardiography. Mainly used in TTE modality, 3D imaging has been proved efficient in evaluating TV complex morphology[37] as well as locating the regurgitant orifice and measuring tenting volume and height in patients affected by tricuspid regurgitation (TR)[49,104]. With 3D TTE, Ton-Nu and co-workers[31] demonstrated that the typical non-planar configuration of the tricuspid annulus markedly changes in FTR, becoming flatter and increasing dimension mainly along the ventricle free-wall (antero-posterior direction). By means of TEE modality, Ring et al.[105] investigated much more in detail the anatomical and physiological alterations which affect TV in abnormal dilated right hearts. Providing also dynamic analysis of annular structures, they gained insight into the FTR-related dilation mechanism as a prognostic indicator, proving the decrease of septo-lateral motility as the main contributor of TV area change.

Nonetheless, TV investigation through 3D TTE is challenging because of its unfavorable retrosternal position and the high variability of its anatomy. TV can be optimally visualized from a single mid- esophageal four-chamber view using the zoom mode only in 11% of patients, largely because this valve is anteriorly located, and has thinner leaflets compared with the mitral valve[37]. Thus, although 3D TTE remaining pivotal in the intraoperative guidance of implantable devices[106] and a better and more advanced understanding of spatial relationships among TV components is required[107]. To this aim, thanks to its greater spatial resolution, CT scans offers complementary information, such as amount and type of annular tissue (e.g., presence of calcification) as well as relative position of TV annulus respect to the right coronary artery[108], for instance.

Tethering of leaflets as a result of annular remodeling and flattening has been proved as key-hallmark in FTR, even when a TA dilation does not occur[109]. In this study, performing a CMR image-based analysis, the author found that in FTR patients with non-dilated TA the 3D non-planar shape of the annulus is maintained, whereas both the tenting height and the annular longitudinal displacement altered, potentially being considered as one of FTR triggering factors.

Ventricles: evaluation of in-vivo ventricular size and motion along the cardiac cycle are by far the most common reasons for performing echocardiography in the adult patient. Important diagnostic, prognostic, and treatment decisions rest upon their morphology analysis, even considering that a really good correlation with CMR in terms of volume, mass and ejection fraction measurement has already been proved[110]. Moreover, echocardiographic imaging is the unique alternative when facing with LV- or RV-implanted scenario. In these cases, CT or CMR cannot be performed due to the high patient comorbidity and technical limit, respectively. Conversely, ultrasound images can be exploited in order to quantitively define ventricular shape and, more interestingly, remodeling; in this way it could be used to track differential local change in the ventricular wall, potentially being pivotal in predicting disease occurrence[111].

However, CMR remains a valid alternative in the physiological scenario, especially for providing adequate spatial resolution, that is worth to taken into account when focusing on motion modeling and strains analysis[112].

1.2.3 Biomechanical analysis

In this increasingly growing scenario, patient-specific 3D models have been introduced, before in the research field and now beginning to impact the clinical treatment. As numerical and engineering tool, computational models have become pivotal in cardiac research[113]. Moving beyond the accurate anatomical investigation performable by means novel imaging modalities, computational models can be effectively considered a step forward, providing quantitative analysis on the biomechanical behavior in terms of stress-strain response and other multifactorial parameters.

Based on the numerical solution of the equations of continuum mechanics applied to complex systems, they are naturally appealing, since they are flexible and versatile, if compared to the typical high costs and non-repeatability related to the experimental animal models. In particular, over the two last decades, their applications have been ranging from elucidating the heart biomechanics underlying different patho-physiological conditions[114] to predicting the effects of either surgical or percutaneous procedures, even comparing several implantation techniques and devices[115].

The most widely used numerical models mainly rely on two different approach, namely the finite element (FE) and the finite volume theories. The former is suitable for structural problem where the presence of the fluid is neglected and its effect is accounted for by means of equivalent pressure loading boundaries; the latter is exploited in the computational fluid dynamics (CFD) studies. In either case, the initial geometry, as a complex domain, is subdivided into smaller, simpler ones (*discretization*), so the governing partial differential equation (PDE) problem can be approximated with system of algebraic or ordinary differential equations. Then, defining the proper physical material properties, boundary and loading conditions, such method allows for the evaluation of several field variables which cannot be directly computed or measured through any experimental tool, mainly strain and stress fields. Higher is the level of detail in the problem modeling, more accurate will be the solution, as well as greater will be also the computational cost. However, the implementation of a fully realistic FE model of a cardiac district still represents a challenging task, because of the high complexity of the issues to be addressed at once, namely the morphology, the tissue mechanical response, the dynamic loading and boundary conditions and the interaction with the surrounding structures.

At the early stage, most of the studies focused on FE modeling in cardiac environment were based on paradigmatic models[116–123]. It means that models' geometry showed a coarse representation of the real anatomy, since they were derived from animal or population-based ex-vivo measurements and laid over simplifying assumptions and idealization even of the mechanical behavior. Such

these models are typically exploited to mimic physiological function, to understand the pathology-induced biomechanical alterations on the considered anatomical district as well as related surgical corrections. However, their paradigmatic nature, while allowing to infer conclusions of general validity, has the drawback of limiting the applicability of these results, since the patho-physiological "real" scenario necessarily differs from this idealized representation. This mismatch could be of primary importance when dealing with selection and tuning of surgical repair techniques in different clinically relevant scenario. To this aim, nowadays the current generation of computational models heavily exploits the detailed anatomical information yielded by medical imaging to provide patient-specific analyses, paving the way toward the development of virtual surgical-planning tools[124–128].

In the latter scenario, where FE strategy proves to be too time-demanding to be used in a real clinical setting[129], mass-spring models (MSMs) have been recently proposed as a valid alternative. They differ from classical FE approach since the continuum structure is described as a discrete cloud of nodal masses connected through a mesh of springs, able to simulate its mechanical response. Such a numerical strategy does not allow for a comprehensive evaluation of the biomechanical variables (e.g., stress and strain) but may provide an effective trade-off between time-efficiency and reliability, potentially supporting surgical planning in high-risk clinical scenarios[130].

Furthermore, the application of CFD models in the cardiovascular scenario is wide ranging, most notably thanks to their capability in analyzing CVDs' progression from a biomechanics perspective. They can be exploited to study the complex relation between pathology onset and altered flow patterns, e.g. aneurysm[131], to aid surgical decision-making in order to achieve better clinical outcomes, e.g. TAVR[132], as well as to improve hemodynamic performance of mechanical circulatory devices, e.g. LVADs[133].

The implementation of a fully realistic FE model of the atrioventricular valves represents a challenging task: the model should include all the substructures and should account for their time-dependent change in shape, proportions and mutual

positions, thus information provided by volumetric acquisitions (3DTEE/TTE, CMR, CT) prove to be crucial to this aim.

Reviewing the scientific literature, in the last decade most of the studies has been focused on 3D echo-derived FE models, mainly concerning the MV scenario[134–140]. Nonetheless, it is worth to notice that all the morphological and functional information potentially achievable from such imaging technique was has been not fully exploited. In one of the first example reported by Votta et al.[136], the geometrical model accounted for in-vivo extension and inclination of the MV leaflets, but their profile was idealized through a sinusoidal function, as well as PMs position and displacement, not easily detectable from ultrasound images, were defined merging in-vivo data with ex-vivo measurements. MV repair techniques were also studied, again basing the model implementation on 3D TEE data[126,140–142]. In particular, Mansi and colleagues[141], developed a MV model to explore the overall valvular behavior following the MitraClip® (Abbott, Abbott Park, Illinois, USA); to this aim, the model did not take into account the typical anisotropic mechanical response of the leaflet tissue, simply described as linear and isotropic material. The same assumption was adopted by Pouch et al.[143], who aimed to assess chordal pattern influence on systolic MV configuration, through a model obtained performing a semi-automated segmentation on 3D TEE images. However, pinpointing a common aspect among such kind of works, it is barely true that ultrasound imaging cannot comprehensively detect the whole complex valve structure, such as chordal origin and insertion or PMs motion field, due to its limited spatial and temporal resolution[144].

CMR imaging can be effectively used as an alternative source of data in order to build MV patient-specific models, given its higher time resolution and better blood-to-tissue contrast respect to echocardiography. As a consequence, CMR constitutes a valuable imaging technique for a detailed quantification of several nuances of the valvular apparatus, such as annular and papillary muscle function, or leaflet geometry[145,146]. Starting from cine-CMR sequence acquisition, one of the first patient-specific MV computational model was proposed by Stevanella et al.[147]: thanks to imaging features, authors were able to capture the complete

end-diastolic leaflets' profile as well as the time-dependent position of PM tips throughout the cardiac cycle. Moreover, as shown in the last decade literature, several research groups have obtained *in vivo* MV geometry from CMR imaging basically to test and compare MV repair procedures improving patient selection, rather than to predict personalized interventions outcomes for the specific subject[124,148–151]. Thus, CMR may allow for more flexibility and precision in the modelling procedure, thanks to the fact that image quality is not affected by the quality of the acoustic window. Nonetheless, although an *ad hoc* rotational acquisition can be set preventing operator-dependent artefacts, such an imaging sequence is not routinely adopted in the study of MV apparatus, thus being a limitation in aiming at the development of a decision-support tool for clinical practice.

However, various degrees of assumptions were made in the aforementioned studies to simplify the mitral valve geometry: due to the inadequate spatial resolution of the previously mentioned *in vivo* MV images, chordal length, chordal origins on the papillary muscles, and chordal insertion points in MV models are still based on generic paradigmatic pattern derived from *ex vivo* observations[136,147,152]. Realistic-like chordae and leaflet reconstruction could be achieved by using CT, specifically Micro-CT (μ-CT), as proved by the whole of studies recently published[144,153–156]. Chordae tendineae play a major role in determining the shape and the stress field on the valve, thus their geometry must be well characterized. In particular, it is known that some MV repair strategies rely on chordal structure rearrangement to improve leaflet coaptation[157]; in this context, FE strategies should take into account the accurate anatomical description of sub-valvular structures to improve treatment outcome. For instance, He et al.[158] performed anatomic, biomechanical, and hemodynamic measurements of MV function and showed that the spatial distribution of chords significantly impacts MV competence, concept proved even by Lomholt and colleagues[159] who reported elevated chordal tensile forces in different chordae tendineae under ischemic conditions. In a human study, Gunnal et al.[160] recently investigated 116 cadaveric hearts and defined more than 21 classes to describe the chordal geometry. Nonetheless, although *in vivo* imaging of the MV leaflets

has improved significantly in the past decade, the chordal apparatus geometric properties remain largely unresolvable in current clinical imaging setups[161], as well as in the scientific literature[162], even though chordal histology has been elucidated[13,163–166].

What has been pointed out so far is even more valid if the topic moves on the TV side, remembering that scientific literature has been referring to as "forgotten valve" until the last decade. The first complete TV numerical model was born as the result of the finite element (FE) approach developed by Stevanella et al.[121] in 2010. It was a generic paradigmatic model, since no imaging acquisition was performed to define the valve geometry, which instead was accomplished merging experimental measurements on porcine and human samples with data taken from literature[34]. Considering the increasing clinical interest in TV diseases and treatments, as well as the parallel growth of transcatheter heart valves therapies, this study has certainly paved the way to the development of computational tools for TV biomechanical evaluation, even if such these treatments remain still heavily challenging because little is known about the complex geometry and function of TV apparatus. In this scenario, Kong and colleagues[167] have recently proposed a patient-specific TV FE model, deriving valve geometry from multi-slice computed tomography (MSCT) acquisitions. Accounting for well-detailed morphology and including the typical anisotropic hyperelastic behavior of leaflets tissue, this computational approach may be pivotal for support pre-operative planning in complex TV repair procedures in the future.

The combined use of numerical simulations and clinical imaging for research and diagnosis can also provide additional investigation of the relationship between cardiac pathology and the associated abnormal blood flow pattern even related to pathological scenarios[168], as well as allowing for examination of different treatment options[169]. Global and regional hemodynamic variables, such as ventricular wall motion, spatial and temporal distribution of blood pressure, and myocardial stress and strains, can be obtained through CFD simulations[170].

To achieve a detailed and reliable hemodynamic analysis whose results are not overly approximated, a left ventricular CFD model should have the following properties: i) reproduce the patient-specific geometry of the LV; ii) the imposed LV wall motion should replicate the cardiac one, thus accounting for myocardial fibers torsion, as well as for LV wall contraction/dilation over the different phases of the cardiac cycle. These specifications are required since vortex dynamics, stagnation areas and recirculation patterns are strongly dependent on the LV morphology and cardiac wall motion.

According to the literature, the first comprehensive patient-specific LV CFD model was proposed in 2016 by Bavo and colleagues[171]: they aimed at evaluating the abnormal flow patterns in impaired hearts, applying prescribed moving boundary conditions directly extracted from real-time 3D TEE images. As a matter of fact, being also the main limitation, this study did not account for LV torsional component of motion, due to an interpolation process in the motion field computation. The moving boundary conditions of the LV wall has been, and it is still now, an open issue in the LV CFD simulation implementation, given the not trivial challenge in extracting this information from the volumetric imaging dataset. Liao et al., in 2016[172], and Prisco et al.[169], one year later, proposed a model of LVAD-assisted left ventricle in order to investigate the influence of different inflow cannula geometry and the impact of its position, respectively, on the intraventricular flow; however, the CT-derived model completely neglected LV wall motion. To overcome this issue, more recently, Liao and colleagues[173], published a new study presenting a 3D multiscale computational fluid dynamic model of the LV, to evaluate the risk of thrombosis with varying inflow cannula insertion lengths in a dilated LV.

1.3 Motivation

In silico models have proven to provide powerful prediction tools to build insight into the valvular physiology[167,174], design medical prosthetics[175], and optimize surgical treatments[126,169]. Reviewing the literature, the fact that earlier modelling

studies relied on morphological and mechanical assumptions mainly coming from *ex vivo* measurements is noteworthy[176]. Subsequently, several research studies focused on improving heart valve computational simulations by enhancing geometric models[177], constitutive models[178,179], and simulation frameworks[180–182]. Moreover, to ultimately utilize computational simulations in clinical applications, the geometric fidelity, the structural precision and the comprehensive flow field description of the models must be substantially improved, such as to increase predictive power. On this latter observation relies the reason why the majority of the recent studies is based on CMR or CT/micro-CT acquisitions, and, very recently, on 4D-CT, given both the spatial and the temporal resolution which can be achieved[124,140,148–151,154,156,167,183–185]. As for CMR imaging, CT (specifically multi-detector CT) can provide meaningful information about 3D anatomy and contractile function of the heart and heart's structures[186]. Nonetheless, although such imaging techniques allows for real-like accurate anatomical reconstruction potentially providing a way to address some of the key challenges related to *in vivo* modelling, they cannot be applied routinely in clinical practice. On one hand, CMR lasts a long scan time, is often based on contrast agent use and cannot be performed when a device is present. On the other hand, even though the acquisition time is likely one third respect to CMR, CT is highly expensive and massively invasive and there is no way in its exploitation in patients with high comorbidity. Thus, 3D computational models directly derived from in vivo CT imaging are far to be obtained, still remaining focused on ex vivo benchmark acquisitions.

In this scenario, 3D echocardiography has been progressively emerging as the imaging modality of choice, since it is routinely employed as the gold standard in the clinical practice for diagnosis[187]. Aiming at developing patient-specific FE models from *in vivo* clinical imaging, echocardiography presents a series of advantages compared to CT and CMR. The ultrasounds have no harmful effects on the patient with respect to the ionizing radiation used in a tomographic scan and no radiopaque contrast agents are needed to perform echocardiographic

acquisitions. Echocardiography is widely available, since it is found in virtually all hospitals, and cost-effective, both in terms of equipment and facility costs.

Despite these advantages, 3D volumetric ultrasound imaging shows intrinsic limitations beyond its limited resolution, being heavily depending on the operator but also on the acoustic window characteristics of the patient. Specifically, the imaging depth is not always satisfactory, thus not allowing for discriminating among different structures, or not encompassing them at all in the field of view. So, the first limitation is strictly related to a lack in the morphological information in the volumetric data. The clever example in this case is characterized by the scenario that involves the TV investigation. In this context, the information yielded by volumetric imaging data has not been yet standardized: TV was completely under investigated up to the last decade, most likely owing to its not so trivial detection given its position and orientation, as well as the limited availability of such technologies. As result, with respect to the mitral valve, little has been done to quantify the biomechanics of the TV apparatus, with many of these studies being conducted *ex vivo* on porcine tissue[188–190]. Specifically concerning the FE approach, to the best of our knowledge only two TV models have been proposed, the first idealized one being part of the research activity of our group[121] and the second very recently published by Kong and colleagues[167], to be noted as the first patient-specific TV FE model. Nonetheless, none of them is based on *in vivo* echocardiographic data. The inherent limitations of the clinical imaging modalities like real-time 3D echocardiography (rt-3DE) have long hampered the development of high-fidelity models on a patient-specific basis even in MV scenario. Indeed, even if *in vivo* imaging has brought FE approach to be capable to gain insight into valve function and disease, developing models strictly from clinical imaging data to faithfully predict MV repair treatments still remains not fully addressed. The reason relies on the fact that most of pathologies are related to simultaneous anatomical variations and patient-specific tissue remodelling, the latter being something that a numerical model is not able to account for, since in the image-derived reconstruction a stress-free assumption on the initial geometry is always

made[124,151,176,191]. The functional MV regurgitation, due to ischemic disease, is the perfect case study in this context. It is characterized by a leaflet tissue remodelling resulting from abnormal stretching in the chordae owing to PMs dislocation. Thus, chordae will have a pre-stretched/pre-stressed condition which can play an important role in simulating MV dynamics, as already reported by Pham et al.[144], but again starting from multi-slice CT scans. Nonetheless, by means of 3D ultrasound imaging, chordal apparatus is not visible with the only alternative to include it exploiting ex vivo-derived paradigmatic patterns, and thus the issue to take into account the tethering effect. Finally, 3D TEE is also routinely accomplished intraoperatively in high-risk surgical interventions, such as LVAD implantation, as reported by the America Society of Echocardiography (ASE) guidelines[192]. TEE can provide a wealth of information on the changes incurred on the anatomy as well as on the hemodynamics altered by the new device-induced configuration[193]. Given that, everything becomes actually more challenging if aiming at the development of a numerical model. Patient-specific LV-LVAD computational models can be exploited for the fluid-dynamics assessment by means of CFD approach, aiding to better evaluate the thrombogenic potential in terms of blood flow characteristics (e.g., shear stresses, stagnation zones, recirculation patterns)[171,194]. In this scenario, one must be aware that both the morphological accuracy of the pre-operative geometry and the post-operative device configuration must be considered. Something, however, that remains challenging, since the model has to be derived from ultrasound volumetric data, 3D TTE being the available technique of choice to be performed in this case, but a standardized acquisition protocol is still lacking.

1.4 Aims and outline of the work

In the previously described scenario, the main aim of this work to propose numerical strategies which can aid to overcome intrinsic limitations of the echocardiographic imaging.

Specifically, the first specific objective was the development of a novel approach integrating in vitro imaging and FE modeling to evaluate TV biomechanics,

facing with the lack of information on anatomical features owing to the clinically evident demanding detection of this anatomical district through *in vivo* imaging. The second specific aim was the implementation of a computational framework able to reproduce a functionally equivalent model of the MV sub-valvular apparatus through chordae tendineae topology optimization. In details, starting from TEE imaging data, patient-specific mass-spring models (MSMs) were exploited aiming at chordae rest length rearrangement, with the long-term perspective to include it as a preparatory tool in the FE models' development, improving their accuracy and, thus, their predictive power.
Finally, facing with the issue related to particular high-risk clinical scenarios where 3D TTE is the only available technique to be used but without any acquisition protocol, the last specific aim was the creation of a numerical strategy able to allow for patient-specific geometrical reconstruction both pre- and post-LVAD implantation, as a real-life clinical case resembling the limitations of ultrasound imaging and thus how is possible to overcome them.

1.5 Structure of the thesis

According to the above described framework, in the present thesis, after an introductory part describing the anatomy and pathophysiology of the cardiac districts herein considered and a review of their scientific investigation in terms of morphological and biomechanical modelling, the following chapters are presented:

- *Chapter 2*: a novel approach for the study of the tricuspid valve biomechanics is proposed, integrating experimental in vitro data and computational elaborations towards the development of the first 3D echo-based complete finite element model of the valve. The acquired **3D ultrasound** images are used to reconstruct the leaflets profile at end diastole and to define the time-dependent geometry of the annulus as well as the papillary muscles position. Altogether, this information could be taken as input to define the FE model, implementing appropriate material mechanical properties specifically derived for the TV.

- *Chapter 3*: exploiting a novel mass spring model approach, an ad-hoc iterative algorithm is developed aiming at reproducing the effect of native chordal anatomy on the mitral valve early-systolic configuration. Focusing on the relevant scenario of the functional mitral valve regurgitation (FMR) and starting from standard **3D ultrasound** data, the goal was to improve the accuracy of the model with the implementation of a paradigmatic but functionally equivalent sub-valvular apparatus, allowing for the capability to consider the chordae tethering effect, managing their geometrical topology.
- *Chapter 4*: proposed as a side-project, this chapter provides a case-study strategy on how to face with the challenging issues related to standard (**3D ultrasound**) *in vivo* imaging with respect to high-risk clinical scenario, such as ventricular assist device implantation. Aiming to a subsequent fluid-dynamic analysis as detailed and reliable as possible, the proposed workflow allowed for patient-specific model implementation in terms of both the geometry and the wall motion, accounting for contraction/dilation as well as for myocardial torsion.
- *Chapter 5*: this chapter provides a general discussion and the conclusive remarks of the PhD dissertation.

The works described in this thesis were realized basing on the collaboration with different clinical and technical centers. In specific, the entire PhD project was developed under the technical supervision of prof. Emiliano Votta and prof. Alberto Redaelli at the Biomechanics Group of Politecnico di Milano (Department of Electronics, Information and Bioengineering). The studies described in chapters 2 and 4 were carried out in collaboration with ForCardioLab in Ospedale Luigi Sacco (Milan) and Ospedale San Raffaele (Milan), respectively.

1.6 Bibliography

1. Kaplan, S. R. *et al.* Three-dimensional echocardiographic assessment of annular shape changes in the normal and regurgitant mitral valve. *Am. Heart J.* **139,** 378–87 (2000).
2. Itoh, A. *et al.* Mitral annular hinge motion contribution to changes in mitral septal-lateral dimension and annular area. *J. Thorac. Cardiovasc. Surg.* **138,** 1090–9 (2009).
3. Fyrenius, A., Engvall, J. & Janerot-Sjöberg, B. Major and minor axes of the normal mitral annulus. *J. Heart Valve Dis.* **10,** 146–52 (2001).
4. Kunzelman, K. S., Cochran, R. P., Verrier, E. D. & Eberhart, R. C. Anatomic basis for mitral valve modelling. *J. Heart Valve Dis.* **3,** 491–6 (1994).
5. Grande-Allen, K. J. & Liao, J. The heterogeneous biomechanics and mechanobiology of the mitral valve: implications for tissue engineering. *Curr. Cardiol. Rep.* **13,** 113–20 (2011).
6. Kunzelman, K. S. *et al.* Differential collagen distribution in the mitral valve and its influence on biomechanical behaviour. *J. Heart Valve Dis.* **2,** 236–44 (1993).
7. Cochran, R. P., Kunzelman, K. S., Chuong, C. J., Sacks, M. S. & Eberhart, R. C. Nondestructive analysis of mitral valve collagen fiber orientation. *ASAIO Trans.* **37,** M447-8
8. Kunzelman, K. S. & Cochran, R. P. Stress/strain characteristics of porcine mitral valve tissue: parallel versus perpendicular collagen orientation. *J. Card. Surg.* **7,** 71–8 (1992).
9. May-Newman, K. & Yin, F. C. Biaxial mechanical behavior of excised porcine mitral valve leaflets. *Am. J. Physiol.* **269,** H1319-27 (1995).
10. Grashow, J. S., Yoganathan, A. P. & Sacks, M. S. Biaixal Stress–Stretch Behavior of the Mitral Valve Anterior Leaflet at Physiologic Strain Rates. *Ann. Biomed. Eng.* **34,** 315–325 (2006).
11. Krishnamurthy, G. *et al.* Material properties of the ovine mitral valve anterior leaflet in vivo from inverse finite element analysis. *Am. J. Physiol. Heart Circ. Physiol.* **295,** H1141–H1149 (2008).
12. Itoh, A. *et al.* Active stiffening of mitral valve leaflets in the beating heart. *Am. J. Physiol. Circ. Physiol.* **296,** H1766–H1773 (2009).
13. Ritchie, J., Jimenez, J., He, Z., Sacks, M. S. & Yoganathan, A. P. The material properties of the native porcine mitral valve chordae tendineae: An in vitro investigation. *J. Biomech.* (2006). doi:10.1016/j.jbiomech.2005.01.024

14. Lam, J. H., Ranganathan, N., Wigle, E. D. & Silver, M. D. Morphology of the human mitral valve. I. Chordae tendineae: a new classification. *Circulation* **41,** 449–458 (1970).
15. Kunzelman, K. S. & Cochran, R. P. Mechanical properties of basal and marginal mitral valve chordae tendineae. *ASAIO Trans.* **36,** M405-8 (1990).
16. Sakai, T. *et al.* Distance between mitral anulus and papillary muscles: Anatomic study in normal human hearts. *J. Thorac. Cardiovasc. Surg.* **118,** 636–641 (1999).
17. Dagum, P. *et al.* Coordinate-free analysis of mitral valve dynamics in normal and ischemic hearts. *Circulation* **102,** III62-9 (2000).
18. Nkomo, V. T. *et al.* Burden of valvular heart diseases: a population-based study. *Lancet (London, England)* **368,** 1005–11 (2006).
19. He, S., Fontaine, A. A., Schwammenthal, E., Yoganathan, A. P. & Levine, R. A. Integrated mechanism for functional mitral regurgitation: leaflet restriction versus coapting force: in vitro studies. *Circulation* **96,** 1826–34 (1997).
20. Tibayan, F. A. *et al.* Geometric Distortions of the Mitral Valvular-Ventricular Complex in Chronic Ischemic Mitral Regurgitation. *Circulation* **108,** 116II--121 (2003).
21. Yosefy, C. *et al.* Mitral regurgitation after anteroapical myocardial infarction: new mechanistic insights. *Circulation* **123,** 1529–36 (2011).
22. Dal-Bianco, J. P., Beaudoin, J., Handschumacher, M. D. & Levine, R. A. Basic mechanisms of mitral regurgitation. *Can. J. Cardiol.* **30,** 971–81 (2014).
23. Deja, M. A. *et al.* Mechanisms of functional mitral regurgitation in cardiomyopathy secondary to anterior infarction. *Eur. J. Cardiothorac. Surg.* **45,** 1089–96 (2014).
24. Levine, R. A. *et al.* Mitral valve disease--morphology and mechanisms. *Nat. Rev. Cardiol.* **12,** 689–710 (2015).
25. Feldman, T. & Young, A. Percutaneous Approaches to Valve Repair for Mitral Regurgitation. *J. Am. Coll. Cardiol.* **63,** 2057–2068 (2014).
26. Bonow, R. O. *et al.* ACC/AHA 2006 Guidelines for the Management of Patients With Valvular Heart Disease. *Circulation* **114,** e84-231 (2006).
27. Nappi, F., Avatar Singh, S. S., Santana, O. & Mihos, C. G. Functional mitral regurgitation: an overview for surgical management framework. *J. Thorac. Dis.* **10,** 4540–4555 (2018).
28. Schmitto, J. D. *et al.* Functional mitral regurgitation. *Cardiol. Rev.* **18,** 285–91

(2010).

29. Silver, M. D., Lam, J. H., Ranganathan, N. & Wigle, E. D. Morphology of the human tricuspid valve. *Circulation* **43,** 333–48 (1971).
30. Yacoub, M. H. & Cohn, L. H. Novel approaches to cardiac valve repair: from structure to function: Part II. *Circulation* **109,** 1064–72 (2004).
31. Ton-Nu, T.-T. *et al.* Geometric Determinants of Functional Tricuspid Regurgitation. *Circulation* **114,** 143–149 (2006).
32. Fawzy, H. *et al.* Complete mapping of the tricuspid valve apparatus using three-dimensional sonomicrometry. *J. Thorac. Cardiovasc. Surg.* **141,** 1037–43 (2011).
33. Tsakiris, A. G., Mair, D. D., Seki, S., Titus, J. L. & Wood, E. H. Motion of the tricuspid valve annulus in anesthetized intact dogs. *Circ. Res.* **36,** 43–8 (1975).
34. Hiro, M. E. *et al.* Sonometric study of the normal tricuspid valve annulus in sheep. *J. Heart Valve Dis.* **13,** 452–60 (2004).
35. Fukuda, S. *et al.* Three-Dimensional Geometry of the Tricuspid Annulus in Healthy Subjects and in Patients With Functional Tricuspid Regurgitation: A Real-Time, 3-Dimensional Echocardiographic Study. *Circulation* **114,** I-492-I-498 (2006).
36. Miglioranza, M. H. *et al.* Dynamic changes in tricuspid annular diameter measurement in relation to the echocardiographic view and timing during the cardiac cycle. *J. Am. Soc. Echocardiogr.* **28,** 226–35 (2015).
37. Muraru, D., Badano, L. P., Sarais, C., Soldà, E. & Iliceto, S. Evaluation of tricuspid valve morphology and function by transthoracic three-dimensional echocardiography. *Curr. Cardiol. Rep.* **13,** 242–9 (2011).
38. Rogers, J. H. & Bolling, S. F. The Tricuspid Valve. *Circulation* **119,** 2718–2725 (2009).
39. Cohn, L. H. Tricuspid regurgitation secondary to mitral valve disease: when and how to repair. *J. Card. Surg.* **9,** 237–41 (1994).
40. Misfeld, M. & Sievers, H.-H. Heart valve macro- and microstructure. *Philos. Trans. R. Soc. Lond. B. Biol. Sci.* **362,** 1421–36 (2007).
41. Anwar, A. M. *et al.* Assessment of normal tricuspid valve anatomy in adults by real-time three-dimensional echocardiography. *Int. J. Cardiovasc. Imaging* **23,** 717–724 (2007).
42. Nigri, G. R., Di Dio, L. J. & Baptista, C. A. Papillary muscles and tendinous cords of the right ventricle of the human heart: morphological characteristics.

Surg. Radiol. Anat. **23,** 45–9 (2001).

43. Aktas, E. O., Govsa, F., Kocak, A., Boydak, B. & Yavuz, I. C. Variations in the papillary muscles of normal tricuspid valve and their clinical relevance in medicolegal autopsies. *Saudi Med. J.* **25,** 1176–85 (2004).
44. Mascherbauer, J. & Maurer, G. The forgotten valve: lessons to be learned in tricuspid regurgitation. *Eur. Heart J.* **31,** 2841–3 (2010).
45. Spinner, E. M. *et al.* Correlates of Tricuspid Regurgitation as Determined by 3D Echocardiography: Pulmonary Arterial Pressure, Ventricle Geometry, Annular Dilatation, and Papillary Muscle Displacement. *Circ. Cardiovasc. Imaging* **5,** 43–50 (2012).
46. Taramasso, M. *et al.* Percutaneous tricuspid valve therapies: the new frontier. *Eur. Heart J.* **38,** ehv766 (2016).
47. Topilsky, Y. *et al.* Burden of Tricuspid Regurgitation in Patients Diagnosed in the Community Setting. *JACC. Cardiovasc. Imaging* (2018). doi:10.1016/j.jcmg.2018.06.014
48. Kilic, A., Saha-Chaudhuri, P., Rankin, J. S. & Conte, J. V. Trends and Outcomes of Tricuspid Valve Surgery in North America: An Analysis of More Than 50,000 Patients From The Society of Thoracic Surgeons Database. *Ann. Thorac. Surg.* **96,** 1546–1552 (2013).
49. Fukuda, S. *et al.* Determinants of Recurrent or Residual Functional Tricuspid Regurgitation After Tricuspid Annuloplasty. *Circulation* **114,** I-582-I-587 (2006).
50. Badano, L. P., Muraru, D. & Enriquez-Sarano, M. Assessment of functional tricuspid regurgitation. *Eur. Heart J.* **34,** 1875–1885 (2013).
51. Taramasso, M. & Maisano, F. Transcatheter tricuspid valve intervention: state of the art. *EuroIntervention* **13,** AA40-AA50 (2017).
52. Ho, S. Y. Anatomy and myoarchitecture of the left ventricular wall in normal and in disease. *Eur. J. Echocardiogr.* **10,** iii3-iii7 (2009).
53. Adhyapak, S. M. & Parachuri, V. R. Architecture of the left ventricle: insights for optimal surgical ventricular restoration. *Heart Fail. Rev.* **15,** 73–83 (2010).
54. Streeter, D. D., Spotnitz, H. M., Patel, D. P., Ross, J. & Sonnenblick, E. H. Fiber orientation in the canine left ventricle during diastole and systole. *Circ. Res.* **24,** 339–47 (1969).
55. Rüssel, I. K. *et al.* Left ventricular torsion: an expanding role in the analysis of myocardial dysfunction. *JACC. Cardiovasc. Imaging* **2,** 648–55 (2009).

56. Lorenz, C. H., Pastorek, J. S. & Bundy, J. M. Delineation of normal human left ventricular twist throughout systole by tagged cine magnetic resonance imaging. *J. Cardiovasc. Magn. Reson.* **2,** 97–108 (2000).
57. Notomi, Y. *et al.* Enhanced Ventricular Untwisting During Exercise. *Circulation* **113,** 2524–2533 (2006).
58. Sengupta, P. P., Tajik, A. J., Chandrasekaran, K. & Khandheria, B. K. Twist Mechanics of the Left Ventricle. *JACC Cardiovasc. Imaging* **1,** 366–376 (2008).
59. Roberts, W. C., Siegel, R. J. & McManus, B. M. Idiopathic dilated cardiomyopathy: analysis of 152 necropsy patients. *Am. J. Cardiol.* **60,** 1340–55 (1987).
60. Feild, B. J. *et al.* Left ventricular function and hypertrophy in cardiomyopathy with depressed ejection fraction. *Circulation* **47,** 1022–31 (1973).
61. Wallis, D. E., O'Connell, J. B., Henkin, R. E., Costanzo-Nordin, M. R. & Scanlon, P. J. Segmental wall motion abnormalities in dilated cardiomyopathy: a common finding and good prognostic sign. *J. Am. Coll. Cardiol.* **4,** 674–9 (1984).
62. Douglas, P. S., Morrow, R., Ioli, A. & Reichek, N. Left ventricular shape, afterload and survival in idiopathic dilated cardiomyopathy. *J. Am. Coll. Cardiol.* **13,** 311–5 (1989).
63. McNally, E. M. & Mestroni, L. Dilated Cardiomyopathy. *Circ. Res.* **121,** 731–748 (2017).
64. Dec, G. W. & Fuster, V. Idiopathic Dilated Cardiomyopathy. *N. Engl. J. Med.* **331,** 1564–1575 (1994).
65. Kirklin, J. K. *et al.* Seventh INTERMACS annual report: 15,000 patients and counting. *J. Hear. Lung Transplant.* **34,** 1495–1504 (2015).
66. Kirklin, J. K. *et al.* Pump thrombosis in the Thoratec HeartMate II device: An update analysis of the INTERMACS Registry. *J. Hear. Lung Transplant.* **34,** 1515–1526 (2015).
67. Marsden, A. L., Bazilevs, Y., Long, C. C. & Behr, M. Recent advances in computational methodology for simulation of mechanical circulatory assist devices. *Wiley Interdiscip. Rev. Syst. Biol. Med.* **6,** 169–88 (2014).
68. Rogers, J. G. *et al.* Intrapericardial Left Ventricular Assist Device for Advanced Heart Failure. *N. Engl. J. Med.* **376,** 451–460 (2017).
69. Mehra, M. R., Naka, Y. & Salerno, C. Left Ventricular Assist Devices for Advanced Heart Failure. *N. Engl. J. Med.* **376,** 1893–1895 (2017).

70. Starling, R. C., Blackstone, E. H. & Smedira, N. G. Increase in Left Ventricular Assist Device Thrombosis. *N. Engl. J. Med.* **370,** 1463–1466 (2014).
71. Najjar, S. S. *et al.* An analysis of pump thrombus events in patients in the HeartWare ADVANCE bridge to transplant and continued access protocol trial. *J. Hear. Lung Transplant.* **33,** 23–34 (2014).
72. Adams, D. H., Rosenhek, R. & Falk, V. Degenerative mitral valve regurgitation: best practice revolution. *Eur. Heart J.* **31,** 1958–1966 (2010).
73. Jacobs, S., Grunert, R., Mohr, F. W. & Falk, V. 3D-Imaging of cardiac structures using 3D heart models for planning in heart surgery: a preliminary study. *Interact. Cardiovasc. Thorac. Surg.* **7,** 6–9 (2008).
74. Lee, L. C. *et al.* Applications of computational modeling in cardiac surgery. *J. Card. Surg.* **29,** 293–302 (2014).
75. Sun, W., Martin, C. & Pham, T. Computational Modeling of Cardiac Valve Function and Intervention. *Annu. Rev. Biomed. Eng.* **16,** 53–76 (2014).
76. Hung, J. *et al.* 3D Echocardiography: A Review of the Current Status and Future Directions. *J. Am. Soc. Echocardiogr.* **20,** 213–233 (2007).
77. Zhang, L. *et al.* Quantitative Assessment of Mitral Apparatus Geometry Using Dual-Source Computed Tomography in Mitral Regurgitation. *Int. Heart J.* **56,** 408–414 (2015).
78. Kim, J. H., Kim, E. Y., Jin, G. Y. & Choi, J. B. A Review of the Use of Cardiac Computed Tomography for Evaluating the Mitral Valve before and after Mitral Valve Repair. *Korean J. Radiol.* **18,** 773–785 (2017).
79. Piazza, N. *et al.* Anatomy of the Aortic Valvar Complex and Its Implications for Transcatheter Implantation of the Aortic Valve. *Circ. Cardiovasc. Interv.* **1,** 74–81 (2008).
80. Kochav, J., Simprini, L. & Weinsaft, J. W. Imaging of the right heart--CT and CMR. *Echocardiography* **32 Suppl 1,** S53-68 (2015).
81. Gomez, C. K., Schiffman, S. R. & Hobbs, S. K. The Role of Computed Tomography in Predicting Left Ventricular Assist Device Infectious Complications. *J. Clin. Imaging Sci.* **6,** 43 (2016).
82. Yu, S. N. *et al.* Late outcomes of subcostal exchange of the HeartMate II left ventricular assist device: a word of caution. *Eur. J. Cardio-Thoracic Surg.* **54,** 652–656 (2018).
83. Baumgartner, H. *et al.* 2017 ESC/EACTS Guidelines for the Management of Valvular Heart Disease. *Rev. Española Cardiol. (English Ed.* **71,** 110 (2018).

84. Muraru, D., Badano, L. P., Vannan, M. & Iliceto, S. Assessment of aortic valve complex by three-dimensional echocardiography: a framework for its effective application in clinical practice. *Eur. Heart J. Cardiovasc. Imaging* **13,** 541–55 (2012).

85. Maffessanti, F. *et al.* Quantitative analysis of mitral valve apparatus in mitral valve prolapse before and after annuloplasty: a three-dimensional intraoperative transesophageal study. *J. Am. Soc. Echocardiogr.* **24,** 405–13 (2011).

86. Bohs, L. N. & Trahey, G. E. A novel method for angle independent ultrasonic imaging of blood flow and tissue motion. *IEEE Trans. Biomed. Eng.* **38,** 280–6 (1991).

87. Maffessanti, F. *et al.* Three-dimensional dynamic assessment of tricuspid and mitral annuli using cardiovascular magnetic resonance. *Eur. Heart J. Cardiovasc. Imaging* **14,** 986–95 (2013).

88. Chandra, S. *et al.* A three-dimensional insight into the complexity of flow convergence in mitral regurgitation: adjunctive benefit of anatomic regurgitant orifice area. *Am. J. Physiol. Heart Circ. Physiol.* **301,** H1015-24 (2011).

89. Ionasec, R. I. *et al.* Patient-specific modeling and quantification of the aortic and mitral valves from 4-D cardiac CT and TEE. *IEEE Trans. Med. Imaging* **29,** 1636–51 (2010).

90. Elattar, M. A. *et al.* Dynamics of the aortic annulus in 4D CT angiography for transcatheter aortic valve implantation patients. *PLoS One* **12,** e0184133 (2017).

91. Caiani, E. G. *et al.* Quantification of mitral annulus dynamic morphology in patients with mitral valve prolapse undergoing repair and annuloplasty during a 6-month follow-up. *Eur. J. Echocardiogr.* **12,** 375–83 (2011).

92. Grbic, S. *et al.* Complete valvular heart apparatus model from 4D cardiac CT. *Med. Image Anal.* **16,** 1003–1014 (2012).

93. Noack, T. *et al.* Four-dimensional modelling of the mitral valve by real-time 3D transoesophageal echocardiography: proof of concept. *Interact. Cardiovasc. Thorac. Surg.* **20,** 200–8 (2015).

94. Pepi, M. *et al.* Head-to-head comparison of two- and three-dimensional transthoracic and transesophageal echocardiography in the localization of mitral valve prolapse. *J. Am. Coll. Cardiol.* **48,** 2524–30 (2006).

95. Watanabe, N. *et al.* Quantitation of mitral valve tenting in ischemic mitral regurgitation by transthoracic real-time three-dimensional echocardiography. *J. Am. Coll. Cardiol.* **45,** 763–769 (2005).

96. Ryan, L. P. *et al.* Mitral valve tenting index for assessment of subvalvular remodeling. *Ann. Thorac. Surg.* **84,** 1243–9 (2007).
97. Cawley, P. J., Maki, J. H. & Otto, C. M. Cardiovascular Magnetic Resonance Imaging for Valvular Heart Disease. *Circulation* **119,** 468–478 (2009).
98. Gulsin, G. S., Singh, A. & McCann, G. P. Cardiovascular magnetic resonance in the evaluation of heart valve disease. *BMC Med. Imaging* **17,** 67 (2017).
99. Sturla, F. *et al.* Dynamic and quantitative evaluation of degenerative mitral valve disease: a dedicated framework based on cardiac magnetic resonance imaging. *J. Thorac. Dis.* **9,** S225–S238 (2017).
100. Han, Y. *et al.* Cardiovascular Magnetic Resonance Characterization of Mitral Valve Prolapse. *JACC Cardiovasc. Imaging* **1,** 294–303 (2008).
101. BOLT, W., HOLLMANN, W., KANN, J., VALENTIN, H. & VENRATH, H. [Behavior of pulmonary circulation time and pulmonary capillary pressure in congenital and acquired heart failures]. *Z. Kreislaufforsch.* **46,** 438–45 (1957).
102. Bruce, C. J. & Connolly, H. M. Right-sided valve disease deserves a little more respect. *Circulation* **119,** 2726–34 (2009).
103. Luxford, J., Bassin, L. & D'Ambra, M. Echocardiography of the tricuspid valve. *Ann. Cardiothorac. Surg.* **6,** 223–239 (2017).
104. Min, S.-Y. *et al.* Geometric changes after tricuspid annuloplasty and predictors of residual tricuspid regurgitation: a real-time three-dimensional echocardiography study. *Eur. Heart J.* **31,** 2871–80 (2010).
105. Ring, L. *et al.* Dynamics of the tricuspid valve annulus in normal and dilated right hearts: a three-dimensional transoesophageal echocardiography study. *Eur. Heart J. Cardiovasc. Imaging* **13,** 756–62 (2012).
106. Mediratta, A. *et al.* 3D Echocardiographic Location of Implantable Device Leads and Mechanism of Associated Tricuspid Regurgitation. *JACC Cardiovasc. Imaging* **7,** 337–347 (2014).
107. van Rosendael, P. J. *et al.* Tricuspid valve remodelling in functional tricuspid regurgitation: multidetector row computed tomography insights. *Eur. Heart J. Cardiovasc. Imaging* **17,** 96–105 (2016).
108. Ancona, F. *et al.* Multimodality imaging of the tricuspid valve with implication for percutaneous repair approaches. *Heart* **103,** 1073–1081 (2017).
109. Maeba, S., Taguchi, T., Midorikawa, H., Kanno, M. & Sueda, T. Four-dimensional geometric assessment of tricuspid annulus movement in early functional tricuspid regurgitation patients indicates decreased longitudinal

flexibility. *Interact. Cardiovasc. Thorac. Surg.* **16,** 743–9 (2013).

110. Monaghan, M. J. Role of real time 3D echocardiography in evaluating the left ventricle. *Heart* **92,** 131–136 (2006).
111. Addetia, K. *et al.* Three-dimensional echocardiography-based analysis of right ventricular shape in pulmonary arterial hypertension. *Eur. Hear. J. – Cardiovasc. Imaging* **17,** 564–575 (2016).
112. Yang, D. *et al.* 3D Motion Modeling and Reconstruction of Left Ventricle Wall in Cardiac MRI. *Funct. imaging Model. Hear. ... Int. Work. FIMH ..., proceedings. FIMH* **10263,** 481–492 (2017).
113. Zuin, M., Rigatelli, G., Faggian, G. & Roncon, L. Mathematics and Cardiovascular Interventions: Role of the Finite Element Modeling in Clinical Decision Making. *JACC. Cardiovasc. Interv.* **9,** 507–8 (2016).
114. Votta, E. *et al.* A novel approach to the quantification of aortic root in vivo structural mechanics. *Int. j. numer. method. biomed. eng.* **33,** e2849 (2017).
115. Tasca, G. *et al.* Aortic Root Biomechanics After Sleeve and David Sparing Techniques: A Finite Element Analysis. *Ann. Thorac. Surg.* **103,** 1451–1459 (2017).
116. Kunzelman, K. S., Reimink, M. S. & Cochran, R. P. Flexible versus rigid ring annuloplasty for mitral valve annular dilatation: a finite element model. *J. Heart Valve Dis.* **7,** 108–116 (1998).
117. Labrosse, M. R., Lobo, K. & Beller, C. J. Structural analysis of the natural aortic valve in dynamics: from unpressurized to physiologically loaded. *J. Biomech.* **43,** 1916–22 (2010).
118. Labrosse, M. R., Boodhwani, M., Sohmer, B. & Beller, C. J. Modeling leaflet correction techniques in aortic valve repair: A finite element study. *J. Biomech.* **44,** 2292–2298 (2011).
119. Prot, V., Skallerud, B. & Holzapfel, G. A. Transversely isotropic membrane shells with application to mitral valve mechanics. Constitutive modelling and finite element implementation. *Int. J. Numer. Methods Eng.* **71,** 987–1008 (2007).
120. Kunzelman, K. S., Einstein, D. R. & Cochran, R. P. Fluid-structure interaction models of the mitral valve: function in normal and pathological states. *Philos. Trans. R. Soc. Lond. B. Biol. Sci.* **362,** 1393–1406 (2007).
121. Stevanella, M., Votta, E., Lemma, M., Antona, C. & Redaelli, A. Finite element modelling of the tricuspid valve: A preliminary study. *Med. Eng. Phys.* **32,**

1213–1223 (2010).

122. Ovcharenko, E. A. *et al.* Modeling of transcatheter aortic valve replacement: Patient specific vs general approaches based on finite element analysis. *Comput. Biol. Med.* **69,** 29–36 (2016).

123. Avanzini, A., Donzella, G. & Libretti, L. Functional and structural effects of percutaneous edge-to-edge double-orifice repair under cardiac cycle in comparison with suture repair. *Proc. Inst. Mech. Eng. Part H J. Eng. Med.* **225,** 959–971 (2011).

124. Wong, V. M. *et al.* The Effect of Mitral Annuloplasty Shape in Ischemic Mitral Regurgitation: A Finite Element Simulation. *Ann. Thorac. Surg.* **93,** 776–782 (2012).

125. Votta, E. *et al.* Toward patient-specific simulations of cardiac valves: state-of-the-art and future directions. *J. Biomech.* **46,** 217–28 (2013).

126. Choi, A., Rim, Y., Mun, J. S. & Kim, H. A novel finite element-based patient-specific mitral valve repair: virtual ring annuloplasty. *Biomed. Mater. Eng.* **24,** 341–7 (2014).

127. Ge, L. *et al.* Measurement of mitral leaflet and annular geometry and stress after repair of posterior leaflet prolapse: virtual repair using a patient-specific finite element simulation. *Ann. Thorac. Surg.* **97,** 1496–503 (2014).

128. Baillargeon, B. *et al.* Human Cardiac Function Simulator for the Optimal Design of a Novel Annuloplasty Ring with a Sub-valvular Element for Correction of Ischemic Mitral Regurgitation. *Cardiovasc. Eng. Technol.* **6,** 105–16 (2015).

129. Hammer, P. E., Sacks, M. S., del Nido, P. J. & Howe, R. D. Mass-Spring Model for Simulation of Heart Valve Tissue Mechanical Behavior. *Ann. Biomed. Eng.* **39,** 1668–1679 (2011).

130. Pappalardo, O. A. *et al.* Mass-spring models for the simulation of mitral valve function: Looking for a trade-off between reliability and time-efficiency. *Med. Eng. Phys.* **47,** 93–104 (2017).

131. Xenos, M. *et al.* Progression of abdominal aortic aneurysm towards rupture: refining clinical risk assessment using a fully coupled fluid-structure interaction method. *Ann. Biomed. Eng.* **43,** 139–53 (2015).

132. Bianchi, M. *et al.* Effect of Balloon-Expandable Transcatheter Aortic Valve Replacement Positioning: A Patient-Specific Numerical Model. *Artif. Organs* **40,** E292–E304 (2016).

133. Girdhar, G. *et al.* Device thrombogenicity emulation: a novel method for

optimizing mechanical circulatory support device thromboresistance. *PLoS One* **7,** e32463 (2012).

134. Ryan, L. P. *et al.* A methodology for assessing human mitral leaflet curvature using real-time 3-dimensional echocardiography. *J. Thorac. Cardiovasc. Surg.* **136,** 726–34 (2008).
135. Verhey, J. *et al.* Finite-element-method (FEM) model generation of time-resolved 3D echocardiographic geometry data for mitral-valve volumetry. *Biomed. Eng. Online* **5,** 17 (2006).
136. Votta, E. *et al.* Mitral valve finite-element modelling from ultrasound data: a pilot study for a new approach to understand mitral function and clinical scenarios. *Philos. Trans. R. Soc. A Math. Phys. Eng. Sci.* **366,** 3411–3434 (2008).
137. Xu, C. *et al.* A novel approach to in vivo mitral valve stress analysis. *Am. J. Physiol. Circ. Physiol.* **299,** H1790–H1794 (2010).
138. Zhang, F. *et al.* Towards patient-specific modeling of mitral valve repair: 3D transesophageal echocardiography-derived parameter estimation. *Med. Image Anal.* **35,** 599–609 (2017).
139. Grbic, S. *et al.* Personalized mitral valve closure computation and uncertainty analysis from 3D echocardiography. *Med. Image Anal.* **35,** 238–249 (2017).
140. Rim, Y., Choi, A., McPherson, D. D. & Kim, H. Personalized computational modeling of mitral valve prolapse: Virtual leaflet resection. *PLoS One* (2015). doi:10.1371/journal.pone.0130906
141. Mansi, T. *et al.* An integrated framework for finite-element modeling of mitral valve biomechanics from medical images: Application to MitralClip intervention planning. *Med. Image Anal.* (2012). doi:10.1016/j.media.2012.05.009
142. Morgan, A. E. *et al.* Neochord placement versus triangular resection in mitral valve repair: A finite element model. *J. Surg. Res.* **206,** 98–105 (2016).
143. Pouch, A. M. *et al.* Semi-automated mitral valve morphometry and computational stress analysis using 3D ultrasound. *J. Biomech.* **45,** 903–7 (2012).
144. Pham, T. *et al.* Finite Element Analysis of Patient-Specific Mitral Valve with Mitral Regurgitation. *Cardiovasc. Eng. Technol.* **8,** 3–16 (2017).
145. Yu, H.-Y. *et al.* Functional mitral regurgitation in chronic ischemic coronary artery disease: analysis of geometric alterations of mitral apparatus with magnetic resonance imaging. *J. Thorac. Cardiovasc. Surg.* **128,** 543–51 (2004).

146. Kaji, S. *et al.* Annular geometry in patients with chronic ischemic mitral regurgitation: three-dimensional magnetic resonance imaging study. *Circulation* **112,** I409-14 (2005).

147. Stevanella, M. *et al.* Mitral Valve Patient-Specific Finite Element Modeling from Cardiac MRI: Application to an Annuloplasty Procedure. *Cardiovasc. Eng. Technol.* **2,** 66–76 (2011).

148. Wenk, J. F. *et al.* First finite element model of the left ventricle with mitral valve: insights into ischemic mitral regurgitation. *Ann. Thorac. Surg.* **89,** 1546–53 (2010).

149. Sturla, F. *et al.* Is it possible to assess the best mitral valve repair in the individual patient? Preliminary results of a finite element study from magnetic resonance imaging data. *J. Thorac. Cardiovasc. Surg.* **148,** 1025–1034 (2014).

150. Morrel, W. G. *et al.* Effect of mitral annuloplasty device shape and size on leaflet and myofiber stress following repair of posterior leaflet prolapse: a patient-specific finite element simulation. *J. Heart Valve Dis.* **23,** 727–34 (2014).

151. Sturla, F. *et al.* Functional and Biomechanical Effects of the Edge-to-Edge Repair in the Setting of Mitral Regurgitation: Consolidated Knowledge and Novel Tools to Gain Insight into Its Percutaneous Implementation. *Cardiovasc. Eng. Technol.* (2015). doi:10.1007/s13239-014-0208-4

152. Prot, V., Skallerud, B., Sommer, G. & Holzapfel, G. A. On modelling and analysis of healthy and pathological human mitral valves: two case studies. *J. Mech. Behav. Biomed. Mater.* **3,** 167–77 (2010).

153. Prot, V., Haaverstad, R. & Skallerud, B. Finite element analysis of the mitral apparatus: annulus shape effect and chordal force distribution. *Biomech. Model. Mechanobiol.* **8,** 43–55 (2009).

154. Wang, Q. & Sun, W. Finite Element Modeling of Mitral Valve Dynamic Deformation Using Patient-Specific Multi-Slices Computed Tomography Scans. *Ann. Biomed. Eng.* **41,** 142–153 (2013).

155. Lee, C.-H. *et al.* in 416–424 (Springer, Berlin, Heidelberg, 2013). doi:10.1007/978-3-642-38899-6_49

156. Khalighi, A. H. *et al.* Mitral Valve Chordae Tendineae: Topological and Geometrical Characterization. *Ann. Biomed. Eng.* **45,** 378–393 (2017).

157. Chikwe, J. & Adams, D. H. State of the Art: Degenerative Mitral Valve Disease. *Hear. Lung Circ.* **18,** 319–329 (2009).

158. He, S. *et al.* Geometric distribution of chordae tendineae: an important anatomic

feature in mitral valve function. *J. Heart Valve Dis.* **9,** 495-501; discussion 502–3 (2000).

159. Lomholt, M., Nielsen, S. L., Hansen, S. B., Andersen, N. T. & Hasenkam, J. M. Differential tension between secondary and primary mitral chordae in an acute in-vivo porcine model. *J. Heart Valve Dis.* **11,** 337–45 (2002).
160. Gunnal, S. A., Wabale, R. N. & Farooqui, M. S. Morphological study of chordae tendinae in human cadaveric hearts. *Heart Views* **16,** 1–12 (2015).
161. Dal-Bianco, J. P. & Levine, R. A. Anatomy of the mitral valve apparatus: role of 2D and 3D echocardiography. *Cardiol. Clin.* **31,** 151–64 (2013).
162. Espino, D. M., Shepherd, D. E. T., Hukins, D. W. L. & Buchan, K. G. The role of Chordae tendineae in mitral valve competence. *J. Heart Valve Dis.* **14,** 603–9 (2005).
163. Liao, J. & Vesely, I. A structural basis for the size-related mechanical properties of mitral valve chordae tendineae. *J. Biomech.* **36,** 1125–33 (2003).
164. Pham, T. & Sun, W. Material properties of aged human mitral valve leaflets. *J. Biomed. Mater. Res. Part A* **102,** 2692–2703 (2014).
165. Casado, J. A. *et al.* Determination of the mechanical properties of normal and calcified human mitral chordae tendineae. *J. Mech. Behav. Biomed. Mater.* **13,** 1–13 (2012).
166. Gunning, G. M. & Murphy, B. P. Characterisation of the fatigue life, dynamic creep and modes of damage accumulation within mitral valve chordae tendineae. *Acta Biomater.* **24,** 193–200 (2015).
167. Kong, F. *et al.* Finite Element Analysis of Tricuspid Valve Deformation from Multi-slice Computed Tomography Images. *Ann. Biomed. Eng.* **46,** 1112–1127 (2018).
168. Bavo, A. M. *et al.* Patient-specific CFD models for intraventricular flow analysis from 3D ultrasound imaging: Comparison of three clinical cases. *J. Biomech.* **50,** 144–150 (2017).
169. Prisco, A. R. *et al.* Impact of LVAD Implantation Site on Ventricular Blood Stagnation. *ASAIO J.* **63,** 392–400 (2017).
170. Chan, B. T., Lim, E., Chee, K. H. & Abu Osman, N. A. Review on CFD simulation in heart with dilated cardiomyopathy and myocardial infarction. *Comput. Biol. Med.* **43,** 377–385 (2013).
171. Bavo, A. M. *et al.* Patient-specific CFD simulation of intraventricular haemodynamics based on 3D ultrasound imaging. *Biomed. Eng. Online* **15,** 107

(2016).

172. Liao, S. *et al.* Numerical prediction of thrombus risk in an anatomically dilated left ventricle: the effect of inflow cannula designs. *Biomed. Eng. Online* **15,** 136 (2016).

173. Liao, S., Neidlin, M., Li, Z., Simpson, B. & Gregory, S. D. Ventricular flow dynamics with varying LVAD inflow cannula lengths: In-silico evaluation in a multiscale model. *J. Biomech.* **72,** 106–115 (2018).

174. Lim, K. H., Yeo, J. H. & Duran, C. M. G. Three-dimensional asymmetrical modeling of the mitral valve: a finite element study with dynamic boundaries. *J. Heart Valve Dis.* **14,** 386–92 (2005).

175. Chandra, S., Sugeng, L. & Lang, R. M. Three-dimensional Echocardiography of the Mitral Valve Leaflet Anatomy and Repair. *Curr. Cardiovasc. Imaging Rep.* **3,** 268–275 (2010).

176. Maisano, F. *et al.* An Annular Prosthesis for the Treatment of Functional Mitral Regurgitation: Finite Element Model Analysis of a Dog Bone–Shaped Ring Prosthesis. *Ann. Thorac. Surg.* **79,** 1268–1275 (2005).

177. Witschey, W. R. T. *et al.* Three-Dimensional Ultrasound-Derived Physical Mitral Valve Modeling. *Ann. Thorac. Surg.* **98,** 691–694 (2014).

178. Rego, B. V. & Sacks, M. S. A functionally graded material model for the transmural stress distribution of the aortic valve leaflet. *J. Biomech.* **54,** 88–95 (2017).

179. Mattson, J. M., Wang, Y. & Zhang, Y. Contributions of Glycosaminoglycans to Collagen Fiber Recruitment in Constitutive Modeling of Arterial Mechanics. *J. Biomech.* (2018). doi:10.1016/j.jbiomech.2018.10.031

180. Fan, R. & Sacks, M. S. Simulation of planar soft tissues using a structural constitutive model: Finite element implementation and validation. *J. Biomech.* **47,** 2043–54 (2014).

181. Sun, W. & Sacks, M. S. Finite element implementation of a generalized Fung-elastic constitutive model for planar soft tissues. *Biomech. Model. Mechanobiol.* **4,** 190–199 (2005).

182. Weinberg, E. J. & Kaazempur-Mofrad, M. R. A large-strain finite element formulation for biological tissues with application to mitral valve leaflet tissue mechanics. *J. Biomech.* **39,** 1557–1561 (2006).

183. Otani, T. *et al.* A Computational Framework for Personalized Blood Flow Analysis in the Human Left Atrium. *Ann. Biomed. Eng.* **44,** 3284–3294 (2016).

184. Villard, P.-F., Hammer, P. E., Perrin, D. P., Del Nido, P. J. & Howe, R. D. Fast image-based mitral valve simulation from individualized geometry. *Int. J. Med. Robot.* **14,** e1880 (2018).

185. Kodama, Y. *et al.* Morphological Assessment of Single-Ventricle Atrioventricular Valve Regurgitation on Dual-Source 128-Slice Multidetector Computed Tomography and 4-Dimensional Imaging. *Circ. J.* **80,** 2555–2556 (2016).

186. *Functional Imaging and Modeling of the Heart*. **4466,** (Springer Berlin Heidelberg, 2007).

187. Chambers, J. B., Myerson, S. G., Rajani, R., Morgan-Hughes, G. J. & Dweck, M. R. Multimodality imaging in heart valve disease. *Open Hear.* **3,** e000330 (2016).

188. Amini Khoiy, K. & Amini, R. On the Biaxial Mechanical Response of Porcine Tricuspid Valve Leaflets. *J. Biomech. Eng.* **138,** 104504 (2016).

189. Spinner, E. M., Buice, D., Yap, C. H. & Yoganathan, A. P. The Effects of a Three-Dimensional, Saddle-Shaped Annulus on Anterior and Posterior Leaflet Stretch and Regurgitation of the Tricuspid Valve. *Ann. Biomed. Eng.* **40,** 996–1005 (2012).

190. Troxler, L. G., Spinner, E. M. & Yoganathan, A. P. Measurement of strut chordal forces of the tricuspid valve using miniature C ring transducers. *J. Biomech.* **45,** 1084–91 (2012).

191. Votta, E. *et al.* The Geoform disease-specific annuloplasty system: a finite element study. *Ann. Thorac. Surg.* **84,** 92–101 (2007).

192. Hahn, R. T. *et al.* Guidelines for Performing a Comprehensive Transesophageal Echocardiographic Examination: Recommendations from the American Society of Echocardiography and the Society of Cardiovascular Anesthesiologists. *J. Am. Soc. Echocardiogr.* **26,** 921–964 (2013).

193. Flores, A. S. *et al.* Echocardiographic assessment for ventricular assist device placement. *J. Thorac. Dis.* **7,** 2139–50 (2015).

194. Nguyen, V.-T. *et al.* A Patient-Specific Computational Fluid Dynamic Model for Hemodynamic Analysis of Left Ventricle Diastolic Dysfunctions. *Cardiovasc. Eng. Technol.* **6,** 412–429 (2015).

Image-based analysis of tricuspid valve biomechanics: towards a novel approach integrating *in vitro* 3D echocardiography and finite element modelling

2.1 Introduction

Tricuspid valve (TV) has recently gained attention in cardiovascular research, in particular for setting up surgical as well as interventional approaches for the treatment of its most spread pathology - the functional tricuspid regurgitation (FTR)[1,2].

Currently, the *in vivo* imaging techniques employed by clinicians to visualize the cardiac valves comprise: echocardiography, both transthoracic (TTE) and transesophageal (TEE), magnetic resonance imaging (MRI), and computed tomography (CT). Echocardiography is referred to the gold standard for diagnosis[3]. Differently from the aortic valve and from the mitral valve, the TV cannot be visualized in a single 2D echocardiographic view. Conversely, 3-dimensional echocardiography (3DE) is a reliable and feasible technique to assess TV morphology and function, with important implications on the surgical decisional planning in case of TV diseases[4]. 3DE, with its unique capability of obtaining a short-axis plane of the TV, allows for simultaneous visualization of the three leaflets moving during the cardiac cycle and their attachment in the tricuspid annulus from both the ventricular and the atrial side. Despite its confirmed clinical value, 3D echocardiographic assessment of the TV has some limitations[5]: i) no standard approach to imaging is present; ii) the transducer is so large that, in the presence of narrow intercostal spaces in TTE, the acoustic window restricts the penetration of ultrasound beams and the entire displays of structures are affected; iii) the imaging depth is not satisfactory: in some phases of cardiac cycle, some structures, as the RV and the sub-valvular apparatus, can only be partly displayed.

In the light of biomechanical and anatomical complexity of TV, it is crucial to provide an adequate, pre-clinical predictive testing platform which can effectively elucidate TV substructures and their functional interdependence. To date, mock circulation loops (MCLs) are the only available environment in which innovative devices and repair procedures can be tested, by studying the hemodynamic effects induced on the valve. However, MCLs cannot provide a pointwise description of the state of stress and deformation generated on the

leaflet tissue, which is important to evaluate potential stress- or strain-mediated remodelling and inflammation induced by the procedure.

In this context, the development of computational simulations of TV repair procedures would be useful and clinically relevant, providing quantitative information on stress and strain induced on the valve that cannot be obtained experimentally. To this aim, patient-specific finite element (FE) models could be considered the suitable tool. Nonetheless, so far, two TV FE model are available in literature: i) a CMR-based paradigmatic model[6] and ii) a patient-specific model, completely derived from CT acquisition[7]. Thus, we herein proposed a framework to obtain anatomically detailed TV FE models accounting for dynamic boundary conditions and for realistic TV tissue mechanical properties[8], starting from 3D ultrasound acquisition. To develop and test our method, we integrated FE modelling with *in vitro* experiments, so to obtain input data under repeatable conditions and to be able to compare numerical results vs. experimental evidence.

2.2 Mock Circulation Loop for the right heart

The MCL, designed at Department of Electronics, Information and Bioengineering of Politecnico di Milano[9] allows to simulate the pulmonary circulation through the set-up presented in Figure 2-1.

The system houses a swine right heart (a) and is by a positive-displacement piston pump that reciprocated fluid (saline solution at room temperature) to and from the right ventricle by a trans-septal access (b). The afterload simulator (c), representing the pulmonary impedance, is connected to the heart at the level of the pulmonary valve (PV), while the preload (d), open-to-air chamber, is connected to the atrium. The pump is specifically designed to replicate the cardiac systolic and diastolic flow waves and to reproduce different physiological and pathological conditions, by setting the angular velocity and stroke of the piston, corresponding respectively to the heart frequency and stroke volume.

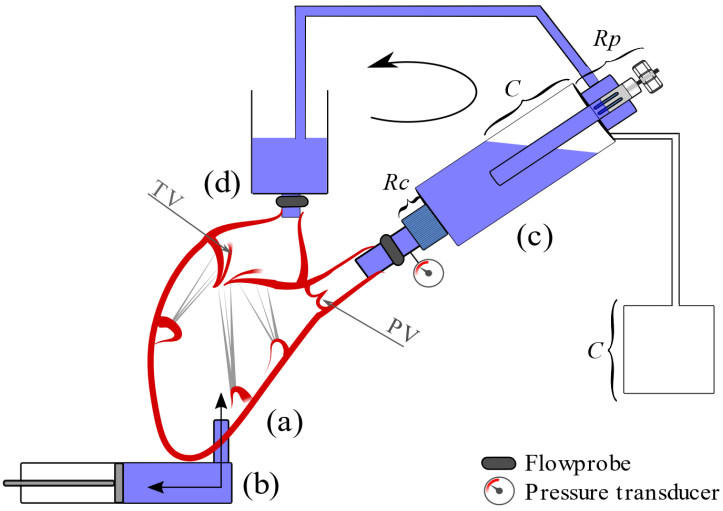

Figure 2-1 MCL scheme. a: right porcine heart, b: pumping system, c: pulmonary impedance system, d: preload. The arrow indicates direction of fluid flow. RC: Characteristic resistance, C: Compliance chamber (divided in two compartments), RP: Peripheral resistance with adjustment mechanism. PV: pulmonary valve, TV: tricuspid valve.

A key-aspect that is worth to underline is the fact that, since it is passive, the right ventricle tends to dilate under pressure once it is connected to the MCL. This dilation resulted in a displacement of the PMs anchored to the free wall and in the TV annulus enlargement in the antero-posterior direction, thus being a prefect model of FTR[9]. On this basis, in order to achieve a competent configuration of the valve a band was placed at annular level and a stitch, inserted from inter-ventricular septum to outer ventricular wall (A-SW configuration), was exploited to approximate PMs (Figure 2-2).

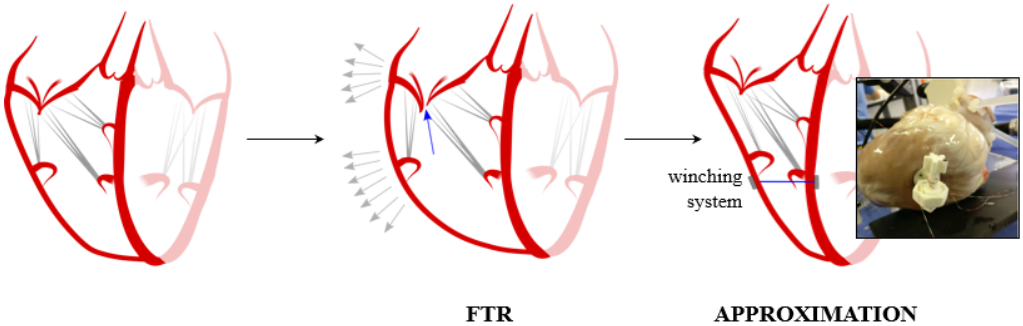

Figure 2-2 External regulation system used to adjust the tension of the stitch inserted from the septal to the ventricular wall.

The shortenings of the intraventricular portion of the stitch was accomplished up to 60% of approximation percentage and were calculated based on the initial length of the stitch in pathological conditions obtained from an echocardiographic measurement.

2.3 3D Echocardiography data

Three-dimensional echocardiography (3DE) is a widely available technique as well as cost-effective. With appropriate trade-off between spatial and temporal resolution, it enables the evaluation of the valvular dynamics throughout the whole cardiac cycle. The spatial resolution, even if inferior as compared to the one of CT scans, allows for the assessment of complex structures, resulting in high quality images. Moreover, the echocardiographic acquisitions can be performed noninvasively, with only the probe interacting with the MCL.

Data acquisitions from the MCL, both for FTR and PM approximation (PMA) configuration, were performed using real-time 3-dimensional echocardiography (RT-3DE) (iE33, Philips, shown in Figure 3.1) and a TEE probe (CX7-2t). ECG-gating on four beats was set to improve temporal resolution (30 frames/cycle), while having a spatial resolution of 0.696x0.688x0.538; the probe was positioned in contact with the epicardium, in between the afterload and preload connector allowing for an atrial view of the valve.

2.4 Image Processing

Each volumetric dataset was initially navigated using the open-source software platform 3D Slicer[10]: the long-axis two-chamber planes were manually identified, and these planes were used to identify the true long axis passing through the centre of the TV. Custom software developed in MATLAB® (The Mathworks, Inc., Natick, MA, US) was used for the analysis of the morphology of the TV[11].

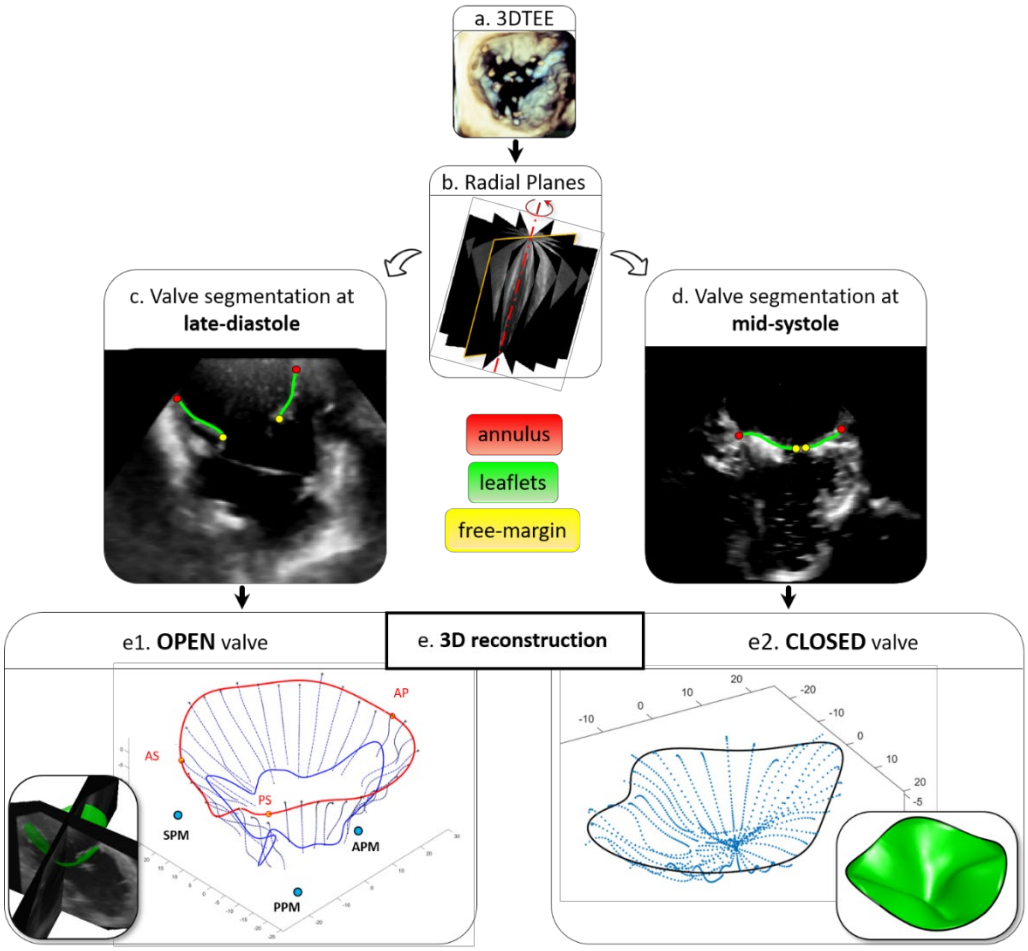

Figure 2-3 Workflow of the 3D TV geometry reconstruction.

In specific, 18 planes evenly rotated around the TV axis were automatically defined by interpolating the volumetric data (Figure 2-3 b). In-plane resolution was set isotropic and equal to the minimum spatial resolution of the original volumetric data.

At the frame corresponding to late-diastole (LD), the open valve configuration was obtained starting from FTR data acquisition only (Figure 2-3 e1). In each analysed plane two annular points were manually identified, and leaflets were manually traced (Figure 2-3 c). In details, on each image plane, manually traced leaflet points were interpolated by a 2D cubic spline, which was resampled at 64 uniformly distributed points. Through principal component analysis of the Cartesian coordinates of the annular points, their best-fit plane was identified, and coordinates were recomputed into a reference frame centred in the centre of the annulus and having the z-axis orthogonal to the best-fit plane. The resulting

3D point-cloud (36x64) representing the valve was oversampled ad interpolated, level by level, through cubic-splines. Sampled points were connected, to preliminarily discretize leaflets surfaces, into a mapped mesh of 3-node triangular element.

To note, annulus was even traced up to mid-systole, obtaining its displacement field to be included in the systolic closure FE simulation.

Commissures positioning: manual detection was performed on the TV short-axis plane in 3D Slicer (Figure 2-4-a). The RAS (intrinsic right-hand coordinate system in 3D Slicer) coordinates were exported and processed in MATLAB®: applying a roto-translation, the points were placed with respect to the origin previously defined, and their angular position detected on the annular profile (Figure 2-4-b).

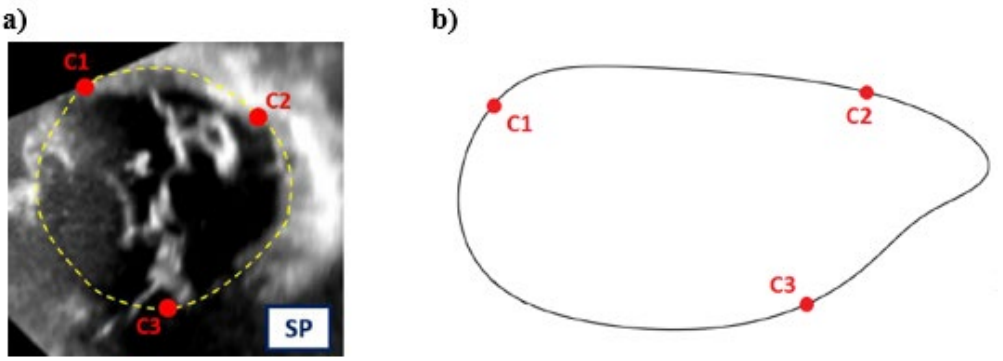

Figure 2-4 a) Segmentation of the three commissures on TV short-axis plane. SP: systolic peak; b) Positioning of the three commissures on the TV annulus.

Commissures identification: to this aim, an external anatomical landmark was selected, possibly choosing either the pump connector or the stitch. The former resembled the septum and the position of the commissure with respect to it is known[12]; for the latter, knowing a priori its positioning, it was possible to know which PMs it is connected with and, thus, the corresponding commissures on the annular plane (Figure 2-5).

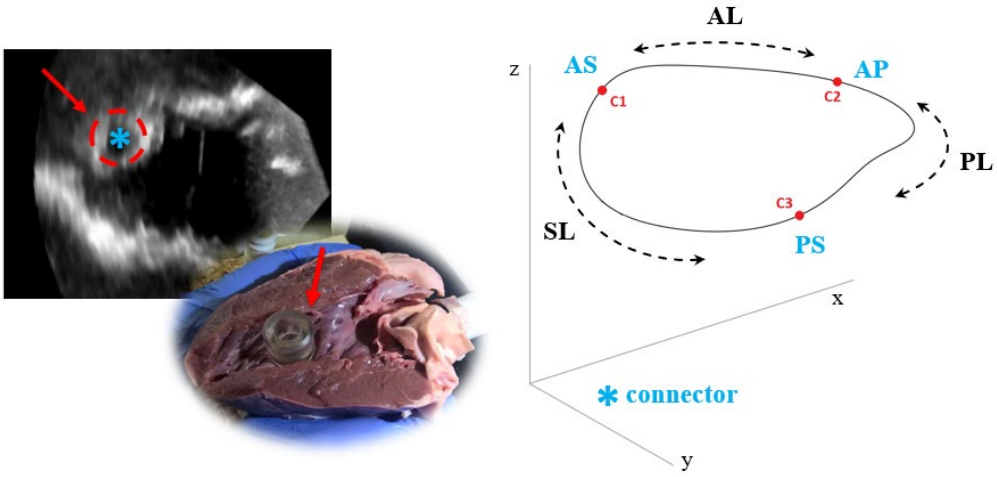

Figure 2-5 Tracing of the refence connector point on the image (left) and its co-registration with the annular profile (right) to identify the commissures (AS: antero-septal, AP: antero-posterior, PS: postero-septal) and, thus, the leaflets (AL: anterior leaflet, PL: posterior leaflet, SL: septal leaflet).

Sub-valvular apparatus: with the same rationale, PMs were traced and identified by navigating the ultrasound images in 3D Slicer. To note, PMs were simply detected at the end-diastole frame, since it is barely possible tracking them along the cardiac cycle. Chordae tendineae were modelled following the anatomical classification. Their branched structure and the insertion sites on the leaflets were defined according to *ex vivo* findings provided by Stevanella et al.[6] and to anatomical description reported by Silver and colleagues[13].

At the frame corresponding to mid-systole (MS), aiming to a comprehensive morphological assessment, the TV closed configuration was segmented, both from FTR and PMA configurations (Figure 2-3 d). TV 3D reconstruction was achieved following almost the same aforementioned steps, apart from the final one, where the 3D leaflets' point-cloud was fitted through a Loess function[14] to yield the continuous 3D valve surface (Figure 2-3 e2). Moreover, PMs-chordae apparatus was not included.

2.5 Morphological evaluation

Experimental measurements were performed on the five tested hearts to quantitatively describe the morphological features of the tricuspid valve. The valves were excised and cut-open by cutting at the postero-septal commissure and the following quantities were estimated: i) annular perimeter, ii) leaflet length (from one commissure to the consecutive one, along the annular profile), iii) leaflet height (measured from the annulus to the free margin at the midpoint of each leaflet) and iv) commissure height (measured from the annulus to the free margin at the commissural position). For the sake of comparison and in order to evaluate the reconstruction algorithm, these data were compared with the analytical ones resulting from the imaging data processing concerning the LD frame (Figure 2-6). In addition, through the semi-automatic tool, 3D and 2D area were also evaluated, even tracking annular geometrical changes over the considered frames.

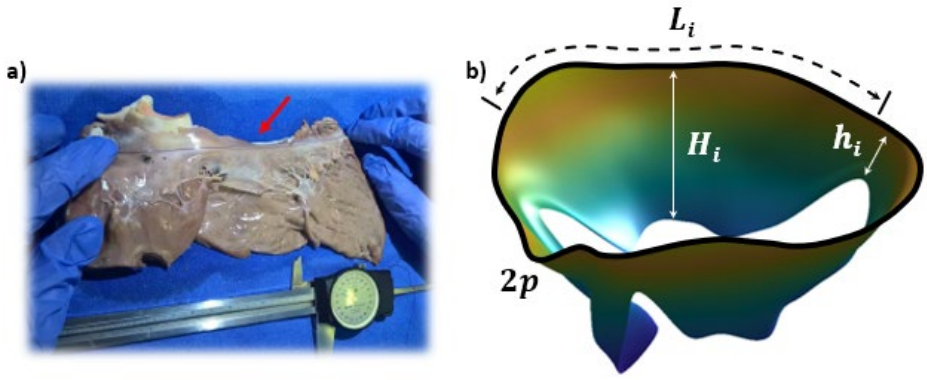

Figure 2-6 a) Experimental measure of the annulus perimeter, evaluated through a thread and a vernier calliper; b) Analytical variables: H_i (leaflet height), L_i (leaflet extent, as a fraction of the annular perimeter), h_i (commissure height), $2p$ (perimeter).

Subsequently, as a proof of winching system functioning, the following morphological parameters, graphically depicted in Figure 2-7, were measured at MS:

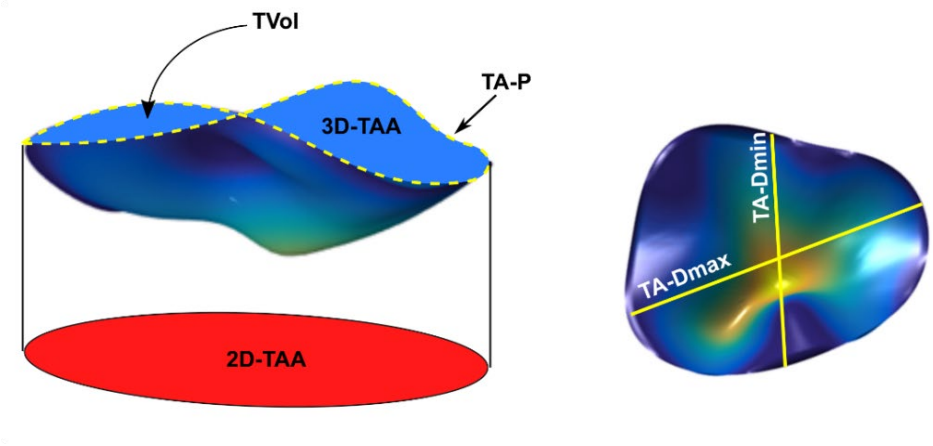

Figure 2-7 Measurements of tricuspid valve morphology based on 3D reconstructions of echocardiographic volumetric data.

- Tenting Volume (TVol), in mL, the space enclosed between TV leaflets surface and 3D tricuspid annulus (TA) plane,
- TA 3D area (3D-TAA), in cm^2, area enclosed within 3D annular profile,
- TA 2D area (2D-TAA), in cm^2, portion of area delimited by projection of the 3D annular profile,
- TA 3D perimeter (TA-P), in cm, obtained from 3D annular profile,
- TA maximal diameter (TA-Dmax), in cm, as the longest chord connecting two annular points crossing through the centre of the TA,
- TA minimal diameter (TA-Dmin), in cm, as the shortest chord connecting two annular points crossing through the centre of the TA.

These morphological variables were computed at 30% and 60% level of PMs approximation in A-SW direction, respectively.

2.6 Finite Element (FE) modelling

Starting from the 3D TV reconstruction at LD, the implementation of the corresponding FE model was achieved by complementing the geometry with the physical properties and the appropriate boundary and loading conditions.

Leaflets' surface was remeshed in 3D solid elements (i.e. 1-layer eight-node hexahedral C3D8R elements), with a uniform thickness equal to 0.623 mm,

obtained as average among the experimental measurements performed on the samples, and an in-plane characteristic dimension equal to 1 mm. The chordae were discretized into *truss* (T3D2) elements to make their resistance to axial compressive loads negligible. Since a branched chordal paradigm was adopted by our previous work[6], the cross-section of the main branches starting from PMs tips, set equal to 1 mm^2 [15], was progressively divided by the number of sub-branches arising at each branching point.

2.6.1 Mechanical properties

The mechanical behaviour of leaflets and chordae tendineae was assumes hyperelastic and described through large deformation theory. The density of all biological tissue included in the model was set equal to 1.1 g/cm^3 [16–18].

Valve leaflets

The mechanical properties of TV leaflets were described through the model proposed by Holzapfel et al.[19,20], with the following invariant-based strain energy function φ (1):

$$\varphi = C_{10}(I_1 - 3) + \frac{k_1}{2k_2}\sum_{\alpha=1}^{N}\left\{exp\left[k_2\left(k(I_1 - 3) + (1 - 3k)\left(I_{4,\alpha} - 1\right)\right)^2\right] - 1\right\} \quad (1)$$

where $I_1 = trace(\boldsymbol{C})$, $I_4 = a_0 \cdot \boldsymbol{C} \cdot {a_0}^{20}$ are respectively the first and fourth invariants of the Cauchy-Green strain tensor $\boldsymbol{C}$ and N is the number of fibres families, assumed circumferentially oriented. C_{10}, k_1, k_2, k, constitutive parameters of the model, were identified by fitting the equi-biaxial tensile tests data acquired by Amini et al.[8] on porcine TV samples. Heterogeneous and leaflet-specific mechanical properties were considered.

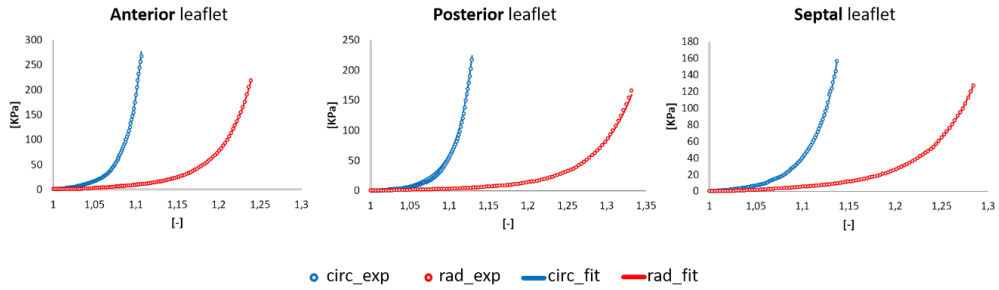

Figure 2-8 Fitting of the experimental data from equi-biaxial test [Amini 2018] (dot) with Holzapfel strain energy function (line). Stress are expressed as Cauchy Stress [**σ**], with respect to the stretch ratio [**λ**]; *circ* and *rad* depict the circumferential and radial direction, respectively.

Table 1 Values of the identified constitutive parameters, detailed for each TV leaflet.

	C_{10} [MPa]	k_1 [MPa]	k_2	k
Anterior	2.91E-03	828.60E-03	119.25	3.08E-01
Posterior	1.0E-08	282.93E-03	45.25	2.93E-01
Septal	1.86E-03	379.52E-03	49.20	3.08E-01

Chordae tendineae

The mechanical response of chordae tendineae was assumed non-linear isotropic and was modelled through a second order polynomial function, fitting the only available data in literature obtained by Lim[15]. A lower state of stress was considered for the basal chordae, keeping the same deformation, based on the results for the mitral valve obtained by Jimenez et al.[21].

2.6.2 Loading and boundary conditions

CML-derived transvalvular pressure curve (Figure 2-9 a) and image-based annular kinematic (Figure 2-9 b) were imposed as loading and motion boundary conditions to simulate the systolic closure (from LD to MS). PMs displacement along the traced frames was neglected, since the images spatial resolution was not enough to detect them during time.

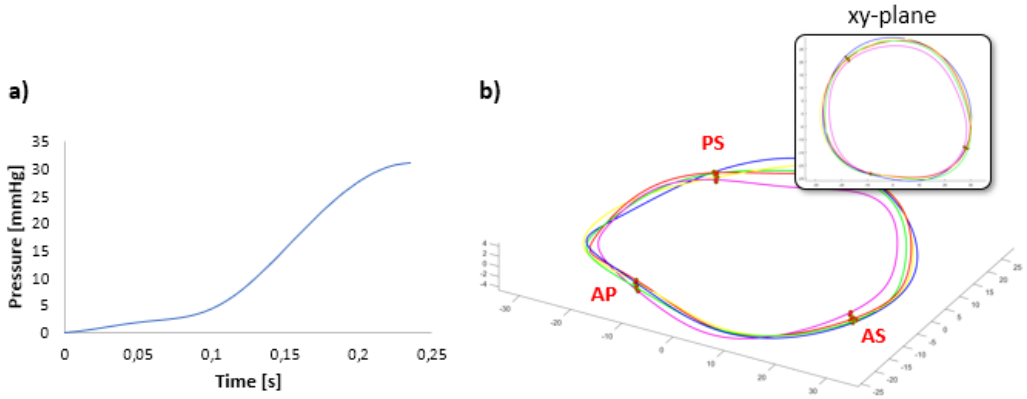

Figure 2-9 Experimental transvalvular pressure curve (a) and image-derived annular displacement (b) from LD to MS.

2.6.3 Simulation settings

All the simulations were run in ABAQUS/Explicit 6.10-1 (Simulia, Providence, Rhode Island, USA). Leaflets coaptation was modelled using a general contact algorithm with scale penalty formulation, already included in software library: the friction coefficient between the interacting surfaces was assumed equal to 0.05[6].

However, two different simulation settings were implemented:

1) FTR model: TV systolic closure was simulated in a single step, along a time period equal to 0.235 s;
2) PMA model: always starting from FTR model geometry, a double-step simulation was implemented by preceding the TV closure step with the simulation of the 60% PMs approximation (step time = 0.5 s). The winching system effect was replicated exploiting axial *connector* element[22] connecting anterior (APM) and septal (SPM) papillary muscles. Also, annulus displacement was herein neglected as to simulate the effect of the annular band used in the benchmark tests.

It is noteworthy that the herein FE analysis was accomplished only on two TV samples (referred to as TV01 and TV02), thus the results that will be presented concerning the FE models have to be considered at least preliminary, actually aiming to a first comparison between pre- vs. post-treatment models.

2.7 Results

2.7.1 3D echo-based vs. experimental measurements – LD frame

All the measurements performed on the five excised tricuspid valve samples were compared with the 3DE-based variables, deriving from the geometrical reconstruction procedure explained in section 2.4, at LD frame.

Table 2 Comparison between direct (experimental) and 3D echo-based (3DE) measurements accomplished on TV excised samples and their corresponding 3D reconstruction, respectively. *2p*, annular perimeter; L_i, leaflet extension in terms of annular perimeter fraction; H_i, leaflet height from annulus to free-margin; h_i, leaflet height in the commissural zones.

	3DE	**Experimental**
$\boldsymbol{2p}$	149 ± 8.1	151 ± 10.1
$\boldsymbol{L_{ant}}$	52.3 ± 1.5	58 ± 6.2
$\boldsymbol{L_{post}}$	49.7 ± 1.7	47 ± 5.4
$\boldsymbol{L_{sept}}$	41.5 ± 6.4	46 ± 7.2
$\boldsymbol{H_{ant}}$	31.7 ± 2.1	23 ± 5.7
$\boldsymbol{H_{post}}$	30.6 ± 5.5	25 ± 4.3
$\boldsymbol{H_{sept}}$	23.3 ± 5.1	18 ± 8.4
$\boldsymbol{h_{ant}}$	9.2 ± 1.5	5 ± 0.7
$\boldsymbol{h_{post}}$	10.7 ± 2.4	4 ± 1.2
$\boldsymbol{h_{sept}}$	7.3 ± 0.6	4 ± 0.9

From the Table 2, it is worth to note that high consistency between experimental and image-based measurements was found, the latter being not notably affected by the approximations introduced within the TV reconstruction algorithm. In details, this is for sure valid concerning annular perimeter and leaflets' lengths, which differ 1.4% and 8.3% in average, respectively, with respect to experimental ground-truth data. Differently, the leaflets' and the commissures' heights exceed the corresponding value directly extracted from the samples, with the latter showing the largest differences. Such an overestimation is probably due to the following reasons: i) the free-margin of the leaflets were not as clearly

detectable as the annulus in the images, therefore resulting measurements were strongly affected by the manual tracing procedure; ii) the volumetric datum was sampled in 18 evenly spaced radial planes, hence the actual position of the commissures could be in between two consecutive image planes. For sure, we can assess that the aforementioned overestimation was not owing to the point cloud reconstruction, since it was accomplished by means of interpolating splines.

The interobserver variability of the manual tracing procedure was evaluated through the Bland-Altman plot. Consistently with what has been already said, the plot showed a comparable inter-observer level of agreement for the manual tracings of the annulus (Figure 2-10 a) and the leaflets (Figure 2-10 c). A higher variability emerged for the tracing of the TV free-edge (Figure 2-10 b), with median difference of 2.06 mm and 90% limit of agreement range of 5.55 mm.

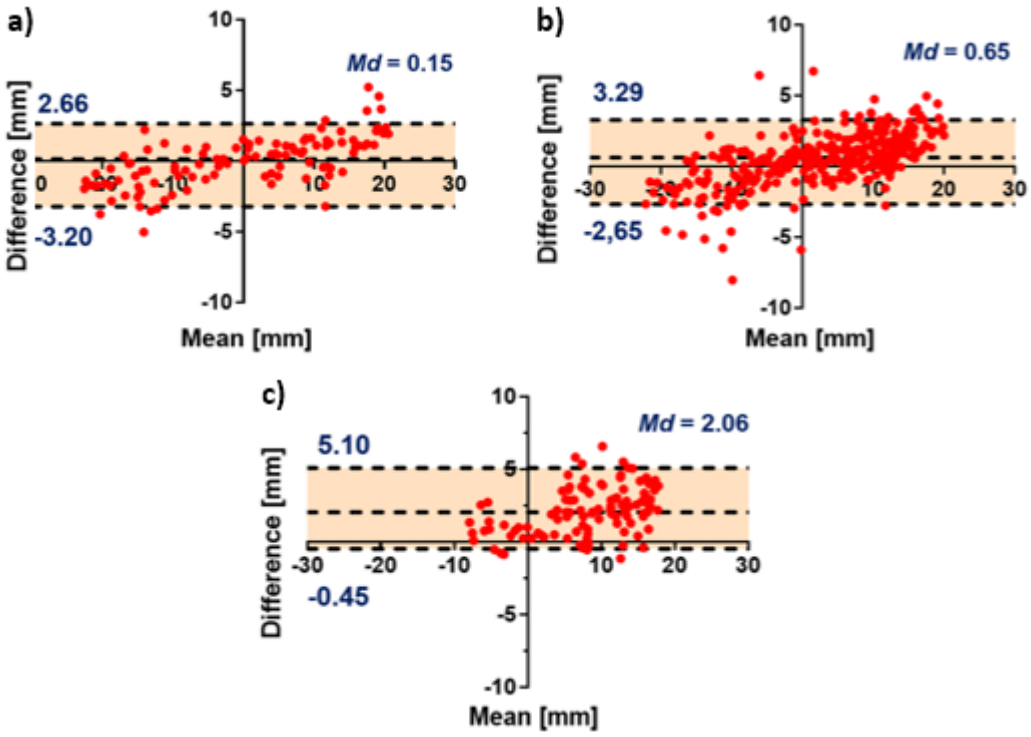

Figure 2-10 Bland-Altman plots comparing the results of manual tracings of TV annulus (a), free-margin (b) and leaflets (c) obtained by two independent observers. Horizontal dotted lines indicate the limits of agreement; Md = median, is reported as measure of bias.

Furthermore, moving from a sheer analysis on static measurements related to LD reconstruction, for the FTR models of the two simulated valves, a quantification of their annular dynamics was even performed. The computed variables, such as perimeter, 2D and 3D area and principal diameters of TV annulus, show almost the same pattern for both the valves, leading to a paradoxical enlargement in the annulus dimensions from late-diastole towards the systolic peak (Figure 2-11). However, this is consistent with the benchmark working condition: since the *in vivo* muscle contraction is lacking, the employed pumping system induces paradoxical motion of the ventricle.

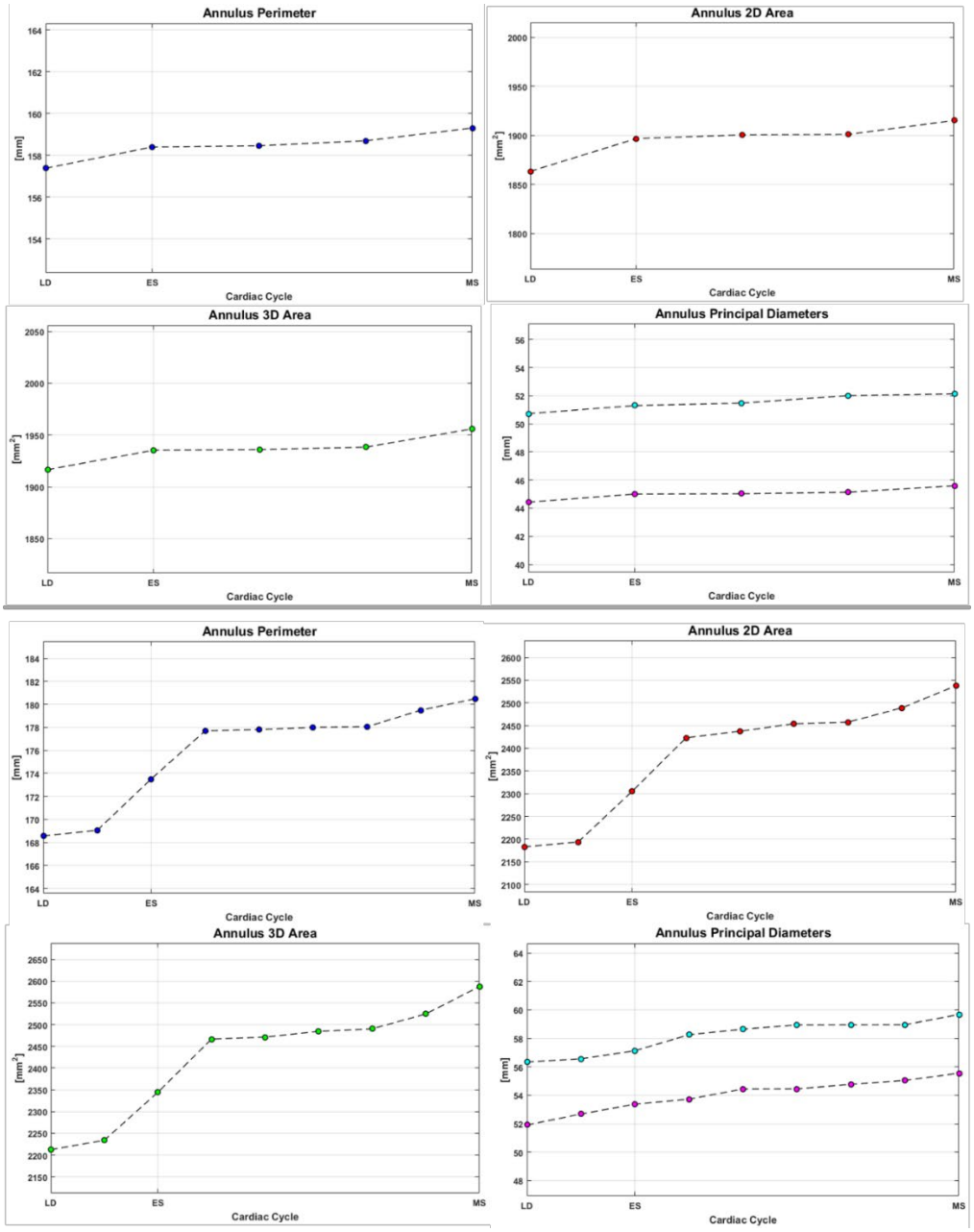

Figure 2-11 Dynamics of the TV annulus morphological features along the traced frames (from LD to MS), reported for both TV01 (top) and TV02 (bottom). LD, late diastole; ES, early systole; MS, mid systole. All the graphs are automatically extracted as result from the developed reconstruction tool.

2.7.2 Morphological assessment of PMs approximation – MS frame

Treatment of FTR with PM approximation (PMA) technique in an ex-vivo beating heart model demonstrated significant reduction of TV regurgitation and reconfigured TV apparatus morphology including reduction of TV leaflets tethering and TA size.

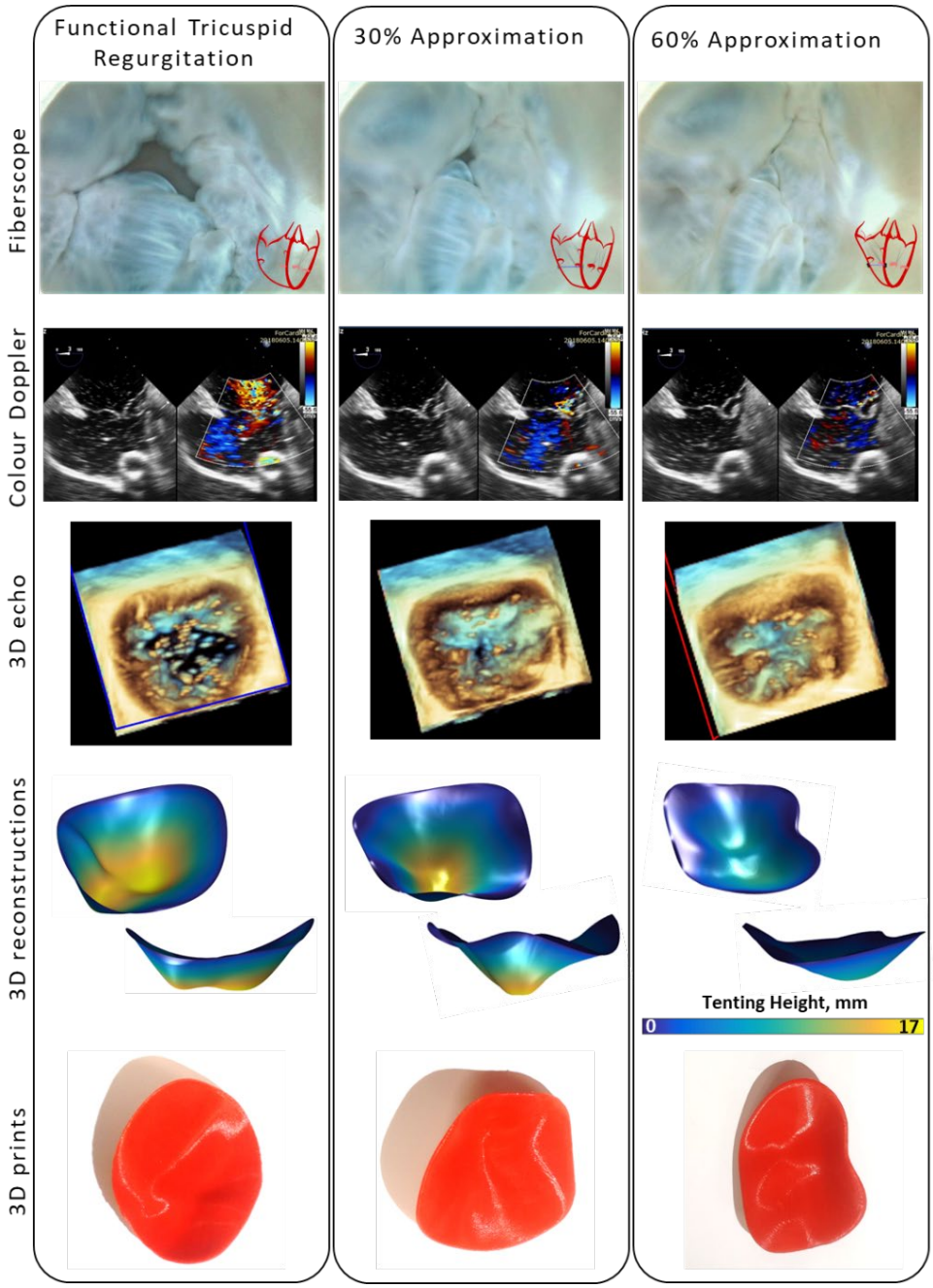

Figure 2-12 Representative TV views from fiberscope (surgeon-like view), Colour Doppler, 3D echocardiography, 3D computational reconstructions and 3D prints at FTR, 30% PMA and 60% PMA, respectively.

Figure 2-12 shows TV in mid-systole at pathological and post-treatment conditions in surgeon-like view from the fiberscope, Colour Doppler images, 3D echocardiography, computational reconstructions and 3D printed models.

Table 3 displays summary of the 3D reconstruction-derived echocardiographic parameters at pathological conditions and at post-treatment at A-SW direction and at two levels of approximation (30%, 60%).

Table 3 Overall echocardiographic assessment of papillary muscle approximation (PMA) treatment performed in A-SW direction after 30% and 60% of approximation. Data presented as mean ± standard deviation (p-value vs. FTR conditions). p-value columns correspond to comparison between 30% and 60% of approximation. NS=not significant according to ANOVA for repeated measures.

Parameter	**FTR**	**A-SW**		
		30%	60%	p-value
TVol [mL]	10.6±3.1	6.8±2.7 (p=0.003)	5.9±2.2 (p=0.002)	NS
3D-TAA [cm^2]	21.3±2.7	18.9±2.3 (p<0.001)	18.0±2.0 (p<0.001)	0.3
2D-TAA [cm^2]	20.2±2.8	17.6±2.4 (p=0.003)	16.7±1.9 (p=0.001)	0.4
TA-P [cm]	16.1±1.1	15.8±1.0 (p=0.001)	15.4±0.9 (p<0.001)	0.03
TA-Dmax [cm]	5.5±0.4	5.3±0.5 (p=0.07)	5.1±.0.4 (p=0.006)	NS
TA-Dmin [cm]	4.6±0.4	4.1±0.4 (p=0.04)	4.0±0.4 (p=0.02)	NS

The treatment induced significant changes to TV apparatus morphology. The major observed changes in respect to FTR conditions were related to leaflets tenting as evidenced by reduction of TVol by 44% on average following the 60% PMA in A-SW (p=0.002) directions, respectively (Figure 2-13 a). We also observed changes of the TA dimensions following the treatment evidenced by significant decrease of 3D-TAA (Figure 2-13 b), 2D-TAA (Figure 2-13 c) and TA-P in both levels of approximation (p<0.05). Increase of the approximation level reduced the average value of 3D-TAA, 2D-TAA and TA-P in A-SW (without statistical significance) direction. Following the systematic changes of

in TA area and perimeter in post-treatment, TA-Dmax and TA-Dmin reduced significantly after 60% of approximation in A-SW direction.

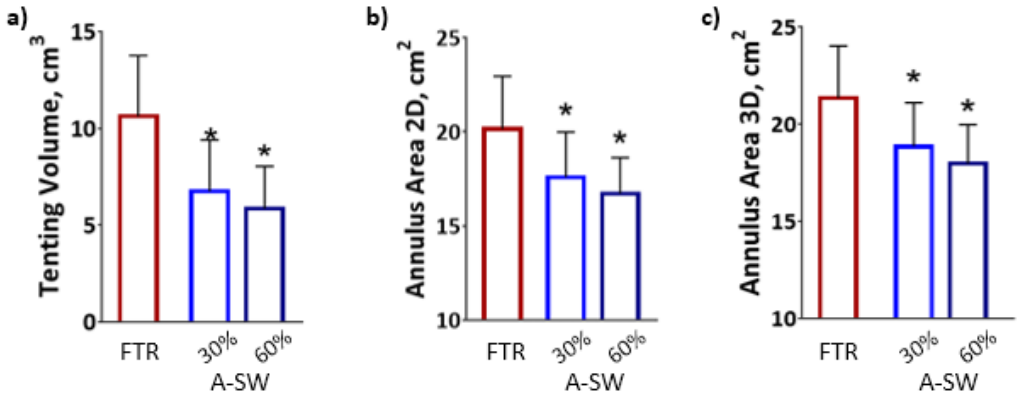

Figure 2-13 Echocardiographic assessment functional tricuspid regurgitation (FTR) treatment with papillary muscle approximation (PMA) technique after different approximation levels: Tenting volume (a), 2D annulus area (b) and 3D annulus area (c).

Figure 2-14 presents exemplary 3D reconstructions of the valve samples in the PMA treatment direction and provides qualitative insights. It was noted that the direction of the approximation influenced local changes in valve tenting, pinpointed with grey arrows, and induced characteristic indentation of the annulus profile above the septal leaflet (green arrows).

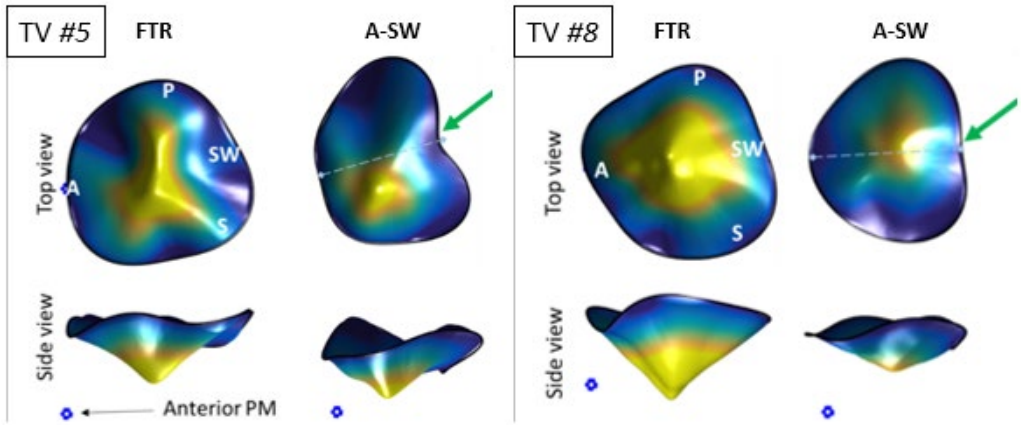

Figure 2-14 Exemplary 3D reconstructions of tricuspid valve following PMA treatment in A-SW direction at 60% of approximation for sample #5 and #8. The valve reconstructions are presented from the top (surgeon like view) and from the side view. Tenting height is color-coded. Blue dot indicates the position of anterior papillary muscle head. Grey dashed arrows indicate local changes in valve tenting related to the direction of the approximation. Green arrows indicate the indentation of tricuspid annulus following A-SW approximation.

2.7.3 Simulation of TV systolic closure

Additionally, morphological features and alterations following such valvular treatments were complemented by the mechanical stress distribution evaluation through structural finite element (FE) analyses, both pre- and post-treatment.

2.7.3.1 Biomechanical analysis: morphology

Figure 2-15 depicts the profile of leaflet midline at the systolic peak (MS) for both the FTR and PMA models of the two simulated valves.

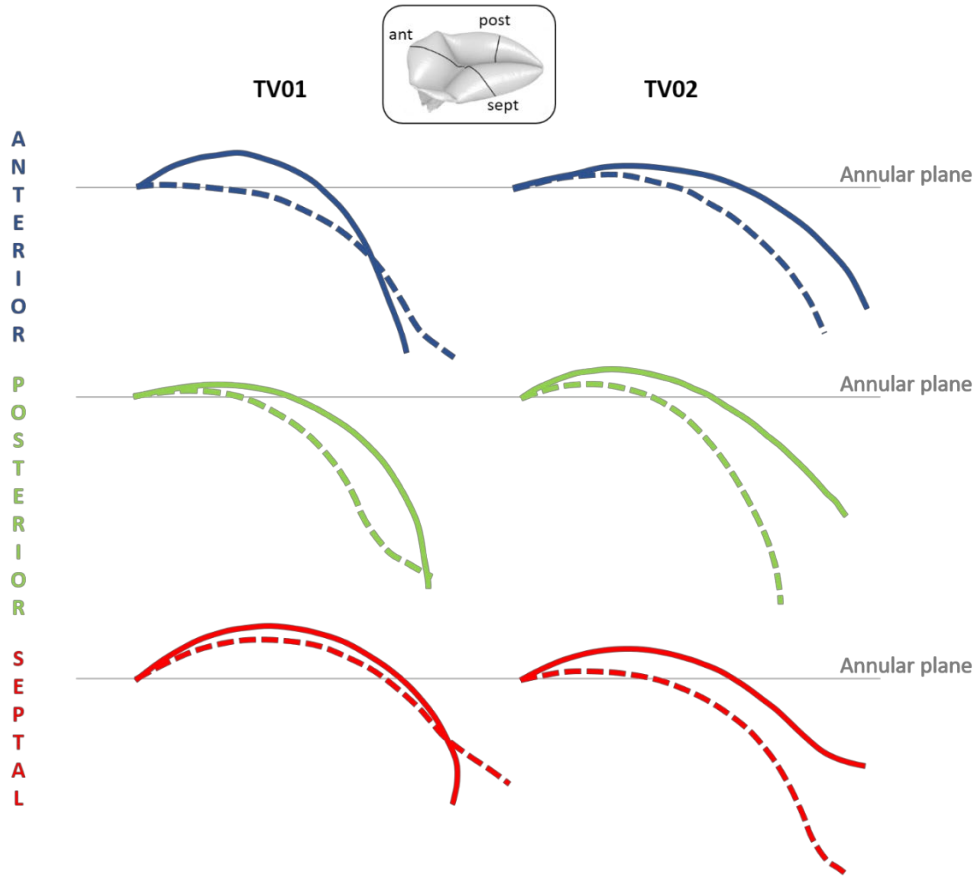

Figure 2-15 Leaflets midline profiles at MS, indicated as a solid line for PMA model and as a dashed line for FTR model, respectively. Box on top: sketch depicting reference midline section.

Bulging towards the right atrium, i.e. the maximum apical displacement above the annular plane, was always higher for PMA scenario with respect to FTR one, being the difference equal to +1.5 mm, +0.67 mm and +1.1 mm for the anterior, posterior and septal leaflet, respectively, if the average is accomplished for the same leaflet between the two models (TV01 and TV02). In particular, we will

name FTR01 and FTR02 the functional regurgitation models, and PMA01 and PMA02 the corresponding PMA models.

Bulging phenomenon appeared to be slightly lower if compared with the results reported from Stevanella and colleagues[6], reasonably assessing that this discrepancy relies on the main difference in the numerical strategy, having the model proposed by Stevanella a 2D topological mesh which is intrinsically more prone to bend. Furthermore, comparing FTR and PMA configurations within the same model, it is generally valid that the former tended to be mostly aligned to the horizontal nearby the annuls insertion and farther from the annular plane, probably owing to a tethering effect exerted by the chordae on the leaflets. Indeed, lack of muscle contraction and the paradoxical movement of the ventricle might result in a PMs dislocation, thus not allowing the valve to properly coapt. As a matter of fact, for both the FTR models, regurgitant area at systolic peak was computed as the percentage ratio between the area encompassed by the free margin profile and the orifice area, i.e. annular area (Figure 2-16).

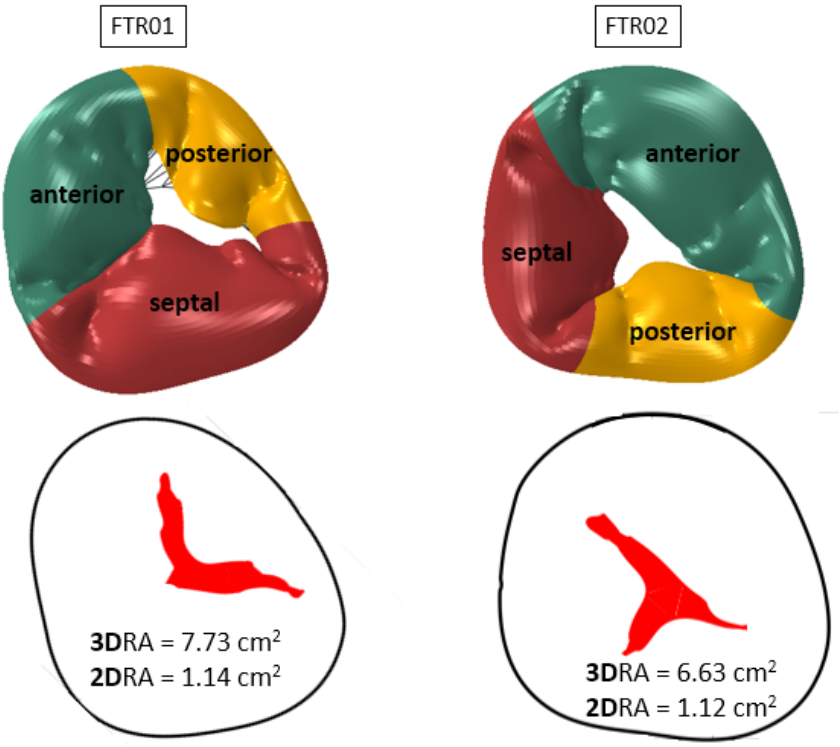

Figure 2-16 Mid systole configuration of the two simulates valves showing, on top, anterior (green), posterior (yellow) and septal (red) leaflets. In the bottom: silhouettes of 2D projected free margin area on annulus surface.

In particular, 3D regurgitation area (3DRA) was defined considering the 3D cartesian coordinates of free-margin point cloud, while 2D regurgitation area (2DRA) as the region silhouetted by 2D projection of TV free margin on annular 2D plane.

Differently, for the corresponding "treated" model (PMA), a complete leaflets coaptation was achieved, thus being able to evaluate systolic configuration in terms of coaptation area as well as valve kinematics.
Concerning the former, in Figure 2-17 the coaptation area for each leaflet is reported as a percentage of the entire leaflet's surface: it is possible to identify a decreasing trend from model PMA01 to model PMA02, but variations are small.

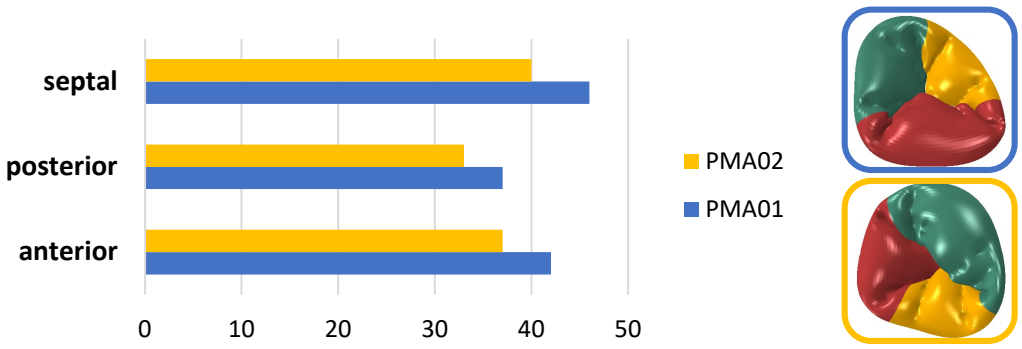

Figure 2-17 Fractional coaptation area (%) for each leaflet (namely anterior, posterior, septal) in the three models. Square boxes on the right: mid systole valve configuration after PMA simulation.

Secondly, valve kinematics was assessed by means of closing time computation, i.e. the time towards the systolic closure when the first contact between leaflets surfaces happens. Complete valve closure took about 153 ms and 167 ms for PMA01 and PMA02 model, respectively. Values were found far from what has been reported in literature[6,23], being almost double probably due to the fact that in our study model discretization was carried out by means of 3D solid elements, which intrinsically exhibit higher inertial behaviour. However, in both the simulated valves full coaptation occurred for a pressure drop equal to about 15 mmHg, three times less than in the model proposed by Kunzelman[23] but anyway

coherent since the latter reproduces a mitral valve model, whose thickness is about three times with respect to TV, thus resulting in a different bending stiffness.

2.7.3.2 Biomechanical analysis: stress and strain

Leaflet stresses and strains were assessed, for each leaflet, averaging values extracted from the integration points of a 15x15 elements patch.

The maximum principal stress (S_{max}) field is reported in Figure 2-18 for both the investigated TV model (column), in both the simulated configurations (rows). From a qualitative standpoint, stress distribution on the leaflets at the systolic peak (t = 0.235 s) exhibited almost the same behaviour. At first glance, the patterns seemed very similar. As expected, large tensile stresses were located in the belly region and to a lesser extent near the annular tract, here also depending on the extension of the leaflet surface, whilst values tend to be nearly null moving from the midline to the commissures.

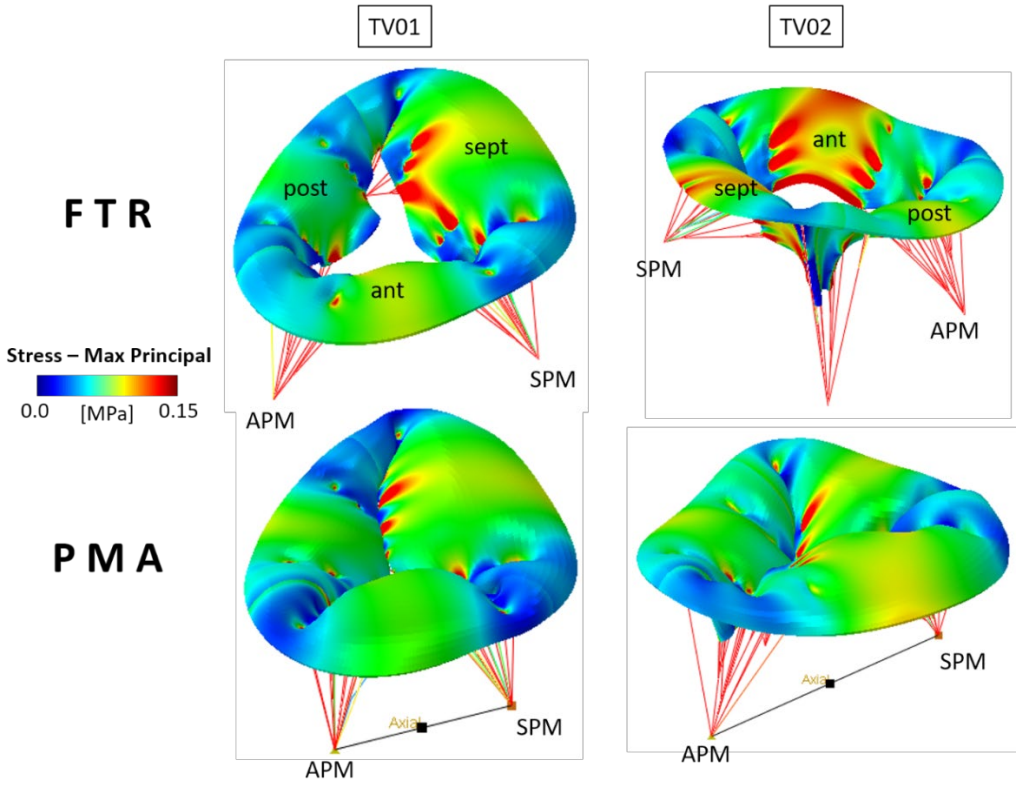

Figure 2-18 Maximum principal stress (S_{max}) patterns on tricuspid leaflets, at mid systole. Results are depicted for both the model TV01 and TV02, each one in both the FTR and PMA configuration; ant, anterior; post, posterior; sept, septal.

Nonetheless, going deeper towards a comparative analysis, a common decreasing trend was pinpointed as a direct consequence as soon as PMA is performed. As clearly visible for TV02 anterior leaflet, colour map of the FTR models (1st row of the figure) showed greater regions with high stresses, probably owing to the non-complete coaption of the leaflet as well as the tethering effect of the chordae on the valve (peak values range: 0.2 – 0.4 MPa).

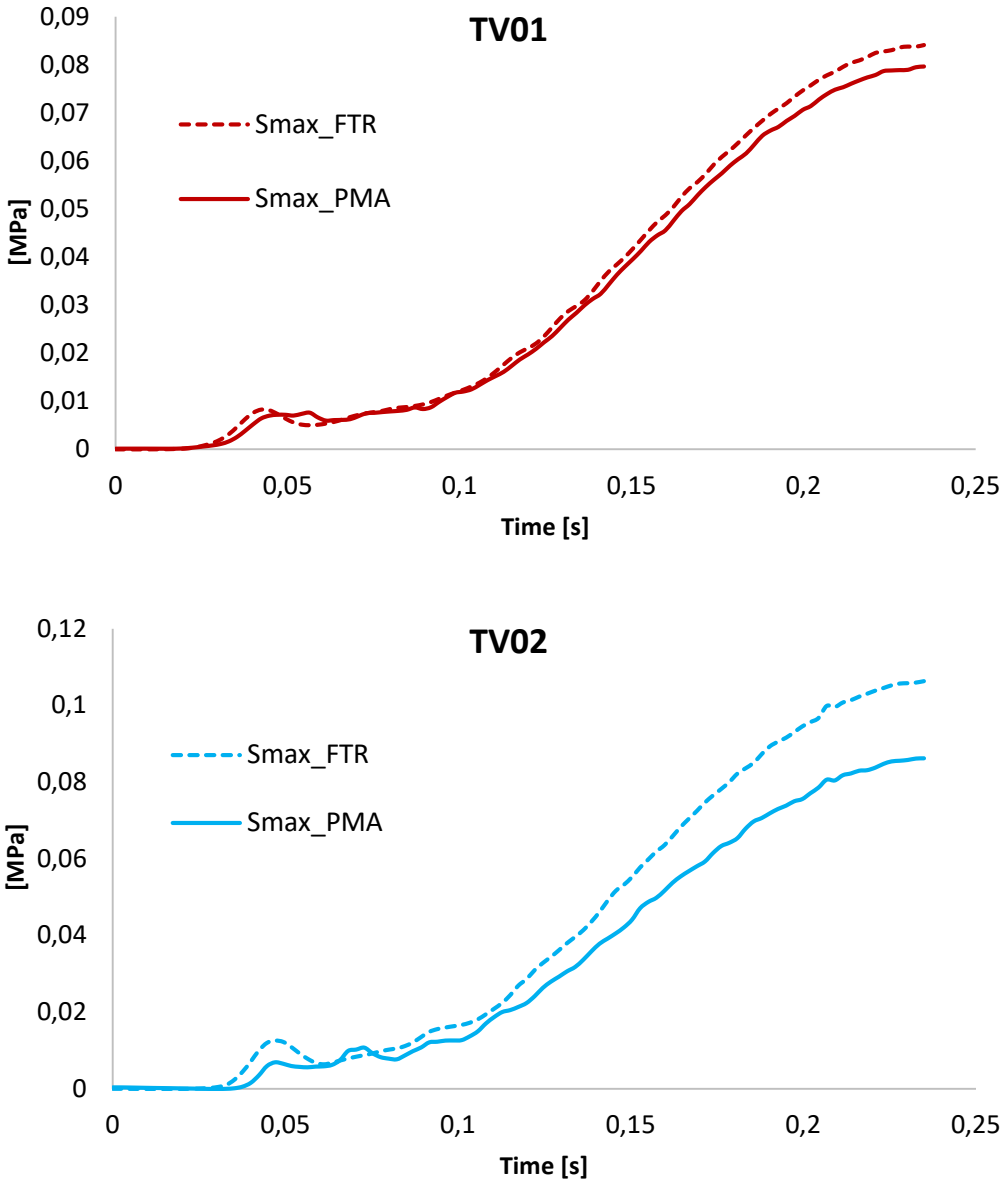

Figure 2-19 Time course of the maximum principal stress (S_{max}), reported for each model averaged on the three leaflets. FTR indicates the non-competent valve models, PMA indicates the competent valve models following PMs approximation.

This is also confirmed by analysing the S_{max} time course over the entire systolic phase (Figure 2-19): indeed, peak values at MS, namely 0.094 MPa and 0.107 MPa for FTR01 and FTR02, were found to be around 19% and 24% higher with respect to the corresponding PMA models. Here, at mid systole, values range of 0.078-0.096 MPa, 0.072-0.075 MPa, 0.088-0.090 MPa were extracted for

anterior, posterior and septal leaflets, respectively, even evincing a good agreement with results provided by other similar studies in literature[6,7].

Nominal strain time courses were assessed as their maximum values distribution but even both in circumferential and longitudinal (or radial) directions, i.e. respectively parallel and perpendicularly to the annulus.

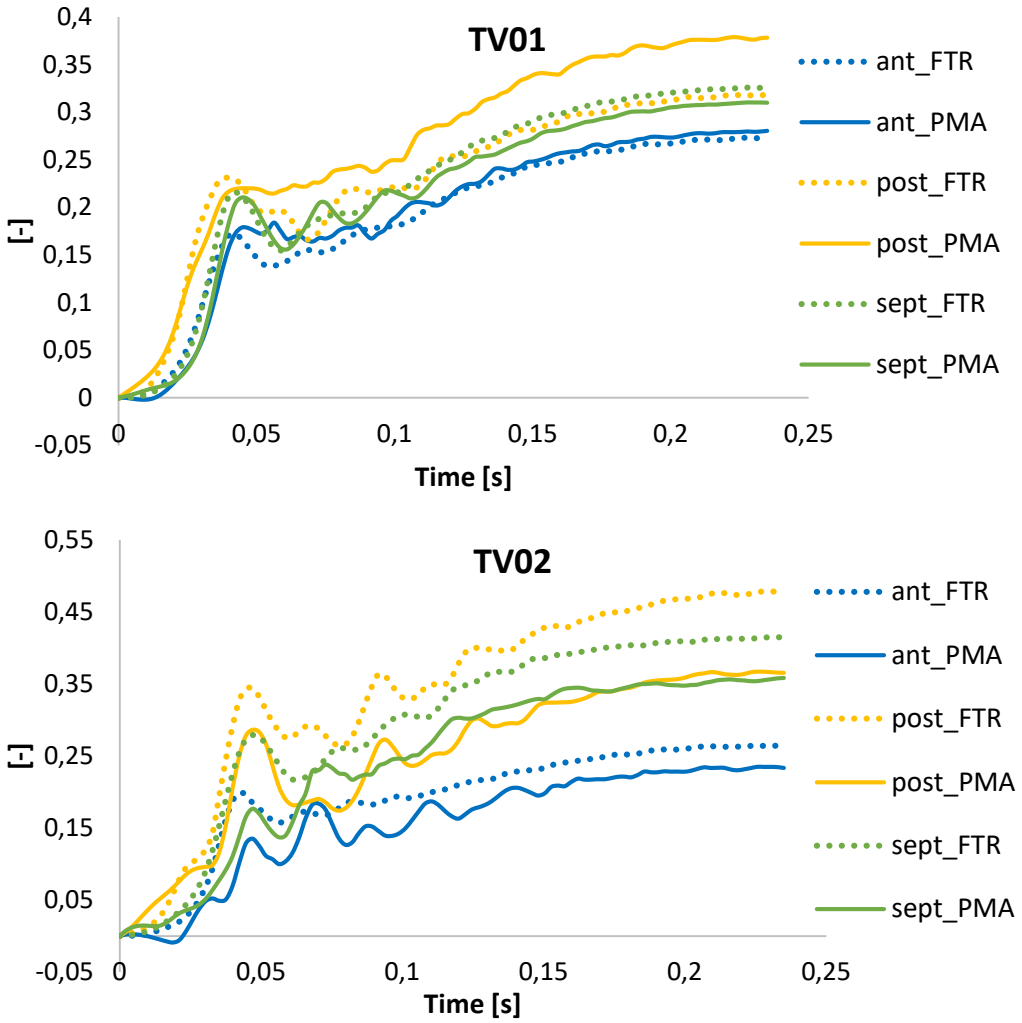

Figure 2-20 Time course of maximum nominal strain (NE_{max}), separately reported for each leaflet of each simulated model (FTR01, FTR02, PMA01, PMA02). FTR, dashed lines; PMA, solid lines.

Concerning the former, within the same model (TV01 or TV02), results herein reported separately for each leaflet (Figure 2-20), confirmed what has been previously asserted describing the stress distribution, with an overall decreasing passing from FTR to corresponding PMA model. Th e only exception was found

for posterior leaflet in the first model, being the strain about 5% higher in the competent valve model.

As a proof of concept, this latter finding was proved exploring the strain pattern in circumferential and radial directions. As expected, at MS, the former showed an overall compressive state, mostly nearby the commissural regions, coherently with stress distribution. In detail, circumferential tensile strain values were found to range from -4% to 5% and from -3% to -0.7% for FTR and PMA models, respectively, whereas radial patterns ranged from 3.5% to 18% and from 8% to 13% for FTR and PMA models, respectively. Accordingly, aiming to a deeper investigation of the influence of the PMA technique on the valve biomechanics, the second model (TV02) revealed a lower strain state.

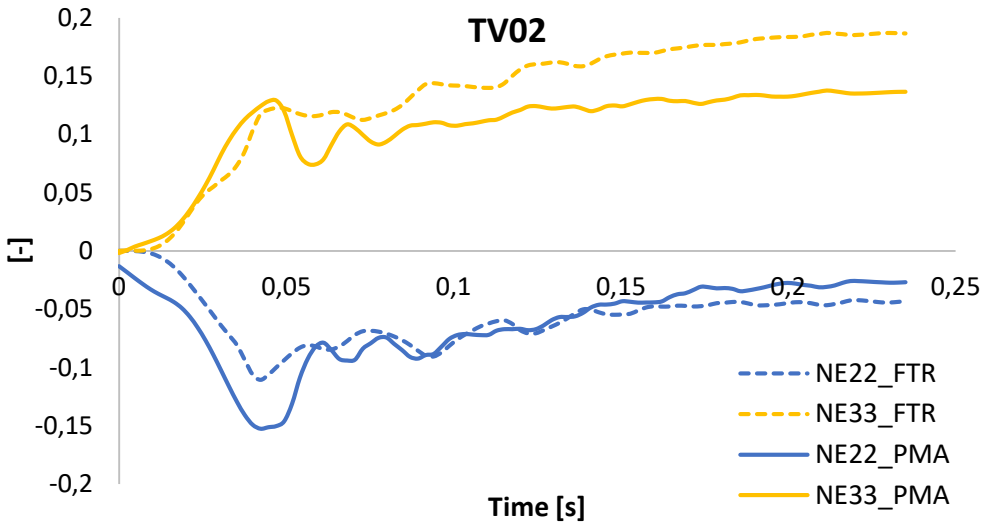

Figure 2-21 Time course of circumferential (NE22) and radial nominal strain (NE33), reported for the second simulated TV model, for both FTR (dashed line) and PMA (solid line) configurations.

As shown in Figure 2-21, radially, FTR02 appeared more stretched (approximately +10%) and, to a lesser extent, even in circumferential direction (+3%); as our suggestion, the reason relies more on the dislocation of the PMs, as a direct effect of pressurization of a passive ventricle, rather than on the non-complete coaptation of the valve.

Differently, the same cannot be asserted for the first model (TV01) (Figure 2-22). Here, FTR01 showed, as absolute values, lower strain both in

circumferential and radial direction. We are fairly aware that the reason has to be found in the inverse behaviour exhibited by the posterior leaflet, as previously emerged from maximum nominal strain analysis.

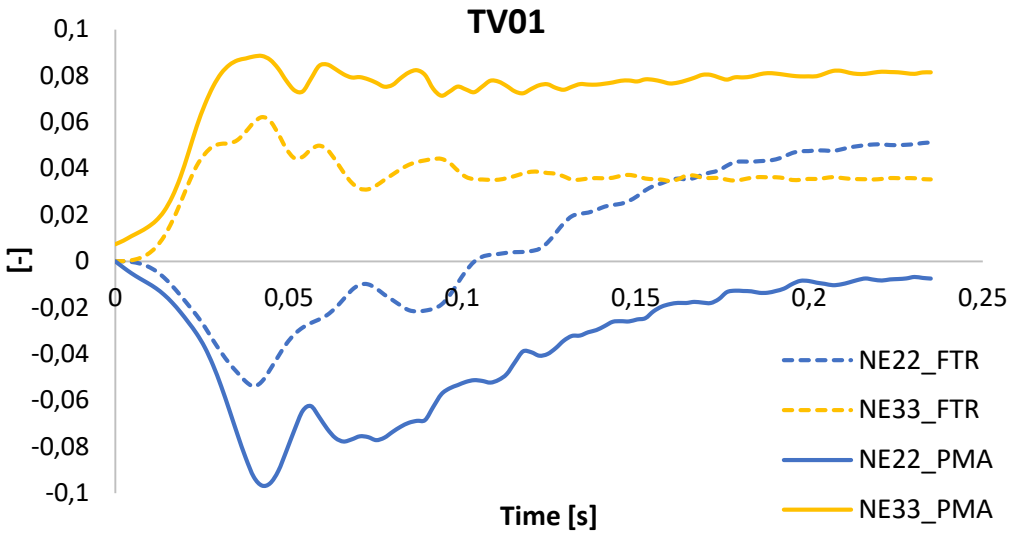

Figure 2-22 Time course of circumferential (NE22) and radial nominal strain (NE33), reported for the first simulated TV model, for both FTR (dashed line) and PMA (solid line) configurations.

On the contrary, ranges yielded by PMA01 model were coherent with the ones resulting from PMA02 model, and consistent with results provided by recent study[7], being at least 20% lower than values reported by Stevanella et al.[6], where

TV leaflets experience extremely large longitudinal strains, almost unrealistic in physiological conditions.

As a measure of PM-chordae acting reaction to systolic closure, force exerted by papillary muscles were computed, at MS, as the stress in the main branch arising from PM tip multiplied by the chorda cross-section area (Table 4).

Table 4 Reaction force (in N) at the systolic peak on the three papillary muscles (PMs) in all the simulated models. APM, anterior PM; PPM, posterior PM; SPM, septal PM.

	FTR01	**PMA01**	**FTR02**	**PMA02**
APM	0.341 N	0.297 N	0.458 N	0.390 N
PPM	0.387 N	0.301 N	0.442 N	0.374 N
SPM	0.342 N	0.268 N	0.448 N	0.352 N

To note, this variable always experienced higher values in FTR configuration with respect to the PMA one, probably owing to the fact that chordae have to exert more pulling action since coaptation among the leaflets is not happening. For the sake of comparison, values associated to PMA models were found to be in the same order of magnitude as compared with results obtained by Stevanella et al.[6], exploiting the same chordal apparatus paradigm.

2.8 Novelty of the study and conclusions

In this study we presented a novel approach for the study of the tricuspid valve (TV) biomechanics, integrating experimental in vitro data and computational elaborations towards the development of one of the first image-based complete finite element model (FEM) of the valve, the first starting from ultrasound imaging data. The new designed method would allow to carry out in vitro tests on a right porcine heart housed in a mock circulation loop (MCL) and to perform imaging of the TV structures. Our work showed that the MCL presented in section 2.2 was a suitable environment to perform experimental campaigns on the TV, allowing to replicate physiologic-like working conditions of the valve, in terms of pulsatile flow rate, frequency and pressure acting on the system. The

acquisition protocol and the computational processing of the echocardiographic images resulted in a reconstructed TV geometry that was globally more accurate as compared to the paradigmatic one proposed by Stevanella et al.[6], and absolutely comparable with the CT-derived model described by Kong and colleagues[7].

The morphological evaluation showed that the PMA could be a feasible approach to treat FTR. It systematically reduced the anomalies associated with tricuspid regurgitation and TV leaflets tenting. Although PMA was a successful approach to treat FTR, we demonstrated that complete counteracting FTR mechanism by addressing the PM displacement and TA dilation had additional advantages, by implementing a band system to constrain the annular enlargement.

The final part of the study focused on the simulation of the TV biomechanics. The models included realistic anatomical TV apparatus geometries reconstructed from 3D echo images, human nonlinear anisotropic hyperelastic material properties, and realistic boundary conditions. As mentioned in section 2.7.3.2, FE analysis was carried out aiming at adding further general information, to better investigate how such a treatment (PMA) could beneficially or negatively influence TV biomechanics. Given that, reported results have to be considered preliminary, also considering some simplifying assumptions associated to the proposed approach, being the needing of a validation step the first future development of the proposed framework. Indeed, the intrinsically limited temporal resolution of echocardiographic acquisition did not allow for PMs motion to be accounted for as boundary condition in the simulations setting, thus being neglected. Moreover, owing to poor spatial resolution, chordal insertion locations and origins were paradigmatically assumed. Concerning this latter aspect, although the adopted paradigmatic model proved to be flexibly adapted to every TV geometry, it relies on small amount of ex vivo data and lacks the prestress/prestrain state that chordae have in their LD configuration.

The herein proposed study evaluated the potential of a technique (PMA) that could not be directly applied clinically but the effects of the possible surgical or

interventional approach were simulated, being possibly pivotal in the introduction of a new FTR treatment procedure.

2.9 Bibliography

1. Dreyfus, G. D., Martin, R. P., Chan, K. M. J., Dulguerov, F. & Alexandrescu, C. Functional Tricuspid Regurgitation. *J. Am. Coll. Cardiol.* **65,** 2331–2336 (2015).
2. Taramasso, M. *et al.* Percutaneous tricuspid valve therapies: the new frontier. *Eur. Heart J.* **38,** ehv766 (2016).
3. Chambers, J. B., Myerson, S. G., Rajani, R., Morgan-Hughes, G. J. & Dweck, M. R. Multimodality imaging in heart valve disease. *Open Hear.* **3,** e000330 (2016).
4. Badano, L. P., Agricola, E., de Isla, L. P., Gianfagna, P. & Zamorano, J. L. Evaluation of the tricuspid valve morphology and function by transthoracic real-time three-dimensional echocardiography. *Eur. J. Echocardiogr.* **10,** 477–484 (2009).
5. Xie, M.-X. *et al.* Real-Time 3-Dimensional Echocardiography: A Review of the Development of the Technology and Its Clinical Application. *Prog. Cardiovasc. Dis.* **48,** 209–225 (2005).
6. Stevanella, M., Votta, E., Lemma, M., Antona, C. & Redaelli, A. Finite element modelling of the tricuspid valve: A preliminary study. *Med. Eng. Phys.* **32,** 1213–1223 (2010).
7. Kong, F. *et al.* Finite Element Analysis of Tricuspid Valve Deformation from Multi-slice Computed Tomography Images. *Ann. Biomed. Eng.* **46,** 1112–1127 (2018).
8. Khoiy, K. A., Pant, A. D. & Amini, R. Quantification of Material Constants for a Phenomenological Constitutive Model of Porcine Tricuspid Valve Leaflets for Simulation Applications. *J. Biomech. Eng.* **140,** 094503 (2018).
9. Jaworek, M. *et al.* Functional Tricuspid Regurgitation Model in a Beating Heart Platform. *ASAIO J.* **63,** 438–444 (2017).
10. Kikinis, R., Pieper, S. D. & Vosburgh, K. G. in *Intraoperative Imaging and Image-Guided Therapy* 277–289 (Springer New York, 2014). doi:10.1007/978-1-4614-7657-3_19
11. Pappalardo, O. A. NOVEL STRATEGIES FOR THE MORPHOLOGICAL AND BIOMECHANICAL ANALYSIS OF THE CARDIAC VALVES BASED ON VOLUMETRIC CLINICAL IMAGES. (2018). at <https://iris.univr.it/handle/11562/977217#.W-6fM-hKjb0>
12. Taramasso, M. *et al.* The Growing Clinical Importance of Secondary Tricuspid Regurgitation. *J. Am. Coll. Cardiol.* **59,** 703–710 (2012).

13. Silver, M. D., Lam, J. H., Ranganathan, N. & Wigle, E. D. Morphology of the human tricuspid valve. *Circulation* **43,** 333–48 (1971).
14. Cleveland, W. S. Robust Locally Weighted Regression and Smoothing Scatterplots. *J. Am. Stat. Assoc.* **74,** 829–836 (1979).
15. Lim, K. O., Boughner, D. R. & Perkins, D. G. Ultrastructure and mechanical properties of chordae tendineae from a myxomatous tricuspid valve. *Jpn. Heart J.* **24,** 539–48 (1983).
16. Tasca, G. *et al.* Aortic Root Biomechanics After Sleeve and David Sparing Techniques: A Finite Element Analysis. *Ann. Thorac. Surg.* **103,** 1451–1459 (2017).
17. Sturla, F. *et al.* Dynamic and quantitative evaluation of degenerative mitral valve disease: a dedicated framework based on cardiac magnetic resonance imaging. *J. Thorac. Dis.* **9,** S225–S238 (2017).
18. Caimi, A. *et al.* Prediction of stenting related adverse events through patient-specific finite element modelling. *J. Biomech.* **79,** 135–146 (2018).
19. Holzapfel, G. A., Gasser, T. C. & Ogden, R. W. A New Constitutive Framework for Arterial Wall Mechanics and a Comparative Study of Material Models. *J. Elast.* **61,** 1–48 (2000).
20. Gasser, T. C., Ogden, R. W. & Holzapfel, G. A. Hyperelastic modelling of arterial layers with distributed collagen fibre orientations. *J. R. Soc. Interface* **3,** 15–35 (2006).
21. Jimenez, J. H., Soerensen, D. D., He, Z., Ritchie, J. & Yoganathan, A. P. Mitral Valve Function and Chordal Force Distribution Using a Flexible Annulus Model: An In Vitro Study. *Ann. Biomed. Eng.* **33,** 557–566 (2005).
22. in (Dassault Systèmes, Providence, RI, USA, 2010). at <http://abaqusdoc.ucalgary.ca/books/stm/default.htm>
23. Kunzelman, K. S., Einstein, D. R. & Cochran, R. P. Fluid-structure interaction models of the mitral valve: function in normal and pathological states. *Philos. Trans. R. Soc. Lond. B. Biol. Sci.* **362,** 1393–1406 (2007).

Patient-specific tuning of mitral valve chordal apparatus: a framework based on mass-spring modelling using 3D echocardiographic images

3.1 Introduction

When computing the structural mechanics of a system through finite element modelling, the initial configuration of the model is assumed either stress-free or characterized by a pre-stress field that is known *a priori*.

In the specific context of patient-specific and image-based modelling of the structural mechanics of atrioventricular valves, this general condition leads to defining the initial geometry of the modelled valve at end-diastole, when the valve is still open and the trans-valvular pressure load acting on the leaflets is approximately equal to 0 mmHg, and to assuming leaflets and chordae tendineae completely unloaded.

As explained in chapter 2, to this aim the patient-specific anatomy of valve leaflets and annulus, as well as the position of papillary muscle heads are obtained by processing medical images. Chordae tendineae, instead, are typically defined based on some standard template, because their geometry cannot be reconstructed from standard medical images. This limitation inherently hampers the high-fidelity modelling of valve systolic closure and of the associated biomechanics: chordae tendineae tissue is about ten times stiffer than leaflet tissue; hence, small deviations of the assumed chordae length, cross-sectional area and branching pattern from the real patient-specific features can reflect into non-negligible errors in the computed loaded geometry of the valve as compared to ground truth evidence. In of principle, one could limit this inconsistency by the fine tuning of the chordae model, by acting on its geometry so to make it consistent with the real one. However, the high number of chordae and the complexity of their branched structure would make such tuning hardly feasible. Alternatively, one could aim at replicating the constraining effect of the real chordal apparatus through a functionally equivalent model of the chordae tendineae[1]. In this second case, the fine tuning of the modelled chordae is not aimed at replicating their morphology in detail, but rather at replicating their stiffness at the organ length-scale, e.g., by tuning their initial pre-stress or their cross-sectional area.

The aforementioned aspects become even more relevant when modelling pathological atrioventricular valves, which are often characterized by

abnormally extensible chordae, as in degenerative diseases[2], or by a pre-loading of chordae tendineae secondary to ventricular dilation and papillary muscle dislocation, as in the case of functional or ischemic regurgitation[3]. In these cases, not only the lack of image-based morphological information has to be compensated for, but also the lack of patient-specific information on the location and severity of the chordal abnormalities has to be coped with.

Motivated by these considerations, and by the paucity of methods proposed in the literature to tackle the patient-specific tuning of chordae tendineae models, a novel method for improving the patient-specific modelling of chordae tendineae was conceived, implemented and tested.

3.2 Methods

3.2.1 Imaging Data

The method herein proposed aims to improving the high fidelity of patient-specific finite element models of the atrioventricular valves based on time-efficient and low-cost imaging modalities, namely based on real time 3D trans-esophageal echocardiography (RT3DTEE). The method was developed with specific reference to the mitral valve (MV), and it was tested on RT3DTEE data (GE Vivid E90; space resolution: 0.8571x0.8571x0.5911 mm; time resolution: about 20 frames/cycle) of 5 patients affected by functional mitral regurgitation with no comorbidities (age: 36-66 years old; gender: 2 males, 3 females). The datasets were provided by the Leiden University Medical Centre (LUMC) in Leiden (the Netherlands).

3.2.2 The method at a glance

The method consists in the iterative tuning of the tethering effect of chordae tendineae by exploiting mass-spring modelling (MSM), which allows for almost real time simulations. The method is summarized in Figure 3-1, and consists in the following steps:

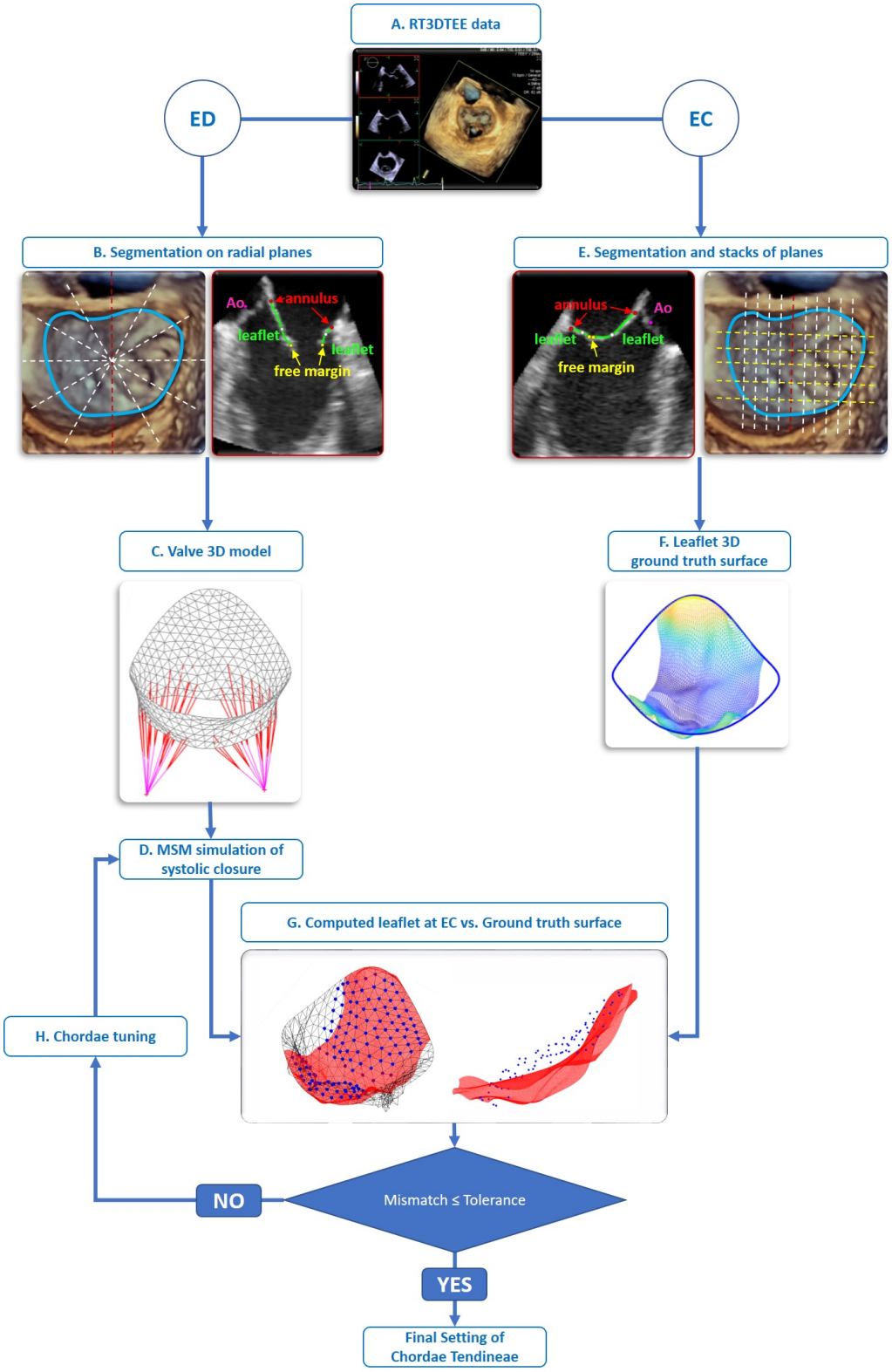

Figure 3-1 Flowchart summarizing the working pipeline of the proposed method. A) Original ultrasound data (RT3DTEE=Real-time 3D trans-oesophageal echocardiography). B) Tracing of mitral valve substructures ad end diastole (ED) on radial planes (white dashed lines). For one radial plane (red dashed line), an example of tracing is depicted. C) Reconstructed 3D geometry

of the mitral valve, where leaflets are obtained as a triangulated surface and their patient-specific geometry is complemented by paradigmatic chordae tendineae. D) Simulation of mitral valve closure through mass-spring modelling (MSM). E) Tracing of mitral valve substructures ad early closure (EC) on two stacks of parallel planes, orthogonal (white dashed lines) and parallel (yellow dashed lines) to the commissure-commissure diameter of the valve. For one plane (red dashed line), an example of tracing is depicted. F) 3D triangulated surface representing the reconstructed leaflet surface at EC, to be used as ground truth data. G) Comparison of computed leaflet configuration (white triangles) at EC vs. the corresponding ground truth data (red surface). The mismatch is quantified at a subset of points (blue points). H) If the mismatch exceeds a pre-defined threshold, the initial configuration of chordae tendineae is tuned and the MSM simulation is iterated.

1. selection of the end-diastolic frame (ED, end diastole) in the RT3DTEE dataset, i.e., the last frame before the transient closure of the MV, and reconstruction of the MV 3D geometry at end diastole (ED). Concomitantly, the position of papillary muscles (PMs) and the annular profile are reconstructed at every frame from ED to the onset of MV coaptation (EC, early coaptation), and the corresponding time-dependent motion is obtained. The MV geometry at ED and the motion of PMs and annulus are inputs to the simulation of MV systolic closure until EC through MSM;
2. selection, within the RT3DTEE dataset, of the frame when MV leaflets start coapting (EC) and reconstruction of the corresponding 3D geometry of the MV. The reconstructed EC geometry is used as ground truth data;
3. quantitative comparison of the EC configuration computed through MSM (Γ_{EC_comp}) vs. the ground truth EC configuration (Γ_{EC_gt}) and computation of local mismatches;
4. if the mismatch exceeds a given tolerance, tuning of the modelled chordae tendineae initial length to compensate for the computed mismatch.

Steps 1-4 are iterated until the mismatch between (Γ_{EC_comp}) and Γ_{EC_gt} falls within the tolerance or until a maximum number of iterations are run. Each step is described in detail in the following paragraphs.

3.2.3 MV tracing and 3D reconstruction at ED

Definition of the rotational planes for MV tracing - The volumetric RT3DTEE datasets were processed through a custom Matlab® script (Matlab, The Mathworks, Inc, Natick, MA) equipped with a graphical user interface (GUI), which allows for selecting any time frame and for navigating the datasets by moving three mutually orthogonal planes, each one providing a cross section of the volumetric dataset. The planes were positioned so to identify the left atrium, the left ventricle, the mitral valve and the aortic valve (Figure 3-2).

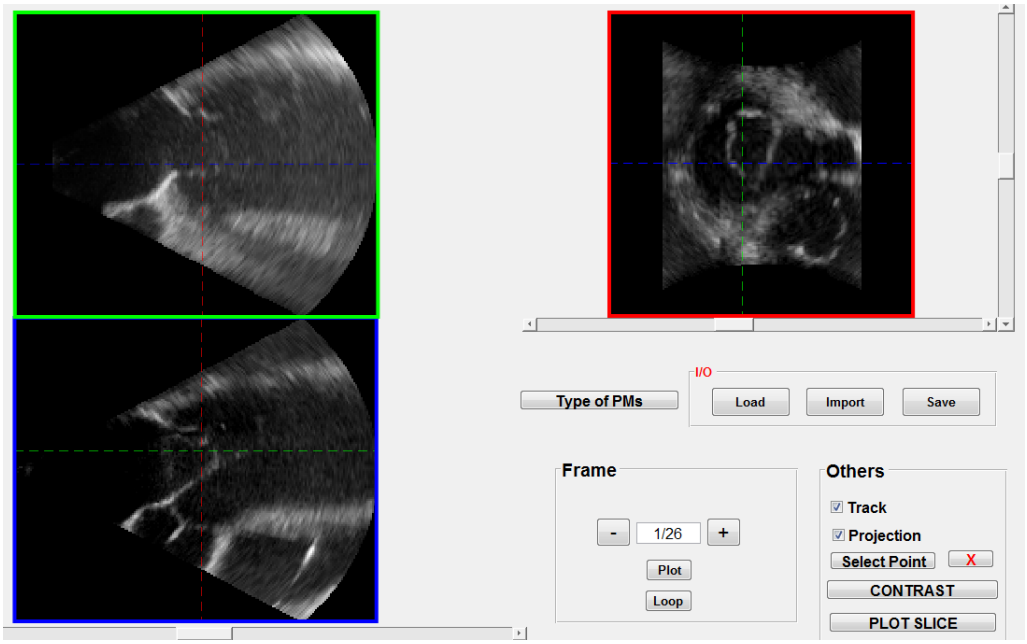

Figure 3-2 Graphical user interface of the Matlab® script allowing for the navigation of RT3DTEE datasets. The three mututally orthogonal cross-sectional planes are visible. The cross-sections framed in blue and green are approximately passing through the centre of the MV orifice and perpendicular to the CC and SL diameter of the annulus, respectively.

Also, two out of the three planes are approximately passing through the centre of the MV orifice and perpendicular to the commissure-commissure (CC) and septo-lateral (SL) diameter, respectively; the two planes are named π^{CC} and π^{SL}. On each one of these two views, two annular points were selected and the corresponding 3D cartesian coordinates are stored ($\boldsymbol{P}_1^{CC}, \boldsymbol{P}_2^{CC}$ and $\boldsymbol{P}_1^{SL}, \boldsymbol{P}_2^{SL}$). Also, an extra point within the atrial chamber was selected and the corresponding 3D cartesian coordinates are stored ($\boldsymbol{P}^A$). The centre of the mitral orifice ($\mathbf{C}$) was defined as the centre of mass of the four selected annular points:

$$\mathbf{C} = (\mathbf{1/4}) \cdot \left(\mathbf{P_1^{CC}} + \mathbf{P_2^{CC}} + \mathbf{P_1^{SL}} + \mathbf{P_2^{SL}}\right) \quad (1)$$

The axis orthogonal to the MV annular plane ($\hat{\boldsymbol{n}}$) was defined by the axis contained in both π^{CC} and π^{SL} and pointing towards the atrium:

$$\hat{\boldsymbol{n}} = (\hat{\boldsymbol{n}}^{CC} \times \hat{\boldsymbol{n}}^{SL}) \cdot \boldsymbol{sign}\{(\hat{\boldsymbol{n}}^{CC} \times \hat{\boldsymbol{n}}^{SL}) \cdot (\boldsymbol{P^A} - \boldsymbol{C})\} \quad (2)$$

$\hat{\boldsymbol{n}}$ was used to define a polar reference frame, where eighteen cross-sectional planes were generated: these all passed through $\hat{\boldsymbol{n}}$ and each one plane was rotated by 10° around $\hat{\boldsymbol{n}}$ with respect to the adjacent one (Figure 3-3 A). These virtually generated planes provided 2D views where the position and the spackle of each pixel was obtained by interpolating the voxels of the raw volumetric data and the corresponding spackle value[4].

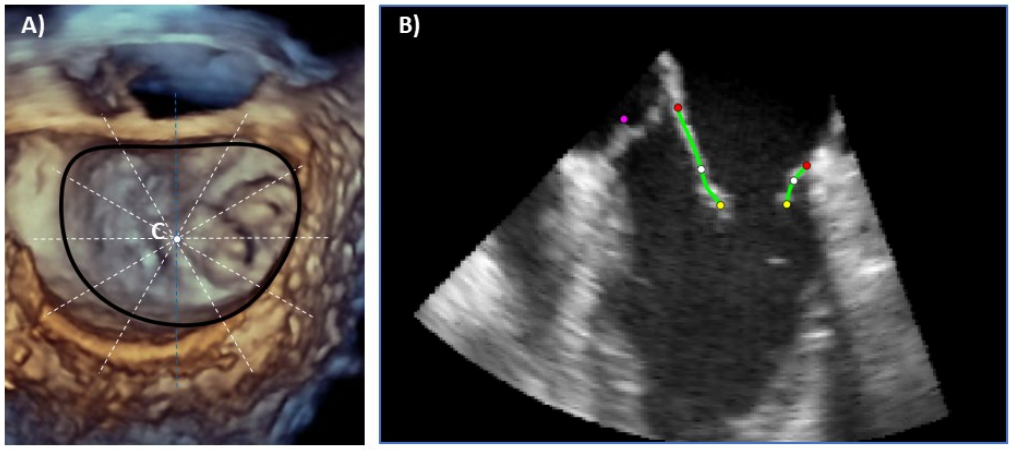

Figure 3-3 A) View of the RT3DTEE data along the $\hat{\mathbf{n}}$ axis. Six out of the eighteen radial planes passing through C are sketched (dashed lines) and through the axis Example of MV section as visible on one of the eighteen rotational planes. Pink dot=position of the aortic valve; red dots=MV annular points; yellow dots=MV leaflet free margin; green lines=cubic splines connecting the points traced on the leaflet profile.

Tracing of MV substructures on the rotational planes – On each rotational plane, the following MV sub-structures were manually traced (Figure 3-3 B):

- two annular points;
- multiple points on each leaflet profile; the point at the opposite end of the profile with respect to the annular point is automatically identified as

free margin. For each leaflet profile, the in-plane, i.e., 2D, coordinates of the points running from the annulus to the free margin were interpolated by a cubic spline, which was resampled at 32 uniformly distributed positions;

- one point for each papillary muscle tip, where visible;
- one point falling within the aortic lumen, which was subsequently used as reference point to discriminate between the anterior and the posterior sides of the MV in the 3D reconstruction.

Reconstruction of the MV 3D geometry at ED – Three MV structures were set to define the 3D end-diastolic configuration of the MV:

- the leaflets, obtained from the manual tracings on ultrasound data
- the PMs, obtained from the manual tracings on ultrasound data
- the chordae tendineae, defined based on a standard template.

In order to define the 3D geometry of the leaflets, which were described as a triangulated surface owing to their membranous structure, the 3D coordinates on the points associated to each rotational image plane were reconstructed based on the space resolution of the rotational plane and on its orientation and position in space (Figure 3-4 A). To this aim, the following formula was used for every point P originally on an image plane π:

$$\boldsymbol{P^{3D} = O^{\pi} + res_x^{\pi} \cdot P_x^{\pi} \cdot V_x^{\pi} + res_y^{\pi} \cdot P_y^{\pi} \cdot V_y^{\pi}} \qquad (3)$$

where $\boldsymbol{P}^{3D}$ is the 3D position vector of the point P, $\boldsymbol{O}^{\pi}$ is the 3D position vector of the left-upper corner of the image plane π, $\boldsymbol{V}_x^{\pi}$ and $\boldsymbol{V}_y^{\pi}$ are the two unitary vectors defining the orientation in the 3D space of the two orthogonal sides of the image plane originating from $\boldsymbol{O}^{\pi}$, P_x^{π} and P_y^{π} are the components of the in-plane position of P, expressed in pixels, along the two directions, res_x^{π} and res_y^{π} are the space resolution of the image plane in the two directions.

This coordinate transformation yielded a 3D point cloud that was inherently organized in 32 curvilinear parallels, running circumferentially around the annular profile, and 36 curvilinear meridians, running from the annulus to the free edge of the leaflets (Figure 3-4). The 3D coordinates of the point cloud, being the result of manual tracing, were noisy. Hence, they were smoothed

through low-pass filtering: the least square plane of the annular points, i.e., the points in the first curvilinear parallel, was computed and the normal to this plane was considered as the z-direction in a cylindrical reference frame (ρ,θ,z). The origin of the cylindrical reference frame was set in the centre of mass of the points in the last parallel, which corresponded to the leaflet free margin.

For each curvilinear parallel, the cartesian coordinates of the corresponding points were transformed in the cylindrical reference frame and then approximated by fourth order Fourier functions in the form:

$$\begin{cases} \boldsymbol{R(\theta) = a_0 + \sum_{i=1}^{4} [a_i \cos i\theta + b_i \sin i\theta]} \\ \boldsymbol{z(\theta) = c_0 + \sum_{i=1}^{4} [c_i \cos i\theta + d_i \sin i\theta]} \end{cases} \quad (4)$$

where the coefficients a_i, b_i, c_i, d_i are identified by least square fitting of the continuous functions $R(\theta)$ and $z(\theta)$ on the raw ρ and θ coordinates. The continuous functions were then resampled at 300 angular positions uniformly distributed in the range [0;π].

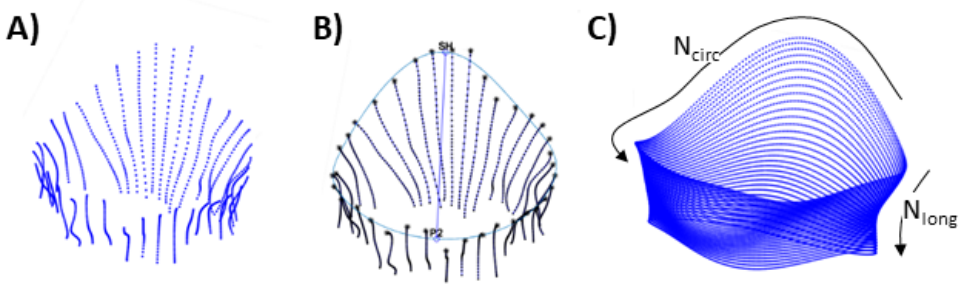

Figure 3-4 A) 3D position of the points obtained by resampling at 32 positions the splines that represent the leaflet profile on each one of the 18 radial planes. Annular points are those at the top. B) Approximation of the annular points by a Fourier function and identification of the saddle horn (SH) and of the mid-point of the posterior annulus (P2). C) Point-cloud obtained after applying the Fourier approximation on each of the 32 levels of points and resampling each Fourier function at Ncirc positions (Ncirc=300 in this case). Ncirc indicates the general number of points in the annulus-to-free edge direction (Nlong=32 in this case).

For the first curvilinear parallel, i.e., for the annulus, the saddle horn (SH), the mid-point of the posterior annulus (P2), and the commissures were identified.

To this aim, the 3D position of the aortic lumen was identified based on the previously traced aortic point. Consistently, the anterior and posterior sides of the annulus were identified: the SH was defined as the point with angular position θ_{SH} that maximizes $z(\theta)$, P2 was defined as the point with angular position $\theta_{SH} + \pi$. The commissures were defined as the two points at maximum distance from each other along the direction perpendicular to SH-P2 (Figure 3-4 B-C); based on SH and P2 the septo-lateral (SL) diameter was computed, based on the commissures the commissure-commissure (CC) diameter was computed. The filtered cylindrical coordinates of the annular and leaflet points were finally transformed back in the original cartesian reference frame and triangulated by means of a simple mapped scheme (Figure 3-5 A), yielding 18600 triangular elements with characteristic dimension in the order of 0.1 mm, thus capturing anatomical details such as local leaflet 3D curvature, but hampering the possibility to run time-efficient MSM simulations of MV closure. The number of triangular elements was reduced, while preserving the level of anatomical detail, by resampling the triangulated surface through the open mesh editing software Meshmixer (Meshmixer, Autodesk Inc., San Rafael, CA, USA) (Figure 3-5 B).

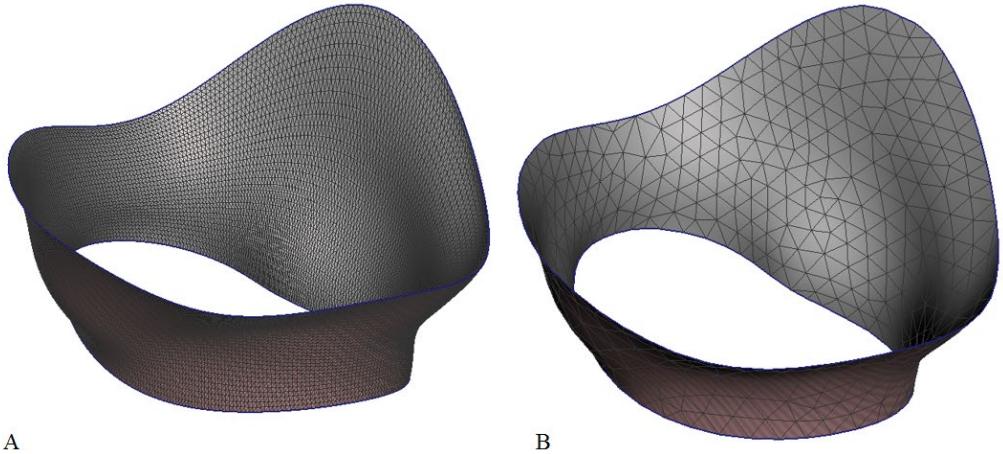

Figure 3-5 A) leaflet triangulated surface as obtained by triangulating through a mapped scheme the 3D point-cloud yielded by Fourier approximation and resampling. B) the same triangulated surface is resampled by preserving its geometrical features by means of Meshmixer (in the depicted example, the final element characteristic dimension is 2 mm).

For each of the five valves considered in the study, three leaflet triangulated meshes were defined, with element characteristic dimension set to 3, 2.5 and 2 mm, respectively, for the sake of a subsequent mesh sensitivity analysis.
In order to reconstruct the PMs in the 3D space, the same coordinate transformation defined by Eq. 3.3 was applied to the points traced on papillary muscles tips. In the 3D cartesian coordinate system, points were clustered into two clusters, each one corresponding to a papillary muscle. For each cluster, the centre of mass was computed and set as the tip of the corresponding papillary muscle, which is also the origin of the associated chordae tendineae.

Table 1 Number of nodes for the three triangulated mesh used to discretize the leaflet geometry in each one of the five MVs considered in the study.

	Number of nodes		
	Mesh size 3 mm	**Mesh size 2.5 mm**	**Mesh size 2 mm**
MV 1 F01	244	349	511
MV 2 F02	294	448	715
MV 3 F04	234	334	513
MV 4 F10	298	449	660
MV 5 F12	173	253	352

The 3D end-diastolic geometry of the MV was completed by a standard template of chordae tendineae, whose length and insertion position were automatically adapted to the patient-specific configuration of leaflets and PMs by the Matlab® script. The template was borrowed by previous work by our group[5] and improved so to account for some of the branched structures in the chordal apparatus, with a cross-sectional area set equal to 1 mm^2 at the main branches[6]. Namely, the template consisted in:

- 20 1st order chordae, inserted on the leaflet free margin, and 40 2nd order chordae, inserted on the leaflet rough zone. These chordae were clustered in 20 branched structures, each one consisting in a main trunk that gives origin to a 1st order chorda and to two 2nd order chordae (Figure 3-6 A). The position of the branching point was defined by a normalized

coordinate β; given the position of the PM where the chorda originates from ($\boldsymbol{P}_{PM}$) and the position of the insertion point of the 1st order chorda ($\boldsymbol{P}_{1st}$), the position of the branching point ($\boldsymbol{P}_{\beta}$) was defined by

$$\mathbf{P_{\beta}} = \mathbf{P_{PM}} + \boldsymbol{\beta}(\mathbf{P_{1st}} - \mathbf{P_{PM}}) \qquad \boldsymbol{\beta} \in [\mathbf{0}; \mathbf{1}] \qquad (5)$$

Of note, for a given combination of leaflet and PMs configuration, chordae tendineae cross-sectional area and stress-strain response of chordae tissue, the global stiffness of the chordal apparatus, and hence its tethering effect on the leaflets, is inherently influenced by the value of β.

Out of the 20 branched structures, 10 were inserted on the anterior leaflet, 4 were inserted on the P2 posterior cusp and 3 were inserted on the P1 and P3 cusp, respectively;

- 21 basal chordae, inserted on the leaflet clear zone;
- 2 strut chordae, inserted on the anterior leaflet;
- 2 para-commissural chordae

All chordae types were evenly associated to the two papillary muscles.

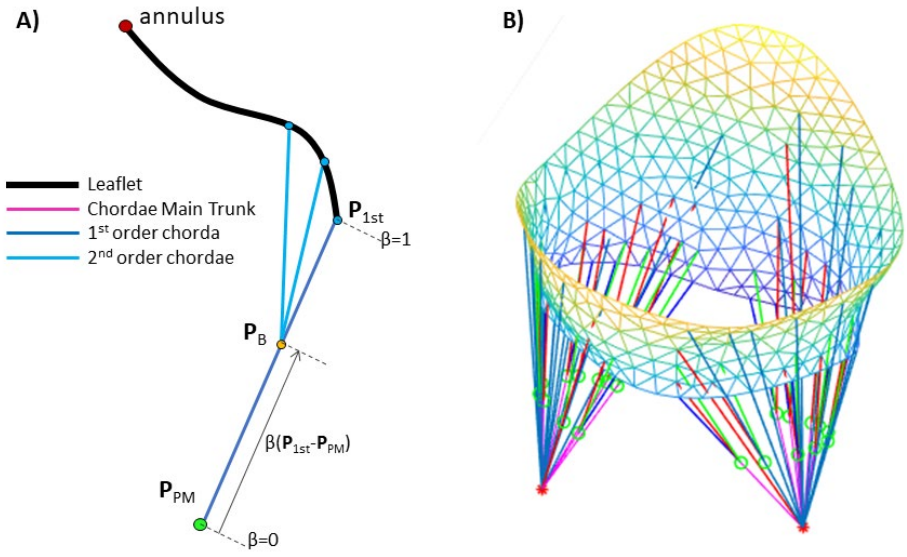

Figure 3-6 A) Sketch of the branched structure of each chordae cluster consisting in one 1st order chorda and two 2nd order chordae. The position of the branching point P_B is defined by the normalized coordinate β. B) Complete MV configuration at end diastole. Chordae are color-coded based on the chorda type.

The complete discretized end-diastolic configuration of the MV (Figure 3-6 B) was the input for the subsequent iterative MSM simulations of MV closure during early systole, i.e., from ED to EC.

3.2.4 MV leaflet tracing and 3D reconstruction at EC

At EC, owing to the closed configuration of MV leaflets, the reconstruction of the leaflet 3D geometry was carried out through a different process as compared to the one adopted at ED. Instead of radial image planes, two stacks of parallel planes were considered to trace the relevant structures:

- 10 commissural planes, orthogonal to the CC diameter as identified at ED. These planes were uniformly distributed of the central tract of the CC diameter, whose extent was equal to $3 \cdot L_{cc}/5$, where L_{cc} is the total length of the CC diameter (Figure 3-7);
- 5 septo-lateral planes, orthogonal to the SL diameter. These planes were uniformly distributed of the central tract of the SL diameter, whose extent was equal to $3 \cdot L_{SL}/5$, where L_{SL} is the total length of the SL diameter (Figure 3-7);

As for the radial planes, also the commissural and septo-lateral planes were obtained by interpolating in the 3D space the spackle value of the voxels of the raw RT3DTEE data.

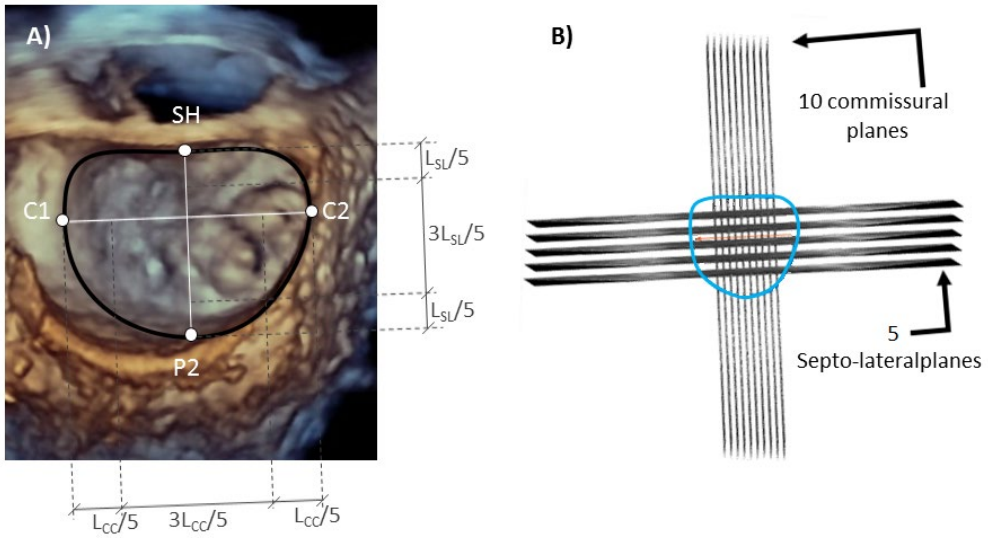

Figure 3-7 A) MV orifice as seen from the atrium. The CC and SL diameters are sketched together with the corresponding tract relevant to the definition of the commissural and septo-lateral image planes. B) Example of commissural and septo-lateral planes.

On each commissural plane, the following MV sub-structures were manually traced: two annular points, leaflet profile, two points indicating either the leaflet free margin (in case of lack of coaptation) or the boundary between the coapting and non-coapting regions of the leaflets (in case of coaptation), and a point into the aortic lumen if visible (Figure 3-8).

On the septo-lateral planes, only the annular points were traced, so to obtain exhaustive data to reconstruct the annular profile.

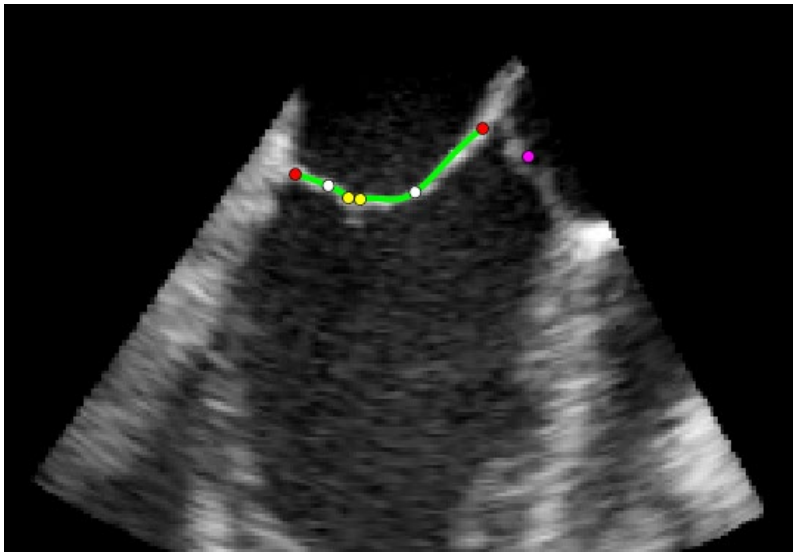

Figure 3-8 Example of commissural plane. The traced structures are highlighted: aortic point (pink), annular points (red), leaflets (green) and start of the coapting region (yellow).

The annular points were processed as for the end-diastolic configuration: their coordinate in the 3D cartesian space are obtained through (3), a cylindrical reference frame was defined with the origin in the center of mass of the annular points and with the z-axis normal to the least square plane fitting the annular points. In this reference frame, the positions of the annular points were fitted by fourth order Fourier functions (4), which were subsequently resampled yielding the final annular points, whose coordinates were transformed back in the original cartesian reference frame (Figure 3-9 A).

The points traced on the leaflets on each commissural plane were instead fitted by a 2D cubic spline, which was uniformly resampled at 32 positions, whose

coordinates in the 3D space are obtained through (3). Overall, a cloud of 32·10 points was obtained, which was organized in 10 parallels running from the anterior to the posterior leaflet and 32 meridians running from commissure to commissure. The points of each meridian were then fitted by a 3D cubic spline, which was uniformly resampled at 60 positions. This procedure finally yielded a cloud of 1860 points (Figure 3-9 B), which were triangulated to obtain the ground truth leaflet surface (Figure 3-9 C).

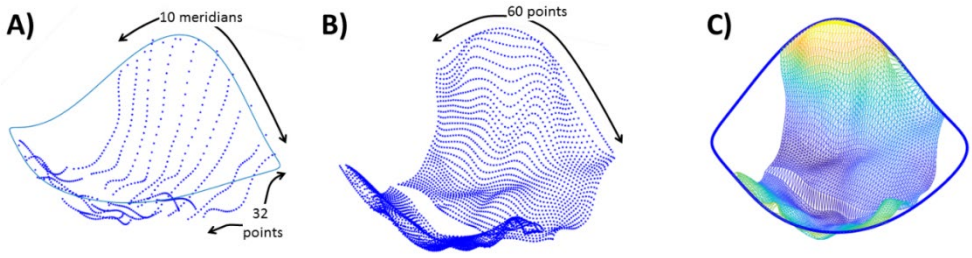

Figure 3-9 3D reconstruction of annulus and leaflets geometry at EC. A) Cloud of points originally traced on the leaflet profiles once transformed in the 3D space (blue points) and Fourier function approximating the annulus (cyan line). The number of meridians and the number of points in each meridian are highlighted. B) Leaflet point-cloud after resampling in the commissure-commissure direction. C) Triangulated leaflet surface and annular profile.

3.2.5 MSM simulation of MV closure from ED to EC

MSM simulations were run through an in-house script implemented in Matalb®. In MSM simulations, each point in the discretized geometry, i.e., each point of the leaflet triangulated surface, the two points representing the PMs and the branching points of the chordae tendineae, is considered as a point mass. Contextually, each segment connecting two masses is considered as a spring. Hence, the dynamics of the point masses is governed by the second Newton's law:

$$\mathbf{F_{tot}} = \boldsymbol{M}\ddot{\boldsymbol{x}} \tag{6}$$

Where $\mathbf{M}$ is the matrix storing the masses, $\ddot{\boldsymbol{x}}$ and $\mathbf{F_{tot}}$ are the vectors storing the component s of the 3D acceleration and load vectors associated to the point masses.

Numerical integration scheme: The definition of the forces acting on each point and the solution of the governing differential equations through a forward explicit Euler scheme were borrowed from Pappalardo et al.[5]:

$$\begin{cases} \ddot{\boldsymbol{x}} = \boldsymbol{M^{-1}F_{tot}} \\ \dot{\boldsymbol{x}}(\boldsymbol{t}+\Delta\boldsymbol{t}) = \dot{\boldsymbol{x}}(\boldsymbol{t}) + \ddot{\boldsymbol{x}}(\boldsymbol{t})\Delta\boldsymbol{t} \\ \boldsymbol{x}(\boldsymbol{t}+\Delta\boldsymbol{t}) = \boldsymbol{x}(\boldsymbol{t}) + \dot{\boldsymbol{x}}(\boldsymbol{t})\Delta\boldsymbol{t} \end{cases} \quad (7)$$

where $\dot{\boldsymbol{x}}$ and $\boldsymbol{x}$ are the vectors storing the 3D velocities and positions of the point masses, and Δt is the integration time increment, set to 2.5 ×10^{-7} s.

Definition of the masses: Mass values are assigned to points based on two different criteria depending on whether these are part of the leaflets or part of the chordae tendineae. In the former case, the mass assigned to the i-th point is:

$$\boldsymbol{M_i} = (\boldsymbol{1/3}) \sum_{\boldsymbol{j}} \boldsymbol{A_j h_i \rho} \quad (8)$$

where $\sum_j A_j$ is the total surface area of the triangular elements sharing the point, ρ is the density of leaflet tissue, which is set to 1100 kg/m^3 , and h_i is the leaflet thickness at the i-th node, which is set homogeneous over the leaflets and equal to 1 mm.

In the latter case, the mass assigned to the i-th point is:

$$\boldsymbol{M_i} = (\boldsymbol{\rho/2}) \sum_{\boldsymbol{j=1}}^{\boldsymbol{n}} \boldsymbol{S_j l_j} \quad (9)$$

Where ρ is the density of chordae tissue, which is set to 1040 kg/m^3, n is the number of chordal elements insisting on the point mass, and S_j and l_j are the cross-sectional area and the length, respectively, of the chordal elements. S_j is set to 0.7 mm^2 or to 0.14 mm^2 depending on whether the j-th chordal segment is a main chorda trunk or a branch.

Definition of the loads: The loads acting on the masses are decomposed as:

$$\boldsymbol{F_{tot}} = \boldsymbol{F_{el}} + \boldsymbol{F_{visc}} + \boldsymbol{F_{cont}} + \boldsymbol{F_{ext}} \quad (10)$$

where i) $\boldsymbol{F}_{el}$ represents the loads generated by the elastic recoil of the springs, which is aimed at replicating the effect of the elastic behavior of MV tissues, ii) $\boldsymbol{F}_{visc}$ represents the loads generated by a viscous effect, which is not aimed at

mimicking any visco-elastic stress-strain behavior of MV tissue, but rather at stabilizing the simulation preventing from excessive and unrealistic mass velocities, iii) $\boldsymbol{F}_{cont}$ represents the loads associated to contact interactions and iv) $\boldsymbol{F}_{ext}$ represents the contribution of external loads, which in this specific application consist in the pressure load acting on the leaflet nodes only.

Definition of $\boldsymbol{F}_{el}$: as previously mentioned, $\boldsymbol{F}_{el}$ is generated by the elastic recoil of the springs that mimic the effect of MV tissue elastic behaviour. As such, $\boldsymbol{F}_{el}$ depends on the elastic constant k of every spring insisting on a mass and k is defined so to account for tissue non-linear and anisotropic stress-strain response whenever relevant.

As regards leaflets, k is defined as[7]:

$$\boldsymbol{k} = \frac{\boldsymbol{E}(\boldsymbol{\varepsilon}, \boldsymbol{\alpha_0}) \boldsymbol{h} \sum_i \boldsymbol{A_i}}{|\boldsymbol{l_0^2}|} = [\boldsymbol{E_{cf}}(\boldsymbol{\varepsilon}) \cos \boldsymbol{\alpha_0^2} + \boldsymbol{E_f}(\boldsymbol{\varepsilon}) \sin \boldsymbol{\alpha_0^2}] \frac{\boldsymbol{h} \sum_i \boldsymbol{A_i}}{|\boldsymbol{l_0^2}|} \quad (11)$$

where E is the elastic modulus of the material of the spring and depends on i) the current spring strain ε (and hence on its current length), ii) on the initial space-orientation of the spring quantified by the initial angle α_0 identified by the spring and the direction of the circumferentially aligned collagen fibers in MV leaflet tissue (Figure 3-10), and iii) on the strain-dependent elastic modulus of MV leaflet tissue in the fiber and cross fiber direction, respectively ($E_{cf}(\varepsilon)$ and $E_f(\varepsilon)$).

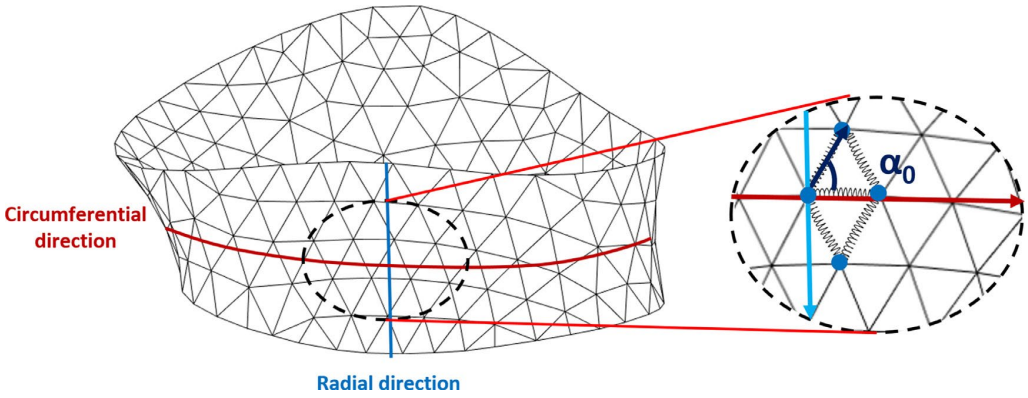

Figure 3-10 Sketch representing the definition of the angle $\boldsymbol{\alpha_0}$ that quantifies the orientation of leaflet springs with respect to the circumferential direction, which is the preferential direction of collagen fibers in MV leaflet tissue[5].

$E_{cf}(\varepsilon)$ and $E_f(\varepsilon)$ are set based on the fitting of stress-strain experimental data from equi-biaxial tests[8] with piecewise functions of ε:

$$\boldsymbol{\sigma_f} = \begin{cases} \mathbf{100}\boldsymbol{\varepsilon}_f & \boldsymbol{\varepsilon}_f < \mathbf{0.21} \\ \mathbf{10^{-4}}\boldsymbol{e}^{\mathbf{57.7}\boldsymbol{\varepsilon}_f} & \boldsymbol{\varepsilon}_f \geq \mathbf{0.21} \end{cases} \tag{12}$$

$$\boldsymbol{\sigma_{cf}} = \begin{cases} \mathbf{100}\boldsymbol{\varepsilon}_{cf} & \boldsymbol{\varepsilon}_{cf} < \mathbf{0.21} \\ \mathbf{3.2812710^{-5}}\boldsymbol{e}^{\mathbf{58}\boldsymbol{\varepsilon}_{cf}} & \boldsymbol{\varepsilon}_{cf} \geq \mathbf{0.21} \end{cases} \tag{13}$$

And hence:

$$\boldsymbol{E_f(\varepsilon_f)} = \frac{\boldsymbol{d\sigma_f}}{\boldsymbol{d\varepsilon_f}} = \begin{cases} \mathbf{100} & \boldsymbol{\varepsilon}_{cf} < \mathbf{0.21} \\ \mathbf{57.7 \cdot 10^{-4}}\boldsymbol{e}^{\mathbf{57.7}\boldsymbol{\varepsilon}_f} & \boldsymbol{\varepsilon}_{cf} \geq \mathbf{0.21} \end{cases} \tag{14}$$

$$\boldsymbol{E_{cf}(\varepsilon_{cf})} = \frac{\boldsymbol{d\sigma_{cf}}}{\boldsymbol{d\varepsilon_{cf}}} = \begin{cases} \mathbf{100} & \boldsymbol{\varepsilon}_{cf} < \mathbf{0.21} \\ \mathbf{58 \cdot 3.2812710^{-5}}\boldsymbol{e}^{\mathbf{58}\boldsymbol{\varepsilon}_{cf}} & \boldsymbol{\varepsilon}_{cf} \geq \mathbf{0.21} \end{cases} \tag{15}$$

As regards chordae tendineae, k is defined as:

$$\boldsymbol{k} = \frac{\boldsymbol{E(\varepsilon)S_0}}{\boldsymbol{l_0}} \tag{16}$$

where $E(\varepsilon)$ is the strain-dependent elastic modulus of chordae tissue, S_0 and l_0 are the cross-sectional area and the length, respectively, of the modeled chorda in the initial configuration. $E(\varepsilon)$ is set based on the fitting of experimental stress-strain data from uniaxial tensile tests[9] by means of a cubic function:

$$\boldsymbol{\sigma(\varepsilon)} = \boldsymbol{a\varepsilon^3} + \boldsymbol{b\varepsilon^2} + \boldsymbol{c\varepsilon} \tag{17}$$

Hence,

$$\boldsymbol{E(\varepsilon)} = \frac{\boldsymbol{d\sigma}}{\boldsymbol{d\varepsilon}} = \mathbf{3}\boldsymbol{a\varepsilon^2} + \mathbf{2}\boldsymbol{b\varepsilon} \tag{18}$$

In order to cope with the non-linearity of the stress-strain behavior, which implies a non-linearity in the force-elongation behavior of the springs, $\boldsymbol{F_{el}}$ was expressed in an incremental fashion and linearized as following:

$$\boldsymbol{F_{el}(t)} = [\|\boldsymbol{F_{el}(t - \Delta t)}\| + \boldsymbol{k(l(t))(l(t) - l(t - \Delta t))}]\boldsymbol{n} \tag{19}$$

where t indicates the current configuration of the system, $(t - \Delta t)$ indicates the previous configuration of the system and $\boldsymbol{n}$ represents the unitary vector that identifies the orientation of the spring in the 3D space.

Definition of $\boldsymbol{F}_{visc}$: consistently with numerical integration strategies available in commercial solvers, a fictitious viscous energy dissipation is introduced into the model by setting a viscous damper in parallel to each spring. The force exerted by the damper on each mass at its extremities is:

$$\boldsymbol{F_{visc}} = -\boldsymbol{\eta}\Delta\dot{\boldsymbol{x}} \tag{20}$$

where $\Delta\dot{\boldsymbol{x}}$ is the relative velocity of one mass with respect to the mass at the opposite end of the spring and η is viscosity, which is set to 0.001 Pa·s.

Definition of $\boldsymbol{F}_{cont}$: the computation of contact forces requires the definition of two sets of nodes that can interact with each other. In the simulations herein reported, these consist in the nodes of the A2 and P2 region, respectively, which are treated as two potentially contacting triangulated surfaces (S_{A2}, S_{P2}). Their interaction is managed through three steps:

1. In the initial, i.e., ED, configuration of the MV, for each triangular element within S_{A2} or S_{P2}, a characteristic dimension is computed, i.e., the maximum distance between each of the triangle's vertexes and their center of mass. The mean value of the characteristic dimensions ($\bar{d}$) is then obtained.
2. At time *t*, point mass m_i within S_{A2} can interact with a triangular element e_j of the surface S_{P2} only if:

$$\boldsymbol{d_{ij}^{e}(t)} < \bar{\boldsymbol{d}} \ \wedge \ \boldsymbol{d_{ij}^{\pi}(t+\Delta t)} < \overline{\boldsymbol{d_{ij}^{\pi}}} \tag{21}$$

   Where d_{ij}^{e} is the distance of m_i from the center of mass of e_j, d_{ij}^{π} is the signed distance of m_i from the plane π_j containing e_j, and d_{ij}^{π} is a second threshold that is set to 1 mm in the simulations herein presented. If these two conditions are both satisfied, the contact force applied to the point mass m_i is

$$\boldsymbol{F_{i\_cont}} = \begin{cases} |\boldsymbol{F_{i\_tot}}|\boldsymbol{e}^{-\frac{\boldsymbol{kd_{ij}^{\pi}}}{|\boldsymbol{F_{i\_tot}}|}}\boldsymbol{n} \ \ \boldsymbol{d_{ij}^{\pi}(t)} > \boldsymbol{0} \\ \left(\left|\boldsymbol{F_{i\_tot}}\right| - \boldsymbol{kd_{ij}^{\pi}}\right)\boldsymbol{n} \ \ \boldsymbol{d_{ij}^{\pi}(t)} \leq \boldsymbol{0} \end{cases} \tag{22}$$

where $\boldsymbol{n}$ is the outward normal to the plane π_j and k is a parameter set to 10 N/m[10].

Of note, since the endpoint of the SMS simulations is EC, contact forces play a role only in the very last time increments. Hence, the computational expense associated to the computation of contact forces, which is typically the most time-consuming feature, remains limited.

Definition of $\boldsymbol{F}_{press}$: the forces generated by the time-dependent pressure load acting on the leaflet ventricular surface are computed as:

$$\boldsymbol{F_{press}} = \frac{\boldsymbol{p \sum_i A(T_i) n_i}}{\boldsymbol{3}} \tag{23}$$

where the index i loops over the triangles that share the point mass, $\boldsymbol{n}_i$ is the inward normal to the leaflet ventricular surface, $A(T_i)$ is the surface area of the i-th triangle and p is the pressure load. The time-dependent pressure p was assumed physiological and described by:

$$\boldsymbol{P = 60\ mmHg \cdot \left(\sin\left(4\pi t - \frac{\pi}{2}\right) + 1\right); t\ \epsilon\ [0; 0.25\ s]} \tag{24}$$

where t=0 at ED. The value of p at EC was obtained by identifying in the systolic pressure waveform the timeframe spanning from ED to EC (Figure 3-11).

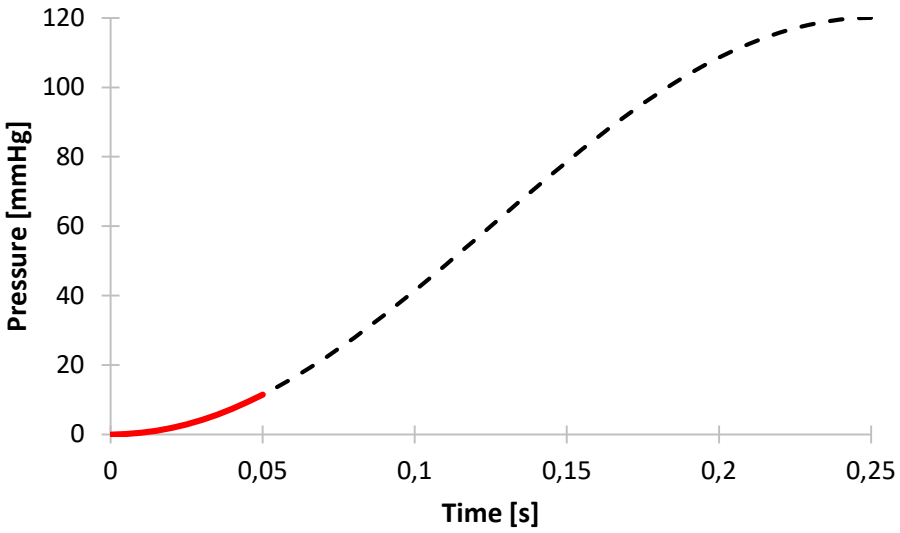

Figure 3-11 Time-course of the trans-mitral pressure p from ED (time = 0 s) to peak systole (time = 0.25 s). The red tract of the plot corresponds to the timeframe from ED to EC.

Definition of the kinematic boundary conditions: the motion of annulus and PMs was imposed as a set of time-dependent velocities, based on the frame-by-frame tracing of the corresponding MV sub-structures from ED to EC. As regards the annulus, tracings were processed at each frame, as for ED, and the commissures were identified, leading to the distinction between the anterior and posterior tracts of the annulus. Under the assumption that within each tract strains are homogeneously distributed, at each frame the two tracts were discretized so to preserve the number of point masses falling within them as well as the proportions between the length of the different springs defining the annular profile. For each annular point mass, the time-dependent velocity was obtained from:

$$\boldsymbol{x_i(t + \Delta t) = x_i(t) + v_i(t)\Delta t} \quad (25)$$

The same equation was exploited to obtain the velocity of PMs based on their time-dependent position as yielded by their tracing.

3.2.6 Fine-tuning of the chordae tendineae via iterative MSM simulations

As previously mentioned, the fine tuning of the chordae tendineae was based on the iterative MSM simulation of MV closure from ED to EC. At the end of each simulation, the leaflet geometrical configuration yielded by the simulation Γ_{EC_comp} was compared vs. the EC geometry Γ_{EC_gt} directly obtained by the processing of the RT3DTEE data. If the mismatch between Γ_{EC_comp} and Γ_{EC_gt} exceeded a pre-determined threshold, the chordae tendineae were tuned and the MSM simulation was iterated. This process was carried out under the assumption that the tuning of a chorda tendinea only affects the position of the point masses in the leaflets that are closer to its own insertion as compared to the insertion of the other chordae.

Comparison of computed vs. ground truth configuration: Based on this criterion, the point masses over A2 and P2 were clustered based on their closest chordal insertion (Figure 3-12).

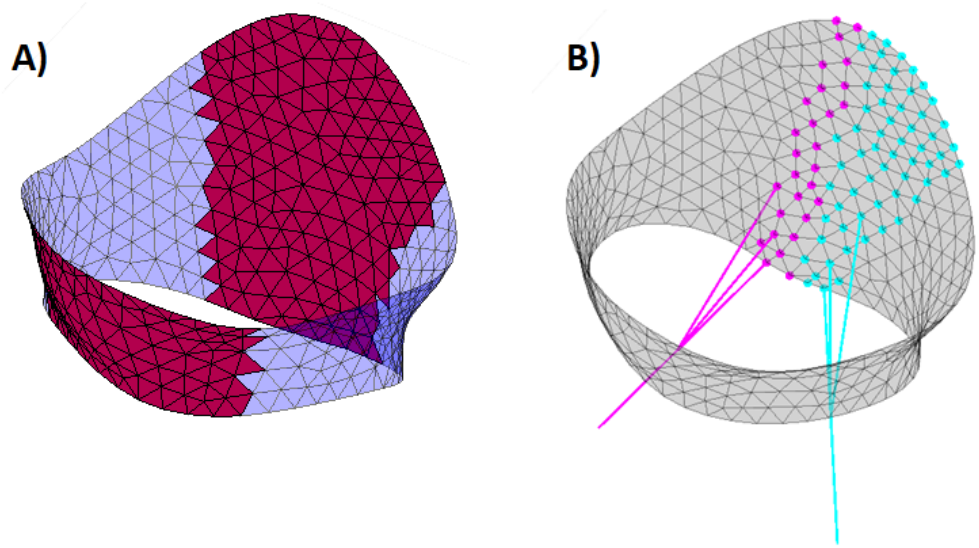

Figure 3-12 A) The leaflet regions corresponding to A2 and P2 are highlighted in red. B) Clustering of the nodes falling within A2 or P2, based on the corresponding closest chordal insertion. For the sake of clarity, in the figure only two clusters and the corresponding chordae tendineae are depicted.

Contextually, the point masses falling within A2 or P2, and not falling on the annulus nor in the coaptation region at EC, were used as control points (Figure 3-13).

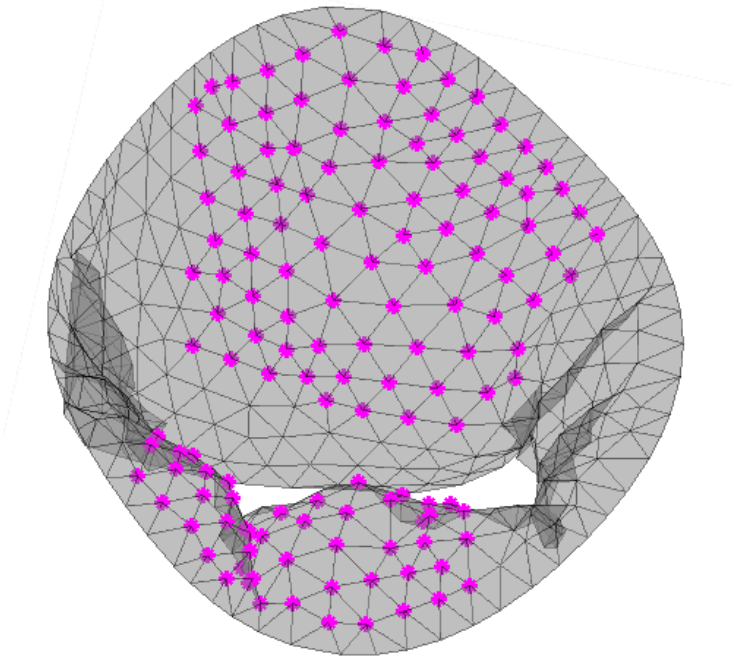

Figure 3-13 Atrial view of one of the modelled MVs at EC. The point masses highlighted in purple are used as control points to check for consistency between $\boldsymbol{\Gamma_{EC\_comp}}$ and $\boldsymbol{\Gamma_{EC\_gt}}$.

At the end of each MSM simulation, for every control point on Γ_{EC_comp} the signed distance d_j from the triangulated surface Γ_{EC_gt} was computed through the ad hoc Matlab® script *point2trimesh*, originally implemented by Daniel Frisch: a positive distance indicates that the computed configuration Γ_{EC_comp} is locally more displaced towards the atrium as compared to the ground truth datum Γ_{EC_gt}, a negative distance indicates that Γ_{EC_comp} remains more displaced towards the ventricular apex as compared to Γ_{EC_gt} (Figure 3-14).

For every cluster of point masses, the average distance from Γ_{EC_gt} was computed:

$$\overline{\boldsymbol{err}}_{\boldsymbol{c}} = \frac{\sum_{j=1}^{n} \boldsymbol{d_j}}{\boldsymbol{n}} \tag{26}$$

If $\overline{err}_c > 2imres$, where $imres$ is the spatial resolution of the RT3DTEE data, chordae tendineae were tuned.

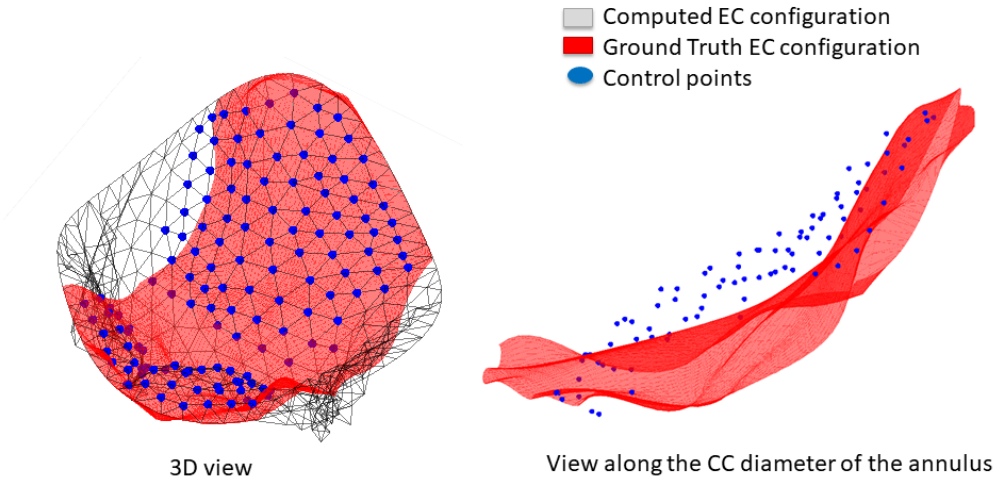

Figure 3-14 3D position of the control points on $\boldsymbol{\Gamma_{EC\_comp}}$ (blue dots on the grey grid) with respect to the ground truth leaflet geometry $\boldsymbol{\Gamma_{EC\_gt}}$ (red).

Tuning of chordae tendineae: The tethering effect of chordae tendineae was iteratively tuned by acting on the parameter l_0 that appears in the definition of the elastic stiffness of the springs that represent chordae tendineae (Eq. 3.16): reducing the value of l_0 leads to stiffening the spring, increasing the value of l_0 leads to making the spring more extensible. Namely, the tuning procedure was applied to the main trunk of 1st order and 2nd order chordae tendineae, i.e., to the chordal tract running from a PM to a branching point. As far as strut chordae are

concerned, these were tuned based on the calculations performed for the two central chordae inserted on the free margin of the anterior leaflet.

At the end of the i-th MSM simulation, for every cluster of control points the quantity $\overline{err_c}(i)$ was computed and the the value of l_0 for the corresponding chorda was updated as:

$$\boldsymbol{l_0^{(c)}(i+1) = l_0^{(c)}(i) - b \cdot \overline{err}_c(i)} \tag{27}$$

where b is an under-relaxation factor that can range from 0.2 to 1.0, and $l_0^{(c)}(i) = l_0^{(c)}$ when $i = 1$, i.e., the value of the initial length is initially determined by the actual position of the masses in the MSM model, when the first MSM simulation is performed.

The iterative process ended when either $\overline{err_c}(i) \leq 2imres \; \forall \; c$ or when the maximum number of iterations was performed.

Sensitivity analysis: in the different steps of the semi-automated process that leads from MV tracings to the final outcome of chordae tuning, the setting of some parameters was involved, with a potential impact on the reliability of the results or the time-expense of the procedure:

- the characteristic dimension of the triangular elements defined in the discretization of MV leaflets, which was set to 2.0, 2.5 and 3.0 mm;
- the position of chordae branching points as defined by the normalized coordinate β (Eq. 3.5), which was set to 0.2, 0.5, and 0.8;
- the under-relaxation factor b (Eq. 3.26), which was set to 0.3 and 0.5

A sensitivity analysis was performed by applying the entire procedure to each one of the five considered MVs and with each combination of the values considered for the above-mentioned parameters. For each variant, the maximum number of iterations allowed for was set to 5.

3.3 Results and discussion

Inter-valve variability and inter-leaflet differences: The whole set of simulations yielded a notable amount of data. In order to avoid an extremely verbose report while still highlighting the key findings, results are here reported with reference to a subset of simulations.

In particular, results are here reported with the aim to discuss the mismatches between Γ_{EC_comp} and Γ_{EC_gt}, as well as the effects of chordae tuning on these mismatches, in relation to the following concepts:

- differences between the anterior and posterior leaflets
- valve-dependent variability of results
- effect of mesh size, branches configuration and under-relaxation factor

From a qualitative standpoint, the magnitude of the initial mismatch between Γ_{EC_comp} and Γ_{EC_gt}, as well as its reduction through the tuning of chordae tendineae, was strongly dependent on the specific simulated MV. Still, some features were observed quite consistently over the small population considered in the study.

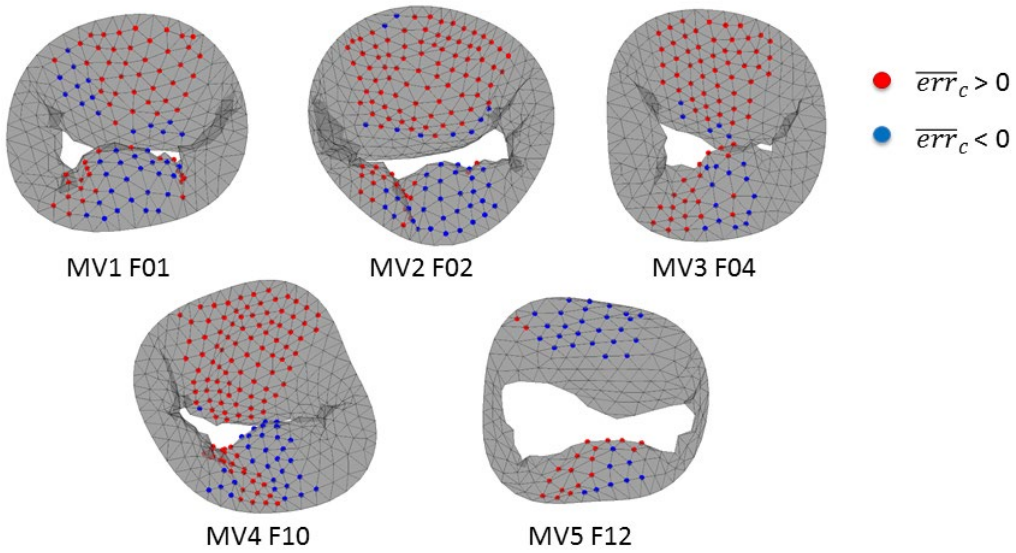

Figure 3-15 Spatial distribution of the sign of $\overline{\boldsymbol{err}_c}$ obtained at EC for the five simulated valves for meshes with a 2 mm characteristic dimensions and with the following combination of parameters: $\boldsymbol{\beta = 0.5}$, b=0.3.

The anterior and posterior leaflets showed two different behaviours in terms of mismatch between Γ_{EC_comp} and Γ_{EC_gt}: before the iterative tuning of chordae

tendineae, the anterior leaflet in Γ_{EC_comp} was consistently characterized by excessive billowing into the atrium, with the only exception of valve MV5 F12, which exhibited an opposite trend. Conversely, in all simulated valves the posterior leaflet was characterized by an inhomogeneous distribution of errors, with regions of P2 excessively displaced towards the atrium and other regions of P2 excessively tethered towards the ventricular apex (Figure 3-15). This difference remained unchanged after the iterative tuning of the chordal apparatus.

Indeed, this qualitative and evident difference between the results obtained for the anterior and the posterior leaflet is consistent with the fact that, in the real MV, the posterior leaflet experiences a minor motion during systole, whereas the anterior leaflet undergoes large displacements even in early systole, i.e. even with minor pressure loads acting on it. Hence, it is reasonable that correctly capturing the much wider motion of the anterior leaflet is more difficult than mimicking the motion of the posterior one.

Moreover, the tendency of the simulated anterior leaflet to billow towards the atrium has been reported by most of the published studies focused on the numerical simulation of systolic MV closure through finite element modelling[11–15] or through MSM[5,16,17]. This issue is due to the fact that typically those studies neglect at least one of the two features of the anterior leaflet that allow for this structure to not buckle when pressurized from the ventricular side: the compound pattern of 3D curvature of the leaflet, which already at ED is convex towards the ventricle in the belly region[18,19], and the active contraction on the anterior leaflet, which makes the leaflet more resistant to bending and buckling owing to the presence of valvular interstitial cells and of smooth muscle cells within the extracellular matrix of the anterior MV leaflet[20–23].

Finally, it is worth recalling that in the iterative tuning of chordae tendineae strut chordae, which insert into the belly of the anterior leaflet and may play a role in limiting its billowing, were not tuned independently from the other chordae. Instead, they were tuned based on the changes to be imposed to the virtual initial length of the marginal chordae inserted in the central part of the free margin of the anterior leaflet. It is reasonable to hypothesize that allowing for the

independent optimization of strut chordae stiffness could improve the capability of the model to capture the real changes in the configuration of the MV anterior leaflet.

Magnitude of the errors in the computed MV configuration at EC: from a more quantitative standpoint, the two leaflets still showed differences. As far as the anterior leaflet is concerned, when the most refined mesh was used (characteristic dimension=2mm), the magnitude of the mean mismatch ranged between 1.08 mm and 3.71 mm, while the peak mismatch recorded over the five anterior leaflets was approximately 5mm in magnitude. On the posterior leaflet, much smaller mismatches were recorded: when the most refined mesh was used, the magnitude of the mean value ranged between 0.12 mm and 0.96 mm and the magnitude of the peak mismatch was approximately 2 mm. Both trends and values were affected by the mesh size to a minor extent, at least when considering the range of element characteristic dimensions adopted in this study (Table 2).

These outcomes are consistent with those reported in previously published studies that presented a quantitative analysis of the fidelity of the deformed configuration of MV leaflets as computed by numerical simulations as compared to ground truth data. Mansi and colleagues simulated the systolic closure of patient-specific pathological MVs based on RT3DTEE data and by means of co-rotated finite element modelling[24]. When assuming a standard chordal apparatus, they obtained mismatches by 3.17±1.98 mm between the computed closed configuration of the leaflets and the corresponding ground truth data. After tuning the chordal apparatus through an iterative procedure, they reduced the magnitude of the mismatch to 2.59 ±1.59 mm. Similar results were reported also in a different study from the same research group, where initial average errors by 3.2 mm were reduced to 1.92 mm through iterative tuning of the chordal apparatus[24].

Moreover, it is worth mentioning that the mismatches reported in the referred studies as well as in this one are comparable to the inter-operator variability observed among the manual tracings of the MV from ultrasound data by four independent operators[25].

Table 2 Effect of mesh size on the distribution (mean value±standard deviation) of the mismatch between $\boldsymbol{\Gamma_{EC\_comp}}$ and $\boldsymbol{\Gamma_{EC\_gt}}$ reported for different valves and different combination of parameter. For valves MV1 F01 and MV2 F02, $\boldsymbol{\beta}$ and b were both set to 0.5. For the remaining valves, $\boldsymbol{\beta}$ and b were set to 0.5 and 0.3, respectively. Ant and Post indicate the anterior and posterior leaflets, respectively.

			Mesh Size		
Valve	**Leaflet**		**2 mm**	**2.5 mm**	**3 mm**
MV 1 F01	Ant	Initial error	1.08±1.52	1.44±1.43	1.33±1.68
		Final error	1.02±1.26	1.22±1.32	1.30±1.41
	Post	Initial error	-0.12±1.10	-0.22±1.17	-0.01±1.27
		Final error	-0.20±1.30	-0.51±1.27	-0.08±1.39
MV 2 F02	Ant	Initial error	2.14±1.56	2.22±1.44	2.42±1.42
		Final error	1.59±1.35	1.67±1.20	1.61±1.27
	Post	Initial error	-0.30±1.18	-0.27±1.15	-0.05±1.18
		Final error	-0.45±1.41	-0.56±1.5	-0.28±1.40
MV 3 F04	Ant	Initial error	3.64±1.86	2.55±1.44	2.54±1.40
		Final error	3.35±1.86	2.08±1.41	2.12±1.39
	Post	Initial error	-0.39±1.28	0.20±1.49	0.08±1.42
		Final error	-0.42±1.60	0.32±1.66	0.28±1.48
MV 4 F10	Ant	Initial error	3.71±2.14	3.45±1.95	3.70±1.64
		Final error	3.29±1.88	3.04±1.71	3.15±1.43
	Post	Initial error	-0.28±2.00	-0.12±2.52	0.01±2.26
		Final error	0.02±2.25	-0.23±2.57	-0.12±2.80
MV 5 F12	Ant	Initial error	-1.29±1.05	-1.32±1.12	-1.43±0.99
		Final error	-1.32±1.05	-1.35±1.12	-1.22±0.88
	Post	Initial error	0.96±1.36	1.02±1.21	0.58±1.48
		Final error	1.06±1.24	1.25±1.21	0.41±1.48

Effect of the position of chordae branching points: three values of the parameter β were considered. No major effects were observed when changing the value of this parameter. However, a consistent trend was observed for the anterior leaflet: before tuning the chordae tendineae, reducing the value of β slightly increased the tethering effect of the chordae tendineae. Hence, the mean mismatch between Γ_{EC_comp} and Γ_{EC_gt} was reduced when the anterior leaflet in Γ_{EC_comp} was excessively displaced towards the atrium, but increased in MV5 F12, in whose

model the anterior leaflet was already too tethered towards the ventricular apex. Also, the smaller the value of β, the smaller the reduction in mismatch induced by the tuning of chordae tendineae (Table 3).

Table 3 Effect of the position of the branching points on the chordae tendineae, quantified by the normalized coordinate **β**, on the distribution (mean value±standard deviation) of the mismatch between $\mathbf{\Gamma_{EC\_comp}}$ and $\mathbf{\Gamma_{EC\_gt}}$. Results are reported for the five valves with a leaflet mesh of characteristic dimension equal to 3 mm. Ant and Post indicate the anterior and posterior leaflets, respectively.

Valve	Leaflet		$\boldsymbol{\beta = 0.8}$	$\boldsymbol{\beta = 0.5}$	$\boldsymbol{\beta = 0.2}$
MV 1 F01	Ant	Initial error	1.41±1.63	1.33±1.68	1.26±1.71
		Final error	1.30±1.39	1.30±1.41	1.12±1.66
	Post	Initial error	-0.10±1.25	-0.01±1.27	0.07±1.28
		Final error	-0.14±1.40	-0.08±1.39	0.01±1.35
MV 2 F02	Ant	Initial error	2.51±1.45	2.42±1.42	2.30±1.40
		Final error	1.56±1.14	1.61±1.27	1.92±1.31
	Post	Initial error	-0.13±1.20	-0.05±1.18	-0.07±1.10
		Final error	-0.42±1.45	-0.28±1.40	-0.11±1.28
MV 3 F04	Ant	Initial error	2.61±1.37	2.54±1.40	2.45±1.43
		Final error	2.08±1.39	2.12±1.39	2.22±1.42
	Post	Initial error	0.01±1.44	0.08±1.42	0.15±1.40
		Final error	0.31±1.40	0.28±1.48	0.17±1.44
MV 4 F10	Ant	Initial error	3.80±1.74	3.70±1.64	3.58±1.59
		Final error	3.16±1.50	3.15±1.43	3.32±1.47
	Post	Initial error	0.05±2.41	0.01±2.26	0.14±2.29
		Final error	0.09±2.80	-0.12±2.80	0.24±2.47
MV 5 F12	Ant	Initial error	-1.41±0.99	-1.43±0.99	-1.55±0.94
		Final error	-1.19±0.87	-1.22±0.88	-1.44±0.91
	Post	Initial error	0.51±1.53	0.58±1.48	0.66±1.47
		Final error	0.38±1.55	0.41±1.48	0.39±1.45

Effect of the under-relaxation factor: the under-relaxation parameter b proved almost crucial. High values of b lead to excessively large changes in l_0 between two consecutive MSM simulations. As a result, chordae tend to become alternatively too slack or too stiff, causing the local mismatch between Γ_{EC_comp} and Γ_{EC_gt} to oscillate over the iterative simulations. For the MV configuration

at EC to become asymptotically stable as simulations are iterated, b had to set to small values.

Computational expense: Finally, it is worth analysing the computational expense of the procedure herein proposed to tune the chordal apparatus. When the maximum number of iterations was set to 5, the time required by chordae tuning ranged from 30 minutes, when the coarsest mesh was considered, to 90 minutes, when the most refined mesh was considered.

In all cases, the method was more time-efficient than that recently proposed by Mansi and colleagues, which required up to 5 hours and 10 minutes[25]. Yet, the method is not fast enough to be exploited in the context of fast, or even almost real-time, simulations. On the other hand, the method herein proposed could be exploited as the preliminary step in a working pipeline devoted to the high-fidelity finite element simulation of MV systolic function: in that case, the final simulation would take 4-6 hours even if run on a supercomputing system; hence, an extra computational cost in the order of one hour or less would be reasonable if beneficial to the reliability of computational results.

3.4 Conclusion

In the proposed study, an iterative algorithm, based on the mass-spring modelling (MSM) approach, was developed for the optimization of the chordae tendineae rest length in patient-specific models of insufficient mitral valve. Definitely, we tried to address a key still challenging topic, as the chordal apparatus modelling is to date. In this context, studies have been recently published on establishing a rigorous foundation to develop more reliable *in vivo* MV computational models[26–28], still debating whereas a micro-CT-derived fully realistic tree-like patient-specific MV chordal apparatus is better rather than its well-defined synthetic paradigm that can be calibrated to mimic the functionality. To the best of our knowledge, the one herein provided is the first example of such a study based on volumetric ultrasound images.

The yielded results showed that the algorithm actually lowered the error between the simulated valves and *ground truth* data, although the intensity of this

improvement was strongly valve-dependent. However, once the implemented iterative algorithm was applied, the detected discrepancies were found to be coherent and comparable if compared with findings reported in the modern literature[24,25].

Nevertheless, limitations have to be declared as ideas for further improvements. Firstly, the input 3D ultrasound data unavoidably introduced some bias into the error computation that have to be well analysed and validated, that is to say that a large cohort of patients should be considered. Moreover, as a more technical matter, it is also worth mentioning that we only focused on chordae which insert into the rough and commissural regions of the leaflets; structural chordae should be accounted for in order to have a more comprehensive topological optimization of the sub-valvular apparatus.

Concluding, the goal of the herein proposed strategy was to provide a tool to gain insight into patient-specific mitral valve computational modelling, complemented with a functionally equivalent tuned sub-valvular apparatus, which might be used for a preparatory refinement step towards a deepened valvular mechanics assessment through a finite element (FE) analysis, as well as for predictively simulating different surgical treatments[5] exploiting the profitable trade-off accuracy vs. computational cost provided by MSM approach.

3.5 Bibliography

1. Khalighi, A. H. *et al.* Development of a Functionally Equivalent Model of the Mitral Valve Chordae Tendineae Through Topology Optimization. *Ann. Biomed. Eng.* (2018). doi:10.1007/s10439-018-02122-y
2. Coutinho, G. F. & Antunes, M. J. Mitral valve repair for degenerative mitral valve disease: surgical approach, patient selection and long-term outcomes. *Heart* **103,** 1663–1669 (2017).
3. Nappi, F., Avatar Singh, S. S., Santana, O. & Mihos, C. G. Functional mitral regurgitation: an overview for surgical management framework. *J. Thorac. Dis.* **10,** 4540–4555 (2018).
4. Pappalardo, O. A. NOVEL STRATEGIES FOR THE MORPHOLOGICAL AND BIOMECHANICAL ANALYSIS OF THE CARDIAC VALVES BASED ON VOLUMETRIC CLINICAL IMAGES. (2018). at <https://iris.univr.it/handle/11562/977217#.W-6fM-hKjb0>
5. Pappalardo, O. A. *et al.* Mass-spring models for the simulation of mitral valve function: Looking for a trade-off between reliability and time-efficiency. *Med. Eng. Phys.* **47,** 93–104 (2017).
6. Khalighi, A. H. *et al.* Mitral Valve Chordae Tendineae: Topological and Geometrical Characterization. *Ann. Biomed. Eng.* **45,** 378–393 (2017).
7. Gelder, A. Van. Approximate Simulation of Elastic Membranes by Triangulated Spring Meshes. *J. Graph. Tools* **3,** 21–41 (1998).
8. May-Newman, K. & Yin, F. C. A constitutive law for mitral valve tissue. *J. Biomech. Eng.* **120,** 38–47 (1998).
9. Kunzelman, K. S. & Cochran, R. P. Mechanical properties of basal and marginal mitral valve chordae tendineae. *ASAIO Trans.* **36,** M405-8 (1990).
10. Hammer, P. E., Del Nido, P. J. & Howe, R. D. Anisotropic mass-spring method accurately simulates mitral valve closure from image-based models. in *Lecture Notes in Computer Science (including subseries Lecture Notes in Artificial Intelligence and Lecture Notes in Bioinformatics)* (2011). doi:10.1007/978-3-642-21028-0_29
11. Votta, E. *et al.* Mitral valve finite-element modelling from ultrasound data: a pilot study for a new approach to understand mitral function and clinical scenarios. *Philos. Trans. R. Soc. A Math. Phys. Eng. Sci.* **366,** 3411–3434 (2008).
12. Votta, E. *et al.* Toward patient-specific simulations of cardiac valves: state-of-the-art and future directions. *J. Biomech.* **46,** 217–28 (2013).

13. Rim, Y., Choi, A., McPherson, D. D. & Kim, H. Personalized computational modeling of mitral valve prolapse: Virtual leaflet resection. *PLoS One* (2015). doi:10.1371/journal.pone.0130906
14. Mansi, T. *et al.* An integrated framework for finite-element modeling of mitral valve biomechanics from medical images: Application to MitralClip intervention planning. *Med. Image Anal.* **16,** 1330–1346 (2012).
15. Wong, V. M. *et al.* The Effect of Mitral Annuloplasty Shape in Ischemic Mitral Regurgitation: A Finite Element Simulation. *Ann. Thorac. Surg.* **93,** 776–782 (2012).
16. Tenenholtz, N. A. *et al.* in *Functional imaging and modeling of the heart : ... International Workshop, FIMH ..., proceedings. FIMH* **7945,** 106–113 (2013).
17. Skornitzke, S. *et al.* Mass-spring systems for simulating mitral valve repair using 3D ultrasound images. *Comput. Med. Imaging Graph.* **45,** 26–35 (2015).
18. Stevanella, M. *et al.* Mitral leaflet modeling: Importance of in vivo shape and material properties. *J. Biomech.* **44,** 2229–2235 (2011).
19. Kvitting, J.-P. E. *et al.* Anterior Mitral Leaflet Curvature During the Cardiac Cycle in the Normal Ovine Heart. *Circulation* **122,** 1683–1689 (2010).
20. Prot, V., Skallerud, B. & Holzapfel, G. A. Transversely isotropic membrane shells with application to mitral valve mechanics. Constitutive modelling and finite element implementation. *Int. J. Numer. Methods Eng.* **71,** 987–1008 (2007).
21. Swanson, J. C. *et al.* Vagal nerve stimulation reduces anterior mitral valve leaflet stiffness in the beating ovine heart. *J. Biomech.* **45,** 2007–2013 (2012).
22. Swanson, J. C. *et al.* Multiple mitral leaflet contractile systems in the beating heart. *J. Biomech.* **44,** 1328–1333 (2011).
23. Krishnamurthy, G. *et al.* Material properties of the ovine mitral valve anterior leaflet in vivo from inverse finite element analysis. *Am. J. Physiol. Circ. Physiol.* **295,** H1141–H1149 (2008).
24. Zhang, F. *et al.* Towards patient-specific modeling of mitral valve repair: 3D transesophageal echocardiography-derived parameter estimation. *Med. Image Anal.* (2017). doi:10.1016/j.media.2016.09.006
25. Grbic, S. *et al.* Personalized mitral valve closure computation and uncertainty analysis from 3D echocardiography. *Med. Image Anal.* (2017). doi:10.1016/j.media.2016.03.011
26. Ayoub, S., Tsai, K. C., Khalighi, A. H. & Sacks, M. S. The Three-Dimensional

Microenvironment of the Mitral Valve: Insights into the Effects of Physiological Loads. *Cell. Mol. Bioeng.* **11,** 291–306 (2018).

27. Bloodworth, C. H. *et al.* Ex Vivo Methods for Informing Computational Models of the Mitral Valve. *Ann. Biomed. Eng.* **45,** 496–507 (2017).
28. Drach, A., Khalighi, A. H. & Sacks, M. S. A comprehensive pipeline for multi-resolution modeling of the mitral valve: Validation, computational efficiency, and predictive capability. *Int. j. numer. method. biomed. eng.* **34,** e2921 (2018).

In vivo 3D echocardiography exploitation for computational analysis in LVAD-treated patients

This chapter was based on:

Matteo Selmi[1,2], Wei-Che Chiu[3], Venkat Keshav Chivukula[4], Giulio Melisurgo[5], Jennifer Ann Beckman[6], Claudius Mahr[6], Alberto Aliseda[4], Emiliano Votta[1], Alberto Redaelli[1], Marvin J Slepian[3,7], Danny Bluestein[3], Federico Pappalardo[5,8,9] and Filippo Consolo[1,8,9]. "*Blood damage in Left Ventricular Assist Devices: Pump thrombosis or system thrombosis?"* The International Journal of Artificial Organ, 2018.

[1] Department of Electronics, Information and Bioengineering, Politecnico di Milano, Italy

[2] Division of Cardiac Surgery, Department of Surgery, Università degli Studi di Verona, Italy

[3] Department of Biomedical Engineering, Stony Brook University, Stony Brook, NY, USA

[4] Department of Mechanical Engineering, University of Washington, Seattle, WA, USA

[5] Anesthesia and Cardiothoracic Intensive Care, San Raffaele Scientific Institute, Milano, Italy

[6] Division of Cardiology, University of Washington, Seattle, WA, USA

[7] Departments of Medicine and Biomedical Engineering, The University of Arizona, Tucson, AZ, USA

[8] Advanced Heart Failure and Mechanical Circulatory Support Program, San Raffaele Scientific Institute, Milano, Italy

[9] Università Vita-Salute San Raffaele, Milano, Italy

4.1 Introduction

Heart failure (HF) is a severe pathological chronic condition where the heart is unable to pump enough blood to support the needs of other organs in the body. Approximately half of the patients with HF is affected by dilated cardiomyopathy (DCM), a syndrome characterized by enlargement, wall hypokinesis, and reduction of the overall contractility (typically < 40%) of left or both ventricles[1–3], which acquire a pathological-dilated nearly spherical shape[4]. Patients with advanced and/or end-stage HF have limited treatment options: indeed, only a small number of patients may qualify for cardiac transplantation. Otherwise, such these patients may undergo implantation of a left ventricular assist device (LVAD) to improve functional capacity, quality of life, and to prolong survival as well, even supplementing the need for heart transplant[5–7]. Continuous axial-flow LVAD is designed to minimize the operative risk, improve durability, and lower the risk of device-related adverse events, providing effective hemodynamic support for weeks to years[8–10].

While many factors depend on successful implantation and outcome of LVADs, echocardiography remains an integral part and is vital to the success of this process[11]. Currently, echocardiography is the most important imaging modality for LVAD pre-implantation assessment and post-implantation follow-up[12], with 3D TEE being also used intraoperatively to aid optimal inflow cannula placement in the left ventricle, according to ASE guidelines[13].

However, despite the widespread clinical use of LVADs, there are several complications associated with the therapy, the most relevant being those associated with the device itself. Thus, for an optimal long-term use of LVAD, patient-specific computational fluid-dynamic (CFD) models might be exploited as they can provide additional information with respect to the in vivo imaging, potentially predicting either blood stagnation within the LV or abnormal LV wall stresses induced by altered flow conditions. To this aim, 3D ultrasound in vivo imaging is the only available technique in this scenario allowing for implementation of numerical model able to mimic realistic anatomical morphology and reliable functionality of the district.

Several studies in literature[14–17] investigated the disturbed hemodynamics and the thrombogenic potential of the LV in presence of LVAD through CFD approach, which provides detailed characterization of the ventricular flow, such as velocity profiles, shear stress distributions (wall shear stresses, WSS), and re-circulation patterns. The most crucial element that can alter the physiological hemodynamics of the LV is the inflow cannula, whose geometry, insertion depth, insertion angle and position may modify the intraventricular flow fields.
However, two weak points, affecting most of the examined literature, were identified. First of all, when modelling ventricular wall motion, only myofibers contraction was included, without considering the torsional contribution, thus preventing to achieve realistic simulations of cardiac dynamics[18,19]. Secondly, when characterizing LV-LVAD hemodynamics, the LV was generally considered as a rigid and static body, neglecting any residual contractility[15,16]. So, in order to overcome some of the limitations of current literature studies, the present work was focused on the implementation of a CFD model accounting for i) the realistic description of both the DCM-affected LV anatomy and the inflow cannula position and orientation; ii) both the LV contraction and torsion as boundary conditions, accomplished by assembling a set of mathematical equations to formulate and model LV wall motion. The model had the general claim to systematically analyse the contribution of LV residual contractility, quantified through the LV ejection fraction (EF%), and LVAD inflow cannula implantation configurations on the LV hemodynamics, gaining insight toward a parametric-like investigation rather than being predictive for the specific examined clinical case.

4.2 Pathological and LVAD-implanted LV geometries

The geometrical model of the pathological patient-specific LV was obtained as a combination of the LV anatomy in the pathological scenario and the LVAD inflow cannula, whose position corresponded with the surgical reality. In detail, 3D Trans-Thoracic Echocardiography (3DTTE) images were collected through a Vivid E9 ultrasound system (GE Healthcare, Little Chalfont,

Buckinghamshire, UK) with ECG gating over 4 consecutive cardiac cycles (4 frames/cycle), performed on a candidate to LVAD implantation, in collaboration with the medical staff of San Raffaele Scientific Institute and the research staff of San Raffaele University. A single patient referred to HeartMate III LVAD (Thoratec Corp, Pleasanton, CA) implantation was considered and two full-volume acquisitions were performed: i) before implantation (*pre*) and ii) less than 1-month post-implantation (*post*). In the former, data were acquired positioning the probe as for acquiring a LV-focused apical 4-chamber view, trying to encompass the entire LV geometry in the ultrasound field of view. In the latter, the probe was positioned as for acquiring a long-axis parasternal 3-chambers projection, the usual 4-chamber view being unfeasible owing to the presence of metallic device armamentarium which may cause critical LVAD-related artifacts in the images.

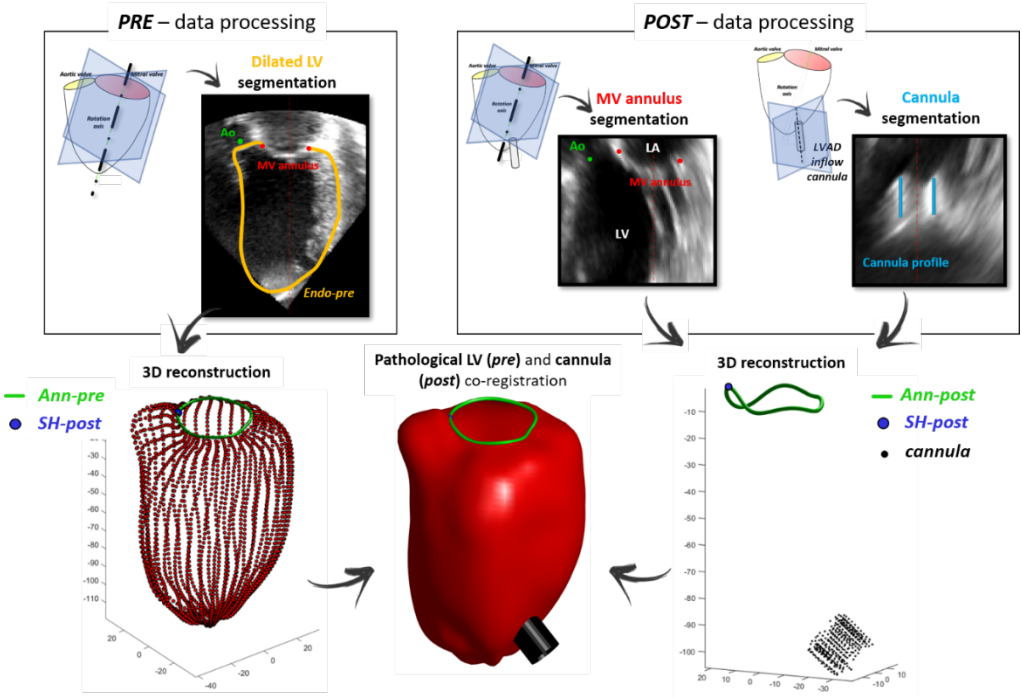

Figure 4-1 Schematics of the procedure for co-registration of the cannula onto the pre-implant LV endocardium volume, allowing reconstruction of the patient-specific 3D model of the LV+LVAD inflow cannula.

Subsequently, an in-house reconstruction strategy, *ad-hoc* developed for this specific purpose within the biomechanics group at Politecnico di Milano, was exploited. 3DTTE data were navigated using the open source software platform

3D Slicer[20] and then offline processed through in-house software developed in MATLAB (The MathWorks Inc., Natick, MA, USA). On the *pre*-dataset, the axis passing through the center of the mitral valve (MV) orifice and the ventricular apex was identified. Then, 18 long-axis planes evenly rotated around this axis were generated by spatial interpolation of the volumetric data acquired. On each plane, the MV annulus and the endocardium were manually traced; thus, the 3D annular profile (*Ann-pre*) and of 3D surface of the endocardium (*Endo-pre*) were subsequently reconstructed by transforming the in-plane coordinates of the traced points in the 3D space. *Ann-pre* was obtained as a point-cloud, whose coordinates were filtered through Fourier functions; *Endo-pre* was obtained as a triangulated surface, and noise effects were ruled out through Taubin smoothing[21]. On the *post* dataset, the same procedure was applied to reconstruct the 3D profile of the annulus (*Ann-post*). Also, the axis of the LVAD inflow cannula was identified and 18 planes evenly rotated around the cannula axis were defined; on each plane, the cannula was manually traced, and its 3D contour was then reconstructed in the same reference frame of *Ann-post*. The point cloud of the cannula profile was rigidly co-registered onto *Endo-pre*; the associated roto-translation was identified as the spatial transformation that makes *Ann-post* matching with *Ann-pre* both in position and orientation. In particular, it is imposed that i) the centroid of *Ann-post* would match the centroid of *Ann-pre*, the least-square fitting plane of *Ann-post* would have the same normal as compared to least-square fitting plane of *Ann-pre*, and iii) the saddle-horn (SH, namely, the peak of the anterior tract of the MV annular profile) -*post* would match *SH-pre*.

A STL file, that is a raw, unstructured triangulated surface, of the LV alone and the cannulated LV, in the end-diastolic configuration, were provided as the results of this reconstruction process.

Although collected ultrasound data were not suitable for a comprehensive assessment, a preliminary morphological evaluation of the LV model was carried out. Firstly, LV height (H_{LV}), as the distance between the MV centroid and LV apex, and LV maximum diameter (D_{LV}), as the maximum segment

perpendicular to H_{LV}, were detected directly on an image plane (RadiAnt, Medixant, Poznan, Poland) resembling the antero-posterior long-axis plane (Figure 4-2 b). A good agreement was found, with reconstruction-based values equal to 107.97 mm for H_{LV} and 78.7 mm for D_{LV} (Figure 4-2 a), with a slight overestimation with respect to image-derived measures (+1.09% and +2.35%, respectively). Since performed on 2D plane, these measurements were not so significative; nonetheless, being the only available ones, they were considered for the sake of an indicative and exemplificative comparison with respect to the reconstructed LV model.

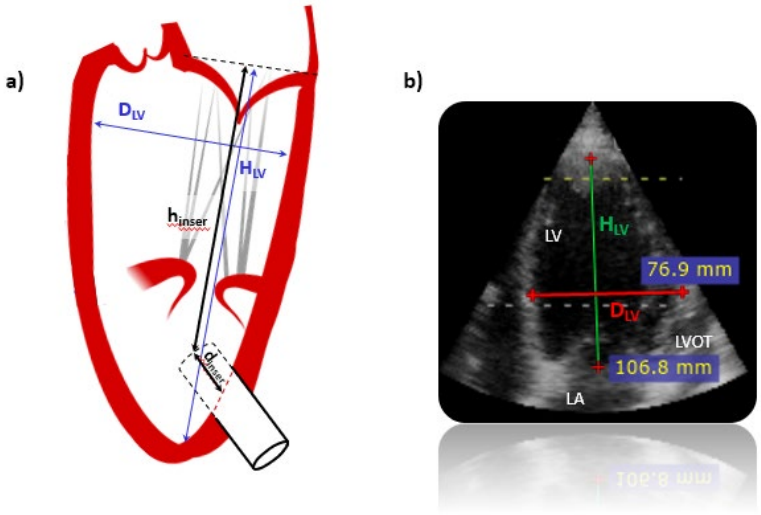

Figure 4-2 a) LV-LVAD scheme with computed geometric variables (H_{LV}, D_{LV}, h_{ins}, d_{ins}, as defined in the text); b) LV 2D long-axis plane exploited for image-based measurements.

Moreover, the STL model coming from the segmentation process was exploited even to gain insight concerning unknown geometrical features of LV cannulation, crucial for the fluid domain implementation. In detail, as depicted in Figure 4-2 a, insertion height (h_{ins} = 87.38 mm), as the distance between the MV centroid and the cannula tip centroid, and insertion depth (d_{ins} = 1.63 mm), as the lower distance between this centroid and the LV endocardial surface, were computed.

Pre-implant pathological model

The STL file of the LV geometry was imported and processed in the 3D CAD Software SpaceClaim (ANSYS 18.1). A shell of the LV was obtained from the

STL thanks to a reverse engineering approach, employing the Skin Surface tool. This tool allowed to create patches, adherent to the surface of the LV and following its curvature, through an automatic surface fitting along triangular facets. Furthermore, to guarantee a fully developed flow during the simulations, a synthetic/paradigmatic portion of the atrium chamber and of the proximal aorta were created (Figure 4-3). The left atrium (LA) was modelled as a circular truncated cone, whose interior profile matched that of the mitral valve of the LV model, while the major basis was a circle (radius 27 mm), sketched about 10 mm above the mitral plane. The aorta (Ao) was approximated with a cylinder (with 12 mm in radius and 14 mm of length), with the interior profile matching the aortic valve orifice in the 3DTTE-derived LV model.

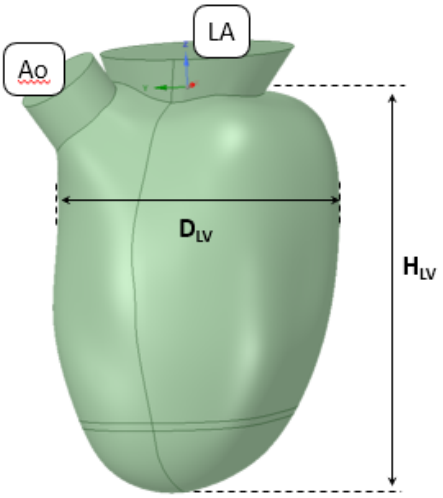

Figure 4-3 *Pre-implant* geometry. LA and Ao indicate the left atrium and aortic root domains, respectively.

Post-implant model A

The post-implantation (*post*) STL file, reconstructed by means of the previously described co-registration algorithm, provided the exact **patient-specific insertion positioning** of the LVAD inflow cannula in the LV myocardial wall.

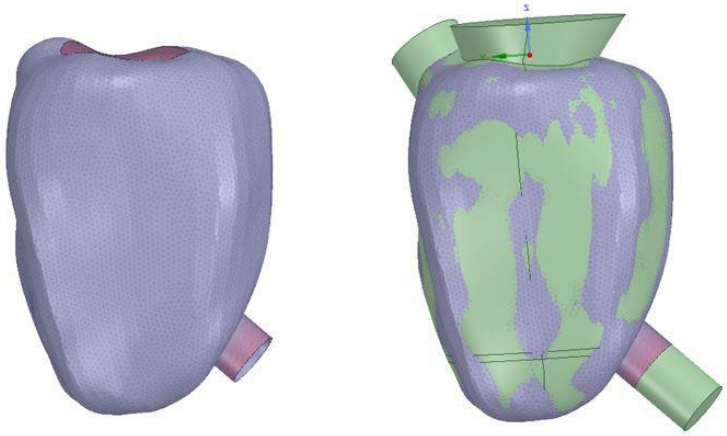

Figure 4-4 Left: *post* STL file as obtained from the segmentation process. Right: superimposition of *pre-implant* model geometry and *post* STL file: the designed and the STL cannula profiles correctly match.

Figure 4-4 shows the adopted strategy to model the LV-LVAD inflow cannula *post*-implant geometry: the *pre*-implant fluid domain and *post*-implantation STL file were overlapped in SpaceClaim (ANSYS 18.1), in order to accurately co-register the cannula insertion region from the STL file to the *pre*-implant LV body. For the same reason explaining the LA and Ao domains, the extension of the cannula length up to 50 mm is noteworthy, its diameter being set equal to 18 mm. Subsequently, an automatic shared topology algorithm was exploited to combine the LV and cannula fluid domains, to guarantee mesh continuity.

Post-implant model B

The third fluid dynamic domain was almost like the previous one, but resembling the typical surgical approach followed for the cannula insertion. Indeed, herein, the cannula tip was inserted directly into the LV apex (**apical positioning**), so that the inflow cannula longitudinal axis intersects the LV apex and the centre of the mitral valve orifice. Thus, the final fluid model was obtained by means of the same last step as for the post-implant model A (Figure 4-5).

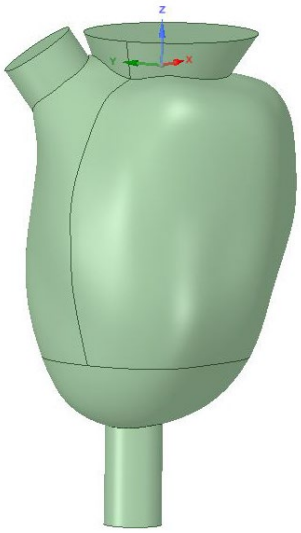

Figure 4-5 *Post-implant* B geometry (LV-LVAD), with the cannula in the apical configuration.

4.3 Generation of the numerical grid

4.3.1 Mesh sensitivity analysis

A mesh sensitivity analysis was performed, in order to identify the proper number of grid elements to guarantee an accurate solution as well as a reasonable computational time. The mesh independence study was carried out on the *pre-implant* model only, being the LV geometry shared by all the implemented models. Six tetrahedral meshes were considered, ranging from a coarse mesh of ~10^5 elements to a finer mesh of ~$6*10^5$ (Table 1).

Table 1 Different mesh configurations exploited for the sensitivity analysis. Neatly, table rows indicate total number of mesh elements, minimum allowed edge size, maximum face size, maximum tetrahedrons size and the growth rate of the mesh, as the increase in element edge length with each succeeding layer of elements.

	Mesh 1	**Mesh 2**	**Mesh 3**	**Mesh 4**	**Mesh 5**	**Mesh 6**
N°. elements	102803	205174	302529	405941	503918	606315
Min size	10^{-4}	10^{-4}	10^{-4}	10^{-4}	10^{-4}	10^{-4}
Max face size	$3.4*10^{-3}$	$2.7*10^{-3}$	$2.37*10^{-3}$	$2.15*10^{-3}$	$2.10*10^{-3}$	$1.88*10^{-3}$
Max tetr size	$3.4*10^{-3}$	$2.7*10^{-3}$	$2.37*10^{-3}$	$2.15*10^{-3}$	$2.10*10^{-3}$	$1.88*10^{-3}$
Growth rate	1.2	1.2	1.2	1.2	1.2	1.2

In order to evaluate the solution discrepancy between meshes, velocity magnitude temporal trends averaged in three pre-defined regions close to the ventricular apex (Figure 4-6) were extracted, the apical zone being the one of interest in this study because potentially involved in flow stagnation phenomena.

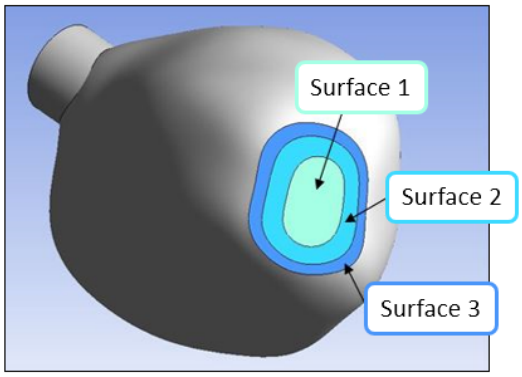

Figure 4-6 Pre-defined apical regions.

Table 2 MPEs between subsequent meshes, computed for each surface.

	Surf 1	**Surf 2**	**Surf 3**
MPE_{1-2}	6.88%	4.03%	3.69%
MPE_{2-3}	2.08%	2.26%	2.21%
MPE_{3-4}	1.95%	2.29%	1.58%
MPE_{4-5}	1.40%	1.75%	1.26%
MPE_{5-6}	1.39%	0.74%	1.61%

Cell centre velocity magnitude values were extracted and stored in ASCII files at each time step (0.001 s in all the simulations), for each grid element of the three zones. Exploiting a MATLAB script, average velocity magnitude trends were computed, one for each of the three regions; this procedure was repeated for all the meshes. Then, considering one region at time, at each time step, the percentage error between average velocity magnitude values, for two subsequent meshes, was determined. After that, the mean percentage error (MPE) was computed, so that three MPE were defined per mesh, one for each apical region. We imposed that the proper mesh must guarantee, for each of the considered zones, a value of MPE lower than 2%. The mesh that fulfilled this criterion was *Mesh 4* (Table 2).

4.3.2 Mesh generation

According to the sensitivity analysis, a homogeneous grid all over the whole domain was obtained, consisting in 405941 tetrahedrons and 71772 nodes for *pre-implant* model (Figure 4-7 a). The same mesh refinement parameter, as listed in Table 1, were adopted also for both the *post-implant* models, obtaining a grid of 414028 tetrahedrons and 73428 nodes for model A (Figure 4-7 b) and a grid of 412824 elements and 73206 nodes for model B (Figure 4-7 c).

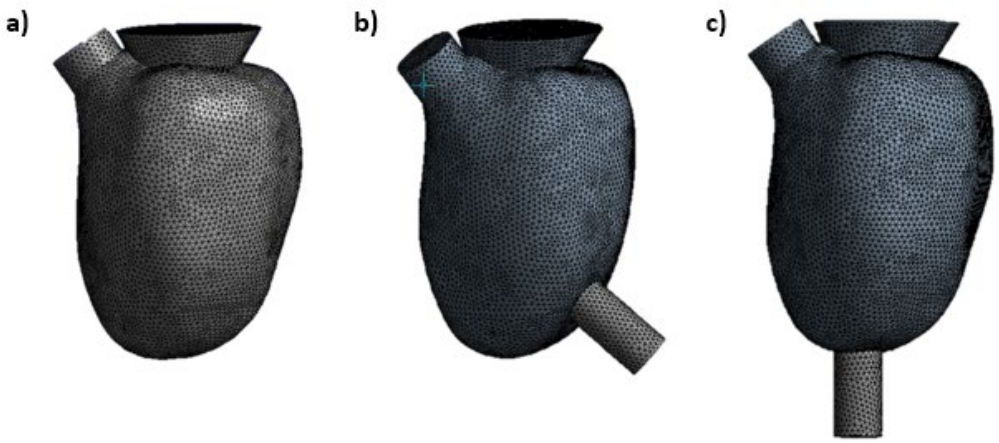

Figure 4-7 Obtained numerical grids for (a) *pre-implant*, (b) *post-implant* A and (c) *post-implant* B models, respectively.

4.4 Grid motion

Since ultrasound volumetric data were highly low resolute in time, LV wall motion was defined through a set of mathematical equations, according to a geometry-prescribed approach, so that the movement of the LV wall was imposed as a boundary condition of the fluid domain. In detail, to reproduce the peculiar contraction/dilation and twist/untwist movement (in systole/diastole, respectively), the mesh motion functionality of ANSYS Fluent 18.1 was exploited, by compiling and loading a specifically set up User-Defined Function (UDF). The C-coded UDFs herein exploited were generated by means of a MATLAB code (The MathWorks Inc., Natick, MA, USA) previously developed within the Biomechanics Group in Politecnico di Milano[22], *ad-hoc* adapted to current geometries and completed with a new feature to allow ventricular motion of the LV-LVAD models.

Pre-implant model

The LV wall motion was modelled accounting for that, during the cardiac cycle, the valvular plane and the nearby ventricular region are fixed, or at least almost fully constrained. As a consequence, only the LV grid nodes below plane A, as depicted in the Figure 4-8, underwent UDF displacement.

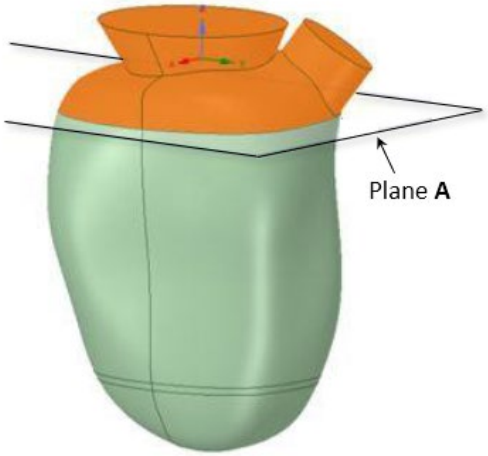

Figure 4-8 Visualisation of the fixed (orange) and moving (green) regions of the LV. The cut plane is orthogonal to the z axis and passes through the contact point (black arrow) between the LV wall and the aorta.

The **contraction/dilation** movement was obtained by assigning to each node a displacement $u_{\perp}(z,t)$, normal to the ventricular wall and expressed as (eq.1):

$$u_{\perp}(z,t) = \pm k \cdot \delta(z) \cdot f(t) \cdot \sigma(z) \cdot g(t) \qquad (1)$$

where the + refers to the systolic phase of the cardiac cycle, while the - to the diastolic one. The paragraphs below are to be intended as a detailed explanation of each term of (1).

$\delta(z)$ is a 15th order polynomial that was used to assign the proper displacement to the mesh nodes as a function of the z coordinate, namely the axial direction of the ventricle. This function was calculated under the hypothesis of homothetic contraction of the LV. The $\delta(z)$ function was determined for each simulation setting, following a standardized procedure. It was obtained by interpolating the elements of a distances vector, these distances being computed between sampled points of two semi-ellipsoids, adopted to describe ventricular profile in the end-systolic and the end-diastolic configuration, respectively.

As first step of the standardized procedure, the moving portion of the LV (in the end-diastolic configuration, starting point of all simulations) was modelled as a half prolate ellipsoid, whose geometrical parameters are reported in Figure 4-9.

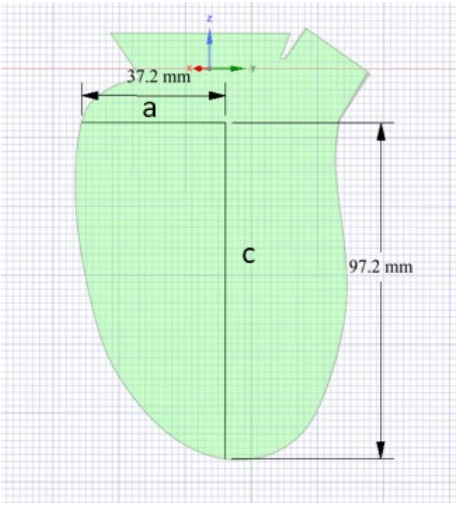

Figure 4-9 LV semi-major (*c*) and semi-minor axes (*a*) are 97.2 mm and 37.2 mm long, respectively.

The LV long axis (semi-major axis of the ellipsoid) was defined as the distance among the LV apex and a plane passing through the contact point between the LV wall and the aorta, closest to the apex. So, the end-diastolic volume, approximated with a semi-ellipsoid, of the moving zone was computed by the following equation (eq. 2):

$$V_{end-diastole} = \frac{{}^{4}/_{3}\,\pi \cdot a \cdot b \cdot c}{2} \tag{2}$$

where *a* and *b* are the two semi-minor axes in the xy plane (LV short-axis cross sectional plane), considered as equal, and *c* is the above-defined semi-major axis (Figure 4-9).

Depending on the desired residual EF% (variable used to assign different degrees of LV residual contractility), a volume variation was applied to the end-diastolic ellipsoid, computed as follows (eq. 3):

$$\Delta V = V_{end-diastole} - V_{end-systole} = EF\% \cdot V_{end-diastole} \tag{3}$$

This equation allowed to determine the volume of the semi-ellipsoid approximating the end-systolic configuration. Thus, it was possible to compute the aforementioned distances between corresponding sampled points on the two surfaces of the two semi-ellipsoid. Finally, $\delta(z)$ function was applied to the mesh nodes to shrink or expand the ventricle, depending on the cardiac phase being

simulated, until a complete overlapping of the starting semi-ellipsoid (end-diastolic) and the calculated one (end-systolic) was achieved.
Given that, in the two phases of the cardiac cycle, the ΔV (LV ejection volume) obtained in each simulation was generally lower than the expected one, making it necessary to introduce a corrective factor. The factor k ensured to obtain the desired ejection volume and was identified thanks to a trial and error process.

$f(t)$ is a cosine Fourier series in systole, reproducing the physiological ejection flow rate trend in time; differently, during diastole, it's a combination of sine and cosine Fourier series to model the physiological LV filling flow rate pattern over time (Figure 4-10).

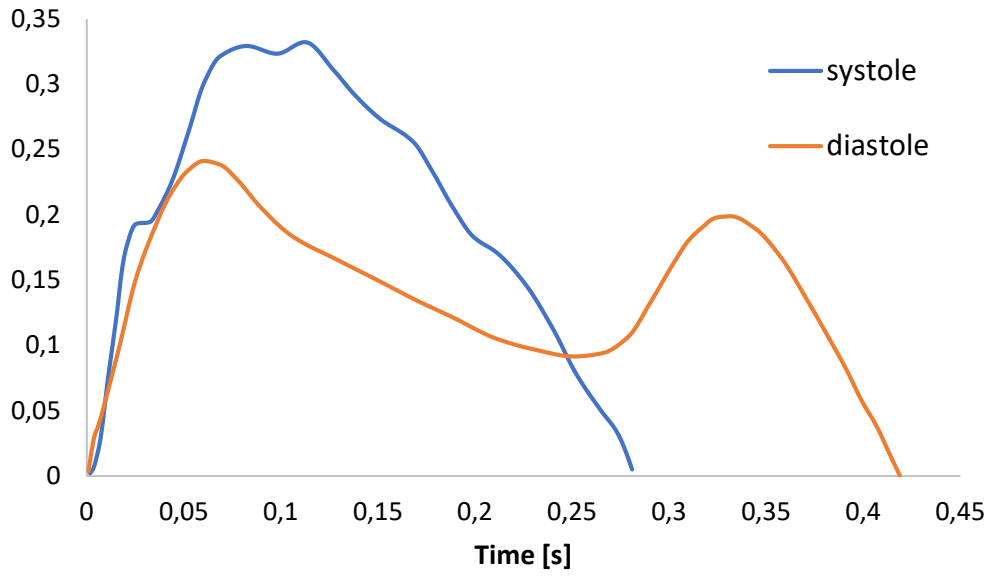

Figure 4-10 Time function f(t) during systole (blue line) and diastole (orange line).

$g(t)$ is a parabolic function, which, multiplying $f(t)$, is intended to make the mass flow rate through the mitral valve to follow the physiological diastolic trend, as depicted in orange in Figure 4-10, avoiding a potential overestimation in the second peak (eq. 4).

$$g(t) = \begin{cases} 5.7\left(\left(\frac{1}{k}\right)^{\frac{1}{8}} - 1\right)t^2 + 1 & diastole \\ 12.6\left(\left(\frac{1}{k}\right)^{\frac{1}{8}} - 1\right)(t^2 - 0.564t) + \left(\frac{1}{k}\right)^{\frac{1}{8}} & systole \end{cases} \quad (4)$$

As earlier mentioned, when applying the mesh motion, only the ventricular wall moved while the valvular plane was standing still. The function $\sigma(z)$ guarantees a smooth link between the still and the moving LV regions. It is equal to i) 0 when the z coordinate is negative, namely when the nodes belongs to the fixed geometrical domains; ii) 1 when the z coordinate is greater than 20 mm in the examined LV models, approximately below 1/5 of the overall vertical extension of the ventricle; iii) otherwise is expressed by a parabolic function, as following (eq. 5):

$$\sigma(z) = \begin{cases} 0 & if\ z \leq 0\ m \\ 8.14\sqrt{z + 0.0004} - 0.1628 & if\ 0 < z \leq 0.02\ m \\ 1 & if\ z > 0.02\ m \end{cases} \quad (5)$$

For what concerns the torsional movement of LV wall (**twist/untwist**) it is well known that during the ejection phase the ventricular apex rotates in a counter clockwise direction while the upper portion is twisted clockwise, whereas the opposite in diastole[23]. Thus, to this aim, a tangential movement to be assigned to each mesh node was implemented through the following equation (eq. 6):

$$u_{\parallel}(z,t) = \pm\ 0.0174 \cdot 0.56 \cdot R \cdot \delta_{rot}(z) \cdot f_{rot}(t) \cdot \sigma(z) \quad (6)$$

where, again, + refers to the systolic phase of the cardiac cycle, - to the diastolic one. The systolic twist, which resembles the wringing of a towel, and the subsequent recoil that occurs in diastole, were realized maintaining the base fixed and linearly increasing the rotation along the ventricular axis, moving towards the apex. Below a detailed description of (6).

R is the radial coordinate of each node, referred to as the radius of the circumference approximating ventricular semi-ellipsoid cross-section in the xy plane.

$\delta_{rot}(z)$ is a linear function that assign the maximum rotation to the ventricular apex, whose coordinate is referred as to z_{max}, and null rotation to the LV base (z_{min}) (eq. 7):

$$\delta_{rot}(z) = \frac{z - z_{min}}{z_{max} - z_{min}} \tag{7}$$

As in the contraction/dilation function, $f_{rot}(t)$ trend depends on the considered cardiac cycle phase (Figure 4-11 *left*, black line between the dashed lines for systole, and elsewhere for diastole). However, for both systole and diastole it is expressed as a sine and cosine Fourier series interpolating the difference between the apical rotational rate and the basal one.

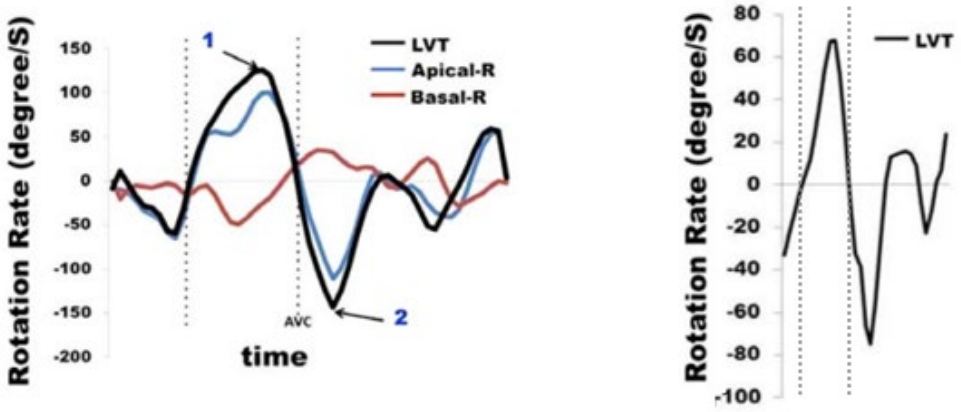

Figure 4-11 Temporal sequence of left ventricular twist (LVT). Left: LV rotational rate curves for LV base (red) and apex (blue) for a healthy subject; AVC indicates aortic valve closure. Right: LVT for DCM affected patient with reduced ejection fraction. Black dashed lines delimit systolic phase.

The 0.56 correction factor in (6) was introduced to take into account the reduced twisting capacity of the pathologically dilated ventricle. According to Omar et al.[23], patients affected by dilated cardiomyopathy and reduced ejection fraction show lower values of peak rotational rate, if compared to the physiological ones,

because of the twist mechanism weakening or depletion. In dilated cardiomyopathy, twist mechanics is blunted because of the increased LV sphericity, which leads to widening of the apex and loss of the oblique architecture of the apical fibres. Actually, for these subjects, the peak rotational rate is found to be equal to 70 °/s (Figure 4-11 *right*), while healthy patients exhibit a value of about 125 °/s (Figure 4-11 *left*, arrow 1).

$\sigma(z)$ is the same linking function previously described for the contraction/dilation movement, while the constant 0.0174 is the converting factor to transform °/s to rad/s.

The grid motion implementation ended up with the $u_{\perp}$ and $u_{\parallel}$ projection in the Cartesian reference system, so to obtain the three displacement components u_x, u_y e u_z for each node of the mesh. This affine transformation was identified by means of ϑ and φ angles, defined as follow (eqs. 9):

$$\vartheta = arctg\frac{z - z_p}{\sqrt{x^2 + y^2}} \qquad \varphi = arctg\frac{y}{x} \tag{8}$$

where x, y and z are the spatial coordinates of each node in the grid, while z_p is a linear function of the z coordinate (eq. 9), which sets the z coordinate of each node equal to the z coordinate of the intersection point between the z axis and the perpendicular to the ventricular semi-ellipsoid, passing through that specific node.

$$z = 0.8535 \cdot z \tag{9}$$

Thus, the equations' system that allowed for cartesian displacements is the following (eqs. 10-12):

$$u_x = -u_{\perp} \cdot cos\vartheta \cdot cos\varphi - u_{\parallel} \cdot sin\varphi \tag{10}$$

$$u_y = -u_{\perp} \cdot cos\vartheta \cdot sin\varphi + u_{\parallel} \cdot \cos\varphi \tag{11}$$

$$u_z = -u_{\perp} \cdot sin\vartheta \tag{12}$$

The so far described UDF worked only on ventricular geometries whose reference frame had a z axis pointing towards the ventricular apex. So, in order to apply the implemented function to the considered pathological patient-specific LV geometry, it was necessary to transform the absolute nodal coordinates to local ones, that is in a local reference frame with the z axis towards the apex and centred in the mitral valve. The transformation of the reference system was obtained through three rotations and a final shift, thus requiring the definition of 3 rotational matrices. The first two rotations were intended to allow the local x axis passing through the apical node (x_{apex}, y_{apex}, z_{apex}), by α (eq. 13) and β (eq. 14) angles, respectively:

$$\alpha = \begin{cases} arccos \dfrac{x_{apex}}{cos\beta \sqrt{x_{apex}^2 + y_{apex}^2 + z_{apex}^2}}, & if\ y_{apex} > 0 \\ 2\pi - arccos \dfrac{x_{apex}}{cos\beta \sqrt{x_{apex}^2 + y_{apex}^2 + z_{apex}^2}}, & if\ y_{apex} < 0 \end{cases} \tag{13}$$

$$\beta = arcsin \frac{z_{apex}}{\sqrt{x_{apex}^2 + y_{apex}^2 + z_{apex}^2}} \tag{14}$$

The third one was an additional simple 90° rotation applied to make the local z axis to pass through the apex. Finally, a shift of the local reference frame origin was performed, to place the z_{local} axis origin at the beginning of LV moving portion, coherently with the previously described kinematic boundary condition at the valvular plane (Figure 4-8).

To summarize, the following equation resumes the sequence of transformations to pass from global to local coordinate system (eq. 15):

$$\begin{bmatrix} x_{local} \\ y_{local} \\ z_{local} \end{bmatrix} = [R_{90°}][R_\beta][R_\alpha] \begin{bmatrix} x_{global} \\ y_{global} \\ z_{global} \end{bmatrix} + \begin{bmatrix} 0 \\ 0 \\ z_{shift} \end{bmatrix} \tag{15}$$

Finally, inversely applying the transformation in (15), the displacement vectors were computed, making possible to update the global nodal coordinates at each time step.

The result of these mesh motion algorithm is provided in Figure 4-12, specifically for *pre-implant* model with a residual EF% equal to 15%.

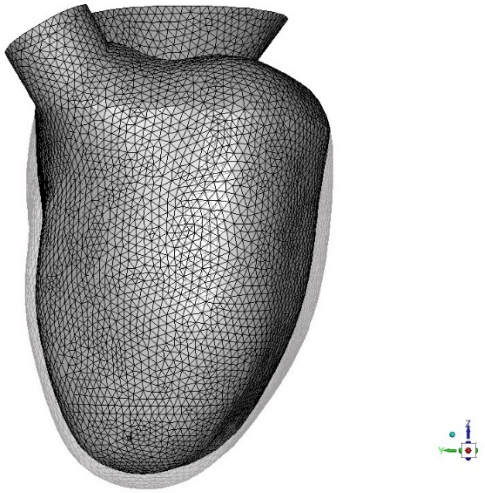

Figure 4-12 Superimposition of the end-systolic and end-diastolic configurations for the patient-specific *pre-implant* model; image provided for 15% residual EF.

Post-implant models

For what concerns the *post* LVAD-implant models, two new UDFs were developed to also account for the cannula motion. Again, for the same reason, the affine transformation from absolute to local coordinates was accomplished, as previously described for the *pre-implant* model. Furthermore, since the cannula was assumed to only translate in the longitudinal direction (z-axis), the portion of the LV wall at the interface with it should move in the same way to avoid unwanted deformations of the cannula itself. Hence, the LV was subdivided in three zones: *i)* the valvular plane, standing still, *ii)* the central region, whose nodes translate and rotate, and *iii)* the apical region, only translating along the z-axis, as the inflow cannula.

Given the fact that the apex did not contract in the x and y directions, it was necessary to define a linking function, in order to obtain a smooth deformation of the LV grid. To this aim, two further functions were introduced: z_{apex} and z_{intime}. The former stores a combination of the coordinates of the apical node, but, since the ventricle moved throughout the cardiac cycle, an algorithm to find out the updated apical coordinates at each time step was implemented. Instead, the latter gives the temporal variation of the z coordinate of the node chosen as

contact point between the cannula and the ventricular wall (i.e. the farthest node from the LV apex, among those at the cannula-LV wall interface). z_{intime} was essential to guarantee synchronous movement between the cannula and the LV. So, given the definition of z_{apex} and z_{intime}, the mathematical expression for the previously mentioned connecting function is the following (eq. 16):

$$y(z_{local}) = \sqrt{\frac{1}{a}\left(z_{local} + \frac{b^2}{4a} - c\right)} - \frac{b}{2a} \tag{16}$$

where: $a = \frac{b^2}{8c}$, $b = 8c - \sqrt{80c^2 - 8cz_{apex}}$, $c = z_{intime}$.

More in detail, displacement $u_{\perp}$ and the functions z_p and $\delta(z)$ were expressed in terms of z_{intime}, when referred to the purely translational ventricular region; while ϑ was function of z_{intime}, x_{ref} and y_{ref}, the last two being the x and y coordinates of the cannula/ventricle contact point.

The result of the just described strategy is appreciable in Figure 4-13, where the superimposition of the end-systolic and end-diastolic configurations is reported for both the *post-implant* models (images provided for a 15% EF).

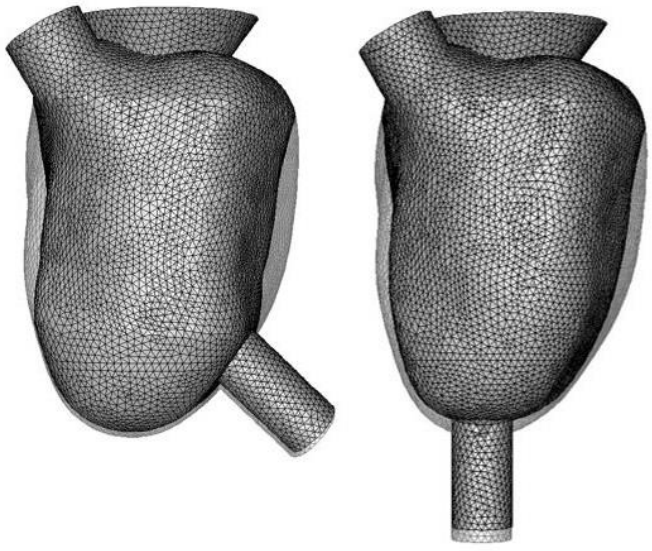

Figure 4-13 Superimposition of the end-systolic and end-diastolic configurations for the patient-specific *post-implant* models A (left) and B (right); images provided for 15% residual EF.

4.5 CFD analysis set-up

The fluid dynamic simulations (3D, transient) were performed exploiting the software ANSYS Fluent 18.1. Blood was modelled as a Newtonian fluid, with viscosity μ=0.003 Pa·s and density ρ=1060 kg/m^3.

The Pressure-Velocity Coupling SIMPLE algorithm was chosen as the numerical scheme, with a 2nd order upwind spatial discretization and a 1st order implicit transient formulation, set as default. For what concerns the under-relaxation factors, the following values were set: 0.3 for pressure and 0.7 for momentum. To ensure solution convergence, the residuals for continuity and x, y, z - velocities were set up to 10−5. Calculations were run with a time step equal to 1 ms and 150 iterations/time step. The number of time steps depended on the phase of the cardiac cycle being simulated: 282 time-steps for systole and 419 time-steps for diastole. Specifically, all simulations started with the systolic phase, followed by the diastole.

4.5.1 Simulations scenario

In this study, three simulations sets were designed to characterize the mutual interactions between i) residual contractility in a failing ventricle, ii) degree of LVAD support (i.e. LVAD flow rate provided to the patient) and iii) LVAD inflow cannula positioning, because these factors were hypothesized to significantly contribute to alter intraventricular flow dynamics and enhance the LV thrombogenic potential.

The implementation details of each set are listed below.

4.5.1.1 *Pre-implant* model (Set-1)

This set consisted of three simulations. The fluid dynamic domain was the pathologically dilated patient-specific LV. Transient CFD simulations of the whole cardiac cycle were carried out, considering three values of residual EF% (15% - 10% - 5%), corresponding to increasing levels of cardiac impairment, that is from moderate to severe LV HF.

Through this set of simulations, the role of LV residual contractility as a possible thrombogenic factor was explored, by examining blood velocity patterns, blood stasis and associated wall shear stress (WSS) trends in the apical region. Furthermore, results from these simulations were used as basis for comparison with corresponding *post* inflow cannula implantation data.
The Table 3 resumes the simulation details in terms of ejection volume, cardiac output and systolic/diastolic *k* values.

Table 3 Parameters of Set-1 three simulations.

	Residual contractility (EF%)		
	5%	**10%**	**15%**
Stroke volume [ml]	14	28	42
Native CO [L/min]	1.20	2.40	3.60
***k* systole**	18.4	18.4	18.4
***k* diastole**	17.8	17.75	17.65

4.5.1.2 *Post-implant* A model (Set-2)

This set consisted of a matrix of 8 test conditions, obtained combining 4 values of residual EF% (0 - 5 - 10 - 15%) with 7 levels of support (LVAD flow rates); to each one of the residual EF% corresponded a native CO, expressed in L/min. Pairs of variables (LVAD CO, LV EF%) were identified having as a target a total CO, given by the sum of native CO and LVAD flow rate, equal to 5 L/min. In this way, the interplay between myocardial residual contractility and LVAD flow rate was evaluated.
The CFD model herein exploited was the one previously described in section 4.2, referred to as *post-implant* model A, where the patient-specific LVAD inflow cannula positioning is coupled with the patient-specific dilated LV geometry.
Simulation details provided in Table 4.

Table 4 Total flow rate [L/min] (CO_{TOT} = native CO + LVAD flow rate), ΔVd applied volume variation [ml] in systole and diastole (i.e. stroke volume), *k* values, for all the simulations.

	Residual contractility (EF%)			
	0%	**5%**	**10%**	**15%**
LVAD CO [L/min]				
2.20			CO_{TOT} = 4.60 ΔVd = 38.34 *k* systole = 28.9 *k* diastole = 28.55	CO_{TOT} = 5.80 ΔVd = 52.34 *k* systole = 28.8 *k* diastole = 28.5
2.70			CO_{TOT} = 5.10 ΔVd = 40.69 *k* systole = 28.9 *k* diastole = 28.5	
3.00			CO_{TOT} = 5.40 ΔVd = 42.10 *k* systole = 28.9 *k* diastole = 28.5	
3.50		CO_{TOT} = 4.70 ΔVd = 30.45 *k* systole = 29 *k* diastole = 28.6		
3.80		CO_{TOT} = 5.00 ΔVd = 31.86 *k* systole = 29 *k* diastole = 28.6		
4.10		CO_{TOT} = 5.00 ΔVd = 33.27 *k* systole = 29 *k* diastole = 28.6		
5.00	CO_{TOT} = 5.00 ΔVd = 23.5 *k* systole = 29.1 *k* diastole = 28.6			

4.5.1.3 *Post-implant* B model (Set-3)

This set consisted of two test conditions, selected from Set-2 simulation matrix, having as selection criterion the total cardiac output (CO) provided to the patient, namely the sum of native residual CO and LVAD flow rate. Specifically, total CO was assumed equal to 5 L/min, a condition mimicking the average cardiac output at rest, so as to refer to real clinical data.

In this third numerical scenario, the position of the cannula was varied with respect to the previous one, accordingly to what described in section 4.2, to simulate apical cannulation. The aim was to quantify the impact of cannula position on LV thrombogenicity.

Simulations details provided in Table 5.

Table 5 Total flow rate [L/min] (COTOT = native CO + LVAD flow rate), ΔVd applied volume variation [ml] in systole and diastole (i.e. stroke volume), k values, for all the simulations.

		Residual contractility (EF%)	
		5%	**10%**
LVAD CO [L/min]	**2.70**		CO_{TOT} = 5.10 L/min ΔVd = 40.69 ml *k* systole = 22.2 *k* diastole = 21.75
	3.80	CO_{TOT} = 5.00 L/min ΔVd = 31.86 ml *k* systole = 22.4 *k* diastole = 21.95	

4.5.2 Boundary conditions

Table 6 resumes all the boundary conditions combination for the different simulation set up.

Table 6 Scheme of the boundary conditions applied in the simulations, for both pre- and post-implant configurations. To note: no differences between A and B boundary settings. LV, left ventricle; LA, left atrium; LVOT, left ventricular outflow tract; MV, mitral valve; AV, aortic

valve; $CANN_{IN}$, cannula portion inside the ventricle; $CANN_{OUT}$ surf, most distal surface of the cannula, not included in the ventricular domain.

	Pre-implant		*Post-implant* (A and B)	
	Systole	**Diastole**	**Systole**	**Diastole**
LV	Moving wall	Moving wall	Moving wall	Moving wall
LA	Stationary wall	Stationary wall	Stationary wall	Stationary wall
LVOT	Stationary wall	Stationary wall	Stationary wall	Stationary wall
MV	Stationary wall	Pressure Inlet	Stationary wall	Pressure Inlet
AV	Pressure Outlet	Stationary wall	Pressure Outlet	Stationary wall
$CANN_{IN}$	/	/	Moving wall	Moving wall
$CANN_{OUT}$ surf	/	/	Velocity Inlet	Velocity Inlet

A pressure of 0 Pa was chosen as boundary conditions for both the aortic valve (AV) and the mitral valve (MV), in systole and diastole respectively, since in our model the LV hemodynamics was strongly influenced by two main factors, the EF% and the LVAD flow rate, and, to a lesser extent, by the systemic circulation. Furthermore, this boundary condition was set equal in all the simulations considered in this study, so that the same bias was introduced in the results.

For the named selection “velocity inlet” the velocity specification method was set as velocity magnitude, normal to boundary, with different cannula suction velocities depending on the test conditions.

4.5.3 Numerical inertia

Moreover, at the beginning of each simulation, the fluid in the LV was at rest so that, in order to reach a periodic solution and a fully developed flow, the computation of several cardiac cycles was required. Accordingly, a preliminary

repeatability solution analysis was carried out, both quantitatively and qualitatively, to prove the third simulated cardiac cycle as the first suitable to perform results analysis. According to the approach described by Doost et al.[24], qualitative comparison of velocity magnitude streamlines, evaluated at the same time step, between five subsequent cardiac cycles, revealed that the flow patterns between the third and fourth cycle were roughly identical (Figure 4-14).

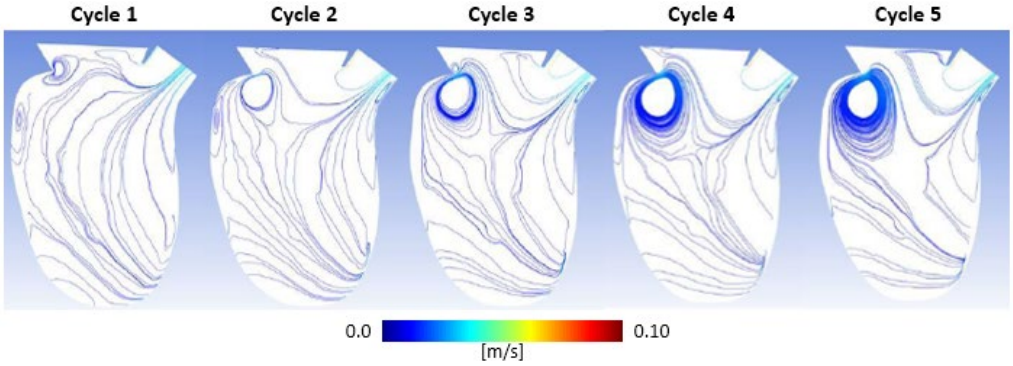

Figure 4-14 End systolic in-plane flow patterns in five subsequent cardiac cycles.

Furthermore, the in-plane averaged velocity magnitude difference, between the third and fourth cardiac cycle, was proven to be less than 2%.

4.6 Control healthy LV model

In this section, a brief description of the healthy patient-specific LV model, developed in a previous work[22], is reported. The patient-specific LV geometry at end-systolic configuration, reconstructed from 3DTTE images and acquired from a healthy volunteer, with as assumed stroke volume equal to 70 ml (Figure 4-15).

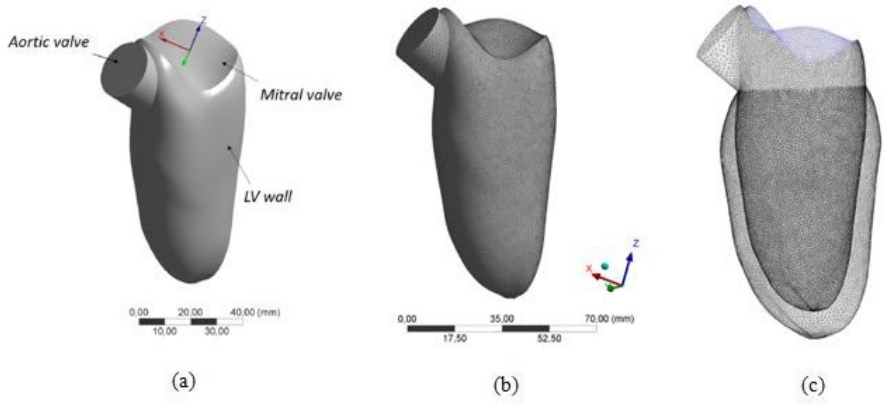

Figure 4-15 (a) Healthy patient-specific LV geometry at end-systolic configuration; (b) Mesh; (c) Superimposition of the end-systolic and end-diastolic configurations (stroke volume 70 ml).

For the systolic phase simulation, the following boundary conditions were imposed: i) Moving wall for the LV, ii) physiological temporal trend of aortic pressure at the AV, iii) Stationary wall for the MV.
For the diastolic phase simulation, the following boundary conditions were imposed: i) Moving wall for the LV, ii) physiological temporal trend of mitral pressure at the MV, iii) Stationary wall for the AV.

4.7 Results

In this chapter, the results obtained from the simulation sets (for details see section 4.6) are reported. Ventricular hemodynamics fundamental characteristics and major features responsible of the thrombogenic potential of the different analysed conditions are herein examined in terms of vortices and velocity fields quantification, as well as thrombogenic potential investigation (WSS).
The following two subsections will briefly explain how these variables were assessed.

Analysis of vortex dynamics

Vortex dynamics was analysed applying the Q-criterion. This method looks at the second invariant of the velocity gradient tensor, Q.
Q-criterion is a three-dimensional vortex identification method, developed by Hunt et al.[25], in 1988, which defines a vortex as a spatial region where (eq.17):

$$Q = \frac{1}{2}[|\Omega|^2 - |S|^2] > 0 \qquad (17)$$

i.e. where the Euclidean norm of the vorticity tensor (asymmetric component) outnumbers the one related to the rate of strain (symmetric component). Hence, a vortex is defined as an area where $Q > 0$.

Analysis of Wall Shear Stress (WSS) patterns

The evaluation of wall shear stress on the apical portion of the ventricular wall was carried out since WSS is a mean to assess blood stasis. Blood stasis and recirculation patterns in the LV chamber are recognized risk factors for intraventricular thrombosis and potential thromboembolic events, as they promote thrombosis through the accumulation of both activated and sensitized platelets, who may get trapped because of the LV limited washout and exposed to low dynamic shear stress for elongated durations, i.e., additional prothrombotic conditions.

The WSS were extracted considering a complete cardiac cycle in three pre-defined regions close to the LV apex (Figure 4-16).

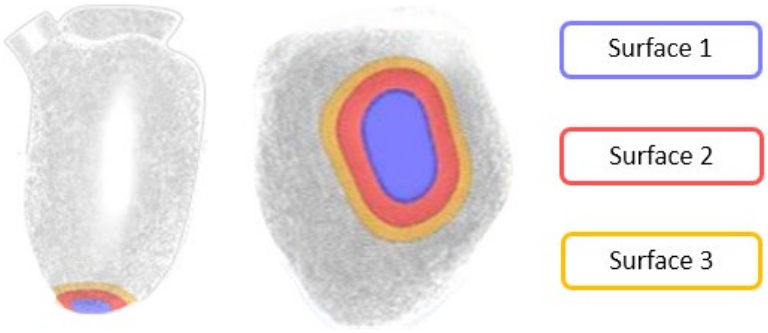

Figure 4-16 Apical regions: 1st region in blue, 2nd region in red, 3rd region in yellow. Left: bottom view. Right: lateral view.

Then, thanks to a MATLAB script, the data were processed in order to obtain the WSS trends in time averaged over each of the aforementioned regions. These regions were identified in between two z coordinates, expressed as percentage of z_{apex}, as follows:

$$1^{st}\ region\ for\ z > 0.99\ z_{apex}$$
$$2^{nd}\ region\ for\ 0.97\ z_{apex} < z < 0.99\ z_{apex}$$
$$3^{rd}\ region\ for\ 0.95\ z_{apex} < z < 0.97\ z_{apex}$$

The WSS were extracted in these three regions to comprehensively map blood behaviour close to the LV apex. Blood stasis was expected to become more evident as moving towards the LV apex.

4.7.1 Patterns of vortex formation and evolution

A fundamental role in determining LV hemodynamics is played by vortexes, since they are responsible for blood mixing, proper cardiac filling and emptying in the diastolic and systolic phases, respectively. Specifically, in healthy LVs, a vortex forms when, during systole, the LV contracts and blood flow impacts the mitral valve, allowing for smooth redirection of flow toward the LV outflow tract (LVOT). In this way, vortices within LV increase cardiac efficiency by maintaining the momentum of inflowing blood during diastole, thereby facilitating the systolic ejection of blood into the LVOT[26].

4.7.1.1 Set-1: *pre-implant* model

For the healthy LV, during the **systolic acceleration** (Figure 4-17 A), the contraction of the LV wall results in multiple vortex structures, distributed along the upper portion of the LV and the LVOT. In peak systole and in the deceleration phase (Figure 4-17 B and C), vortices are disrupted because of the ejection of blood through the AV. By contrast, results from simulation Set-1 showed that, during systole, two vortices develop close to the MV; the smaller vortex remains coherent near the mitral orifice during systolic acceleration, peak and deceleration, while the main one slowly moves downwards, towards the centre of the LV and the LVOT.

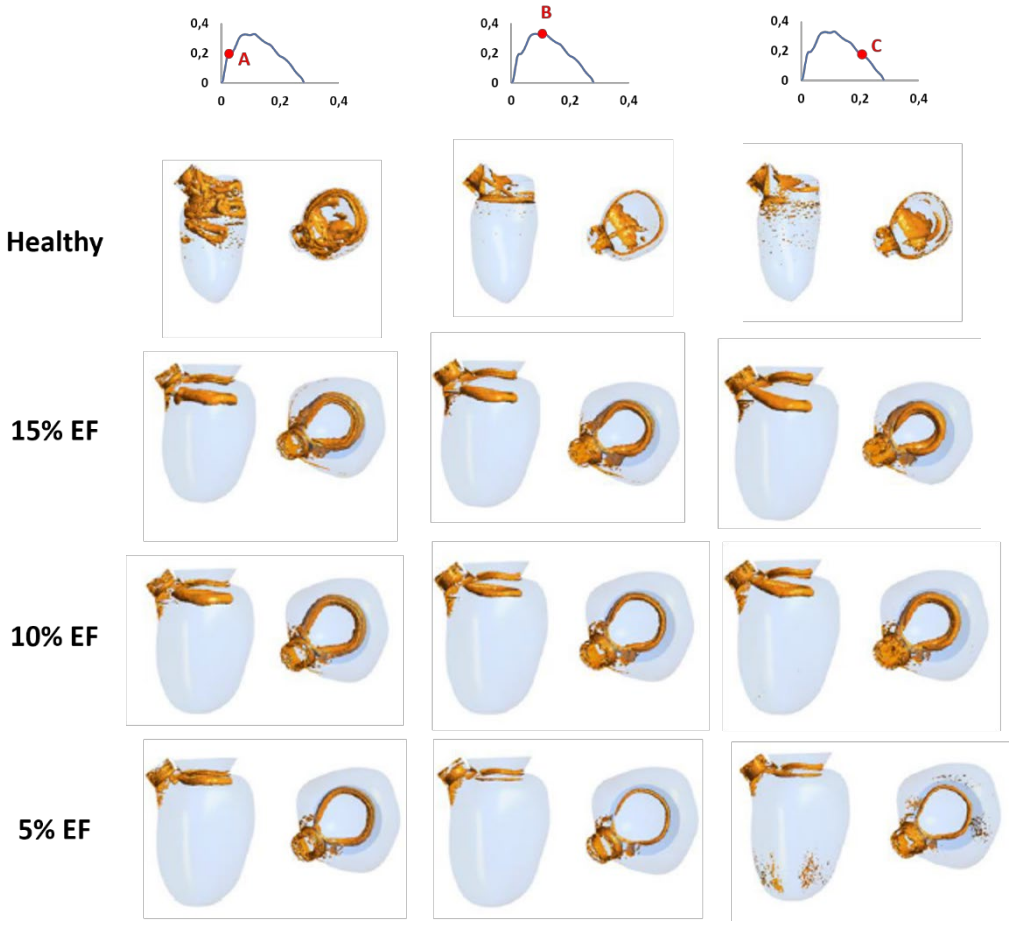

Figure 4-17 3D vortices field in systole obtained applying the Q-criterion. (A) systolic acceleration; (B) systolic peak; (C) systolic deceleration. Results are shown (from left to right) with the scenario getting more pathological, for the healthy LV model[22] and for a residual EF of 15%, of 10% and of 5%, respectively.

Furthermore, it is known from literature that, as the basal posterior LV wall contracts in physiological subjects, the space beneath the MV decreases and becomes so small as to make the vortex to be absorbed with the outflow stream[27]. Differently, as pinpointed in this study, enlargement of the LV results in postero-basal space large enough to form a vortex even in mid or late systolic phase, while EF% progressively decreasing (Figure 4-17 B and C). Specifically, concerning the residual contractility influence, we noticed that the higher the residual EF%, the larger and the more persistent the vortex.

Velocity contours and vectors were also computed to better quantify the velocity field and appreciate vortices direction. In Figure 4-18, these variables are depicted, comparing healthy data with 15% EF pathological ones only, for the

sake of clarity, since vortices direction and rotation was found to be the same among the examined conditions.

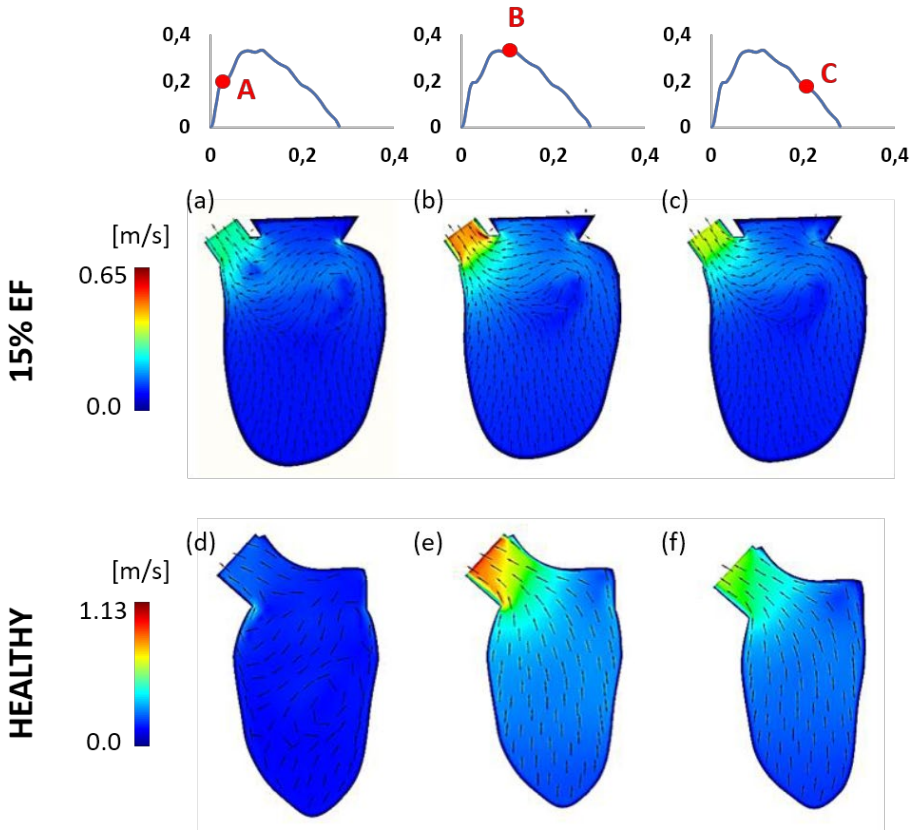

Figure 4-18 Systolic intraventricular flow, considering a residual EF of 15% (top), and for the healthy LV model (bottom). Vectors and velocity magnitude contours on a longitudinal plane across mitral/aortic orifices and LV apex were obtained at systolic acceleration (a and d), systolic peak (b and e), and systolic deceleration (c and f). We herein reported only 15% EF data given the more significant blood velocity, with respect to 5% and 10%.

Considering the healthy LV, in early systole (Figure 4-18 d), two main asymmetrical vortices are generated; the closest to the LV apex is counter clockwise while the second one, closer to the LVOT, moves clockwise. At peak and in late diastole, blood flows towards the AV, and no vortices are generated (Figure 4-18 e and f). On the other hand, in the pathological model, during the systolic phase, a clockwise vortex is formed due to the contact between the blood stream and the LV wall, redirecting the fluid towards the LVOT and the AV (Figure 4-18 b). This latter phenomenon was also reported by Tang et al.[26], who analysed the hemodynamics in a DCM-affected LV by using echocardiographic particle image velocimetry (E-PIV), pointing out how the clockwise vortex

occurring at the centre of the LV was proven to move toward the LVOT, while an overall decreasing of these structures occurs in the rapid ejection phase, with only the clockwise vortex close to the LVOT converted into a laminar flow for blood circulation

If examining the **diastolic phase** (Figure 4-19), vortices number and dimensions increase for healthy LV model, with a unique prevalent vortex arisen beneath the mitral valve evolving in a chaotic distribution of multiple vortices close to the LVOT.

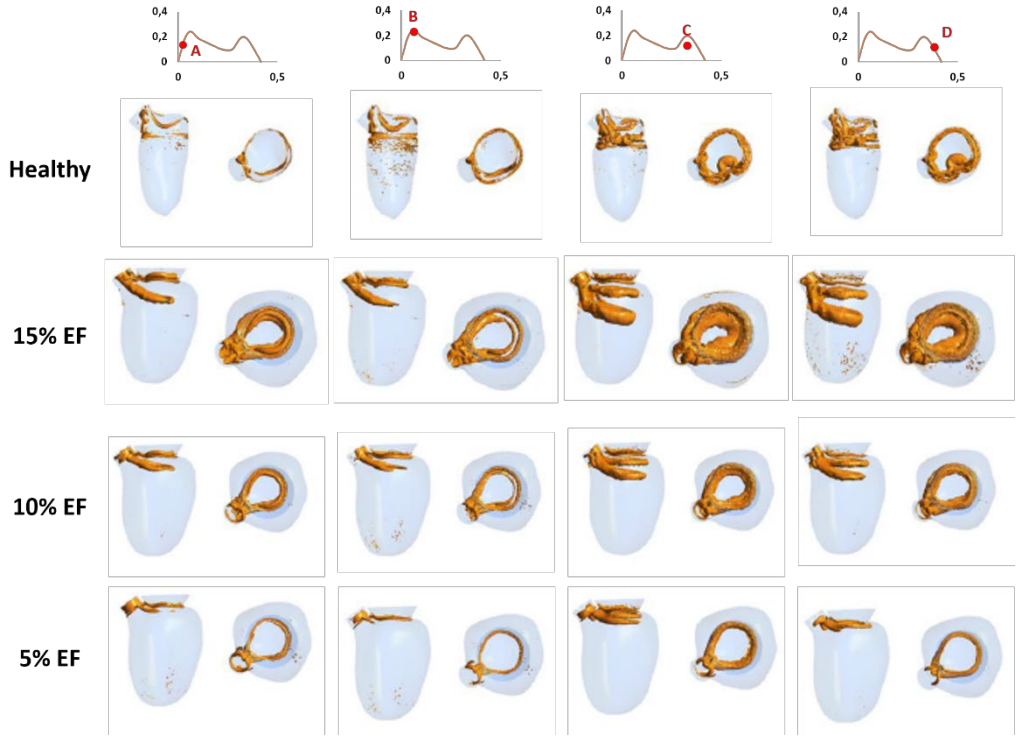

Figure 4-19 3D vortex field in diastole obtained applying the Q-criterion; (A) diastolic acceleration; (B) E wave; (C) A wave; (D) diastolic deceleration. Results are shown (from left to right) for the healthy LV model, for a residual EF of 15%, of 10% and of 5%.

For what concerns the pathological scenarios, diastolic vortices are localized just below the MV and hardly propagate towards the apical region of the LV, because of limited wall contractility, increasing the risk for blood stasis. In detail, for 10% and 15% EF, in early diastole and at the E wave (Figure 4-19 A and B), the 3D vortex ring remains rather compact in the upper part of the LV. In late diastole (Figure 4-19 C and D), two compact rings (being considerably extended in 15% EF) develop in the centre of the LV inducing only local circulation of

blood. In case of severe dilation (5% EF), the described pattern of vortex formation and evolution is barely present.

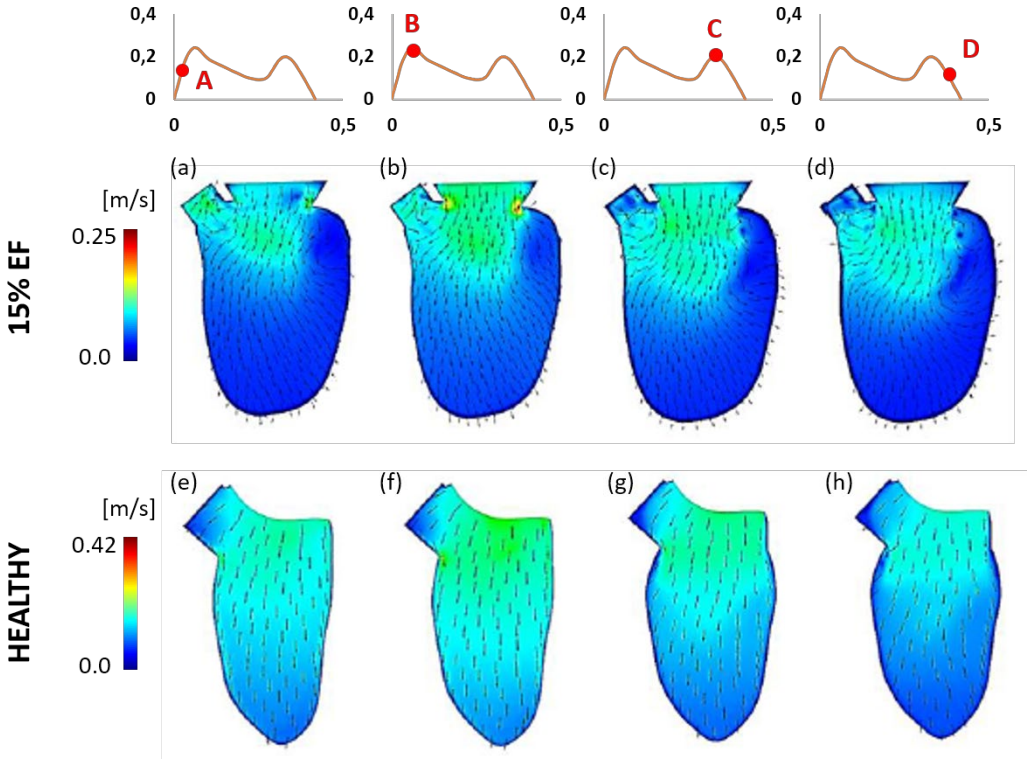

Figure 4-20 Diastolic intraventricular flow, considering a residual EF of 15% (top), and for the healthy LV model (bottom).Vectors and velocity magnitude contours were obtained at diastolic acceleration (a and e), E wave (b and f), A wave (c and g), and diastolic deceleration (d and h).

Furthermore, as done previously, we assessed vortices' velocity contours and vectors for both the healthy and 15% residual EF conditions (Figure 4-20). As it can be noticed comparing the ventricular flow fields, aberrant fluid mechanics appears in the pathological LV model, with disorderly arranged vortices which redirect the blood flow from the LV base toward the LV posterior wall, the LV apex, and the LVOT. This effect reduces the blood flow for systolic ejection in the LVOT and increases the residual blood flow in the LV cavity, as reported by Tang and co-workers[26]. In early diastole and at the peak of the E-wave, indeed, two vortices are formed around the bilateral side of the transmitral inflow (Figure 4-20 a and b), while in the healthy LV, blood flows undisturbed from the MV to the apex (Figure 4-20 e-h).

Also, the reduced cardiac function (15% EF) weakens the diastolic mitral jet (Figure 4-20 c and d), which penetrates less deeply into the wider LV, if compared to the healthy condition, and is unable to support flow redirection towards the outflow, proving even data already reported by Mangual et al.[28].

4.7.1.2 Set-2: *post-implant* model A

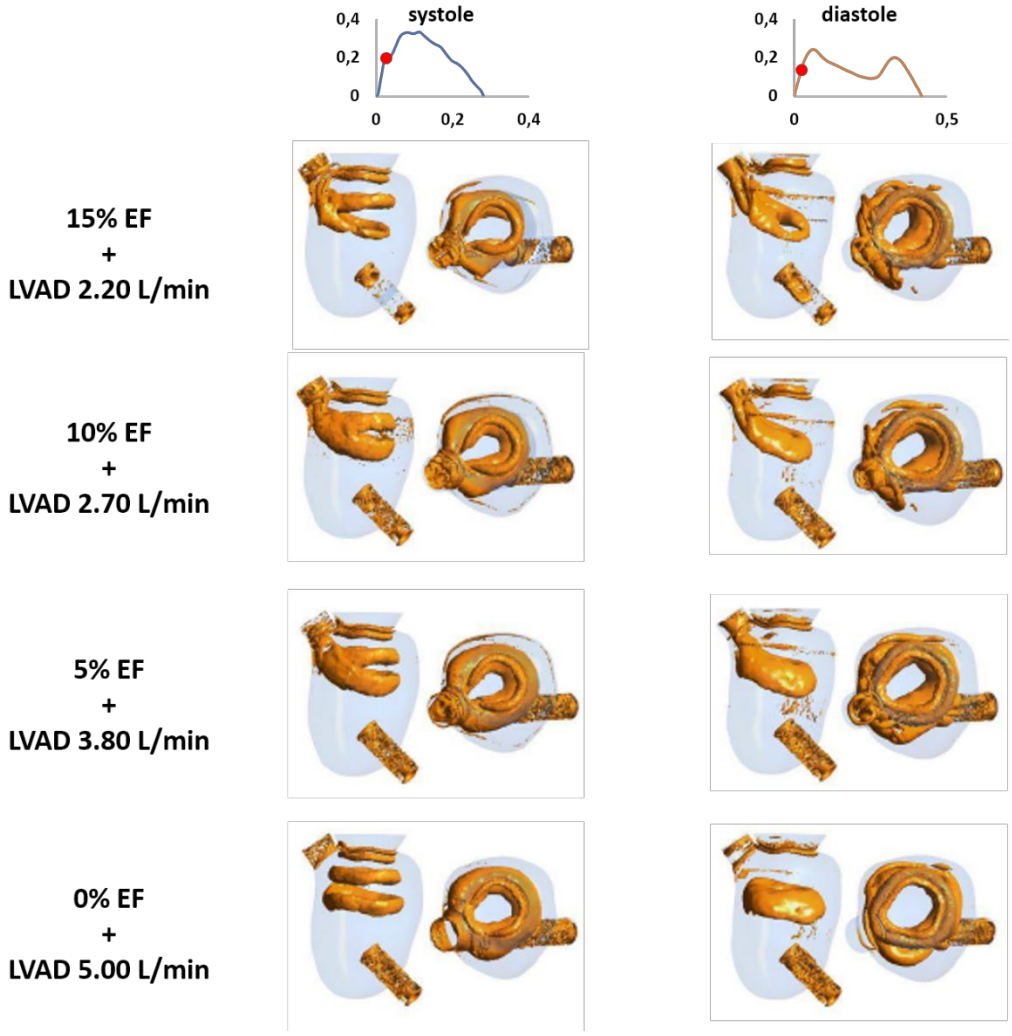

Figure 4-21 3D vortex field during diastolic acceleration, obtained applying the Q-criterion; Test conditions: (a) 15% EF + LVAD 2.20 L/min; (b) 10% EF + LVAD 2.70 L/min; (c) 5% EF + LVAD 3.80 L/min; (d) 0% EF + LVAD 5.00 L/min. Systole on the top, diastole in the bottom.

Firstly, a comparison among the different conditions simulated for this set of simulations pointed out a similar vortices' formation and development, probably since, in the simulated configurations, the LV volume displacements changed

accordingly to the total CO, while the applied kind of motion did not change. Indeed, the difference between the considered test conditions is in terms of the dimension and coherence of the vortexes, rather than in their number and kind of motion. Moreover, a progressive disappearance of secondary vortexes close to the LVOT was noticed, as the EF% decreases to 0% (Figure 4-21).
Furthermore, it was observed that, at the same LV residual EF%, the increase in LVAD flow rate did not determine a significant variation in vortex dynamics.

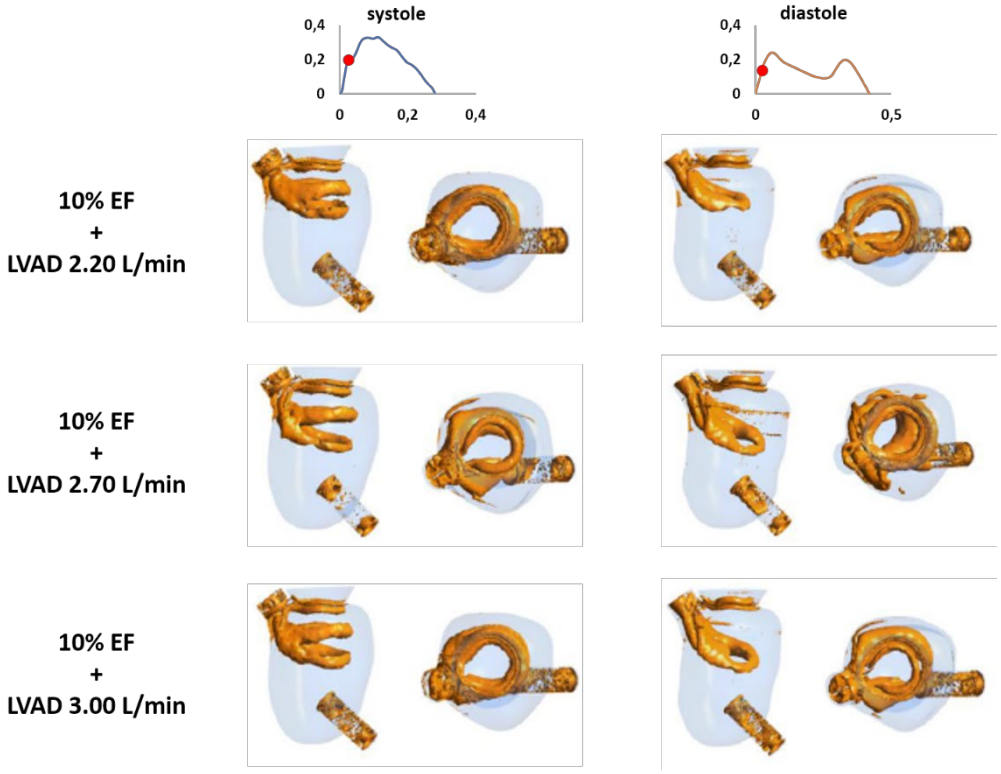

Figure 4-22 3D vortex field during diastolic acceleration, obtained applying the Q-criterion; Test conditions: (a) 10% EF + LVAD 2.20 L/min; (b) 10% EF + LVAD 2.70 L/min; (c) 10% EF + LVAD 3.00 L/min. Systole on the top, diastole in the bottom.

As a matter of fact, during systole, a rise in LVAD flow rate had the sole effect of increasing the distance between the main vortexes (Figure 4-22 top), while, in diastole, the main vortex was lightly stretched toward the inflow cannula (Figure 4-22 bottom). Hence, these observations suggest that LV residual EF% has a predominant role in determining LV hemodynamics, with respect to the LVAD flow rate. Similar observations can be made for test condition sharing a residual EF of 5%.
Thus, results are presented only for one tested case (15% EF + LVAD 2.20).

In early systole and at the systolic peak (Figure 4-23 A and B, top), three vortexes are generated: the smaller one immediately beneath the MV, while two main vortexes in the centre of the LV. In the deceleration phase (Figure 4-23 C, top) the third vortex is disrupted, while the second one moves towards the LV apex. In diastole, the opposite phenomenon occurs: the main vortex in early diastole (Figure 4-24 A and B, top) moves towards the inflow cannula and, in mid and late diastole, it is followed by a second vortex, as blood enters the LV from the mitral orifice (Figure 4-24 C and D, top). In both phases of the cardiac cycle, the LV apical zone was not involved in vortex phenomena, thus resulting in an increased risk for potential thrombus formation.

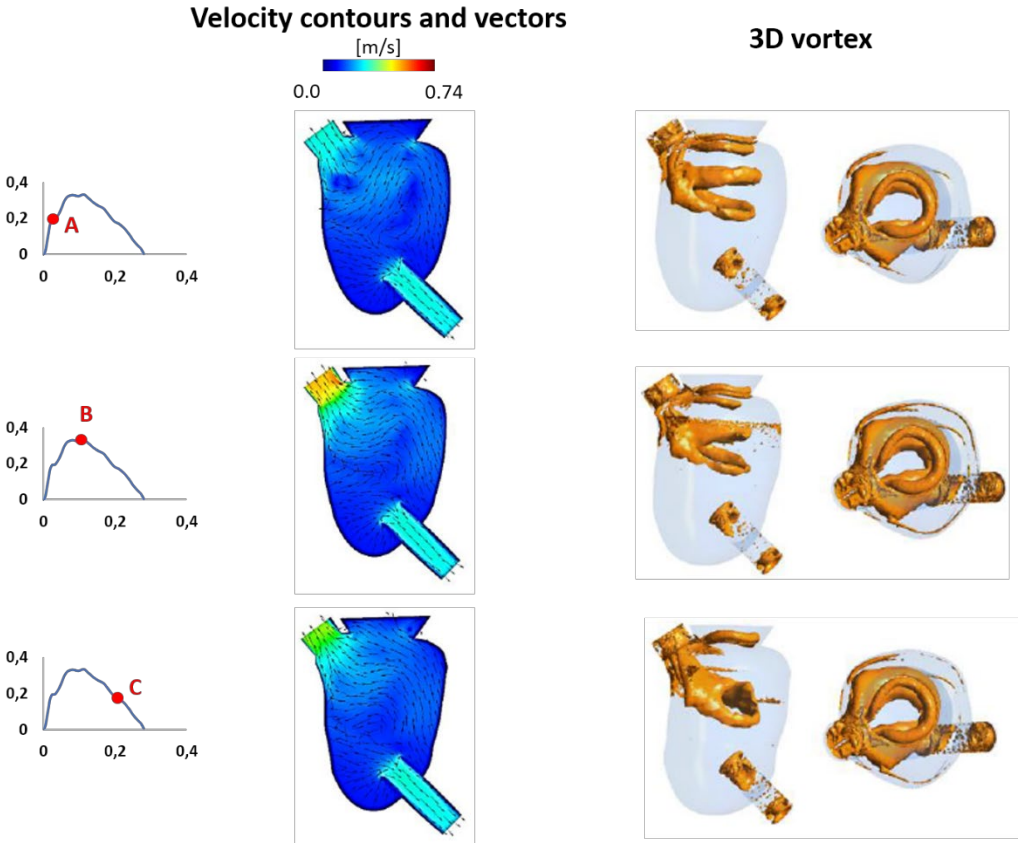

Figure 4-23 3D vortex field (*top*) and Vectors and velocity magnitude contours (*bottom*) in systole; (A) Systolic acceleration; (B) Systolic peak; (C) Systolic deceleration. Test condition reported: 15% EF + LVAD 2.20 L/min.

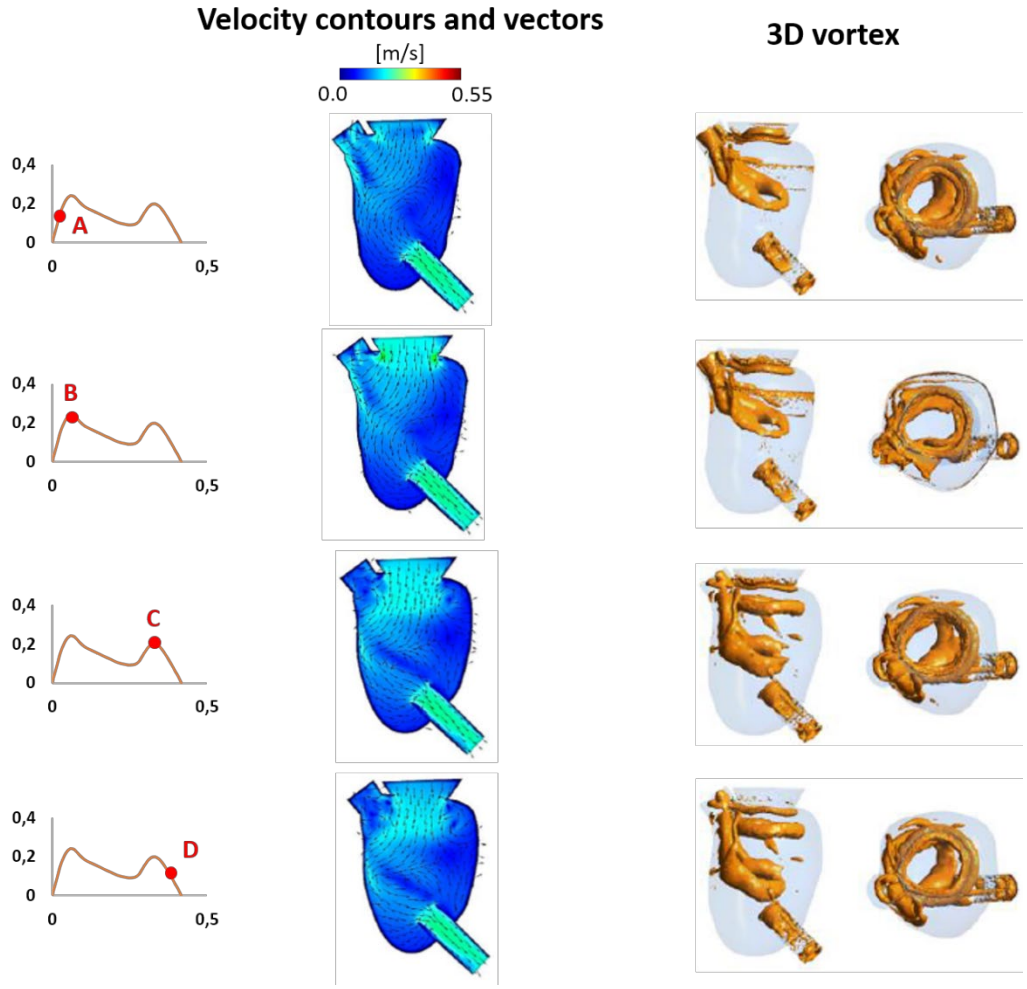

Figure 4-24 3D vortex field (*top*) and Vectors and velocity magnitude contours (*bottom*) in diastole; (A) Systolic acceleration; (B) Systolic peak; (C) Systolic deceleration. Test condition reported: 15% EF + LVAD 2.20 L/min.

Concerning flow field and vortices direction, velocity contours showed that, in systole, blood was simultaneously ejected through both the AV and the LVAD inflow cannula, establishing a parallel flow pattern. Thus, many vortices with different directions of rotation appeared in the LV, which caused the flow to be disorderly, and no predominant clockwise or counter- clockwise rotation was observed in the intraventricular flow patterns, except when systolic deceleration took place. In this phase (Figure 4-23 C, bottom), a large counter-clockwise rotation was formed in the LV, driving the blood stream in the LVAD inflow cannula and towards the AV.

On the other hand, in diastole, the inflow mitral jet hit the intraventricular septum, generating a large counter-clockwise rotation, so as to direct the blood

flow to the inflow cannula. A small, clockwise vortex was formed in the LVOT, however being the most evident in late diastole (Figure 4-24 C and D, bottom).

3D vortex field obtained for Set-2 were further compared with corresponding data from simulation Set-1 (*pre-implant* model), namely considering equal degrees of LV residual contractility (for instance 15% EF *pre-implant* vs. 15% EF + 2.20 L/min LVAD flow rate). In general, pertaining to the *pre-implant* model, the detected vortexes were confined in the upper portion of the LV (especially for the 10 and 5% EF conditions), resulting more compact and smaller than those analysed in Set-2 (Figure 4-23 and Figure 4-24), both in systole and diastole. We suggest that the described phenomenon is due to the cannula suction action that, combined with residual EF, improves LV washout. Moreover, A comparative analysis between the healthy condition and the *post-implant* configurations revealed a substantial difference in vortex dynamics. Indeed, during early systole, only two broad vortices were detected in the examined *post* LVAD implantation LV (Figure 4-21, top), while multiple vortex structures characterized the physiological scenario (Figure 4-19 A).

4.7.1.3 Set-3: *post-implant* model B

The 3D intraventricular vortex field is reported in Figure 4.21b and d, at selected systolic and diastolic time points (i.e. systolic and diastolic acceleration), for test condition 10% EF + LVAD 2.70 L/min. As it can be noticed, qualitatively, the obtained vortex dynamics is apparently not dissimilar from that characterizing corresponding post-implant A simulations (Figure 4-25 a and c).

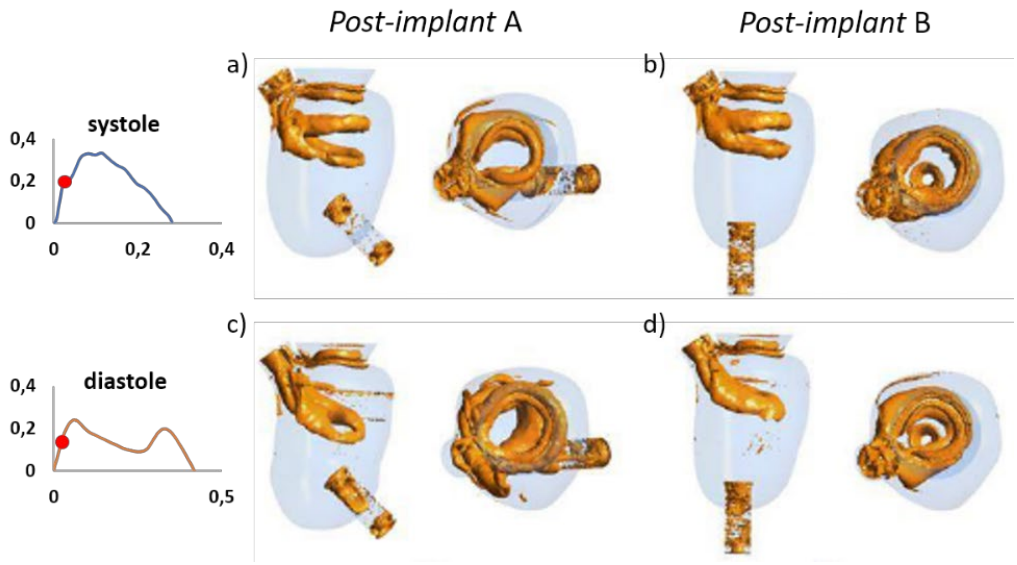

Figure 4-25 3D vortex fields at systolic (top) and diastolic (bottom) acceleration phases for test condition 10% EF + LVAD 2.70 L/min; (a) and (c) refer to *post*-implant model A; (b) and (d) refer to *post*-implant model B.

More interesting is the analysis of the intraventricular flow through velocity vectors.

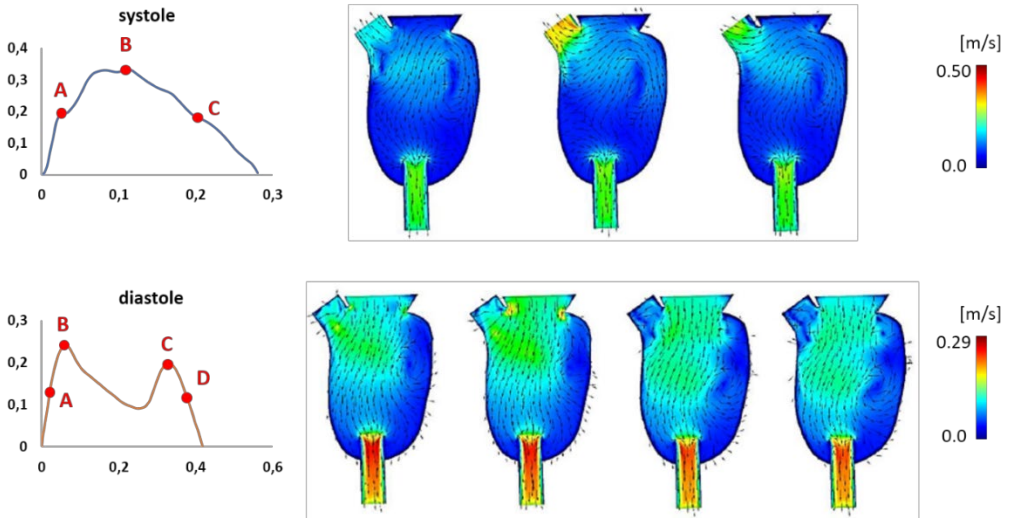

Figure 4-26 *Top*: Systolic intraventricular flow: vectors and velocity magnitude contours were obtained for systolic acceleration (A), systolic peak (B), and systolic deceleration (C). *Bottom*: Diastolic intraventricular flow: vectors and velocity magnitude contours were obtained for diastolic acceleration (A), E wave (B), A wave (C), and diastolic deceleration (D). Reported test condition: 10% EF + LVAD 2.70 L/min.

Differently from matching *post-implant A* simulations, a predominant counter-clockwise rotation was observed throughout the systolic phase (Figure 4-26, top), that directed blood in the LVOT and the cannula inlet. In diastole, when the inflow cannula was inserted in the apex, blood took a more direct route through the LV, from the MV to the inflow cannula (Figure 4-26, bottom), according to findings provided by other authors[29]. In the study, it was proven that inflow cannula angles closer to the apical axis resulted in more linear blood flow from the MV to the LVAD cannula.

Therefore, the comparative analysis suggests that the LVAD inflow cannula in the apical configuration exerts a more effective suction action on blood in the apical region of the LV, with respect to the patient-specific positioning.

4.7.2 Thrombogenic potential: WSS evaluation

In the present study, the evaluation of wall shear stress (WSS) in the apical portion of the ventricular wall was carried as a mean to assess blood stasis. The WSS were extracted considering a complete cardiac cycle in three pre-defined regions close to the ventricular apex (see Figure 4-16) and reported only along the axial direction (zWSS), since x and y components were approximately zero over the whole cardiac cycle.

4.7.2.1 Set-1: *pre-implant* model: influence of residual contractility

The obtained results were compared to the zWSS trends of a healthy LV evaluated, with the same approach, in a previous study[22].

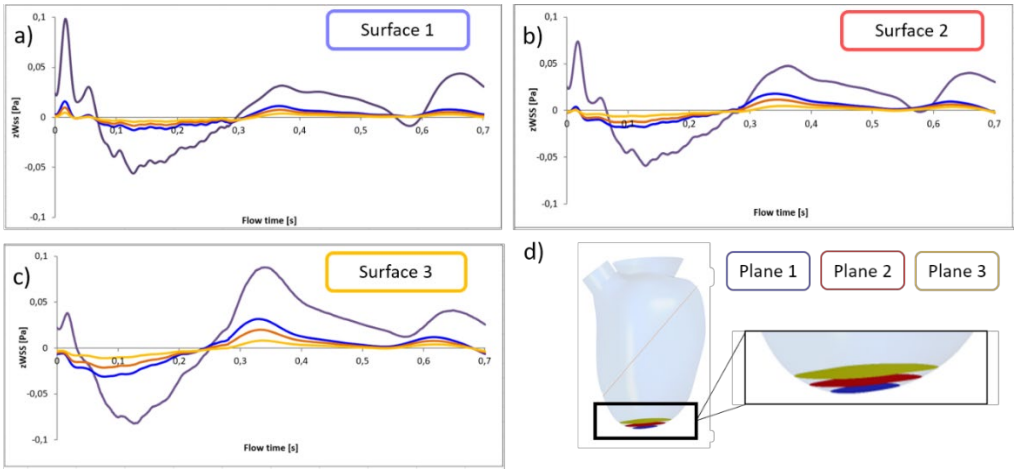

Figure 4-27 (a)-(c): zWSS trends over a whole cardiac cycle for the three different apical surfaces; (d) Scheme of the *ad-hoc* three planes created to compute blood velocity in the apical region.

WSS peak values in the examined pathological conditions are approximately two order of magnitude lower than those in the healthy LV, revealing the presence of a huge stagnation region in the ventricular apex. In particular, Figure 4-27 a-c shows that i) surface 1, the closest to the ventricular apex, is characterized by the lowest values of WSS, for all the considered values of residual EF, and ii) by decreasing EF% degree, the maximum WSS value is lowered by one of order magnitude, from 0.015 Pa (15% EF) to 0.005 Pa (5% EF).

Hence, our results suggest that LV residual contractility plays a key role in promoting potential thrombus formation in a pathologically dilated LV. This phenomenon was also investigated looking at the velocity field, both in systole and diastole, nearby the apical region.

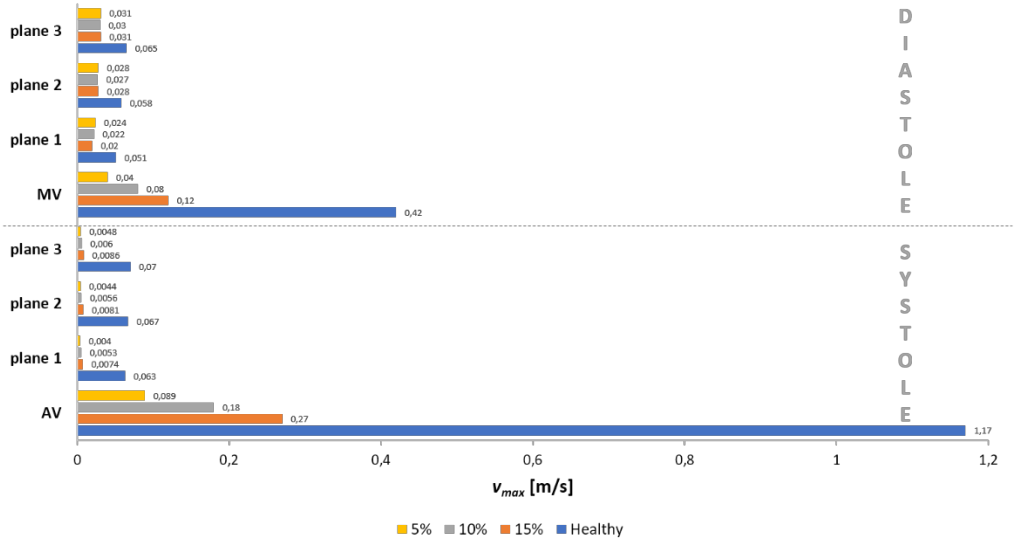

Figure 4-28 Blood maximum velocity (v_{MAX}) values at the systolic peak and at the diastolic E-wave, computed in the apical region of the LV, at the level of three planes (see Figure 4-27 d), and at the AV and MV, in systole and diastole, respectively. Values are expressed in [m/s].

At this aim, three planes were defined as transverse planes crossing apical surfaces 1, 2 and 3, respectively (Figure 4-27 d); then blood maximum velocity (v_{MAX}), at systolic peak and during the diastolic E-wave, was evaluated. As reported in Figure 4-28, firstly an inverse trend between systole and diastole was found, comparing healthy LV with DCM pathological scenario, where, given the reduced LV contractility, blood flow lacks the driving force to be ejected throughout the AV. Hence, the lower the EF%, the lower the v_{MAX}. Differently, in diastole, diastolic v_{MAX} values are one order of magnitude higher than the corresponding values in systole, the opposite being found for the healthy LV. We hypothesized that this behaviour is due to blood mixing in the apical zone, caused by the impact between blood entering from the MV and layers of fluid still in the LV, that were not ejected during the preceding systolic phase; however, values are too low to ensure proper LV washout. Secondly, both in systole and diastole, blood velocity magnitude appeared to be at least one order of magnitude higher for healthy LV than corresponding values for the pathological cases.

4.7.2.2 Set-2: *post-implant* model A: influence of LVAD implantation

For the sake of comparison, WSS associated only to the boundary values of residual EF, namely 0% and 15%, were considered (Figure 4-29 a-b).

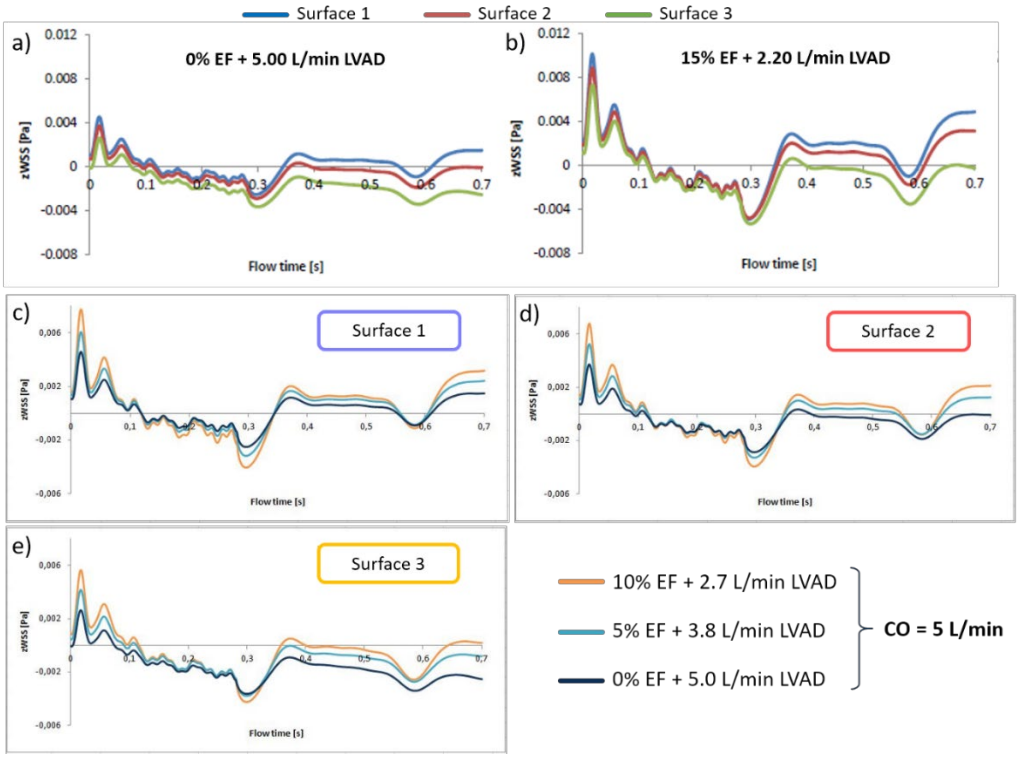

Figure 4-29 zWSS trends for 0% EF + 5.00 L/min LVAD flow rate (a) and for 15% EF + 2.20 L/min LVAD flow rate (b). (c)-(e): zWSS trends for three different combination of EF and LVAD flow rate, providing the total CO of 5 L/min (EF+LVAD flow rate). Values are reported discriminating the trends on every single exploited surface (1,2 and 3), as defined in Figure 4-16.

As the residual EF approaches 0%, WSS maximum values are lowered of one order of magnitude. Therefore, as for the *pre-implant* configurations, our results suggest that LV residual contractility plays a key role in promoting potential thrombus formation. Additionally, comparison with *pre-implant* and healthy LV models were performed. From the former, results suggested that LVAD inflow cannula may determine a further significant risk for thrombus formation, WSS being approximately one order of magnitude lower with respect to the DCM model ones. This difference is even more hampered if comparing *post-implant* A configuration with physiological scenario, with discrepancies up to three order of magnitude.

To be able to discriminate between EF% and cannula thrombogenicity potential contribution, WSS trends were further compared looking at Set-2 simulations which provided the same total cardiac output, namely 5.00 L/min (Figure 4-29c-e). WSS peak values decrease with increasing levels of cardiac impairment; therefore, WSS appear to be strongly influenced by LV residual contractility and, to a lesser extent, by LVAD flow rate.

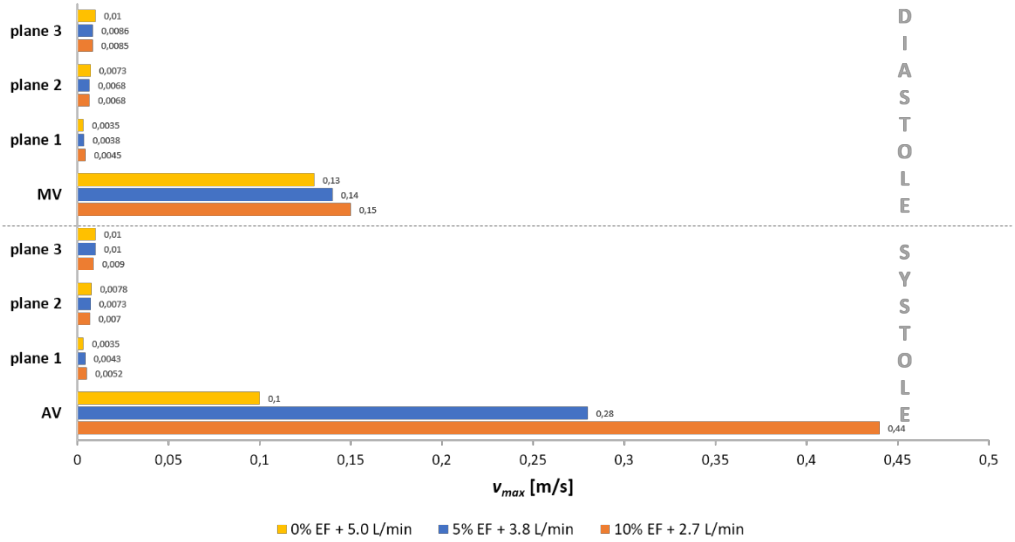

Figure 4-30 Blood maximum velocity (v_{MAX}) values at the systolic peak and at the diastolic E-wave, computed in the apical region of the LV, at the level of three planes (see Figure 4-27 d), and at the AV and MV, in systole and diastole, respectively. Values are expressed in [m/s].

Quantitatively, exploiting the same strategy as described for *pre-implant* model, blood velocity (v_{MAX}) was evaluated at systolic peak and at the diastolic E-wave (Figure 4-30). At the systolic peak, results showed that blood velocity increased with the residual EF%, specifically nearby the AV and the surface closest to the LV apex, while remaining almost constant on the other two surfaces. In diastole, a similar behaviour was observed.

4.7.2.3 Set-3: *post-implant* model B: influence of cannula positioning

Last set of simulations allowed for the investigation of the cannula positioning influence on the thrombogenic potential. For instance, examining test condition 5% EF + 3.80 L/min LVAD flow rate (Figure 4-31), WSS peak value varies from 0.006 Pa, to 0.016 Pa; similar trend was observed in every configuration of this simulations set.

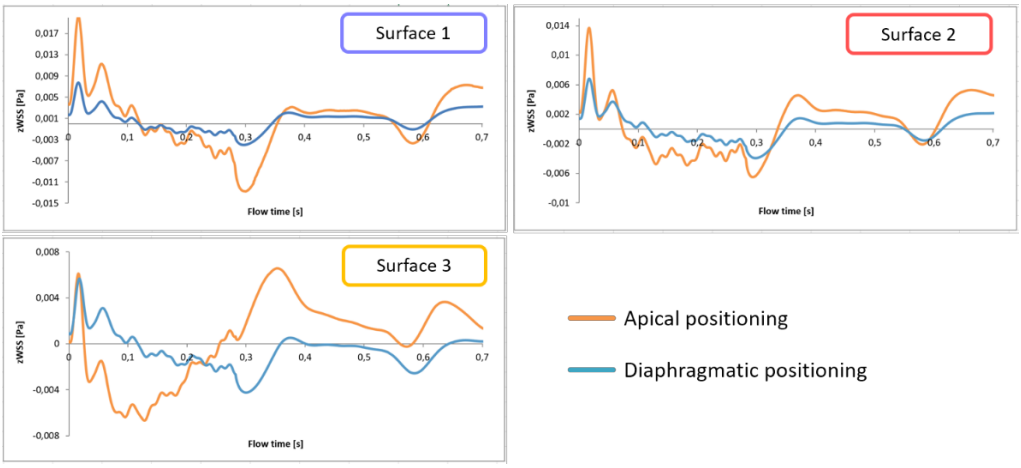

Figure 4-31 zWSS trends on the apical surfaces (as defined in Figure 4-16) for 5% EF + 3.80 L/min LVAD flow rate, with inflow cannula in patient-specific and apical positioning, respectively.

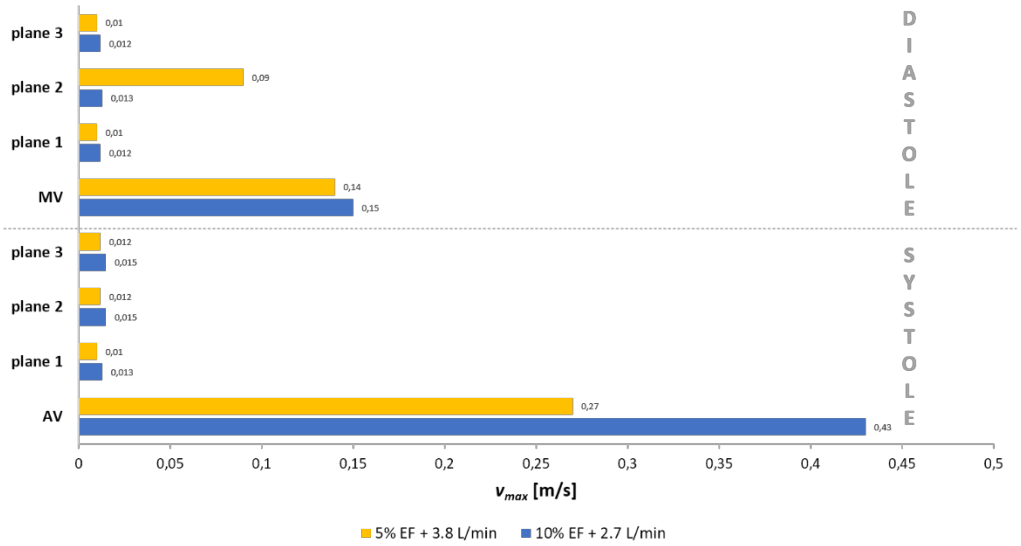

Figure 4-32 Blood maximum velocity (v_{MAX}) values at the systolic peak and at the diastolic E-wave, computed in the apical region of the LV, at the level of three planes (see Figure 4-27 d), and at the AV and MV, in systole and diastole, respectively. Values are expressed in [m/s].

The quantitative analysis, in term of blood peak velocities, corroborates this main finding. Blood v_{MAX} values in the apical configuration were found to be one order of magnitude higher than those from the patient-specific positioning (Figure 4-32). The obtained results suggest that apical configuration might be the less risky in term of thromboembolic events, given i) the lower blood stagnation and ii) the faster blood flow in areas not directly along the path between the inlet (i.e., MV) and the outlets (i.e, LVAD and AV). Differently,

misalignment between the LV apical axis and the LVAD inflow cannula resulted in more convoluted blood trajectories, increasing the potential for platelets to be trapped in the LV apical regions, accumulating higher shear stress owing to their increased residence time[29].

4.8 Conclusions

In this study, the role of LV residual contractility as an additional thrombogenic factor was

investigated, since the thrombus-favourable LV flow dynamics, in the pathological LV, was hypothesized to synergize to the mechanism of platelet activation and thrombus formation. Moreover, given that both the LV residual contractility and the LVAD-induced hemodynamics might have a role in altering the flow behaviour within the LV promoting thrombogenesis, we herein analysed the mutual interactions between these two factors.

Investigation of this hypothesis was carried out by setting up a CFD model of the LV, that systematically analysed the contribution of LV residual contractility and LVAD inflow cannula implantation configurations on the LV thrombogenic potential through three sets of simulations. Concerning the model implementation, we can assert that it fulfilled all the modelling desiderata, since the geometry is patient-specific, LV wall motion is reconstructed taking into account both contraction/dilation and twist/untwist contributions, achieving a fair realism for *pre* as well as for *post* implant models. Furthermore, the implemented method for wall motion can be applied to any kind of geometry, just tuning properly the model parameters.

Concluding, the herein numerical approach proved efficient in achieving the main goals of the study; nonetheless, it showed some limitations to be declared as ideas for further improvements:

i) LV blood flow was assumed to be laminar, as in previous studies[16,17,30], with a maximum Reynolds number at the MV equal to $Re \cong 2000$. A recent CFD study[31], based on a turbulence model exploitation, actually reported turbulent fluctuations in the velocity

field in the LV, but the authors concluded that laminar models can still capture the large-scale flow features.

ii) Influence of mitral leaflets, trabeculae and papillary muscles, that can affect flow orientation and pattern of vortex formation and evolution[32], was ignored. Moreover, an almost instantaneous opening or closing of the valve orifices was assumed: valve motion undoubtedly affects the intraventricular flow, but, as pointed out by Baccani et al.[33], valve dynamics has no fundamental relevance on the LV global hemodynamic field, because of its rapidity.

i) The isovolumetric phases of the cardiac cycle were not included in the simulations even though they influence blood stasis. Furthermore, a constant velocity BC was applied at the inlet of the cannula. By contrast, it is known that cannula suction flow rate depends on the impedance of the systemic circulation.

Nonetheless, with this study we provide further mechanistic insights into the mechanisms related to intraventricular thrombus formation and thromboembolic complications in LVAD-treated patients, suggesting that both residual LV contractility and LVAD inflow cannula positioning are crucial when facing with the LVAD-induced thrombogenicity analysis.

4.9 Bibliography

1. Molisso, C. & Molisso, V. Medico-legal assessment of dilated cardiomyopathy. *G. Ital. Cardiol. (Rome).* **8,** 299–305 (2007).
2. Roberts, W. C., Siegel, R. J. & McManus, B. M. Idiopathic dilated cardiomyopathy: analysis of 152 necropsy patients. *Am. J. Cardiol.* **60,** 1340–55 (1987).
3. Feild, B. J. *et al.* Left ventricular function and hypertrophy in cardiomyopathy with depressed ejection fraction. *Circulation* **47,** 1022–31 (1973).
4. Douglas, P. S., Morrow, R., Ioli, A. & Reichek, N. Left ventricular shape, afterload and survival in idiopathic dilated cardiomyopathy. *J. Am. Coll. Cardiol.* **13,** 311–5 (1989).
5. Miller, L. W. *et al.* Use of a Continuous-Flow Device in Patients Awaiting Heart Transplantation. *N. Engl. J. Med.* **357,** 885–896 (2007).
6. Slaughter, M. S. *et al.* Advanced Heart Failure Treated with Continuous-Flow Left Ventricular Assist Device. *N. Engl. J. Med.* **361,** 2241–2251 (2009).
7. Park, S. J. *et al.* Outcomes in Advanced Heart Failure Patients With Left Ventricular Assist Devices for Destination Therapy. *Circ. Hear. Fail.* **5,** 241–248 (2012).
8. Frazier, O. ., Myers, T. J., Westaby, S. & Gregoric, I. D. Clinical experience with an implantable, intracardiac, continuous flow circulatory support device: physiologic implications and their relationship to patient selection. *Ann. Thorac. Surg.* **77,** 133–142 (2004).
9. Feldman, D. *et al.* The 2013 International Society for Heart and Lung Transplantation Guidelines for mechanical circulatory support: Executive summary. *J. Hear. Lung Transplant.* **32,** 157–187 (2013).
10. Kirklin, J. K. *et al.* Pump thrombosis in the Thoratec HeartMate II device: An update analysis of the INTERMACS Registry. *J. Hear. Lung Transplant.* **34,** 1515–1526 (2015).
11. Lampert, B. C. & Teuteberg, J. J. Right ventricular failure after left ventricular assist devices. *J. Hear. Lung Transplant.* **34,** 1123–1130 (2015).
12. Haglund, N. A. *et al.* Hemodynamic Transesophageal Echocardiography After Left Ventricular Assist Device Implantation. *J. Cardiothorac. Vasc. Anesth.* **28,** 1184–1190 (2014).
13. Stainback, R. F. *et al.* Echocardiography in the Management of Patients with Left Ventricular Assist Devices: Recommendations from the American Society

of Echocardiography. *J. Am. Soc. Echocardiogr.* **28,** 853–909 (2015).

14. Liu, G.-M. *et al.* Numerical Simulation of LVAD Inflow Cannulas with Different Tip. *Int. J. Chem. Eng.* **2012,** 1–8 (2012).
15. Liao, S. *et al.* Numerical prediction of thrombus risk in an anatomically dilated left ventricle: the effect of inflow cannula designs. *Biomed. Eng. Online* **15,** 136 (2016).
16. Prisco, A. R. *et al.* Impact of LVAD Implantation Site on Ventricular Blood Stagnation. *ASAIO J.* **63,** 392–400 (2017).
17. Liao, S., Neidlin, M., Li, Z., Simpson, B. & Gregory, S. D. Ventricular flow dynamics with varying LVAD inflow cannula lengths: In-silico evaluation in a multiscale model. *J. Biomech.* **72,** 106–115 (2018).
18. Loerakker, S., Cox, L. G. E., van Heijst, G. J. F., de Mol, B. A. J. M. & van de Vosse, F. N. Influence of dilated cardiomyopathy and a left ventricular assist device on vortex dynamics in the left ventricle. *Comput. Methods Biomech. Biomed. Engin.* **11,** 649–660 (2008).
19. Bavo, A. M. *et al.* Patient-specific CFD simulation of intraventricular haemodynamics based on 3D ultrasound imaging. *Biomed. Eng. Online* **15,** 107 (2016).
20. Kikinis, R., Pieper, S. D. & Vosburgh, K. G. in *Intraoperative Imaging and Image-Guided Therapy* 277–289 (Springer New York, 2014). doi:10.1007/978-1-4614-7657-3_19
21. Taubin, G. & Gabriel. A signal processing approach to fair surface design. in *Proceedings of the 22nd annual conference on Computer graphics and interactive techniques - SIGGRAPH '95* 351–358 (ACM Press, 1995). doi:10.1145/218380.218473
22. APOSTOLI, A. & BIANCHI, V. Development of an in vitro platform to characterize endothelial cell platelet pro-thrombotic mechanisms associated with left ventricular assist device therapy. at <https://www.politesi.polimi.it/handle/10589/135360>
23. Omar, A. M. S., Vallabhajosyula, S. & Sengupta, P. P. Left Ventricular Twist and Torsion. *Circ. Cardiovasc. Imaging* **8,** (2015).
24. Doost, S. N., Ghista, D., Su, B., Zhong, L. & Morsi, Y. S. Heart blood flow simulation: a perspective review. *Biomed. Eng. Online* **15,** 101 (2016).
25. Hunt, J. C. R. Studying turbulence using direct numerical simulation: 1987 Center for Turbulence Research NASA Ames/Stanford Summer Programme. *J.*

Fluid Mech. **190,** 375 (1988).

26. Tang, C. *et al.* Analysis of left ventricular fluid dynamics in dilated cardiomyopathy by echocardiographic particle image velocimetry. *Echocardiography* **35,** 56–63 (2018).
27. Fukuda, D. *et al.* Lesion characteristics of acute myocardial infarction: an investigation with intravascular ultrasound. *Heart* **85,** 402–6 (2001).
28. Mangual, J. O. *et al.* Comparative numerical study on left ventricular fluid dynamics after dilated cardiomyopathy. *J. Biomech.* **46,** 1611–1617 (2013).
29. Chivukula, V. K. *et al.* Left Ventricular Assist Device Inflow Cannula Angle and Thrombosis Risk. *Circ. Hear. Fail.* **11,** (2018).
30. Khalafvand, S. S., Ng, E. Y. K., Zhong, L. & Hung, T. K. Fluid-dynamics modelling of the human left ventricle with dynamic mesh for normal and myocardial infarction: Preliminary study. *Comput. Biol. Med.* **42,** 863–870 (2012).
31. Chnafa, C., Mendez, S. & Nicoud, F. Image-Based Simulations Show Important Flow Fluctuations in a Normal Left Ventricle: What Could be the Implications? *Ann. Biomed. Eng.* **44,** 3346–3358 (2016).
32. Vedula, V., Fortini, S., Seo, J.-H., Querzoli, G. & Mittal, R. Computational modeling and validation of intraventricular flow in a simple model of the left ventricle. *Theor. Comput. Fluid Dyn.* **28,** 589–604 (2014).
33. Baccani, B., Domenichini, F. & Pedrizzetti, G. Model and influence of mitral valve opening during the left ventricular filling. *J. Biomech.* **36,** 355–61 (2003).

Conclusion

5.1 Main findings

This work was focused on the implementation, development and testing of numerical strategies in order to overcome issues when dealing with 3D ultrasound imaging exploitation towards predictive patient-specific modelling approaches focused on both morphological and biomechanical analyses.

To date, 3D echocardiography (3DE) is the imaging modality of choice, being routinely employed in clinical practice thanks to its practical advantages in terms of almost null invasiveness, low costs and wide availability[1,2]. Nonetheless, despite these evident advantages, the derivation of 3D patient-specific computational models basing on ultrasound imaging is still demanding, even more if aiming at the implementation of a modelling approach to be used as predictive tool in clinical practice.

In this context, novel methods were herein proposed aiming to face *in vivo* 3DE imaging intrinsic troubles, such as i) the deficiency of morphological detail owing to poor spatial and temporal resolution as well as to a not proper acoustic window, ii) the challenge of tailoring computational models to the patient-specific scenario mimicking the morphology as well as the functionality of the investigated cardiac district, and iii) the needing to systematically analyse devices performances when dealing with real-life cases where ultrasound imaging is the only performable technique but lacking of standardized acquisition protocol.

In specific:

- First, an innovative and semi-automated framework was implemented to generate 3D model of tricuspid valve, to quantitively describe its 3D morphology and to assess its biomechanical behaviour. At this aim, an image-based in vitro experimental approach was integrated with numerical models based on finite element (FE) strategy. Experimental measurements directly performed on the benchmark (mock circulation loop) were compared with geometrical features computed on the 3D reconstructed model, pinpointing a global good consistency. Furthermore, obtained realistic reconstructions were used as the input of the FE models, even accounting for proper description of TV leaflets'

anisotropic mechanical response. As done experimentally, simulations reproduced both “incompetent” (FTR) and “competent-induced” (PMA), proving the efficiency of such a treatment and suggesting translational potential to the clinic.

- Secondly, we sought to establish a framework to build geometrically tractable, functionally equivalent models of the mitral valve (MV) chordae tendineae, addressing one of the main topics of the computational scientific literature towards the development of faithful patient-specific models from *in vivo* imaging. Exploiting the mass spring model (MSM) approach, an iterative tool was proposed aiming to the topology optimization of a paradigmatic chordal apparatus of MVs affected by functional regurgitation, in order to be able to equivalently account for tethering effect exerted by the chordae themselves. The results have shown that the algorithm actually lowered the error between the simulated valve and *ground truth* data, although the intensity of this improvement is strongly valve-dependent.
- Finally, in the last chapter, we proposed a numerical approach which allowed for a systematic and selective analysis of the mechanism associated to intraventricular thrombus formation and thrombogenic complications in a LVAD-treated dilated left ventricle (LV). Ad-hoc geometry reconstruction workflow was implemented to overcome limitations associated to imaging acquisition in this specific scenario, thus being able to generate computational model of the LV assisted with LVAD. In details, results suggested that blood stasis is influenced either by LVAD flow rate and, to a greater extent, by LV residual contractility, being the positioning of the inflow cannula insertion mandatory to be considered when dealing with LVAD thrombogenic potential assessment.

5.2 Future Developments

On the basis of the present work, a few main research directions appear as important steps for future developments.

For a general consideration it is worth to note that, despite the algorithms for the quantitative description of the 3D morphology are completely automatic, the segmentation process still requires numerous inputs of the end-user, thus increasing the time necessary to process a single dataset. However, machine learning algorithms based on adaptive models[3–6], could be exploited to heavily improve time-efficiency, trying to be compatible more and more to match clinical need. Obviously, the exploitation of such automated approaches would require a robust validation process of the reconstruction algorithms. This issue could be addressed, for example, performing imaging acquisitions on mock circulation loop, as the strategy proposed in Chapter 2 of this work, so enabling the comparison between physical measurements and virtually reconstructed models. In this way, we were able to evaluate morphological features and alterations following specific treatment, even adding a FE analysis of TV biomechanics relying on accurate morphological reconstruction. Nonetheless, although we preliminarily tackled the mechanical stress investigation pre- and post-treatment (papillary muscles approximation, PMA), the comparison with concomitant or non-concomitant annular treatment (e.g., annuloplasty) should be made to quantify the possible advantages of the sub-valvular treatment on the reduction of leaflets loading. Additionally, joined experimental and computational study could provide an insight on potential regurgitation recurrence risk after treatment with papillary muscle approximation in the setting of progressing annular dilation, possibly pinpointing prognostic potential. Obviously, on the other hand, computational approach has to be strongly validated by comparing yielded results with imaging *ground truth* data.

Concerning the applicability of the proposed numerical strategies to the clinical practice, the framework proposed in Chapter 3 could be considered a great step forward, considering also the impact of such a topic in the contextual scientific literature[7–9]. However, such an approach (namely, mass spring models[10]) provides an advantage as long as the focus of the analysis is assessing

morphological alterations following different possible treatments, being the trade-off between solution accuracy and computational speed is crucial, as well discussed by Pappalardo and colleagues[11]. In this direction, it would be interesting to integrate this kind of solution as a preparatory step in the FE models' implementation workflow, thus potentially improve their accuracy.

Finally, even for strategies not directly intended to be used as clinical patient-specific predicting tools (i.e., Chapter 4) a retrospective study on a large cohort of patients is suggested, exploiting wider availability of 3D echocardiography, to test the diagnostic and prognostic potential of the computed variables.

5.3 Bibliography

1. Drake, D. H., Zimmerman, K. G., Hepner, A. M. & Nichols, C. D. Echo-Guided Mitral Repair. *Circ. Cardiovasc. Imaging* **7,** 132–141 (2014).
2. Chambers, J. B., Myerson, S. G., Rajani, R., Morgan-Hughes, G. J. & Dweck, M. R. Multimodality imaging in heart valve disease. *Open Hear.* **3,** e000330 (2016).
3. Zreik, M. *et al.* Deep learning analysis of the myocardium in coronary CT angiography for identification of patients with functionally significant coronary artery stenosis. *Med. Image Anal.* **44,** 72–85 (2018).
4. Lugo-Fagundo, C., Vogelstein, B., Yuille, A. & Fishman, E. K. Deep Learning in Radiology: Now the Real Work Begins. *J. Am. Coll. Radiol.* (2017). doi:10.1016/j.jacr.2017.08.007
5. Grbic, S. *et al.* Personalized mitral valve closure computation and uncertainty analysis from 3D echocardiography. *Med. Image Anal.* (2017). doi:10.1016/j.media.2016.03.011
6. Grbic, S. *et al.* Complete valvular heart apparatus model from 4D cardiac CT. *Med. Image Anal.* **16,** 1003–1014 (2012).
7. Bloodworth, C. H. *et al.* Ex Vivo Methods for Informing Computational Models of the Mitral Valve. *Ann. Biomed. Eng.* **45,** 496–507 (2017).
8. Drach, A., Khalighi, A. H. & Sacks, M. S. A comprehensive pipeline for multi-resolution modeling of the mitral valve: Validation, computational efficiency, and predictive capability. *Int. j. numer. method. biomed. eng.* **34,** e2921 (2018).
9. Khalighi, A. H. *et al.* Development of a Functionally Equivalent Model of the Mitral Valve Chordae Tendineae Through Topology Optimization. *Ann. Biomed. Eng.* (2018). doi:10.1007/s10439-018-02122-y
10. Hammer, P. E., Sacks, M. S., del Nido, P. J. & Howe, R. D. Mass-spring model for simulation of heart valve tissue mechanical behavior. *Ann. Biomed. Eng.* **39,** 1668–79 (2011).
11. Pappalardo, O. A. *et al.* Mass-spring models for the simulation of mitral valve function: Looking for a trade-off between reliability and time-efficiency. *Med. Eng. Phys.* **47,** 93–104 (2017).